

Measurement of the Higgs boson transverse momentum spectrum in the WW decay channel at 8 TeV and first results at 13 TeV

Lorenzo Viliani
of University of Florence

PhD Thesis

Abstract

The cross section for Higgs boson production in pp collisions is studied using the $H \rightarrow W^+W^-$ decay mode, followed by leptonic decays of the W bosons, leading to an oppositely charged electron-muon pair in the final state. The measurements are performed using data collected by the CMS experiment at the LHC with pp collisions at a centre-of-mass energy of 8 TeV, corresponding to an integrated luminosity of 19.4 fb^{-1} . The Higgs boson transverse momentum (p_T) is reconstructed using the lepton pair p_T and missing p_T . The differential cross section times branching fraction is measured as a function of the Higgs boson p_T in a fiducial phase space defined to match the experimental acceptance in terms of the lepton kinematics and event topology. The production cross section times branching fraction in the fiducial phase space is measured to be $39 \pm 8\text{ (stat)} \pm 9\text{ (syst)}\text{ fb}$. The measurements are compared to theoretical calculations based on the standard model to which they agree within experimental uncertainties.

²⁵ Contents

²⁶ 1. Electroweak and QCD physics at LHC	³
²⁷ 2. The CMS experiment at the LHC	⁵
2.1. The Large Hadron Collider	5
2.2. The <i>Compact Muon Solenoid</i> experiment	9
2.2.1. The solenoid	12
2.2.2. The tracker	13
2.2.3. The electromagnetic calorimeter (ECAL)	17
2.2.4. The hadron calorimeter (HCAL)	19
2.2.5. The muon system	20
2.3. The CMS trigger system	23
2.3.1. The Level-1 trigger	23
2.3.2. The high level trigger (HLT)	25
³⁸ 3. Reconstruction and identification of physics objects	²⁷
3.1. The Particle Flow technique	27
3.2. Leptons reconstruction and identification	29
3.2.1. Muon reconstruction and identification	29
3.2.2. Muon isolation	31
3.2.3. Muon momentum scale and resolution	31
3.2.4. Electron reconstruction and identification	32
3.2.5. Electron isolation	33
3.2.6. Electron momentum scale and resolution	33
3.2.7. Lepton identification and isolation efficiency	34
3.2.8. Lepton trigger efficiency	35
3.3. Jets reconstruction and identification	37
3.3.1. Jet reconstruction in CMS	37
3.3.2. Jet energy correction	39
3.4. Jet b tagging	43
3.5. Missing transverse energy	44
⁵⁴ 4. Measurement of the Higgs boson transverse momentum at 8 TeV using $H \rightarrow WW \rightarrow 2\ell 2\nu$ decays	⁴⁷
4.1. Introduction	47

57	4.2. Data sets, triggers and MC samples	49
58	4.2.1. Data sets and triggers	49
59	4.2.2. Monte Carlo samples	49
60	4.3. Analysis Strategy	52
61	4.3.1. Event reconstruction and selections	52
62	4.3.2. Fiducial phase space	55
63	4.3.3. Binning of the p_T^H distribution	56
64	4.4. Background estimation	58
65	4.4.1. Top quark background	58
66	4.4.2. WW background	67
67	4.4.3. Other backgrounds	71
68	4.5. Systematic uncertainties	75
69	4.5.1. Background normalization uncertainties	75
70	4.5.2. Experimental uncertainties	77
71	4.5.3. Theoretical uncertainties	78
72	4.5.4. Statistics uncertainty of the simulated samples	80
73	4.5.5. Treatment of systematic uncertainties in the shape analysis	81
74	4.6. Signal extraction	81
75	4.6.1. Fitting procedure	82
76	4.6.2. Signal and background yields	85
77	4.7. Unfolding	87
78	4.7.1. Treatment of systematic uncertainties	91
79	4.8. Results	93
80	5. Search for the SM Higgs boson in the $H \rightarrow WW$ channel with the first 13 TeV LHC data	97
82	5.1. Introduction	97
83	5.2. Data and simulated samples	97
84	5.3. Analysis strategy	102
85	5.3.1. Event reconstruction	102
86	5.3.2. Event selection and background rejection	107
87	5.3.3. Signal extraction	109
88	5.4. Background estimation	114
89	5.4.1. WW background	114
90	5.4.2. Top quark background	114
91	5.4.3. Jet-induced (or Fake) background	116
92	5.4.4. DY background	116
93	5.4.5. Other backgrounds	117
94	5.5. Systematic uncertainties	118
95	5.6. Results	120

96	6. Search for high mass resonances decaying to a W boson pair with first	
97	13 TeV LHC data	123
98	6.1. Introduction	123
99	6.2. Data and simulated samples	123
100	6.3. Analysis strategy	125
101	6.4. Background estimation	128
102	6.5. Systematic uncertainties	131
103	6.6. Signal extraction and limit setting	131
104	6.7. Results	135
105	7. Conclusions	141
106	A. Fiducial region definition and optimization	143
107	Bibliography	151

Chapter 1.

₁₀₉ Electroweak and QCD physics at
₁₁₀ LHC

Chapter 2.

¹¹¹ The CMS experiment at the LHC

¹¹² In this chapter, the main characteristics of the Large Hadron Collider (LHC particle
¹¹³ accelerator and Compact Muon Solenoid (CMS) experiment are described.

¹¹⁴ 2.1. The Large Hadron Collider

¹¹⁵ The LHC [1–4] at CERN, officially inaugurated on 21st October 2008, is the largest and
¹¹⁶ most powerful hadron collider ever built. Installed in the underground tunnel which hosted
¹¹⁷ the Large Electron Positron Collider (LEP) [5–7], the leptonic accelerator in operation until
¹¹⁸ 2nd November 2000, the LHC accelerator has the shape of a circle with a length of about
¹¹⁹ 27 km and is located underground at a depth varying between 50 m to 175 m, straddling the
¹²⁰ Franco-Swiss border near Geneva. It is designed to collide two 7 TeV counter-circulating
¹²¹ beams of protons resulting in a center-of-mass energy of 14 TeV, or two beams of heavy
¹²² ions, in particular lead nuclei at an energy of 2.76 TeV/nucleon in the center-of-mass frame.

¹²³ The transition from a leptonic collider to a hadronic collider entailed the following
¹²⁴ advantages: first, it has been possible to build a machine that having the same size of the
¹²⁵ previous one (and therefore accommodated in the same LEP tunnel, substantially reducing
¹²⁶ the cost and time of construction), could reach a higher energy in the center-of-mass
¹²⁷ frame. This is due to the much lower amount of energy loss through synchrotron radiation
¹²⁸ emitted by the accelerated particles, that is proportional to the fourth power of the ratio
¹²⁹ E/m between their energy and their mass. Secondly, the composite structure of protons
¹³⁰ compared to the elementary structure of electrons allows LHC to be able to simultaneously
¹³¹ access a wider energy spectrum, despite the production of many low energies particles in a
¹³² complex environment. This is a particularly important feature for a machine dedicated to
¹³³ the discovery of “new” physics.

¹³⁴ In Fig. 2.1 a schematic description of the accelerator complex installed at CERN is shown.
¹³⁵ The acceleration is performed in several stages [4]. The protons source is a *Duoplasmatron*:
¹³⁶ the protons are obtained by removing electrons from a source of hydrogen gas and then
¹³⁷ sent to the LINAC2, a 36 m long linear accelerator which generates a pulsed beam with
¹³⁸ an energy of 50 MeV using Radio Frequency Quadrupoles (RFQ) and focusing quadrupole
¹³⁹ magnets. The beam is subsequently sent to the Proton Synchrotron Booster (PSB), a
¹⁴⁰ circular accelerator consisting of four superimposed synchrotron rings with a circumference
¹⁴¹ of about 160 m, which increases the proton energy up to 1.4 GeV. Then, protons are

142 injected into the Proton Synchrotron (PS), a single synchrotron ring with a circumference
 143 of about 600 m where the energy is increased to 25 GeV. The sequential combination of
 144 these two synchrotrons also allows to create a series of protons bunches interspersed by
 145 25 ns as required for the correct operation of LHC. The final proton injection stage is the
 146 Super Proton Synchrotron (SPS), a synchrotron with a circumference of approximately
 147 7 km where protons reach an energy value of 450 GeV. Subsequently, protons are extracted
 148 and injected into the LHC ring via two transmission lines, to generate two beams running
 149 in opposite directions in two parallel pipes and which are accelerated up to the energy of
 150 interest. In the two pipes an ultrahigh vacuum condition is maintained (about 10^{-10} Torr)
 151 to avoid the spurious proton interactions with the gas remnants. At full intensity, each
 152 proton beam consists of 2808 bunches and each bunch contains around 10^{11} protons. The
 153 beams are squeezed and collide for a length of about 130 m at four interaction points where
 154 the four main experiments (ALICE, ATLAS, CMS and LHCb) are placed:

- 155 • CMS (Compact Muon Solenoid) [8] and ATLAS (A Toroidal LHC ApparatuS) [9] are
 156 two general-purpose detectors designed to investigate the largest possible spectrum of
 157 physics. In particular, they have been devoted to the detection of particles produced
 158 by a Higgs boson decay and to look for any evidence of possible new physics. The use
 159 of two detectors chasing the same objectives but designed independently is crucial for
 160 a cross-check of any possible new discovery;
- 161 • LHCb (LHC beauty) [10] is an experiment primarily designed to study CP (combined
 162 Charge conjugation and Parity symmetry) violation in electroweak interactions and to
 163 study asymmetries between matter and antimatter through the analysis of rare decays
 164 of hadrons containing b quarks. The detector is also able to perform measurements in
 165 the forward region, at small polar angles with respect to the beam line;
- 166 • ALICE (A Large Ion Collider Experiment) [11] is an experiment studying heavy ions
 167 collisions, through the production of a new state of matter called quark-gluon plasma.

168 Two other smaller experiments are located along the circumference of the LHC accelerator,
 169 TOTEM and LHCf, which focus on particles emitted in the forward direction. TOTEM
 170 (TOTal Elastic and diffractive cross section Measurement) [12] measures the proton-proton
 171 interaction cross section and accurately monitors the luminosity of the LHC using detectors
 172 positioned on either side of the CMS interaction point. LHCf (LHC forward) [13] is made
 173 up of two detectors which sit along the LHC beamline, at 140 m either side of the ATLAS
 174 collision point. It makes use of neutral particles thrown forward by LHC collisions as a
 175 source to simulate the interaction with the atmosphere of very high energy cosmic rays
 176 (between 10^{17} TeV and 10^{20} TeV) in laboratory conditions.

177 A series of about 1200 magnetic dipoles bend the beams along the accelerator ring.
 178 They are located along the “arc” structures of the circumference. The ring, in fact, can
 179 be subdivided into octants, with eight curve regions (the “arcs”) separated by rectilinear
 180 regions. In these straight regions, instead, almost 400 focusing and defocusing quadrupoles
 181 are located, which maintain the beam stable along the orbit, and some other small multipolar
 182 magnets (sextupoles and octupoles) are used to make additional minor corrections to the
 183 beam direction. A radio frequency acceleration system, consisting of 16 superconducting

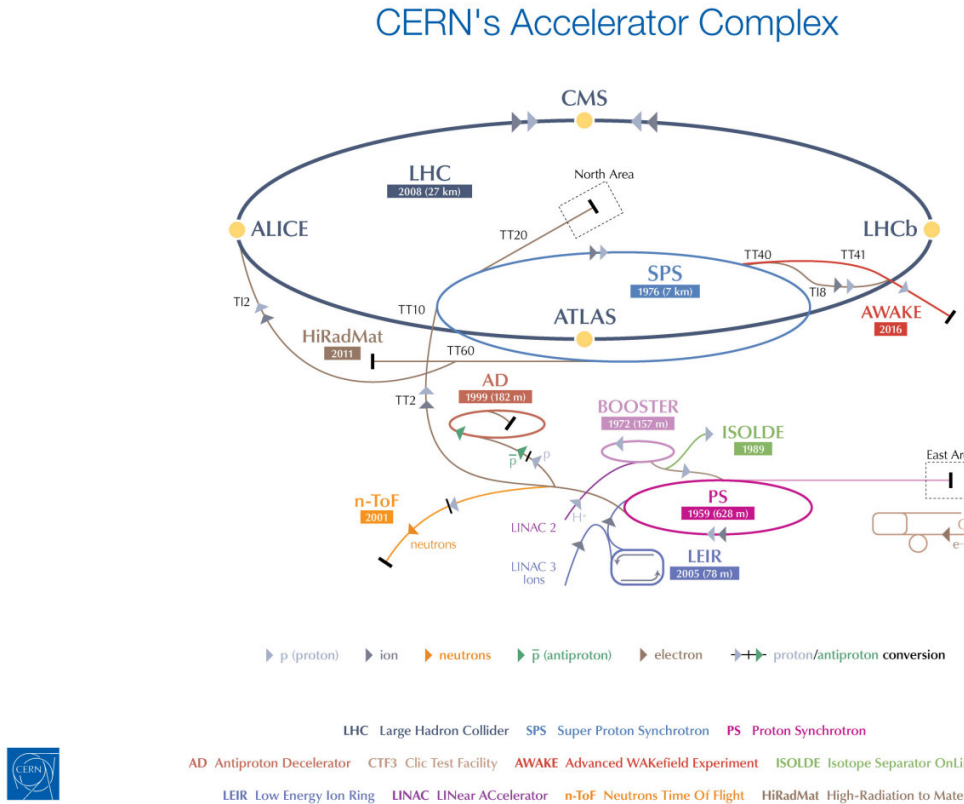


Figure 2.1.: Schematic description of the accelerator complex installed at CERN.

radio-frequency resonant cavities, is used to increase the proton energy by 0.5 MeV with each beam revolution. The 7 TeV per-beam-energy limit on the LHC is not determined by the electric field generated by the radiofrequency cavity but by the magnetic field necessary to maintain the protons in orbit, given the current technology for the superconducting magnets, which is about 5.4 T on average.

One of the most important parameters of an accelerator is the instantaneous luminosity \mathcal{L} , which gives a measure of the rate of events one can expect given the process cross section. In fact, for a given physics process with cross section σ , producing N events for unit of time, the instantaneous luminosity is defined by the following equation:

$$N = \sigma \mathcal{L} \quad . \quad (2.1)$$

The LHC design luminosity is $\mathcal{L} = 10^{34} \text{ cm}^{-2} \text{s}^{-1}$, leading to around 1 billion proton interactions per second.

The instantaneous luminosity is a parameter which depends on the construction characteristics of the accelerator, and can be expressed by the following approximated formula:

$$\mathcal{L} = f \frac{n_1 n_2}{4\pi\sigma_x\sigma_y} , \quad (2.2)$$

where n_1 and n_2 are the number of particles contained in the two bunches colliding at a frequency f , and σ_x and σ_y are the beam sizes in the transverse plane. At LHC, the bunches collide with $f = 40$ MHz and the transverse size of the beam can be squeezed down to around 15 μm . Then, the integrated luminosity L is defined as the time integral of the instantaneous luminosity:

$$L = \int \mathcal{L} dt . \quad (2.3)$$

The main parameters of the LHC machine are listed in Table 2.1.

The LHC started to be operative in September 2008 but, due to a faulty interconnection between two magnets which caused a helium leakage in the tunnel, the operation was stopped and restarted in March 2010. During 2010 and 2011 LHC ran successfully and provided proton proton collisions at a center-of-mass energy of 7 TeV, delivering a total integrated luminosity of about 6.1 fb^{-1} . The encouraging results in the Higgs boson search provided by the ATLAS and CMS Collaborations led to the decision of extending the data taking period to the end of 2012, and to increase the center-of-mass energy up to 8 TeV. During 2012, LHC delivered to the experiments an integrated luminosity of 23.3 fb^{-1} . After the first long shutdown (LS1), a two years period started in the early 2013 where the LHC operation stopped for maintenance and upgrade, the LHC started again delivering proton proton collisions on 3rd June 2015, at the new record center-of-mass energy of 13 TeV. During the 2015 the LHC delivered an integrated luminosity of 4.2 fb^{-1} . Nowadays, LHC is still colliding bunches of protons at $\sqrt{s} = 13$ TeV, reaching unprecedented instantaneous luminosities and delivering a total integrated luminosity of 31 fb^{-1} . The cumulative delivered luminosity versus time for the different LHC data taking periods is shown in Fig. 2.2.

As the instantaneous luminosity increases, the probability of multiple proton proton interactions to occur in a single bunch crossing grows higher as well. In this instance, the main goal is the identification and reconstruction of a single primary collision where the physics event of interest occurs among the background of the additional proton proton interactions. Such backgrounds are due to processes occurring with very high probability, like the production of low- p_T jets. These additional collisions are known as pile up (PU). During the LHC current run the average number of pile up events is 23, with some event exhibiting over 45 pile up collisions.

Table 2.1.: LHC technical parameters for proton proton collisions.

Parameter	Value
Maximum dipole magnetic field	8.33 T
Dipole operating temperature	1.9 K
Beam energy at injection	450 GeV
Beam energy at collision (nominal)	7 TeV
Beam energy at collision (2012)	4 TeV
Beam energy at collision (2015–2016)	6.5 TeV
Maximum instantaneous luminosity (nominal)	$10^{34} \text{ cm}^{-2}\text{s}^{-1}$
Maximum instantaneous luminosity (2012)	$7.7 \cdot 10^{33} \text{ cm}^{-2}\text{s}^{-1}$
Maximum instantaneous luminosity (2015–2016)	$1.2 \cdot 10^{34} \text{ cm}^{-2}\text{s}^{-1}$
Number of bunches per proton beam (nominal)	2808
Number of bunches per proton beam (2012)	1380
Number of bunches per proton beam (2015–2016)	2220
Maximum number of protons per bunch	$1.69 \cdot 10^{11}$
Bunch separation in time (nominal)	25 ns
Bunch separation in time (2012)	50 ns
Bunch separation in time (2015–2016)	25 ns
Collision frequency (nominal)	40 MHz
Collision frequency (2012)	20 MHz
Collision frequency (2015–2016)	40 MHz
Energy loss per turn at 14 TeV	7 keV

2.2. The *Compact Muon Solenoid* experiment

The CMS apparatus is a general purpose detector situated in one of the four LHC interaction points¹. The detector is designed to investigate a wide range of physics, from the search of the Higgs boson, to SM measurements and BSM physics searches. To achieve this goal, the detector is able to identify and reconstruct all the physics objects that may be produced in the proton proton collisions: electrons, muons, photons and jets. The main feature of the CMS detector is a superconducting solenoidal magnet which is capable to produce a

¹The CMS detector is placed in a cavern 100 m underground in the area called Point 5, near the village of Cessy, in France.

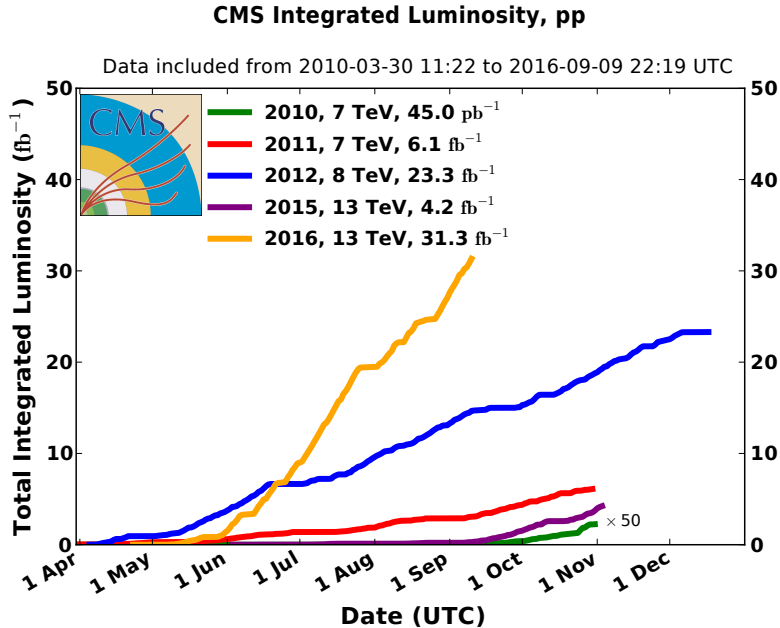


Figure 2.2.: Cumulative luminosity versus day delivered to CMS during proton proton collisions.

3.8 T magnetic field. Such a strong magnetic field is the key aspect which permits to have a compact design of the detector. The detector has a cylindrical structure, which is typical of general purpose detectors, which consists of several cylindrical detecting layers, coaxial with the beam direction (*barrel* region), closed at both ends with detecting disks (*endcap* region), in such a way to ensure the hermetic closure of the apparatus.

The coordinate system used by CMS is a right-handed Cartesian system, with the origin at the center of the detector, in the nominal beam collision point. The x -axis is chosen to point radially towards the center of the LHC circumference and the y -axis is directed upwards along the vertical. The z -axis is oriented along the beam direction, according to the anticlockwise direction of the LHC ring if seen from above. The CMS cylindrical symmetry and the Lorentz invariant description of the proton proton collisions, suggest the use of a pseudo-angular reference frame, described by the triplet of coordinates (r, ϕ, η) , where r is the distance from the z -axis, ϕ is the azimuthal angle, measured starting from the x -axis positive direction, and η is the pseudorapidity, defined by the following equation:

$$\eta = -\ln \left(\tan \frac{\theta}{2} \right) \quad , \quad (2.4)$$

where θ is the polar angle. The use of pseudorapidity is preferred over the polar angle because differences in pseudorapidity are Lorentz invariant under boosts along the z -axis.

249 In the limit of ultrarelativistic particles the pseudorapidity coincides with the rapidity y :

$$y = \frac{1}{2} \ln \left(\frac{E + p_z}{E - p_z} \right) \quad , \quad (2.5)$$

250 where E is the particle energy and p_z is the momentum projection along the z -axis.

251 The schematic view of the CMS detector, which has a length of 21.5 m, a diameter of
252 15 m and a weight of about 14000 tons, is shown in Fig. 2.3. From the inner region to the
253 outer one, the various CMS sub-detectors are:

- 254 • **Silicon tracker:** it occupies the region $r < 1.2$ m and $|\eta| < 2.5$. It is composed of an
255 inner silicon pixel vertex detector and a surrounding silicon microstrip detector, with
256 a total active area of about 215 m². It is used to reconstruct charged particle tracks
257 and vertices;
- 258 • **Electromagnetic calorimeter (ECAL):** placed in the region $1.2 \text{ m} < r < 1.8$ m
259 and $|\eta| < 3$, it consists of many scintillating crystals of lead tungstate (PbWO₄). It is
260 used for the measurement of the trajectory and the energy released by electrons and
261 photons;
- 262 • **Hadronic calorimeter (HCAL):** it is placed in the region $1.8 \text{ m} < r < 2.9$ m and
263 $|\eta| < 5$. It is made up of brass layers alternated with plastic scintillators and it is
264 used to measure the direction and energy deposited by the hadrons produced in the
265 interactions;
- 266 • **Superconducting solenoidal magnet:** it occupies the region $2.9 \text{ m} < r < 3.8$ m
267 and $|\eta| < 1.5$ and generates an internal uniform magnetic field with an intensity of
268 3.8 T, pointing along the direction of the beams. The magnetic field is necessary to
269 bend the trajectories of charged particles, in order to allow the measurement of their
270 momentum through the curvature observed in the tracking system. The magnetic
271 field lines are closed by an external 21 m long iron yoke, that has a diameter of 14 m.
272 Outside the return yoke, a residual 1.8 T magnetic field is present, pointing in the
273 opposite direction with respect to the internal field;
- 274 • **Muon system:** the outermost system, which is placed in the region $4 \text{ m} < r < 7.4$ m
275 and $|\eta| < 2.4$, has the purpose of reconstructing the tracks of muons passing through
276 it. It consists of Drift Tubes (DT) in the barrel region and Cathode Strip Chambers
277 (CSC) in the endcaps. A complementary system of Resistive Plate Chambers (RPC)
278 is used both in the barrel and endcaps. The muon chambers are housed inside the
279 iron structure of the return yoke.

280 In Fig. 2.4 the response of the various CMS sub-detectors to the passage of different types
281 of particles is sketched. In the following sections a brief description of each sub-detector is
282 given.

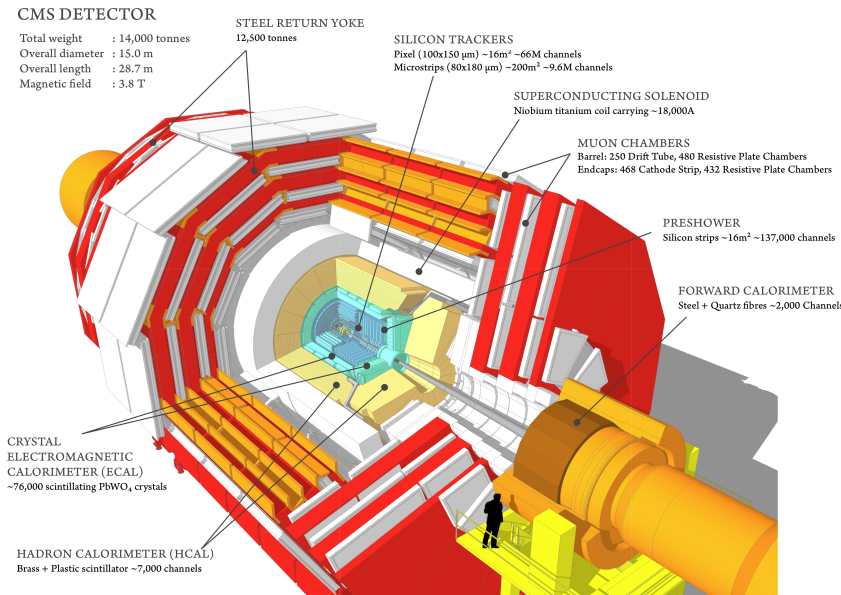


Figure 2.3.: Schematic view of the CMS detector showing its sub-detectors.

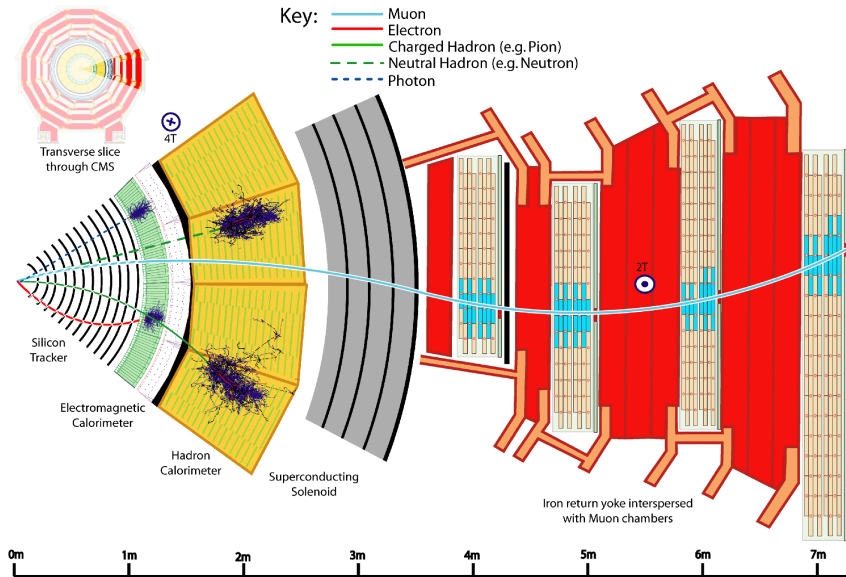


Figure 2.4.: Schematic view of a slice of the CMS detector, showing the sub-detectors response to the passage of different types of particles.

283 2.2.1. The solenoid

284 The CMS magnet [14], which contains the tracker, the electromagnetic and the hadronic
 285 calorimeters, is the biggest superconducting solenoid ever built. The solenoid can generate
 286 a magnetic field of 3.8 T in the internal bore, which has a diameter of 6 m and a length of

287 12.5 m. The energy stored in the magnet is about 2.7 GJ at full current. The superconductor
 288 is made of four Niobium-Titanium layers and it is cooled down to about 4 K through a
 289 liquid Helium cooling plant. In case of a quench, when the magnet loses its superconducting
 290 property, the energy is dumped to resistors within 200 ms. The magnet return yoke of
 291 the barrel is composed with three sections along the z -axis; each one is split into 4 layers
 292 (holding the muon chambers in the gaps). Most of the iron volume is saturated or nearly
 293 saturated, and the field in the yoke is about the half (1.8 T) of the field in the central
 294 volume.

295 2.2.2. The tracker

296 The silicon tracker is the detector closest to the beam collision point. Its goal is the
 297 high resolution reconstruction of the trajectories of charged particles originating from the
 298 interaction point and the identification of the position of secondary vertices produced by
 299 particles with a short mean life time (in particular hadrons containing the b quark, that
 300 decay after few hundred of μm). The events produced in the proton proton collisions can
 301 be very complex and track reconstruction is an entangled pattern recognition problem.
 302 Indeed, at the nominal instantaneous luminosity of operation, an average of about 20 pile up
 303 events overlapping to the event of interest are expected, leading to about 1000 tracks to be
 304 reconstructed every 25 ns. In order to make the pattern recognition easier, two requirements
 305 are fundamental:

- 306 • a low occupancy detector;
- 307 • a large redundancy of the measured points (*hits*) per track.

308 The first requirement is achieved building a detector with high granularity². The redundancy
 309 of the hits is instead achieved having several detecting layers, and is necessary to reduce the
 310 ambiguity on the assignment of the hits to a given track. Nevertheless, the amount of tracker
 311 material has to be as low as possible, in order to avoid compromising the measurement
 312 of the particle trajectory. An excessive amount of material would indeed deteriorate the
 313 measurement, mainly because of the increased probability of particle multiple scattering.
 314 The outer detectors such as ECAL would be influenced by the material as well, for example
 315 because of the increased probability for a photon to convert to an electron-positron pair
 316 in the tracker material. For this reasons, the tracker layers are limited in number and
 317 thickness.

318 The tracker comprises a large silicon strip detector with a small silicon pixel detector
 319 inside it. In the central η region, the pixel tracker consists of three co-axial barrel layers at
 320 radii between 4.4 cm and 10.2 cm and the strip tracker consists of ten co-axial barrel layers
 321 extending outwards to a radius of 110 cm. Both sub-detectors are completed by endcaps on
 322 either side of the barrel, each consisting of two disks in the pixel tracker, and three small
 323 plus nine large disks in the strip tracker. The endcaps extend the acceptance of the tracker

²The granularity of a detector is defined as the angular range ($\Delta\eta \times \Delta\phi$) that each individual element is able to resolve.

324 up to $|\eta| < 2.5$. A three-dimensional schematic view of the tracker is shown in Fig. 2.5,
325 while in Fig. 2.6 a pictorial representation of a slice of the tracker is displayed, showing the
326 various layers of the sub-detectors.

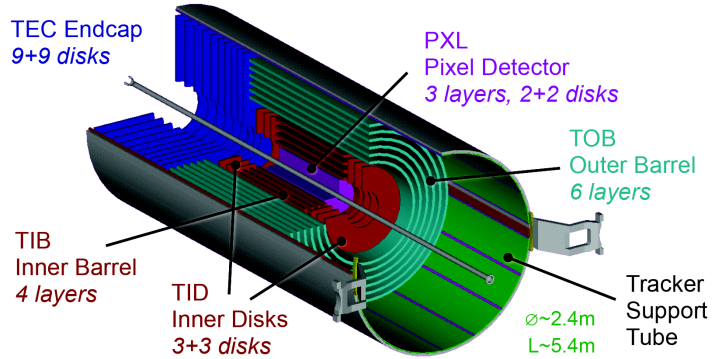


Figure 2.5.: Three-dimensional schematic view of the CMS silicon tracker.

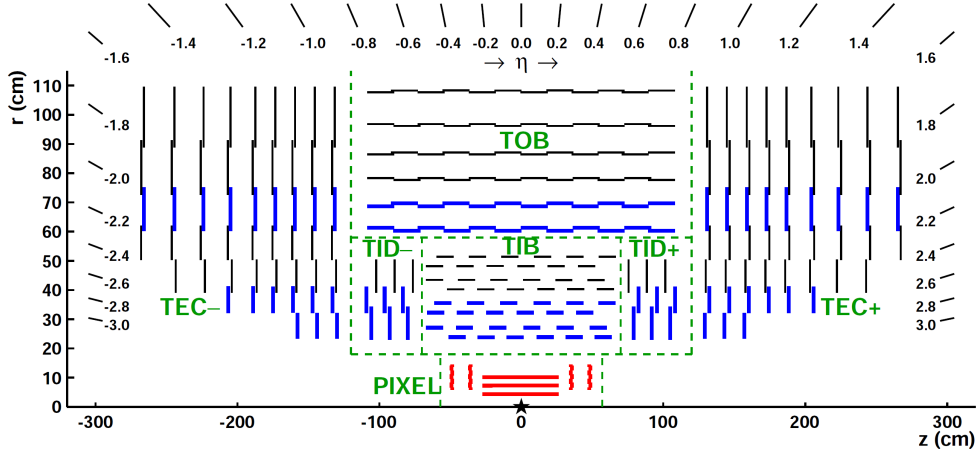


Figure 2.6.: Pictorial view of a tracker slice in the r - z plane. Pixel modules are shown in red, single-sided strip modules are depicted as black thin lines and strip stereo modules are shown as blue thick lines.

327 The whole tracker has a cylindrical shape with a length of 5.8 m and a diameter of 2.5 m,
328 with the axis aligned to the beams direction. The average number of hits per track is 12-14,
329 in order to have a high reconstruction efficiency and a low rate of fake tracks.

330 The material budget of the tracker as obtained from a simulation of the detector is
331 shown in Fig. 2.7, reported both in units of radiation length t/X_0 and in units of nuclear
332 interaction length t/λ_I , as a function of η . The region $1 < |\eta| < 2$ exhibits a larger material
333 budget due to the presence of cables and services.

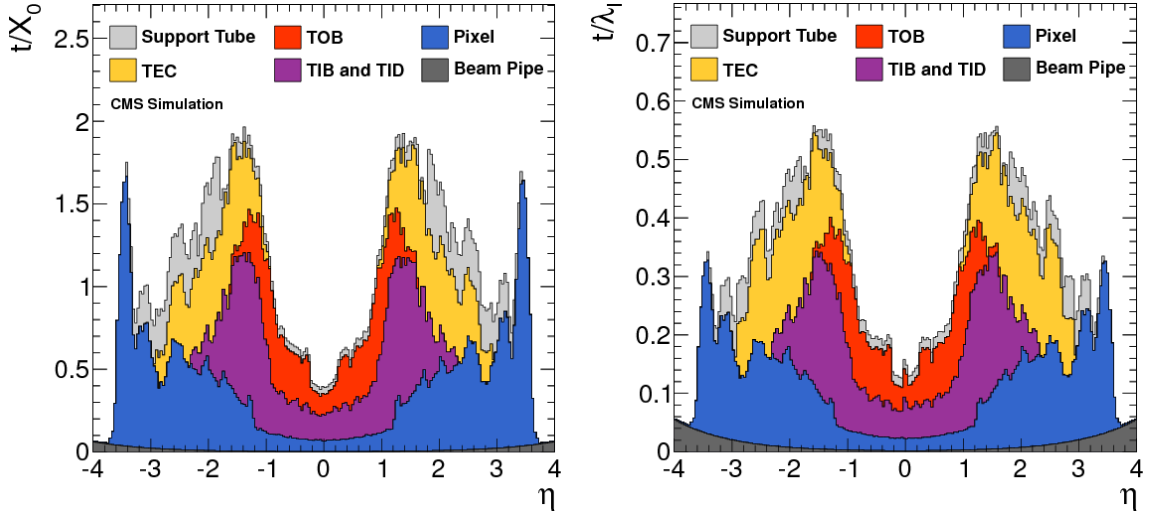


Figure 2.7.: Total thickness t of the tracker material expressed in units of X_0 (left) and λ_I (right), as a function of η . The contribution to the total material budget of each part of the detector is shown.

334 The pixel detector

335 The pixel detector, shown in Fig. 2.8, is mainly used as starting point in the CMS track
 336 reconstruction and is of fundamental importance for the reconstruction of primary and
 secondary vertices. The pixel detector is placed in the closest position to the collision point,

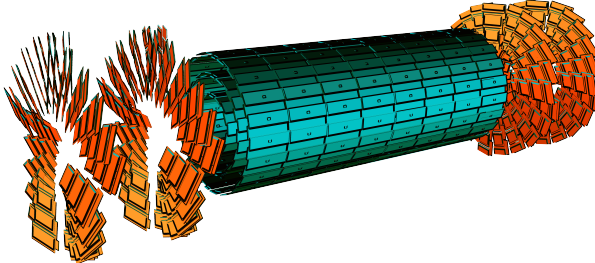


Figure 2.8.: Schematic view of the CMS pixel detector.

337 where the amount of radiation is larger. It is placed in the region $|\eta| < 2.5$ and consists of
 338 three cylindrical layers 53 cm long in the barrel region, located at $r = 4.4, 7.3$ and 10.2 cm,
 339 and two pairs of endcap disks with radii between 6 and 15 cm at $z = \pm 34.5$ and ± 46.5 cm,
 340 covering a total area of about 1 m^2 . The detector is composed of many modules, for a total
 341 of 768 in the barrel and 672 in the endcaps. Each endcap is composed of 24 segments,
 342 each one tilted with respect to the adjacent ones and containing 7 modules. Each module
 343 consists of several units which contain a highly segmented silicon sensor with a thickness of
 344 250 μm . In order to achieve an optimal vertex position resolution in both the (r, ϕ) and
 345

³⁴⁶ z -coordinates, a design with a rectangular pixel shape with an area of $150 \times 100 \mu\text{m}^2$ was
³⁴⁷ adopted, with the $100 \mu\text{m}$ size oriented along the (r, ϕ) direction in the barrel region, and
³⁴⁸ along the z -direction in the endcap region. The achievable hit reconstruction resolution is
³⁴⁹ about $10 - 15 \mu\text{m}$ in the barrel and $15 \mu\text{m}$ in the endcaps.

³⁵⁰ The microstrip detector

³⁵¹ In this region of the detector the radiation flow is low enough to allow the use of a
³⁵² less segmented device, such as the silicon microstrip detector. The microstrip tracker is
³⁵³ composed of 15148 silicon modules, covering a total area of about 193 m^2 with a total of
³⁵⁴ 9.3 million strips. Two types of modules are installed: single sided modules consist of one
³⁵⁵ sensor stucked onto a carbon fiber support together with the readout electronics, with the
³⁵⁶ silicon strips laying along the z direction in the barrel and along the (r, ϕ) direction in the
³⁵⁷ endcaps. The other type of module, referred to as stereo-module, consists of two sensors
³⁵⁸ stucked together back to back and tilted of a relative angle of 100 mrad. This combination
³⁵⁹ allows a three-dimensional measurement of the particle interaction point, providing the
³⁶⁰ information along the z -direction. The whole microstrip tracker is 5.4 m long and extends
³⁶¹ up to $r = 1.1 \text{ m}$. As the pixel detector, the microstrip detector consists of a barrel and an
³⁶² endcap region and is divided into four distinct parts, as shown in Fig. 2.6. The barrel is
³⁶³ made up of the following parts:

- ³⁶⁴ • TIB (*Tracker Inner Barrel*): it consists of four cylindrical coaxial layers, covering the
³⁶⁵ region up to $|z| < 65 \text{ cm}$. In this region the detectors have a thickness of $300 \mu\text{m}$ and
³⁶⁶ the strips are separated by a variable pitch between 80 and $120 \mu\text{m}$. The first two
³⁶⁷ layers are composed of stereo modules while the other layers have single-sided modules.
³⁶⁸ Since the strips are oriented along the z axis, the position resolution is more precise
³⁶⁹ in the (r, ϕ) direction, about $23 - 34 \mu\text{m}$, with respect to the z direction, where a
³⁷⁰ resolution of about $230 \mu\text{m}$ is obtained thanks to the stereo modules.
- ³⁷¹ • TOB (*Tracker Outer Barrel*): it consists of six cylindrical coaxial layers, placed in the
³⁷² region $55 \text{ cm} < r < 65 \text{ cm}$ and $|z| < 110 \text{ cm}$. Stereo modules are mounted on the two
³⁷³ inner layers. Since the density of particles passing through this region is lower with
³⁷⁴ respect to the TIB, the pitch between the strips is larger ($120 - 180 \mu\text{m}$) and the
³⁷⁵ strips are longer (190 mm). The spatial resolution varies in the range $25 - 52 \mu\text{m}$ in
³⁷⁶ the (r, ϕ) direction, and is about $530 \mu\text{m}$ in the z coordinate in the stereo modules.

³⁷⁷ The endcaps are also made up of two parts:

- ³⁷⁸ • TID (*Tracker Inner Disk*): it consists of six disks, three per side, placed orthogonally
³⁷⁹ with respect to the beam axis, between the TIB and the TOB. The modules are
³⁸⁰ positioned in a ring shape, with the strips oriented in the radial direction, and they
³⁸¹ are alternately placed on the internal and on the external side of the disk. The two
³⁸² innermost rings of the TID are equipped with stereo modules. The thickness of the
³⁸³ silicon is $300 \mu\text{m}$.
- ³⁸⁴ • TEC (*Tracker EndCap*): each one of the two TEC is made of nine disks which extend
³⁸⁵ to the region $120 \text{ cm} < |z| < 280 \text{ cm}$. Each disk is divided into 8 slices in each of which

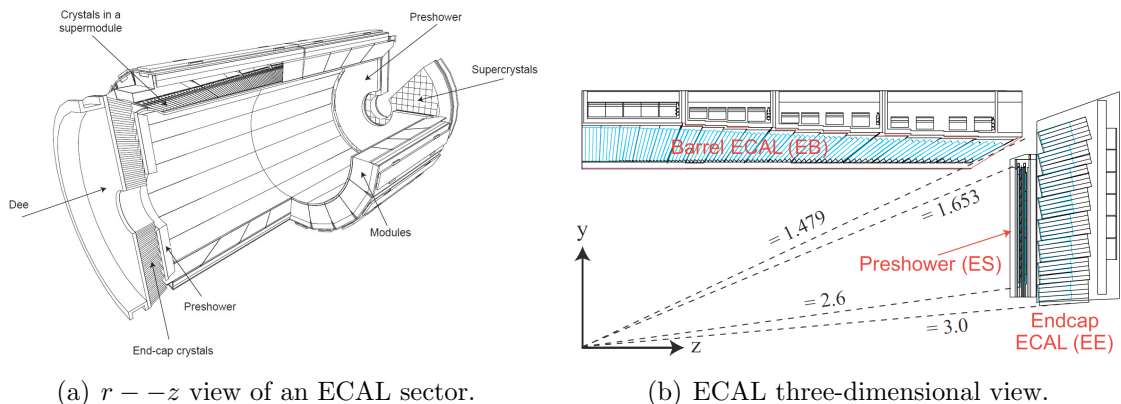
a number ranging from 4 to 7 modules are mounted in a ring shape, depending on the position along z . Also in this case the modules are alternately mounted on the internal and on the external side of the disk, with the strips radially oriented. On the two innermost rings and on the fifth one the stereo modules are installed to measure the z coordinate. The thickness of the sensors range between 300 and 500 μm depending on the disk.

The tracker is operated at low temperature in order to reduce those radiation damage induced effects that have a temperature dependence, such as the increase of the leakage current and the long-term increase of the depletion voltage (also called reverse annealing)³.

The alignment of the tracker modules is very important to obtain a high spatial resolution. Deviations are caused by assembly inaccuracy, deformations due to cooling and stress from the magnetic field. Therefore, three methods are used for the tracker alignment. The geometry was determined during the assembly to an accuracy of 80 to 150 μm . An infrared laser system is used for continuous monitoring of the position of selected tracker modules. The final alignment is done with tracks from well known physics processes, e.g. cosmic muons or muon pairs from the J/Ψ , Υ or Z decays.

2.2.3. The electromagnetic calorimeter (ECAL)

The main function of an electromagnetic calorimeter is to identify electrons and photons and to measure accurately their energy. The CMS electromagnetic calorimeter (ECAL) [15, 16], shown in Fig. 2.9, is a hermetic homogeneous calorimeter with cylindrical geometry, composed of many scintillating crystals of lead tungstate (PbWO_4) with a truncated pyramidal shape. As the other detectors it consists of two parts, the ECAL barrel (EB), which contains 61200 crystals, and two endcaps (EE) containing 7324 crystals each one.



(a) $r - z$ view of an ECAL sector.

(b) ECAL three-dimensional view.

Figure 2.9.: Schematic representation of the CMS electromagnetic calorimeter.

³The tracker in Run 1 was operated at a temperature of +4°C, but during the Long Shutdown 1 a new cooling dry gas plant has been installed and the tracker is now operating at the lower temperature of -15°C.

409 The characteristics of the PbWO₄ crystals make them an appropriate choice for operation
 410 at LHC. The high density ($\rho = 8.3 \text{ g/cm}^3$), short radiation length ($X_0 = 0.89 \text{ cm}$) and
 411 small Molière radius⁴ (2.2 cm) allow to build a compact and high granularity calorimeter.
 412 Another advantage of this material is the radiation hardness and the fast scintillation
 413 decay time ($\tau = 10 \text{ ns}$), that permits to collect about 80% of the produced light within
 414 the 25 ns interval between two consecutive bunch crossings. The main drawbacks of this
 415 material are the low light yield ($\sim 10 \text{ photoelectrons/MeV}$) and the strong dependence
 416 on the operating temperature, that makes it necessary to keep the crystals at a stabilized
 417 temperature (18°C).

418 The crystals are grouped into 5×5 matrices called *towers*. The barrel has an inner
 419 radius of 129 cm, a length of 630 cm and extends in the region $|\eta| < 1.479$. The crystals
 420 in the barrel have the following dimensions: $22 \times 22 \text{ mm}^2$ at the front face, $26 \times 26 \text{ cm}^2$
 421 at the rear face, and a length of 23 cm, corresponding to $25.8X_0$, and are mounted in a
 422 quasi-projective geometry, in order to have the long side tilted by 3° with respect to the
 423 direction pointing to the interaction point, both in the η and ϕ coordinates. This is done to
 424 avoid the empty spaces between adjacent crystals to be aligned with the direction pointing
 425 to the interaction point. The granularity of the EB is about 1°. Avalanche photodiodes
 426 (APDs) are used as photodetectors connected with the crystals in the barrel region.

427 Each endcap covers the region $1.479 < |\eta| < 3$ and is formed by two semicircular
 428 aluminium halves called *dees*. Crystals in endcaps have a length of 22 cm, a frontal area
 429 equal to $28.6 \times 28.6 \text{ mm}^2$ and a rear surface of $30 \times 30 \text{ mm}^2$. In the endcaps the crystals
 430 are arranged in a $\eta - \phi$ symmetry. The photodetectors used to collect the light produced
 431 in the endcap crystals are single stage vacuum phototriodes (VPTs), because this region
 432 experiences a rather high particle flux and VPTs are more robust against radiation damages
 433 with respect to APDs. A preshower system is installed in front of the ECAL endcaps in
 434 order to separate the showers produced by a primary γ from those produced by forward
 435 emitted π^0 . This detector, which covers the region $1.653 < |\eta| < 2.6$, is a sampling
 436 calorimeter consisting of two lead disks ($2X_0$ and $1X_0$ thick respectively) that initiate the
 437 electromagnetic shower from incoming photons or electrons, with silicon strip sensors after
 438 each disk, which measure the deposited energy as well as the shower transverse profile.

439 The energy resolution of a homogeneous calorimeter can be expressed by the sum in
 440 quadrature of three terms, as shown in the following formula:

$$\left(\frac{\sigma_E}{E}\right)^2 = \left(\frac{a}{\sqrt{E}}\right)^2 + \left(\frac{b}{E}\right)^2 + c^2 \quad (2.6)$$

441 The stochastic term a dominates at low energies: it includes the contribution of statistical
 442 fluctuations in the number of generated and collected photoelectrons. This term takes
 443 into account the crystal light emission, the light collection efficiency and the photodetector

⁴The Molière radius R_M characterizes the transverse development of an electromagnetic shower in a calorimeter. On average 90% of the energy deposited by a shower is contained inside a cylinder with radius R_M .

⁴⁴⁴ quantum efficiency⁵. The noise term b includes the contributions of pile up events and
⁴⁴⁵ electronic noise, both due to the photodetector and preamplifier. These contributions
⁴⁴⁶ depend on η and on the LHC operational luminosity. The constant term c , dominant at
⁴⁴⁷ high energies, takes into account several contributions. The most relevant are the non-
⁴⁴⁸ uniformity of the longitudinal light collection, the intercalibration errors and the leakage
⁴⁴⁹ of energy from the rear side of the crystal. The ECAL barrel resolution for electrons was
⁴⁵⁰ measured using test beams to be:

$$\left(\frac{\sigma_E}{E}\right)^2 = \left(\frac{2.8\% \text{ GeV}^{1/2}}{\sqrt{E}}\right)^2 + \left(\frac{12\% \text{ GeV}^{1/2}}{E}\right)^2 + (0.3\%)^2 , \quad (2.7)$$

⁴⁵¹ where E is the energy measured in GeV.

⁴⁵² 2.2.4. The hadron calorimeter (HCAL)

⁴⁵³ The hadron calorimeter (HCAL) [17] is used together with ECAL to make a complete
⁴⁵⁴ calorimetric system for the jet energy and direction measurement. Moreover, thanks
⁴⁵⁵ to its hermetic structure, it can measure the energy imbalance in the transverse plane,
⁴⁵⁶ E_T^{miss} , a typical signature of non interacting particles, such as neutrinos. The HCAL is
⁴⁵⁷ a sampling calorimeter covering the region $|\eta| < 5$. As shown in Fig. 2.10, it is divided
⁴⁵⁸ in four sub-detectors: HB (*Barrel Hadronic Calorimeter*), located in the barrel region
⁴⁵⁹ inside the solenoid, extending up to $|\eta| < 1.4$; HE (*Endcap Hadronic Calorimeter*), placed
⁴⁶⁰ in the endcaps region inside the magnet, covering the region $1.3 < |\eta| < 3$ and partially
⁴⁶¹ overlapping with the HB coverage; HO (*Outer Hadronic Calorimeter*), also known as
⁴⁶² *tail-catcher*, placed along the inner wall of the magnetic field return yoke, just outside of
⁴⁶³ the magnet; HF (*Forward Hadronic Calorimeter*), a sampling calorimeter consisting of
⁴⁶⁴ quartz fibers sandwiched between iron absorbers, consisting of two units placed in the very
⁴⁶⁵ forward region ($3 < |\eta| < 5$) outside the magnetic coil. The quartz fibers emit Cherenkov
⁴⁶⁶ light with the passage of charged particles and this light is detected by radiation resistant
⁴⁶⁷ photomultipliers. In order to maximize particle containment for a precise missing transverse
⁴⁶⁸ energy measurement, the amount of absorber material was maximized, reducing therefore
⁴⁶⁹ the amount of the active material. Since HCAL is mostly placed inside the magnetic coil,
⁴⁷⁰ a non-magnetic material like brass was chosen as absorber. HB and HE are therefore
⁴⁷¹ made with 5 cm brass absorber layers interleaved with 3.7 mm plastic scintillators. The
⁴⁷² scintillation light is collected by wavelength shifting (WLS) fibres and read out by hybrid
⁴⁷³ photodiodes (HPD). The granularity of the calorimeter is $\Delta\eta \times \Delta\phi = 0.087 \times 0.087$ for
⁴⁷⁴ $|\eta| < 1.6$ and $\Delta\eta \times \Delta\phi \approx 0.17 \times 0.17$ for $|\eta| \geq 1.6$. HO is made of 5 rings installed in
⁴⁷⁵ the wheel that compose the return yoke and is divided in 12 sectors, each one covering
⁴⁷⁶ a 30° angle in ϕ . It consists of scintillating layers, with the same granularity as HB, and
⁴⁷⁷ the solenoid coil is used as an additional absorber to increase the effective depth of the

⁵The quantum efficiency is the ratio between the number of collected electron-hole pairs (or photoelectrons)
and the number of photons incident on the photodetector.



Figure 2.10.: Longitudinal view of the CMS detector showing the HCAL sub-detectors.

478 calorimeter in the barrel region, which is extended up to $11.8 \lambda_I$, thus improving the energy
479 resolution.

480 The energy resolution in the different regions of HCAL can be parametrized using a
481 stochastic and a constant term, as follows:

$$\begin{aligned} \left(\frac{\sigma_E}{E}\right)^2 &= \left(\frac{90\% \text{GeV}^{1/2}}{\sqrt{E}}\right)^2 + (4.5\%)^2 && \text{in the barrel/endcap ,} \\ \left(\frac{\sigma_E}{E}\right)^2 &= \left(\frac{172\% \text{GeV}^{1/2}}{\sqrt{E}}\right)^2 + (9\%)^2 && \text{in the HF ,} \end{aligned} \quad (2.8)$$

482 where E is expressed in GeV.

483 2.2.5. The muon system

484 The CMS muon system [18] is dedicated to the identification and measure of high p_T muons,
485 in combination with the tracker. The system is placed outside the magnetic coil, embedded
486 in the return yoke, to fully exploit the 1.8 T return flux. As shown in Fig. 2.11, the system
487 consists of three types of independent gaseous particle detectors:

- 488 • *Drift Tubes* (DT) are placed in the barrel region, where the occupancy is relatively
489 low ($< 10 \text{ Hz/m}^2$);
- 490 • *Cathode Strip Chambers* (CSC) are installed in the endcaps, where the occupancy is
491 higher ($> 100 \text{ Hz/m}^2$);
- 492 • *Resistive Plate Chambers* (RPC) are placed both in the barrel and endcaps.

493 The DT system is placed in the region of the barrel with $|\eta| < 1.2$, where the magnetic
494 field is sufficiently weak and homogeneous. Along the longitudinal direction, the barrel

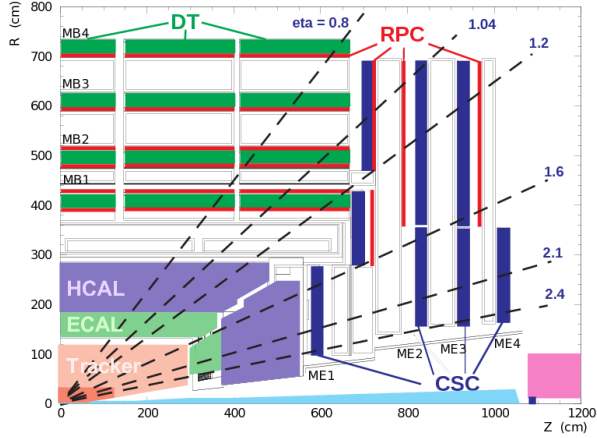


Figure 2.11.: Schematic view of a quadrant of the CMS muon system.

region is divided in 5 wheels, which are subdivided in 12 sectors covering a 30° azimuthal angle each. The wheels are composed of 4 concentric rings of chambers, called *stations*, interspersed in the layers of the iron return yoke, and each one formed by 12 DT chambers. The basic element of the DT system is a rectangular drift tube cell with a transverse size of $13 \times 42 \text{ mm}^2$ and a variable length from 2 to 4 m. The chambers are filled with a gas mixture of Ar (85%) and CO₂ (15%) and are grouped in the radial direction to form detection layers. Groups of four layers form a *superlayer*. In each superlayer two chambers have anode wires parallel to the beam axis and two have perpendicular wires, thus providing two measurements of the (r, ϕ) coordinate and two measurements of the z coordinate of the track hit positions. As shown in Fig. 2.12, each chamber is made of a stainless steel anode

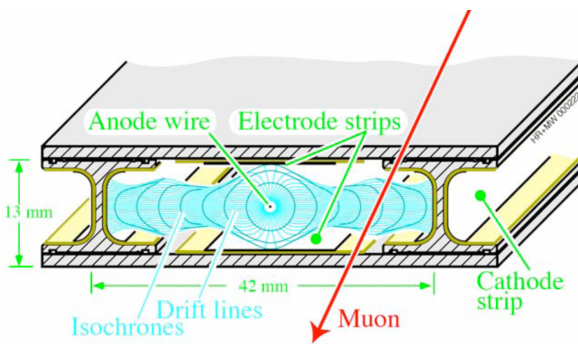


Figure 2.12.: Schematic representation of a drift tube chamber, showing the drift lines in presence of magnetic field.

wire between two parallel aluminium plates with “T” shaped spacer cathodes, isolated from the aluminium plates with polycarbonate plastic, and the hit resolution is about $100 \mu\text{m}$ in both (r, ϕ) and (r, z) directions.

508 In the endcaps, the high and non-uniform magnetic field and the particle rate do not
 509 allow to use drift tubes detectors to perform measurements. Therefore, a solution based
 510 on the CSC detector has been adopted. CSC are multi-wire proportional chambers with
 511 the cathodes segmented into strips oriented radially and transversely with respect to the
 512 anode wires (see Fig. 2.13), allowing a simultaneous measurement of two coordinates (r
 513 through the wires and ϕ using the strips). The CSC chambers are filled with a gas mixture
 514 of Ar (40%), CO₂ (50%) and CF₄ (10%) and provide a spatial resolution of about 80–85 μm .
 515 The drift path of the charge carriers is shorter with respect to the drift tubes, therefore
 516 these detectors can be placed in regions with higher flows of charged particles and less
 homogeneous magnetic fields. The CSC coverage is $0.8 < |\eta| < 2.4$.

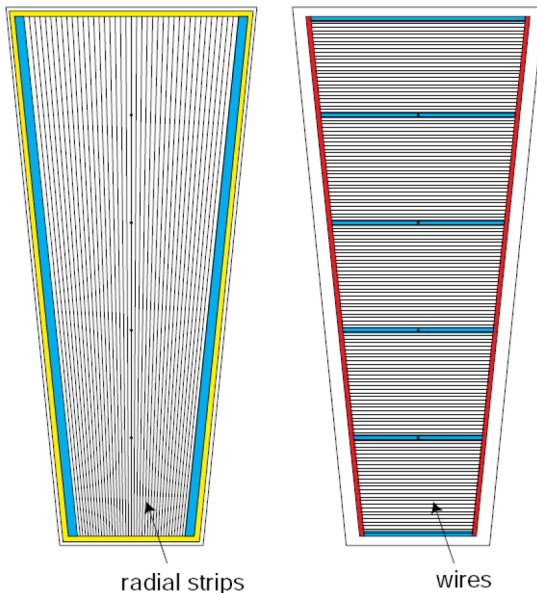


Figure 2.13.: Schematic representation of CSC cathode (left) and anode (right) panels.

517
 518 RPCs are used both in barrel and endcaps, complementing DT and CSC systems, in
 519 order to ensure robustness and redundancy to the muon spectrometer. RPCs are gaseous
 520 detectors characterized by a coarse spatial resolution, but are able to perform precise time
 521 measurements, comparable with the ones provided by scintillators. These chambers are
 522 made of 4 bakelite planes, with a bulk resistivity of 10^{10} – $10^{11} \Omega\text{cm}$. The 2 mm gap between
 523 the plates is filled with a mixture of C₂H₂F₄ (94.5%) and Isobutane. The central part of the
 524 chamber is equipped with insulated aluminum strips, used to collect the signal generated by
 525 crossing particles. In the barrel the strips are rectangularly segmented and run along the
 526 beam axis, whereas the endcaps are equipped with trapezoidal shaped strips. The detector
 527 operates in avalanche mode, and covers the region $|\eta| < 2.1$.

528 2.3. The CMS trigger system

529 The LHC can provide proton-proton interactions at a crossing frequency of 40 MHz and,
 530 for each bunch crossing, several collisions can occur (approximately 20 at the nominal
 531 instantaneous luminosity). Since it is impossible to store and process the large amount
 532 of data associated with the resulting large number of events, a drastic rate reduction has
 533 to be achieved. In fact the speed at which data can be written to mass storage is limited
 534 and, moreover, the vast majority of events produced is not interesting for physics analyses,
 535 because it involves low transverse momentum interactions (also called *minimum bias events*).
 536 The task of reducing this rate is accomplished by the CMS trigger system, which is the start
 537 of the physics event selection. CMS makes use of a two-stage trigger system, consisting of a
 538 *Level-1* trigger (L1) [19] and a *High Level Trigger* (HLT) [20].

539 Level-1 trigger runs on dedicated processors, and accesses coarse level granularity
 540 information from calorimetry and muon system. A L1 Trigger decision has to be taken for
 541 each bunch crossing within $3.2\ \mu\text{s}$. Its task is to reduce the data flow from 40 MHz to about
 542 100 kHz.

543 The High Level Trigger is responsible for reducing the L1 output rate down to a maximum
 544 rate of the order of 1 kHz. The HLT code runs on a farm of commercial processors and can
 545 access the full granularity information of all the sub-detectors.

546 The main characteristics of the CMS trigger system are described in the following.

547 2.3.1. The Level-1 trigger

548 The L1 trigger is responsible for the identification of electrons, muons, photons, jets and
 549 missing transverse energy. It is required to have a high and carefully understood efficiency.
 550 Its output rate and speed are limited by the readout electronics and by the performances
 551 of the data acquisition (DAQ) system [20]. It consists of three main subsystems:

- 552 • L1 Calorimeter Trigger;
- 553 • L1 Muon Trigger;
- 554 • L1 Global Trigger.

555 The L1 Global Trigger is responsible for combining the output of L1 Calorimeter Trigger
 556 and L1 Muon Trigger and for making the decision to either retain the event or discard it.
 557 The organization of CMS L1 Trigger is schematically summarized in Fig. 2.14.

558 L1 Calorimeter Trigger

559 **Controllare se stato cambiato qualcosa nel Run2**

560 The input for the L1 Calorimeter Trigger are calorimeter towers, which are clusters
 561 of signals collected both from ECAL and HCAL. Towers are calculated by calorimeter
 562 high level readout circuits, called Trigger Primitive Generators. The Regional Calorimeter
 563 Trigger identifies electron, photon, τ and jet candidates together with their transverse energy
 564 and sends the information to the Global Calorimeter Trigger. The Global Calorimeter

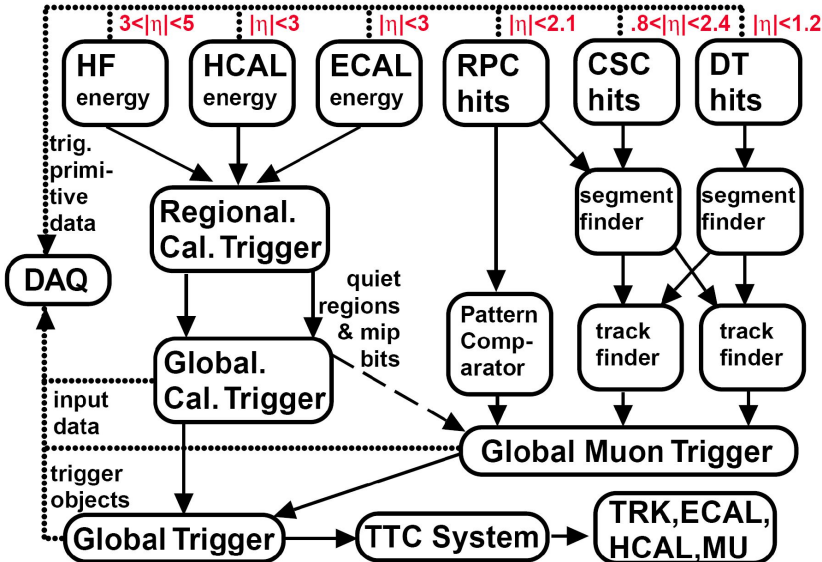


Figure 2.14.: Schematic representation of the Level-1 trigger components.

565 Trigger sorts the candidates according to their transverse energy and sends the first four
 566 objects to the L1 Global Trigger.

567 L1 Muon Trigger

568 Controllare se stato cambiato qualcosa nel Run2

569 The L1 Muon Trigger is actually a composite system itself: information from RPC, CSC
 570 and DT specific triggers are combined in the so called L1 Global Muon Trigger.

571 The RPC trigger electronics builds Track Segments, gives an estimate of their p_T and
 572 sends these segments to the Global Muon Trigger. It also provides the CSC logic unit with
 573 information to solve hit position ambiguities in case of two or more muon tracks crossing
 574 the same CSC chamber.

575 The CSC trigger builds Local Charged Tracks (LCT), that is track segments made out
 576 of the cathode strips only, and assign a p_T value and a quality flag to the LCTs. The best
 577 three LCTs in each sector of nine CSC chambers are passed to the CSC Track Finder, that
 578 uses the full CSC information to build tracks, assigns them a p_T and a quality flag and
 579 sends them to the Global Muon Trigger.

580 DTs are equipped with Track Identifier electronics, which is able to find groups of
 581 aligned hits in the four chambers of a superlayer. Those Track Segments are sent to the
 582 DT Track Correlator that tries to combine segments from two superlayers, measuring the
 583 ϕ angle. The best two segments are sent to the DT Track Finder that builds tracks and
 584 sends them to the Global Muon Trigger.

585 The Global Muon Trigger sorts the RPC, CSC and DT muon tracks and tries to combine
586 them. The final set of muons is sorted according to the quality, and the best four tracks
587 are passed to the L1 Global Trigger.

588 **L1 Global Trigger**

589 **Controllare se stato cambiato qualcosa nel Run2**

590 The L1 Global Trigger is responsible for collecting objects created from the Calorimeter
591 and Muon Triggers and for making a decision whether to retain the event or not. In case
592 the event is accepted, the decision is sent to the Timing Trigger and Control System, that
593 commands the readout of the remaining subsystems.

594 In order to take the decision, the L1 Global Trigger sorts the ranked objects produced
595 by calorimetry and muon system and checks if at least one of the thresholds in the L1
596 trigger table is passed.

597 **2.3.2. The high level trigger (HLT)**

598 The High Level Trigger is designed to reduce the L1 output rate down to about 1000 events/s,
599 which is the amount that will be written to mass storage. HLT code runs on commercial
600 processors and performs reconstruction using the information from all sub-detectors. Events
601 passing the HLT are stored on local disk or in CMS Tier 0⁶.

602 Data read from sub-detectors are assembled by a builder unit and then assigned to
603 a switching network that dispatches events to the processor farm. The CMS switching
604 network has a bandwidth of 1 Tbit/s. This simple design ensures maximum flexibility to
605 the system, the only limitation being the total bandwidth and the number of processors.
606 The system can be easily upgraded adding new processors or replacing the existing ones
607 with faster ones as they become available. Since the algorithms have a fully software
608 implementation, improvements to the algorithms can be easily implemented and do not
609 require any hardware intervention.

610 Event by event, the HLT code is run on a single processor, and the time available to
611 make a decision is about 300 ms. The real time nature of this selection imposes several
612 constraints on the resources an algorithm can use. The reliability of HLT algorithms
613 is of capital importance, because events not selected by the HLT are lost. In order to
614 efficiently process events, the HLT code has to be able to quickly reject not interesting
615 events; computationally expensive algorithms must be run only on good candidates for
616 interesting events. In order to cope with this requirement the HLT code is organized in a
617 virtually layered structure:

⁶The Worldwide LHC Computing Grid (WLCG) is composed of four levels, or “Tiers”, identified with numbers 0, 1, 2 and 3. Each Tier is made up of several computer centres and provides a specific set of services; they process, store and analyse all the data from the Large Hadron Collider (LHC). Tier 0 is the CERN Data Centre. All of the data from the LHC pass through this central hub. Tier 0 distributes the raw data and the reconstructed output to Tier 1’s, and reprocesses data when the LHC is not running.

-
- 618 • Level 2: uses only complete muon and calorimetry information;
619 • Level 2.5: uses also the pixel information;
620 • Level 3: makes use of the full information from all the tracking detectors.
621 Each step reduces the number of events to be processed in the following step. The most
622 computationally expensive tasks are executed in the Level 3; time consuming algorithms
623 such as track reconstruction are only executed in the region of interest. Besides, since the
624 ultimate precision is not required at a HLT level, track reconstruction is performed on a
625 limited set of hits, and is stopped once the required resolution is achieved.

Chapter 3.

626 Reconstruction and identification of 627 physics objects

628 In CMS, the physics object reconstruction and identification is based on standard algorithms
629 developed by the collaboration and used by all the physics analyses. In this section, the
630 techniques used for the reconstruction and identification of the physics objects of interest
631 for $H \rightarrow WW \rightarrow 2\ell 2\nu$ analyses are described.

632 3.1. The Particle Flow technique

633 The Particle Flow (PF) event reconstruction technique [21] aims at the reconstruction
634 and identification of all the stable particles in the event, i.e. electrons, muons, photons,
635 charged and neutral hadrons, with a thorough combination of the information from all CMS
636 sub-detectors, in order to determine their energy, direction and type. These individual
637 particles are then used, for example, to build jets, to measure the missing transverse energy
638 E_T^{miss} , to reconstruct the τ from their decay products, to quantify the charged lepton
639 isolation and to tag b-jets.

640 The CMS detector is well suited for this purpose. Indeed, the presence of a large internal
641 silicon tracker immersed in an intense solenoidal magnetic field allows the reconstruction of
642 charged particles with high efficiency and small fake rate, and provides a high precision
643 measurement of the particle p_T down to about 150 MeV, for $|\eta| \leq 2.6$. The high granularity
644 of the ECAL calorimeter is the additional key element for the feasibility of the PF technique,
645 allowing the reconstruction of photons and electrons with high energy resolution.

646 The first step of the PF technique consists in the reconstruction of the basic elements
647 from the various sub-detectors, such as charged-particle tracks, calorimeter clusters and
648 muon tracks. These elements, which are provided by the sub-detectors with high efficiency
649 and low fake rate, are then connected together with a link algorithm.

650 The good performance of the tracking system are achieved by means of an iterative
651 tracking strategy [22], based on the Kalman Filter algorithm [23]. The basic idea of iterative
652 tracking is that initial iterations search for tracks that are easiest to find, e.g. high p_T tracks
653 produced near the interaction region. After each iteration, hits associated to reconstructed
654 tracks are removed from the hit collection, thereby reducing the combinatorial complexity
655 and simplifying the subsequent iterations, which aim at finding more complicated set of

656 tracks, e.g. low p_T or displaced tracks. The *Iteration 0*, where the majority of tracks are
 657 reconstructed, is designed to identify prompt tracks with $p_T > 0.8$ GeV that have three
 658 hits in the three layers of the pixel detector. *Iteration 1* is used to recover prompt tracks
 659 that have only two pixel hits. *Iteration 2* aims at finding low- p_T prompt tracks while
 660 *Iterations 3–5* are intended to find tracks that originate outside the collision point, i.e.
 661 tracks produced by a secondary vertex, and to recover undetected tracks in the previous
 662 iterations. Each iteration proceeds according to four steps:

- 663 • *seeding*: initial track candidates are obtained using 2 or 3 hits in the innermost layers
 664 (these proto-tracks are called seeds);
- 665 • *pattern recognition*: this step is based on Kalman Filter and searches for hits in the
 666 outer layers that could be associated to the initial track candidate, reconstructing the
 667 particle trajectory;
- 668 • *track fitting*: in this step a fit of the trajectory is performed, using its associated hits
 669 and providing an estimate of the track parameters (p_T , η , ϕ , charge, etc.);
- 670 • *selection*: finally tracks are selected based on quality requirements.

671 The high detection efficiency of the calorimeters is based on a specific calorimeter
 672 clustering algorithm, which is performed separately in each sub-detector. The algorithm is
 673 based on three steps: in the first step, “cluster seeds” are identified as local calorimeter cells
 674 with an energy deposit above a given threshold. Then, “topological clusters” are grown
 675 from the seeds by gathering cells with at least one side in common with a cell already in the
 676 cluster, and with an energy above a given threshold. A topological cluster usually gives rise
 677 to many “particle flow clusters” as seeds, which are identified sharing the energy of each
 678 cell among the particle flow clusters, thereby allowing the determination of the particle flow
 679 cluster energy and position.

680 These elements are then connected to each other using a link algorithm, which identifies
 681 blocks of elements that are topologically compatible. For example, a charged-particle track
 682 is linked to a calorimeter particle flow cluster if the extrapolated position from the track to
 683 the calorimeter is compatible with the cluster boundaries. From these blocks, PF candidates
 684 are identified according to the following order:

- 685 • Muons: a *global muon* gives rise to a *PF muon* if its combined p_T measurement is
 686 compatible within 3 standard deviation with the one provided by the sole tracker. The
 687 corresponding track is removed from the block;
- 688 • Electrons: electrons tend to give rise to short tracks, and to lose energy by Bremsstrahlung
 689 in the tracker layers on their way to the calorimeter. The link between a charged-
 690 particle track (refitted with the Gaussian-Sum Filter (GSF) [24]) and one or more
 691 ECAL clusters identifies a *PF electron*. After the identification, the corresponding
 692 tracks and clusters are removed from the block.
- 693 • Charged hadrons: the remaining tracks give rise to *PF charged hadrons*. Tracks can be
 694 linked to ECAL and HCAL clusters, and the energy is determined taking into account
 695 information from calorimeters;

- Photons and neutral hadrons: ECAL clusters not linked with tracks give rise to *PF photons*, while the remaining HCAL clusters are identified as *PF neutral hadrons*.
- After the identification of all PF candidates in the event, *PF jets* are clustered as described in Sec. ???. The last step is the reconstruction of the *PF \vec{p}_T^{miss}* , which is given by:

$$\vec{p}_T^{\text{miss}} = - \sum_{\text{PF obj}} \vec{p}_T^{\text{PF obj}} , \quad (3.1)$$

where the sum extends over all the PF objects. The E_T^{miss} is defined as the modulus of \vec{p}_T^{miss} .

3.2. Leptons reconstruction and identification

3.2.1. Muon reconstruction and identification

Muons produced at the collision point can go through the entire detector with a negligible energy loss, thus reaching the detector outermost part where the muon chambers are installed (see Sec. 2.2.5). Muons interact through ionization with the layers of the silicon tracker, which is able to reconstruct their tracks (*tracker track*). The muon tracks are also reconstructed using the muon system (*standalone muon track*). Based on these objects, two reconstruction approaches are used [25]: in the first method (outside-in), for each standalone muon tracks a tracker track is searched for by extrapolating the two tracks to a common surface. If a match is found, the hits associated to the two tracks are fitted together giving rise to a *Global Muon*. The second approach (inside-out) consists in considering all tracker tracks with $p_T > 0.5$ GeV as potential muon candidates and are extrapolated to the muon system taking into account the magnetic field, the expected energy losses and the multiple scattering in the detector material. If at least one muon segment (a short track stub made of DT or CSC hits) matches the extrapolated tracks, the corresponding tracker track is identified as a *Tracker Muon*.

The matching with the muon system improves significantly the muon p_T resolution that can be obtained from the tracker only, especially in the region with $p_T > 200$ GeV, as shown in Fig. ??.

Depending on the physics analysis, different muon definitions can be used by changing the selection on the muon identification variables, hence balancing between the muon identification efficiency and purity. The most widely used definition in physics analyses is the so-called *Tight muon selection*¹. This selection requires the muon candidate to be reconstructed as a Global Muon and identified by the PF algorithm. The fit of the global track, which is required to include muon segments in at least two muon stations (this implies that the muon is also reconstructed as a Tracker Muon), must have a $\chi^2/d.o.f.$ less than 10 and use more than 10 inner tracker hits. The transverse impact parameter with

¹Small variations with respect to this baseline definition are adopted by the specific analyses.

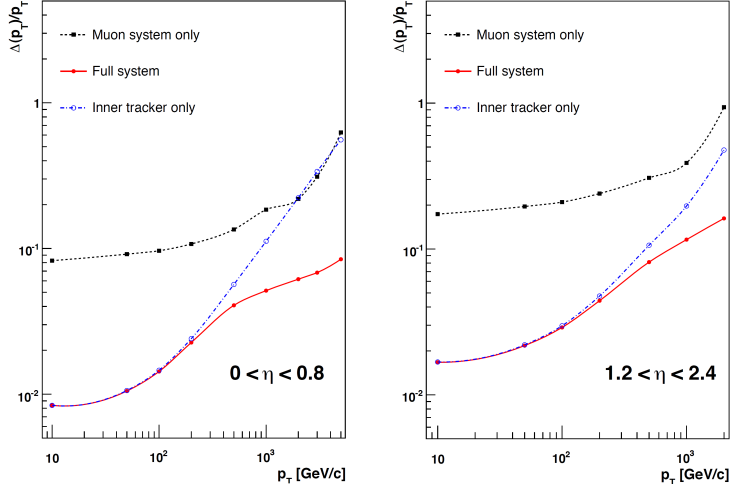


Figure 3.1.: Muon p_T resolution as a function of the muon p_T in the barrel (left) and in the endcap (right) regions. The resolution is provided for the measurement using the tracking system or the muon system only, as well as for the combination of the two methods.

respect to the primary vertex is required to be $|d_{xy}| < 2$ mm, significantly reducing the rate of muons from decays in flight, i.e. non prompt muons. The requirements defining the Tight Muon identification are summarized in Table 3.1.

Table 3.1.: Summary of the muon identification variables and the corresponding selections commonly used by physics analyses.

Observable	Cut
Is Global Muon	true
Is PF muon	true
Tracker layers with valid hits	> 5
Number of valid pixel hits	> 0
Number of valid muon hits	> 0
Number of matched muon stations	> 1
$\chi^2/d.o.f.$	< 10
$d_{xy}(PV)$	< 0.2 cm
$d_z(PV)$	< 0.5 cm

Another selection which is optimised for low- p_T muons coming from in flight decays is called *Soft Muon selection*. This selection requires the muon to be reconstructed as a Tracker

- ⁷³⁴ Muon with loose additional cuts on the transverse and longitudinal impact parameters.
⁷³⁵ This selection is commonly used to identify muons coming from B hadron decays.

⁷³⁶ 3.2.2. Muon isolation

⁷³⁷ One of the most powerful requirements to select prompt muons, as the ones produced from
⁷³⁸ W or Z boson decays, and to reject muons produced by decays in flight, is the isolation.
⁷³⁹ Indeed, prompt muons are expected to be isolated in the event, differently to non prompt
⁷⁴⁰ muons that are generally produced within jets and characterized by many nearby particles.

⁷⁴¹ Muons commonly used to reconstruct the W or Z decays are thus required to pass an
⁷⁴² isolation requirement, which includes a pile up mitigation correction called “ $\Delta\beta$ correction”.
⁷⁴³ This correction is needed to obtain a robust isolation definition that is less sensitive to
⁷⁴⁴ the pile up contribution. Indeed, simultaneous interactions manifest themselves as a mean
⁷⁴⁵ energy deposited over all the detector acceptance, which is not due to the particles produced
⁷⁴⁶ in the primary events, thus spoiling the isolation measurement. The relative isolation
⁷⁴⁷ variable, usually called *PF relative isolation*, is defined as follows:

$$I_{\Delta\beta}^{rel} = \left[\sum_{ChH} p_T + \max \left(0, \sum_{NH} p_T + \sum_{Ph} p_T - 0.5 \sum_{ChHPU} p_T \right) \right] / p_T^{\muon} . \quad (3.2)$$

⁷⁴⁸ The sums in Eq. (3.2) are performed in a cone of radius $\Delta R < 0.4$ around the muon
⁷⁴⁹ direction. The *ChH* subscript refers to charged hadrons, *NH* to neutral hadrons, *Ph* to
⁷⁵⁰ photons and *ChHPU* to charged hadrons not arising from the primary vertex.

⁷⁵¹ The cut applied on the isolation variable is analysis dependent, but a common value is
⁷⁵² $I_{\Delta\beta}^{rel} < 0.15$.

⁷⁵³ A different isolation definition is called *Tracker relative isolation*, I_{trk}^{rel} , which is calculated
⁷⁵⁴ as the scalar sum of all the p_T of the tracker tracks reconstructed inside a cone of radius
⁷⁵⁵ $\Delta R < 0.3$ centred on the muon track direction.

⁷⁵⁶ 3.2.3. Muon momentum scale and resolution

⁷⁵⁷ The measurement of the muon p_T is sensitive to the alignment of the tracker and the muon
⁷⁵⁸ chambers, to the material composition and distribution inside the detector and to the
⁷⁵⁹ knowledge of the magnetic field produced by the solenoid. The imperfect knowledge of the
⁷⁶⁰ magnetic field and the effect of the material distribution introduce a relative bias in the
⁷⁶¹ muon p_T that is generally independent on the p_T itself, while the effect of the alignment is
⁷⁶² known to produce a bias that increases linearly with the p_T .

⁷⁶³ Different methods are used to estimate the muon p_T scale and resolution effects and
⁷⁶⁴ to determine the corresponding uncertainties, depending on the p_T range. At low and
⁷⁶⁵ intermediate p_T (< 100 GeV), the di-muon events arising from the J/Ψ and Z resonance
⁷⁶⁶ decays are used to correct the p_T scale and to measure the p_T resolution. In the high p_T
⁷⁶⁷ regime, the muon p_T scale and resolution are instead measured using cosmic ray muons.

768 One of the methods that is commonly used in the intermediate p_T range is the *MuScaleFit*
 769 (Muon momentum Scale calibration Fit), which provides the muon p_T scale corrections
 770 by fitting the Z boson mass peak in data and simulation. These corrections are meant to
 771 recover the bias of the Z mass peak with respect to the η and ϕ coordinates of the muon.
 772 After applying these corrections, the relative p_T resolution, $\sigma(p_T)/p_T$, is measured as a
 773 function of η and ϕ and is found to be on average of the order of 2% in the barrel and up
 774 to 6% in the endcaps, for muon p_T below 100 GeV.

775 3.2.4. Electron reconstruction and identification

776 The electron reconstruction is based on the combination of tracker and ECAL information.
 777 The reconstruction technique starts by measuring the energy deposits in ECAL by electrons,
 778 which form a “supercluster”. A supercluster is a group of one or more ECAL clusters
 779 associated using an algorithm that takes into account the characteristic shape of the
 780 energy deposited by electrons emitting Bremsstrahlung radiation in the tracker material.
 781 The supercluster shape is characterized by a narrow width profile in the η coordinate
 782 spread over the ϕ direction. The superclusters are matched to tracks, reconstructed in the
 783 tracker with the GSF algorithm, in order to obtain an electron candidate. An additional
 784 reconstruction method, described in details in Refs. [26, 27], is instead seeded by electron
 785 tracks reconstructed in the inner tracker layers.

786 Several strategies are used in CMS to identify prompt isolated electrons (characteristic
 787 of the signal processes of interest), and to separate them from background sources, mainly
 788 originating from photon conversions, jets misidentified as electrons, or electrons from
 789 semileptonic decays of b and c quarks. In order to achieve a good discrimination, several
 790 identification variables are used:

- 791 • $\Delta\eta_{\text{trk,SC}}$ and $\Delta\phi_{\text{trk,SC}}$: the variables measuring the spatial matching between the track
 792 and the supercluster in the η and ϕ coordinates, respectively;
- 793 • $\sigma_{in, in\eta}$: a variable related to the calorimeter shower shape, measuring the width of the
 794 ECAL supercluster along the η direction computed for all the crystals in the 5×5
 795 block of crystals centred on the highest energy crystal of the seed supercluster;
- 796 • H/E : the ratio between the energy deposited in the HCAL tower behind the ECAL
 797 seed and the supercluster seed energy;
- 798 • $|1/E - 1/p|$: the difference of the inverse of energy E measured in ECAL and the
 799 inverse of momentum p measured in the tracker;
- 800 • the number of missing hits in the back-propagation of the track to the interaction
 801 point;
- 802 • d_{xy} and d_z : the transverse and longitudinal impact parameters with respect to the
 803 primary vertex.
- 804 • a photon conversion veto ($\gamma \rightarrow e^+e^-$) based on the primary vertex measurement.

805 Different working points are provided by CMS corresponding to different selections on
 806 the previously defined variables. One of the common working points used by several physics

807 analyses, as the $H \rightarrow WW$ analyses described in Secs. 4, 5 and 6, is the “tight working
808 point”, summarised in Table 3.2.

Table 3.2.: Electron identification selections corresponding to the tight working point.

Variable	Selection	
	$ \eta_{\text{SC}} \leq 1.479$	$1.479 < \eta_{\text{SC}} \leq 2.5$
$\sigma_{i\eta,i\eta}$	0.01	0.028
$ \Delta\eta_{\text{trk,SC}} $	0.009	0.007
$ \Delta\phi_{\text{trk,SC}} $	0.03	0.09
H/E	0.06	0.06
$ 1/E - 1/p $	0.012	0.010
$ d_{xy} $	0.011 cm	0.035 cm
$ d_z $	0.047 cm	0.42 cm
missing inner hits	≤ 2	≤ 1
conversion veto	yes	yes

809 3.2.5. Electron isolation

810 Selected electrons are required to pass an isolation requirement that includes a pile up
811 mitigation correction based on the electron effective catchment area, which is different in
812 different η ranges. The isolation variable is given by the following formula:

$$I_{EA \text{ corrected}}^{\text{rel}} = \left[\sum_{ChH} p_T + \max \left(0, \sum_{Ph} p_T + \sum_{NH} p_T - \rho E A \right) \right] / p_T^{\text{electron}} \quad (3.3)$$

813 where ChH refers to charged hadrons, Ph to photons, NH to neutral hadrons, ρ is the
814 energy density due to pile up events, E is the energy and A is an effective area. The sums
815 are performed inside a cone of radius $\Delta R < 0.4$ around the electron direction. The cut
816 applied on this variable for the tight working point is $I_{EA \text{ corrected}}^{\text{rel}} < 0.04$.

817 3.2.6. Electron momentum scale and resolution

818 The electron momentum is estimated using a combination of the tracker and ECAL
819 measurements. Before making the combination of the two measurements, the ECAL energy
820 response is calibrated. Before doing the clustering, the energy response in individual crystals
821 is calibrated and a correction factor is applied to take into account effects as energy leakage

822 or changes in the crystal transparency induced by radiation ². Then the supercluster energy
 823 is also corrected using an MVA technique, selecting $Z \rightarrow e^+e^-$ events in data and comparing
 824 to simulation. A detailed description of the techniques used to estimate the electron scale
 825 and resolution and the associated uncertainties is given in Ref. [27].

826 3.2.7. Lepton identification and isolation efficiency

827 The efficiency related to the identification and isolation selections applied to muons and
 828 electrons are generally estimated both in data and simulation and the simulated events are
 829 corrected for the observed differences by means of a scale factor (SF), defined as the ratio
 830 of the efficiency measured in data and simulation, i.e. $SF = \varepsilon_{\text{data}}/\varepsilon_{\text{MC}}$.

831 The identification and isolation efficiencies are measured using a Tag and Probe technique.
 832 The Tag and Probe technique is a method to estimate the efficiency of a selection on data.
 833 It can be applied whenever one has two objects in one event, by using one of the two, the
 834 *tag*, to identify the process of interest, and using the second, the *probe*, to actually measure
 835 the efficiency of the selection being studied. Concerning the electron and muon case, the
 836 Tag and Probe method uses a known mass resonance (e.g. J/Ψ , Z) to select particles of the
 837 desired type, and probe the efficiency of a particular selection criterion on these particles.
 838 In general the *tag* is an object that passes a set of very tight selection criteria designed
 839 to isolate the required particle type. Tags are often referred to as a “golden” electrons or
 840 muons and the fake rate for passing tag selection criteria should be very small. A generic
 841 set of the desired particle type (i.e. with potentially very loose selection criteria) known
 842 as *probe* is selected by pairing these objects with tags such that the invariant mass of the
 843 combination is consistent with the mass of the resonance. Combinatorial backgrounds may
 844 be eliminated through any of a variety of background subtraction methods such as fitting,
 845 or sideband subtraction. The definition of the probe objects depend on the specifics of
 846 the selection criterion being examined. The simple expression to get the efficiency ε as a
 847 function of p_T and η is given below:

$$\varepsilon(p_T, \eta) = \frac{N_{\text{pass}}^{\text{probe}}}{N_{\text{pass}}^{\text{probe}} + N_{\text{fail}}^{\text{probe}}} \quad (3.4)$$

848 For the estimation of the electron or muon identification efficiency, the tag is chosen to
 849 be a well identified and isolated electron or muon, while the probe is chosen as an electron
 850 identified with loose selections. The invariant mass of the tag-probe pair is required to
 851 be within a Z boson mass window (the effect of changing the Z mass window is included
 852 as a systematic uncertainty). After that, the probe is required to pass the identification
 853 selections discussed before for electrons and muons, and the efficiency is computed both
 854 in data and simulation. A scale factor is then calculated by taking the ratio of the two
 855 efficiencies and applied to reweight simulated events.

²The continuous monitoring of the crystals transparency is achieved by a laser-monitoring system.

There are two methods to measure the efficiencies: the counting method consists in simply computing the ratio of probe events that pass the selections and total number of probe events, as shown in Eq. (3.4). This method can be used when the tag requirement selects a very pure set of events, with a small background contribution. The other approach is the fitting method, which is used when the background contamination is not negligible. In this latter case, which represents the commonly used method for estimating the lepton identification and isolation efficiencies, the invariant mass distribution of the tag-probe pair for signal and background is fitted choosing proper functions. The signal plus background fit is performed simultaneously in two categories, corresponding to events in which the probe lepton pass or fail the identification requirements, and separately in bins of η and p_T .

A similar approach is used to estimate the lepton isolation efficiency, requiring the probe lepton to pass the isolation requirements instead of the identification ones and calculating the corresponding scale factor.

The identification and isolation efficiency and the scale factor are shown in Fig. 3.2 corresponding to the selections described in Sec. 3.2.4, for events of interest for a typical physics analysis of the $H \rightarrow WW \rightarrow 2\ell 2\nu$ channel (in particular the analyses described in Sec. 5 and 6).

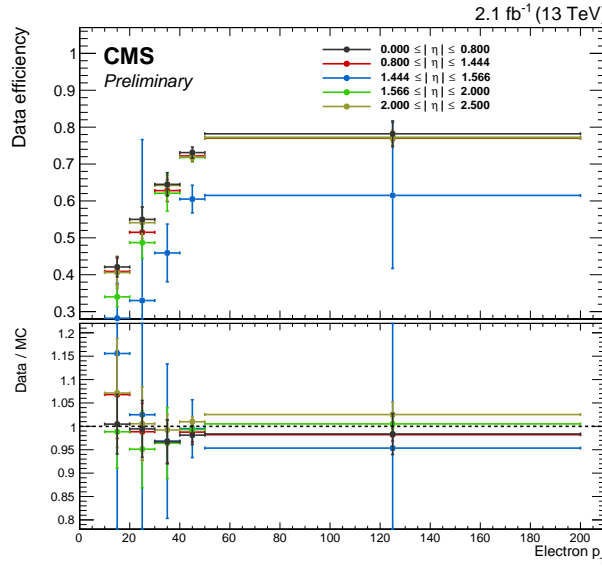


Figure 3.2.: Typical electron identification and isolation efficiencies in data (top panel) and data/simulation scale factor (bottom panel), as a function of the electron p_T and for different η bins.

3.2.8. Lepton trigger efficiency

Analyses that involves leptons in the final state generally select the interesting events using lepton triggers. For instance, the $H \rightarrow WW \rightarrow 2\ell 2\nu$ channel is characterized by the presence

of two leptons in the final state, thereby both single lepton and double lepton triggers are used. The lepton triggers at the HLT level are characterized by p_T thresholds, above which the trigger efficiency is very high (plateau region). Nevertheless, the trigger efficiency as a function of the lepton p_T is not a step function, but is characterized by a steep increase of the efficiency around the p_T threshold (turn-on region). The simulated samples thus need to be corrected in order to properly take into account the trigger efficiency. This can be achieved in two ways: including the HLT trigger in the event simulation or calculating the trigger efficiency in data and then applying it on top of simulated events. Several analyses, such as those related to the $H \rightarrow WW \rightarrow 2\ell 2\nu$ channel, opt for the second approach.

The trigger efficiency for single and double lepton triggers is calculated in bins of η and p_T using a Tag and Probe technique similar to the one described in Sec. 3.2.7, separately for muons and electrons. Since the triggered events arise from a mixture of two different triggers, the combined efficiency has to be computed and applied to simulated samples as an event weight. In the following, the approach used in the $H \rightarrow WW \rightarrow 2\ell 2\nu$ analyses is described.

The event efficiency ε_{ev} for an event with two leptons to pass the single lepton trigger is given by the following formula:

$$\varepsilon_{ev} = 1 - (1 - \varepsilon_{S,\ell 1}) \cdot (1 - \varepsilon_{S,\ell 2}) \quad , \quad (3.5)$$

where $\varepsilon_{S,\ell 1}$ and $\varepsilon_{S,\ell 2}$ are the efficiencies for the leading and subleading lepton to pass the single lepton trigger. In other words, the dilepton event passes the single lepton trigger if either one of the two leptons passes the single lepton trigger, excluding the cases for which both leptons pass the trigger.

For double lepton triggers the efficiency is calculated separately for each leg of the trigger. In the calculation of the efficiencies, the two trigger legs are considered independent, given that the correlations are very small. The combined efficiency is then used as a kinematics-dependent weight to be applied on top of simulated events. The event efficiency can be written as:

$$\varepsilon_{ev} = \varepsilon_{D,\ell 1}^{\text{lead}} \cdot \varepsilon_{D,\ell 2}^{\text{trail}} + (1 - \varepsilon_{D,\ell 1}^{\text{lead}} \cdot \varepsilon_{D,\ell 2}^{\text{trail}}) \cdot \varepsilon_{D,\ell 1}^{\text{trail}} \cdot \varepsilon_{D,\ell 2}^{\text{lead}} \quad , \quad (3.6)$$

where $\varepsilon_{D,\ell 1}^{\text{lead(trail)}}$ is the efficiency of the first lepton to pass the leading (trailing) leg of the double lepton trigger, and $\varepsilon_{D,\ell 2}^{\text{lead(trail)}}$ is the efficiency of the second lepton to pass the leading (trailing) leg of the double lepton trigger. The final event efficiency applied to reweight the events in simulation is given by the boolean OR of the event efficiencies corresponding to the single and double lepton triggers, which, using Eqs. (3.5) and (3.6), can be written as:

$$\begin{aligned}\varepsilon_{\text{ev}} = & 1 - (1 - \varepsilon_{S,\ell 1}) \cdot (1 - \varepsilon_{S,\ell 2}) + \\ & + (1 - \varepsilon_{S,\ell 1}) \cdot (1 - \varepsilon_{S,\ell 2}) \cdot \\ & \cdot [\varepsilon_{D,\ell 1}^{\text{lead}} \cdot \varepsilon_{D,\ell 2}^{\text{trail}} + (1 - \varepsilon_{D,\ell 1}^{\text{lead}} \cdot \varepsilon_{D,\ell 2}^{\text{trail}}) \cdot \varepsilon_{D,\ell 1}^{\text{trail}} \cdot \varepsilon_{D,\ell 2}^{\text{lead}}] \quad .\end{aligned}\quad (3.7)$$

907 3.3. Jets reconstruction and identification

908 Jets are the experimental signature of quarks and gluons produced in high energy physics
 909 processes. They arise from the hadronization of partons, which forms collimated sprays
 910 of particles, and play a predominant role in hadron colliders like the LHC, where the
 911 production cross section is very large. In this section, the jet reconstruction techniques
 912 used in CMS are described.

913 3.3.1. Jet reconstruction in CMS

914 The majority of physics analyses involving jets in the final state make use of particle flow
 915 jets. The PF jets are reconstructed using the technique described in Sec. 3.1, clustering all
 916 particles reconstructed with the PF algorithm, without any distinction of type and energy
 917 threshold. This method allows a remarkable improvement in the jet momentum and spatial
 918 resolutions with respect to the calorimeter jets, which are instead reconstructed using solely
 919 the information from the calorimeters, as the use of the tracker information provides a
 920 better p_T resolution for the charged particles constituting the jets³.

921 Jets are defined through sequential, iterative clustering algorithms that combine the
 922 four-momenta of input particles until certain conditions are satisfied and jets are formed [28].
 923 Several algorithms are available for jet clustering, characterized by different features. From
 924 a theoretical point of view, an ideal jet clustering algorithm should fulfil the following
 925 requirements [29]:

- 926 • *Infrared safety*: infrared singularities should not appear in the perturbative calculations
 927 and the solutions of the algorithm should be insensitive to soft radiation in the event;
- 928 • *Collinear safety*: collinear singularities should not appear in the perturbative calculations
 929 and jets should be insensitive to collinear radiation in the event;
- 930 • *Invariance under boosts*: the solutions of the algorithm should be the same indepen-
 931 dently of boosts in the longitudinal direction. This is particularly important for pp
 932 colliders, where the centre-of-mass of the individual proton proton collisions is typically
 933 boosted along the beam direction;
- 934 • *Order independence*: the algorithm should find the same jets at parton, particle and
 935 detector level;

³On average, the typical jet energy fractions carried by charged particles, photons and neutral particles are 65%, 25% and 10%, respectively.

- *Straightforward implementation*: the algorithm should be straightforward to implement in perturbative calculations.

The ideal algorithm should also follow some experimental attributes. Among them, the performance of the algorithm should be as independent as possible of the detector that provides the data, the algorithm should not amplify the inevitable effects of resolution smearing and angle bias and should not be strongly affected by pile up and high beam luminosities. Furthermore, the algorithm should be easy to implement, efficient to identify all possible jet candidates and should keep at an acceptable level the necessary computing resources.

Two main classes of jet clustering algorithms can be defined. The first one consists in the “cone” recombination, where jets are reconstructed associating together particles whose trajectories lie within a cone of radius ΔR in the η - ϕ plane. The second class of algorithms uses the sequential recombination scheme, that iteratively recombine the closest pair of particles according to some distance measure. The standard algorithms used by CMS are the SISCone, which is a “cone” recombination algorithm, and the k_t , anti- k_t and *Cambridge Aachen* (CA) algorithms, which instead belong to the sequential recombination class. All the analyses presented in Secs. 4, 5 and 6 make use of the sequential recombination scheme, in particular of the anti- k_t algorithm with $R = 0.4$, which is briefly described in the following.

The k_t , anti- k_t and CA algorithms are infrared and collinear safe algorithms characterized by the introduction of two definitions of distance: d_{ij} , the distance the two objects i and j , and d_{iB} , the distance between the object i and the beam. These distances are defined by the following equations:

$$d_{ij} = \min(k_{ti}^{2p}, k_{tj}^{2p}) \frac{\Delta_{ij}^2}{R^2} \quad , \quad (3.8)$$

$$d_{iB} = k_{ti}^{2p} \quad ,$$

where $\Delta_{ij} = (y_i - y_j)^2 + (\phi_i - \phi_j)^2$ and k_{ti} , y_i and ϕ_i are the transverse momentum, rapidity and azimuthal angle of the particle i , respectively. In these formulas, R represents the radial parameter and p is a parameter that is 1 for k_t , 0 for CA and -1 for anti- k_t algorithm. The algorithm proceeds as follows:

- the distances d_{ij} are calculated for all pair of particle i, j and the distances d_{iB} are calculated for each particle i , according to Eq. (3.8);
- the smallest distance, which could be either of type d_{ij} or d_{iB} , is identified;
- if the smallest distance is a d_{ij} , the particles i and j are combined into a single new particle summing their four-momenta and the algorithm restarts from the first step;
- otherwise, if it is a d_{iB} , i is declared to be a final state jet and the algorithm returns to the first step;
- the procedure is repeated until no particles are left.

The physical difference between the three algorithms is the momentum weighting. For the k_t algorithm, the weighting proportional to k_t^2 implies that jets are reconstructed starting from particles with low transverse momentum. Moreover this algorithm produces jets with irregular borders, thereby complicating the correction for effects such as pile up. For the CA algorithm there is no transverse momentum weighting, and the particles are merged following just an angular approach, based on the distance Δ_{ij} . Also this algorithm leads to jets with irregular borders. Finally, the anti- k_t algorithm, uses a weighting proportional to $1/k_t^2$, favouring the merging of high transverse momentum particles. In this case the jets grow around the particles with highest transverse momenta and the jets have a circular shape.

Jets reconstructed with different algorithms starting from the same set of simulated particles are shown in Fig. 3.3.

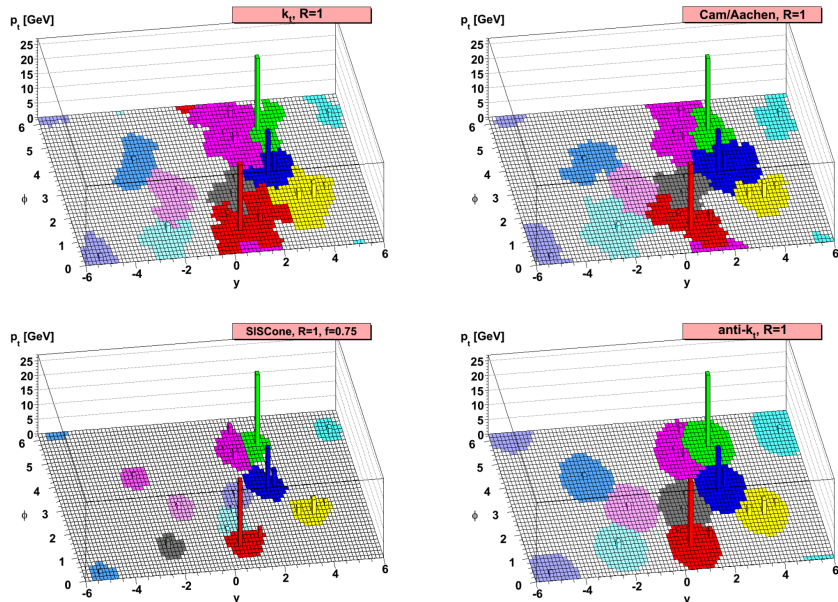


Figure 3.3.: Jets reconstructed with different algorithms starting from the same set of simulated particles. The jets reconstructed with the sequential recombination algorithms described in the text are shown, as well as with the SIScone algorithm.

3.3.2. Jet energy correction

The purpose of jet energy correction is to relate, on average, the jet energy measured in the detector to the true energy of the corresponding final state particle or parton jet. The latter is obtained in simulation by clustering, with the same algorithm used for jets in the detector, all the stable particles, i.e. with $c\tau > 1$ cm, produced in the event excluding neutrinos. This mismatch is mainly ascribable to the non uniform and linear response of the CMS

989 calorimeters, to the electronics noise and to pile up. For this reason, CMS has developed a
 990 sequential procedure to calculate and apply the *jet energy corrections* (JEC) [30].

991 The correction is applied as a multiplicative factor \mathcal{C} to each component of the raw jet
 992 four-momentum p_μ^{raw} (components are indexed by μ in the following):

$$p_\mu^{\text{cor}} = \mathcal{C} \cdot p_\mu^{\text{raw}} , \quad (3.9)$$

993 where p_μ^{cor} is the corrected jet four-momentum. The correction factor is composed of the
 994 offset correction C_{offset} , the MC calibration factor C_{MC} , and the residual calibrations C_{rel}
 995 and C_{abs} for the relative and absolute energy scales, respectively. The offset correction
 996 removes the extra energy due to noise and pile up, and the MC correction removes the bulk
 997 of the non-uniformity in η and the non-linearity in p_T . Finally, the residual corrections
 998 account for the small differences between data and simulation. The various components are
 999 applied in sequence as described by the equation below:

$$\mathcal{C} = C_{\text{offset}}(p_T^{\text{raw}}) \cdot C_{\text{MC}}(p'_T, \eta) \cdot C_{\text{rel}}(\eta) \cdot C_{\text{abs}}(p''_T) , \quad (3.10)$$

1000 where p'_T is the jet p_T after applying the offset correction and p''_T is the jet p_T after applying
 1001 all previous corrections. Each component is briefly described in the following sections.

1002 Offset correction

1003 The offset correction purpose is to estimate and subtract, on average, the energy contribution
 1004 that is not associated with the hard scattering in the event. The energy excess includes
 1005 contributions from electronics noise and pile up. The approach followed for the estimation of
 1006 the offset correction is known as *Jet Area Method*. For each event, an average p_T -density per
 1007 unit area, ρ , is estimated, characterizing the soft jet activity. This p_T -density represents the
 1008 combination of the underlying event, the electronics noise and the pile up effects. The two
 1009 latter components contaminate the hard jet energy measurement and need to be corrected
 1010 for with the offset correction. The key element for this approach is the jet area A_j . A
 1011 very large number of infinitely soft four-momentum vectors (soft enough not to change
 1012 the properties of the true jets) are artificially added in the event and clustered by the jet
 1013 algorithm together with the true jet components. The extent of the region in the η - ϕ
 1014 space occupied by the soft particles clustered in each jet defines the active jet area. The
 1015 p_T -density ρ is calculated with the k_t algorithm with a distance parameter $R = 0.6$. The
 1016 quantity ρ is estimated event by event as the median of the distribution of the variable
 1017 p_{Tj}/A_j , where j runs over all jets in the event, and is not sensitive to the presence of hard
 1018 jets in the event. At the detector level, the measured density ρ is the convolution of the true
 1019 particle-level activity (underlying event, pile-up) with the detector response to the various
 1020 particle types. The event-by-event and jet-by-jet offset correction can thus be defined as:

$$C_{\text{offset}}(p_T^{\text{raw}}, A_j, \rho) = 1 - \frac{(\rho - \langle \rho_{\text{UE}} \rangle) \cdot A_j}{p_T^{\text{raw}}} . \quad (3.11)$$

In the formula above, $\langle \rho_{UE} \rangle$ represents the average p_T -density component due to the underlying event and electronics noise, and is measured in events with exactly one reconstructed primary vertex, i.e. no pile up.

An additional pile up subtraction method that is used in CMS is called *Charged Hadron Subtraction*. This method makes use of PF jets and exploits the excellent CMS tracking capabilities to identify and remove charged hadrons inside jets, which are known to originate from pile up vertices. This is a particle-by-particle method that is applied to jets before calculating the offset correction.

MC calibration correction

The MC calibration is based on the simulation and corrects the energy of the reconstructed jets such that it is equal on average to the energy of the generated jets. In order to evaluate this correction, simulated QCD events are generated and then processed through the CMS detector simulation, based on the GEANT4 software. The jet reconstruction in simulation is identical to the one applied to the data. Each reconstructed jet is spatially matched, in the η - ϕ space, to a generated jet by requiring $\Delta R < 0.25$. In each bin of the generated jet transverse momentum p_T^{gen} , the response variable $\mathcal{R} = p_T^{\text{reco}}/p_T^{\text{gen}}$ and the reconstructed jet transverse momentum p_T^{reco} , are saved. The average correction in each bin is therefore defined as:

$$C_{\text{MC}}(p_T^{\text{reco}}) = \frac{1}{\langle R \rangle} , \quad (3.12)$$

and is expressed as a function of the average reconstructed jet p_T , $\langle p_T^{\text{reco}} \rangle$.

Relative jet energy scale

The goal of the relative jet energy scale correction is to make the jet response flat versus η . This is achieved by employing a Tag and Probe technique, selecting di-jet events in data. The size of this residual correction is of the order of 2–3% in the central η region, while it goes up to about 10% in the forward region.

Absolute jet energy scale

The goal of the absolute jet energy scale correction is to make the jet response at versus p_T . The absolute jet energy response is measured in the reference region $|\eta| < 1.3$ with the *Missing Transverse Energy Projection Fraction* (MPF) method [31], using $\gamma + \text{jets}$ and $Z + \text{jets}$ events. The method is used to estimate the absolute jet energy correction and is based on the fact that $\gamma + \text{jets}$ and $Z + \text{jets}$ events have no intrinsic E_T^{miss} and that, at parton level, the γ and Z boson are perfectly balanced by the hadronic recoil in the transverse plane.

1053 Jet energy uncertainties

1054 The uncertainties in the jet energy estimation arise from several different sources. Generally
 1055 these can be categorized as follows:

- 1056 • physics modelling in MC such as showering, underlying event, etc.;
- 1057 • MC modelling of true detector response and properties;
- 1058 • potential biases in the methodologies used to estimate the corrections.

1059 The sources are combined in different groups: absolute scale, relative scale, pile up, jet
 1060 flavor and time stability. In Fig. 3.4 the effect of each group of uncertainties is shown
 1061 together with the total uncertainty obtained summing all sources in quadrature, both as a
 1062 function of η and p_T . The pile up uncertainty dominates for low values of the jet p_T while
 1063 the relative and absolute uncertainties are more important in the high p_T region.

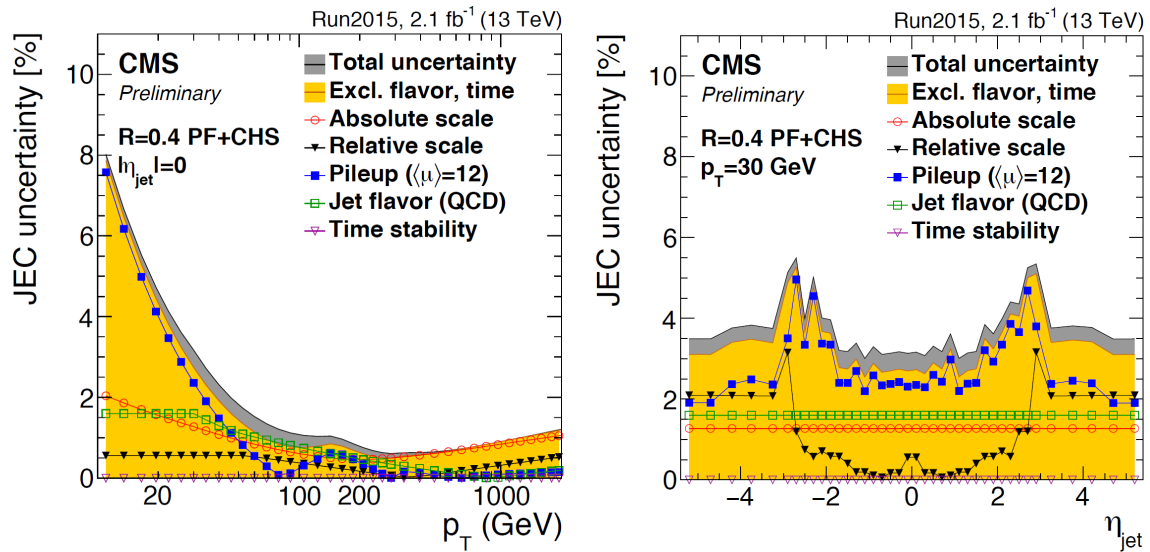


Figure 3.4.: JEC uncertainties as a function of p_T (left) for jets reconstructed with $\eta = 0$ and as a function of η (right) for jets with $p_T = 30$ GeV. All jets are reconstructed with the PF technique and using the anti- k_t algorithm with $R = 0.4$, after applying the CHS correction. Results are based on 2.1 fb^{-1} of data collected at 13 TeV.

1064 Jet energy resolution

1065 Measurements show that the jet energy resolution (JER) in data is worse than in the
 1066 simulation, therefore the simulated jets need to undergo a smearing procedure in order to
 1067 have a better description of the data.

1068 Reconstructed jets in simulated events are corrected for the jet energy resolution using
 1069 a two step procedure. In the first step, the reconstructed jet p_T is scaled for the observed
 1070 p_T difference between reconstructed and generated jets. This method only works for

reconstructed jets that are well matched to generated jets, where the matching is based on ΔR and Δp_T requirements. For reconstructed jets that do not fulfil the matching requirements, a gaussian smearing of the p_T distribution is applied in order to obtain the desired resolution.

jet identification?

3.4. Jet b tagging

Jets that arise from bottom quark hadronization (b-jets) are present in many physics processes, such as the decay of top quarks. The ability to accurately identify b-jets is crucial to reduce the otherwise overwhelming background from these processes to channels involving jets from gluons (g) and light-flavour quarks (u, d, s), and from c-quark fragmentation.

Algorithms for b jet identification (also known as b tagging algorithms) exploit the long life time of b hadrons present in jets originating from the hadronization of b quarks. This long life time results in a decay of the b hadron that is displaced with respect to the primary interaction vertex. This displacement of a few millimetres results in the presence of displaced tracks from which a secondary vertex may be reconstructed. In addition, b hadrons have a probability of around 20% to decay to a muon or electron. Hence, also the presence of these charged leptons can be exploited for b jet identification techniques and for measuring their performance with the collision data.

A variety of reconstructed physics objects, as tracks, vertices and identified leptons, can be used to build observables that discriminate between b and light-quark jets. Several b tagging algorithms have been developed by CMS, each one based on different input information. A common feature of all the algorithms is that each one yields a single discriminator value for each jet, which measures the likelihood that the jet has been produced by the hadronization of a b quark. The minimum thresholds on these discriminators define loose (“L”), medium (“M”), and tight (“T”) operating points with a misidentification probability for light-parton jets close to 10%, 1%, and 0.1%, respectively, at an average jet p_T of about 80 GeV.

Some of the algorithms make use of the track impact parameters (IP) with respect to the primary vertex, defined as the distance between the primary vertex and the track at their point of closest approach, to distinguish the decay products of a b hadron from prompt tracks. The impact parameter has the same sign as the scalar product of the vector pointing from the primary vertex to the point of closest approach with the jet direction. Tracks originating from the decay of particles travelling along the jet axis will tend to have positive IP values. In contrast, the impact parameters of prompt tracks can have positive or negative IP values. The impact parameter significance, defined as the ratio of the IP to its estimated uncertainty, is used as an observable.

The *Track Counting* (TC) algorithm sorts tracks inside a jet by decreasing values of the IP significance. Although the ranking tends to bias the values for the first track to high positive IP significances, the probability to have several tracks with high positive values is low for light-parton jets. Therefore the two different versions of the algorithm use the IP

significance of the second and third ranked track as the discriminator value. These two versions of the algorithm are called *Track Counting High Efficiency* (TCHE) and *Track Counting High Purity* (TCHP), respectively.

A general extension of the TC algorithm, i.e. the *Jet Probability* (JP), combines the IP information of several tracks inside the jet, using an estimate of the likelihood that all tracks associated to the jet come from the primary vertex as a discriminating variable. A variant of the JP algorithm also exists in which the four tracks with the highest impact parameter significance get a higher weight in the jet probability calculation. This algorithm is referred to as *Jet B-Probability* (JBP).

A different approach consists in using the secondary vertices and the related kinematic variables, together with displaced tracks information, to discriminate between b and non-b jets. This algorithm is known as *Combined Secondary Vertex* (CSV)⁴. The magnitude and direction of the vector connecting the primary and secondary vertices are used as discriminating variables and quality requirements are imposed to secondary vertex candidates. In addition, the usage of displaced tracks information allows to increase the efficiency for events where no secondary vertex is found. Several variables related to secondary vertices and displaced tracks are used to build likelihood ratios that have a good discriminating power.

Two algorithms for reconstructing secondary vertices are exploited. For the first algorithm, the tracks associated to jets and fulfilling some quality requirements are used in the adaptive vertex reconstruction (AVR) algorithm [32]. The AVR is the algorithm used for CMS analyses during the 8 TeV data taking. In contrast with this method, the Inclusive Vertex Finder (IVF) algorithm is not seeded from tracks associated to reconstructed jets, but instead makes use of all the tracks in the event, with appropriate selections, to reconstruct the secondary vertices. The latter is the default algorithm used to reconstruct secondary vertices for CMS analyses using 13 TeV data.

A new b jet identification algorithm has been recently developed, combining the discriminators provided by the JP and CSV algorithms with a Boosted Decision Tree (BDT) technique. This combined multivariate algorithm (cMVA) is found to slightly improve the b jet identification efficiency.

The performance of these algorithms is determined using simulated $t\bar{t}$ events, selecting events with at least one jet with $p_T > 30$ GeV. This is shown in Fig. 3.5, where the b jet identification efficiency versus the misidentification probability is reported for the various algorithms. This figure serves as an illustration as the b tagging performance depend on the p_T and η distribution of the jets, and need to be checked for each analysis phase space.

3.4.1. B tagging efficiency

3.5. Missing transverse energy

⁴An improved version of this algorithm, CSVv2, has been developed for Run 2 analyses.

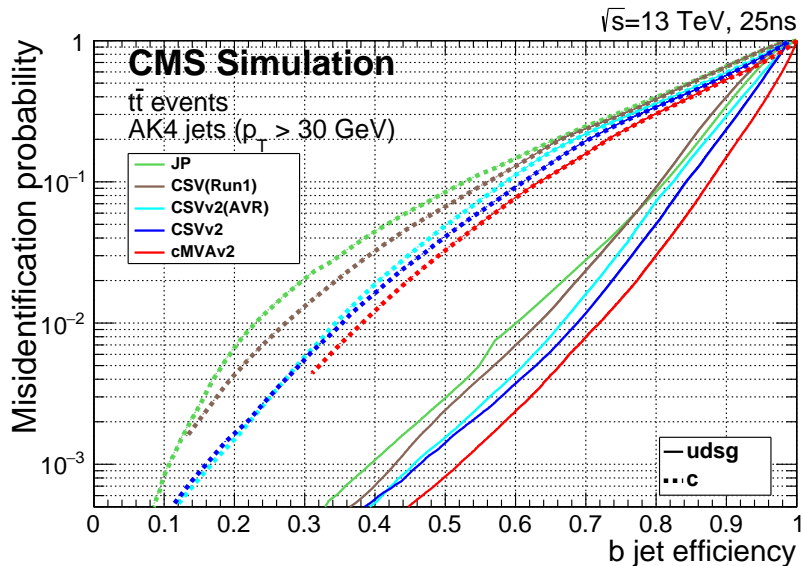


Figure 3.5.: Performance of the b jet identification efficiency algorithms demonstrating the probability for non-b jets to be misidentified as b jet as a function of the efficiency to correctly identify b jets. The curves are obtained on simulated $t\bar{t}$ events using anti- k_t jets clustered with $R = 0.4$ and requiring $p_T > 30$ GeV.

Chapter 4.

¹¹⁴⁸ Measurement of the Higgs boson ¹¹⁴⁹ transverse momentum at 8 TeV using ¹¹⁵⁰ $H \rightarrow WW \rightarrow 2\ell 2\nu$ decays

¹¹⁵¹ 4.1. Introduction

¹¹⁵² The Higgs boson production at hadron colliders is characterized by p_T^H and η . The η
¹¹⁵³ distribution is essentially driven by the PDF of the partons in the colliding hadrons, and it
¹¹⁵⁴ is only mildly sensitive to radiative corrections. The p_T^H distribution is instead sensitive to
¹¹⁵⁵ QCD radiative corrections. Considering the ggH production mode, at LO in perturbation
¹¹⁵⁶ theory, $\mathcal{O}(\alpha_s^2)$, the Higgs boson is always produced with p_T^H equal to zero. Indeed in order
¹¹⁵⁷ to have p_T different from zero, the Higgs boson has to recoil at least against one parton.
¹¹⁵⁸ Higher order corrections to the ggH process are numerically large and are known at NLO
¹¹⁵⁹ including full top quark mass dependence [33, 34], and at NNLO using the so-called large- m_t
¹¹⁶⁰ approximation [35–37], in which the top quark mass is assumed to be very large and the
¹¹⁶¹ fermionic loop is replaced by an effective vertex of interaction. Starting from the NLO,
¹¹⁶² the Higgs boson can be produced recoiling against other final state partons, resulting in
¹¹⁶³ a finite p_T^H . For this reason the LO process for Higgs production at $p_T \neq 0$ is at $\mathcal{O}(\alpha_s^3)$,
¹¹⁶⁴ and the counting of perturbative orders differs between inclusive Higgs boson production
¹¹⁶⁵ and p_T^H distribution. Also, NNLO QCD corrections in the p_T^H observable have recently been
¹¹⁶⁶ shown [38].

¹¹⁶⁷ When $p_T^H \sim m_H$ the QCD radiative corrections to p_T^H differential cross section are
¹¹⁶⁸ theoretically evaluated using fixed-order calculations. When $p_T^H \ll m_H$ the perturbative
¹¹⁶⁹ expansion does not converge due to the presence of large logarithmic terms of the form
¹¹⁷⁰ $\alpha_s^n \ln^{2n} m_H^2/p_T^2$, leading to a divergence of $d\sigma/dp_T$ in the limit of $p_T \rightarrow 0$. For computing
¹¹⁷¹ the p_T^H spectrum in this region soft-gluon resummation techniques are used, and matched to
¹¹⁷² the fixed-order calculation in the $p_T^H \sim m_H$ region. For the p_T^H differential cross section the
¹¹⁷³ large- m_t calculation is a crude approximation, since it is known that the top quark mass
¹¹⁷⁴ has a non-negligible effect on the shape of the spectrum. Moreover the inclusion of the
¹¹⁷⁵ bottom quark contribution in the fermionic loop can significantly modify the p_T^H shape [39],
¹¹⁷⁶ as shown in Fig. 4.1. Hence, a precise experimental measurement of the p_T^H spectrum is
¹¹⁷⁷ important to test the existing SM calculations.

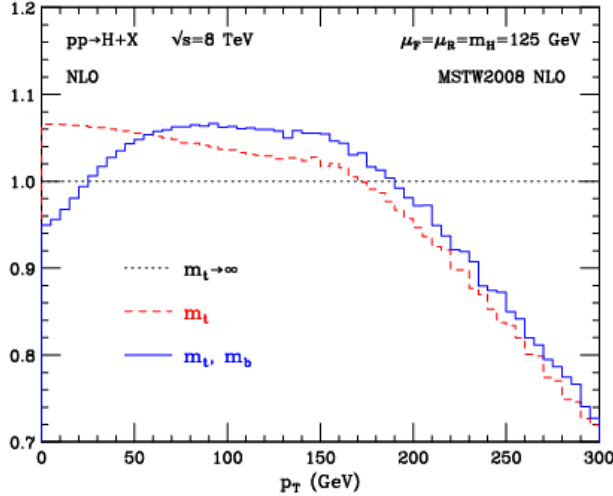


Figure 4.1.: p_T^H distribution computed at NLO (α_s^3) and normalized to the calculation obtained in the large- m_t approximation. The red dashed line corresponds to the calculation including the top quark mass while the blue line refers to the calculation including also the bottom quark effects.

Possible extensions of the SM predict a modification of the Higgs boson couplings to gluons and to the top quark. Many of these models actually predict the existence of new states that interact with the SM Higgs boson, but are beyond the direct production reach at the actual LHC energies. The effect of these new states could however show up as a deviation of the Higgs boson couplings with respect to the SM expectation. The modification of the couplings, as shown in Refs. [40, 41], can change the kinematics of the Higgs boson production and the effect can be particularly sizeable in the tail of the p_T^H distribution. Other models, such as Composite Higgs [42], predict the existence of top-partners, which are heavy resonances with the same quantum numbers as the top quark, that can interact with the Higgs boson in the ggH fermionic loop, changing the p_T^H shape with respect to what the SM predicts [43]. The measurement of the p_T^H spectrum is thus a useful tool for indirect searches of new particles predicted by theories beyond the SM.

Measurements of the fiducial cross sections and of several differential distributions, using the $\sqrt{s} = 8$ TeV LHC data, have been reported by ATLAS [44–46] and CMS [47, 48] for the $H \rightarrow ZZ \rightarrow 4\ell$ ($\ell = e, \mu$) and $H \rightarrow \gamma\gamma$ decay channels. In this chapter a measurement of the fiducial cross section times branching fraction ($\sigma \times \mathcal{B}$) and p_T spectrum for Higgs boson production in $H \rightarrow WW \rightarrow e^\pm \mu^\mp \nu\nu$ decays, based on $\sqrt{s} = 8$ TeV LHC data, is reported.

The analysis is performed looking at different flavour leptons in the final state in order to suppress the sizeable contribution of backgrounds containing a same-flavour lepton pair originating from Z boson decay.

Although the $H \rightarrow WW \rightarrow 2\ell 2\nu$ channel has lower resolution in the p_T^H measurement compared to the $H \rightarrow \gamma\gamma$ and $H \rightarrow ZZ \rightarrow 4\ell$ channels because of neutrinos in the final state, the channel has a significantly larger $\sigma \times \mathcal{B}$, exceeding those for $H \rightarrow \gamma\gamma$ by a factor of 10 and $H \rightarrow ZZ \rightarrow 4\ell$ by a factor of 85 for a Higgs boson mass of 125 GeV [49], and is

characterized by good signal sensitivity. Such sensitivity allowed the observation of a Higgs boson at the level of 4.3 (5.8 expected) standard deviations for a mass hypothesis of 125.6 GeV using the full LHC data set at 7 and 8 TeV [50].

The measurement is performed in a fiducial phase space defined by kinematic requirements on the leptons that closely match the experimental event selection.

The effect of the limited detector resolution, as well as the selection efficiency with respect to the fiducial phase space are corrected to particle level with an unfolding procedure [51], as explained in Sec. 4.7.

4.2. Data sets, triggers and MC samples

This analysis relies on the published $H \rightarrow WW$ measurements [50] in terms of code, selections and background estimates for both the ggH and VBF production mechanisms.

4.2.1. Data sets and triggers

The data sets used for the analysis correspond to 19.4 fb^{-1} at $\sqrt{s} = 8 \text{ TeV}$ of integrated luminosity composed of the following CMS data taking periods during 2012: 2012A (892 pb^{-1}), 2012B (4440 pb^{-1}), and 2012C (6898 pb^{-1}) and 2012D (7238 pb^{-1}). Data have been checked and validated and only data corresponding to good data taking quality are considered. The $e^\pm \mu^\mp$ final state is considered in this analysis.

For the data samples, the events are required to fire one of the unprescaled single-electron, single-muon or muon-electron triggers. Due to the rather high LHC instantaneous luminosity the single-lepton triggers must have high HLT p_T thresholds, otherwise the rate of these triggers would be too large to be sustained. The double-lepton triggers allow to lower down the p_T thresholds while keeping a sustainable trigger rate, thus maintaining a good sensitivity to the Higgs boson signal, for which the lepton p_T can be rather small. A brief overview of the HLT p_T criteria on the leptons is given in Table 4.1. While the HLT lepton p_T thresholds of 17 and 8 GeV for the double lepton triggers accommodate the offline lepton p_T selection of 20 and 10 GeV, the higher p_T thresholds in the single lepton triggers help partially recovering double lepton trigger inefficiencies as a high p_T lepton is on average expected due to the kinematics of the Higgs decay.

The trigger is not simulated in MC samples but the combined trigger efficiency is estimated from data and applied as a weight to all simulated events, as described in Sec. 3.2.8.

4.2.2. Monte Carlo samples

Several Monte Carlo event generators are used to simulate the signal and background processes:

Table 4.1.: Highest transverse momentum thresholds applied in the lepton triggers at the HLT level. Double set of thresholds indicates the thresholds for each leg of the double lepton triggers.

Trigger Path	8 TeV
Single-Electron	$p_T > 27$ GeV
Single-Muon	$p_T > 24$ GeV
Muon-Electron	$p_T > 17$ and 8 GeV
Electron-Muon	$p_T > 17$ and 8 GeV

- The first version of the POWHEG program [52–56] (POWHEG V1) provides event samples for the $H \rightarrow WW$ signal for the gluon fusion (ggH) and VBF production mechanisms, as well as $t\bar{t}$ and tW processes [57], with NLO accuracy.
- The $qq \rightarrow W^+W^-$, Drell-Yan, ZZ, WZ, $W\gamma$, $W\gamma^*$, tri-bosons and $W+jets$ processes are generated using the MADGRAPH 5.1.3 [58] event generator.
- The $gg \rightarrow W^+W^-$ process is generated using the GG2WW 3.1 generator [59] and its cross section is scaled to the approximate NLO prediction [60, 61].
- The VH process is simulated using PYTHIA 6.426 [62].

For leading-order generators samples, the CTEQ6L [63] set of parton distribution functions (PDF) is used, while CT10 [64] is used for next-to-leading order (NLO) ones. Cross section calculations [65] at next-to-next-to-leading order (NNLO) are used for the $H \rightarrow WW$ process, while NLO calculations are used for background cross sections. The $H \rightarrow WW$ process simulation is reweighted so that the p_T^H spectrum and inclusive production cross section closely match the SM calculations that have NNLO+NNLL pQCD accuracy in the description of the Higgs boson inclusive production, in accordance with the LHC Higgs Cross Section Working Group recommendations [49]. The reweighting of the p_T^H spectrum is achieved by tuning the POWHEG generator, as described in detail in Ref. [66]. Cross sections computed with NLO pQCD accuracy [49] are used for the background processes. The contribution of the $t\bar{t}H$ production mechanisms is checked to be negligible in each bin of p_T^H (below 1%) and is not included among the different production mechanisms. In Fig. 4.2 the relative fraction of the four production mechanisms is shown for each p_T^H bin.

For all processes, the detector response is simulated using a detailed description of the CMS detector, based on the GEANT4 package [67].

Minimum bias events are superimposed on the simulated events to emulate the additional pp interactions per bunch crossing (pileup). The number of pile-up events simulated in the MC samples (in the same bunch crossing, in time, or in the previous or following one, out of time pileup) have been generated poissonianly sampling from a distribution similar to what is expected from data. For a given range of analyzed runs, the mean number of pileup interactions per bunch crossing is estimated per luminosity block using the instantaneous luminosity provided by the LHC, integrated over the entire run range and normalized. The

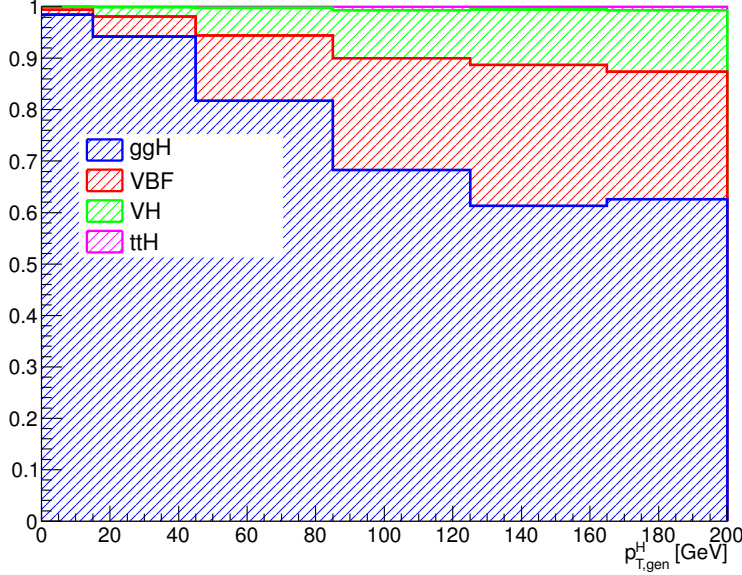


Figure 4.2.: Relative fraction of ggH, VBF, VH and ttH in each bin of the Higgs boson transverse momentum.

average number of pileup events per beam crossing in the 2011 data is about 10, and in the 2012 data it is about 20.

The simulated events are reweighted to correct for observed differences between data and simulation in the number of pileup events, as shown in Fig. 4.3, trigger efficiency, and lepton reconstruction and identification efficiencies [50].

For the comparison of the measured unfolded spectrum with the theoretical predictions, two additional MC generators are used for simulating the SM Higgs boson production in the ggH process: HRES 2.3 [39, 68] and the second version of the POWHEG generator (POWHEG V2) [69]. HRES is a partonic level MC generator that computes the SM Higgs boson cross section at NNLO accuracy in pQCD and performs the NNLL resummation of soft-gluon effects at small p_T . The central predictions of HRES are obtained including the exact top and bottom quark mass contribution to the gluon fusion loop, fixing the renormalization and factorization scale central values at a Higgs boson mass of 125 GeV. The cross section normalization is scaled, to take into account electroweak corrections, by a factor of 1.05 and the effects of threshold resummation by a factor of 1.06 [70, 71]. The upper and lower bounds of the uncertainties are obtained by scaling up and down both the renormalization and the factorization scales by a factor of two. The POWHEG V2 generator is a matrix element based generator that provides a NLO description of the ggH process in association with zero jets, taking into account the finite mass of the bottom and top quarks. The POWHEG prediction is tuned using the POWHEG damping factor *hdump* of 104.17 GeV, in order to match the p_T^H spectrum predicted by HRES in the full phase space. This factor reduces the emission of additional jets in the high p_T regime, and enhances the

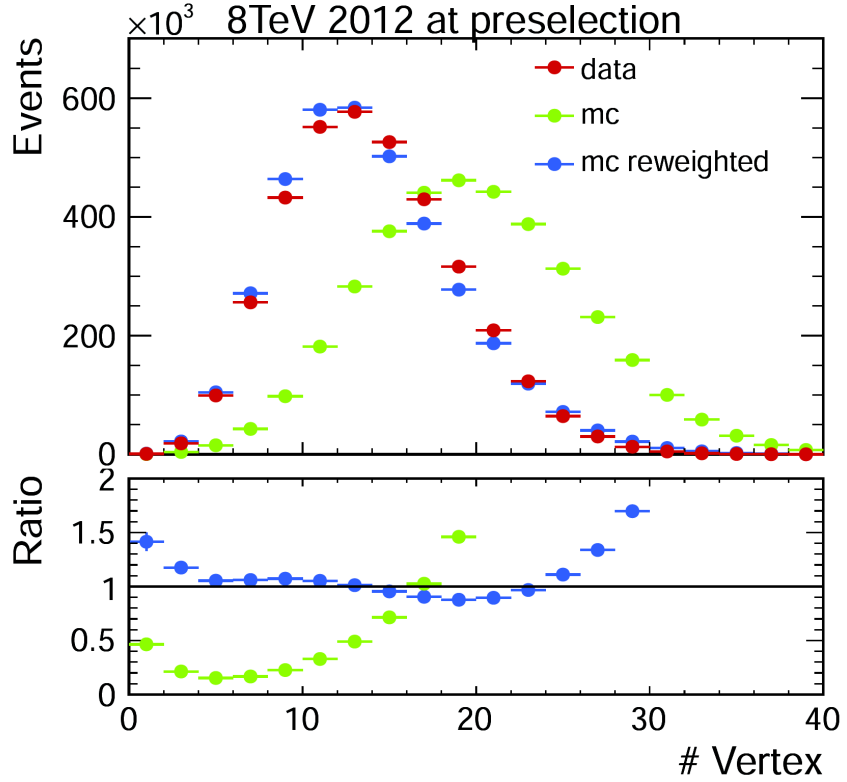


Figure 4.3.: Distribution of the number of vertices in data and in simulation, before and after applying the pile-up reweighting.

contribution from the Sudakov form factor in the limit of low p_T . The POWHEG generator is interfaced to the JHUGEN generator version 5.2.5 [72–74] for the decay of the Higgs boson to a W boson pair and interfaced with PYTHIA 8 [75] for the simulation of parton shower and hadronization effects.

4.3. Analysis Strategy

The analysis presented here is based on that used in the previously published $H \rightarrow WW \rightarrow 2\ell 2\nu$ measurements by CMS [50], modified to be inclusive in the number of jets. This modification significantly reduces the uncertainties related to the modelling of the number of jets produced in association with the Higgs boson.

4.3.1. Event reconstruction and selections

The electron selection is based on two multivariate discriminants, one specialised in identifying the electron object and the other for isolation. The cut value for each discriminant is optimised to provide a good fake electron rejection and to improve the signal acceptance.

Muons are reconstructed using the standard CMS selection and are required to be identified both in the tracker (*Tracker Muon*) and in the muon chambers (*Global Muon*). Additionally quality criteria on the muon track are required, such as to have at least 10 hits in the tracker (at least one of which in the pixel detector) and to have $\chi^2/ndf < 10$. Muon isolation is based on the Particle-Flow algorithm. An MVA approach is considered, based on the radial distributions of the Particle-Flow candidates inside a cone of radius 0.5 around the muon direction.

The efficiencies for the identification and isolation of the electrons and muons are measured in data and in simulation selecting a pure sample of leptons coming from the $Z \rightarrow \ell\ell$ decay, and using a Tag and Probe technique very similar to the one described in Sec. 4.2.1 for the trigger efficiency. In this case, the probe lepton is defined by loose isolation and identification requirements and the efficiency to pass the tight analysis selections is measured performing a simultaneous fit of signal plus background in two categories, corresponding to events in which the probe lepton pass or fail the analysis requirements. For the electrons, the resonant signal contribution in the fit is modelled as the convolution of a Breit-Wigner and a Crystal-Ball function. A polynomial function is added to take into account the tail in the low mass region. For muons the signal is fitted using the sum of two Voigtian functions. For both electrons and muons the background contribution is modelled as a third order Bernstein polynomial function. The efficiencies for data and simulation are extracted as parameters of the fit and are used as scale factors to correct the MC simulation to precisely model the data.

This part would probably end up in the Object Reconstruction chapter

Jets in this analysis are reconstructed by combining the energy measured in the calorimeters and tracks from charged particles on basis of the standard CMS particle flow algorithm and using the anti- k_T clustering algorithm with $R = 0.5$. Events will be classified into zero jet, one jet and VBF topologies by counting jets within $|\eta| < 4.7$ and for $p_T > 30 \text{ GeV}$.

In addition to the standard CMS PF E_T^{miss} , in this analysis a *projected* E_T^{miss} variable is also used. The *projected* E_T^{miss} is defined as the component of \vec{p}_T^{miss} transverse to the nearest lepton if the lepton is situated within the azimuthal angular window of $\pm\pi/2$ from the \vec{p}_T^{miss} direction, or the E_T^{miss} itself otherwise. Since the E_T^{miss} resolution is degraded by pileup, the minimum of two projected E_T^{miss} variables is used: one constructed from all identified particles (full projected E_T^{miss}), and another constructed from the charged particles only (track projected E_T^{miss}).

Background events from $t\bar{t}$ and tW production are rejected applying a soft-muon veto and b-tagging veto. The former selection requires that in the event there are no muons from b-decays passing the following cuts:

- the muon is reconstructed as TrackerMuon;
- the number of hits of the muon in the Silicon Tracker is greater than 10;
- the transverse impact parameter of the muon is less than 0.2 cm;
- if $p_T > 20 \text{ GeV}$ then the muon is required to be non-isolated with $ISO/p_T > 0.1$.

The latter veto rejects events that contain jets tagged as b-jets using two different algorithms for high and low p_T jets. For jets with p_T between 10 and 30 GeV, the Track-Counting-High-Efficiency (TCHE) algorithm, with a cut at 2.1 on the discriminating variable, is applied. For jets above 30 GeV, a better performing algorithm, Jet-Probability (JP), is used. Jets are identified as b-jets by the JP algorithm if the discriminating variable has a value above 1.4. In the following a b-tagged jet is defined as a jet, within $|\eta| < 2.4$ (b-tagging requires the tracker information), with a value of the discriminating variable above the mentioned thresholds for the two algorithms.

The event selection consists of several steps. The first step is to select WW-like events applying a selection that consists of the following set of cuts:

1. Lepton preselection:

- at least two opposite-charge and opposite-flavour ($e\mu$) isolated leptons reconstructed in the event;
- $|\eta| < 2.5$ for electrons and $|\eta| < 2.4$ for muons;
- $p_T > 20$ GeV for the leading lepton. For the trailing lepton, the transverse momentum is required to be larger than 10 GeV.

2. Extra lepton veto: the event is required to have two and only two opposite-sign leptons passing the lepton selection.

3. E_T^{miss} preselection: particle flow E_T^{miss} is required to be greater than 20 GeV.

4. projected E_T^{miss} selection: minimum projected E_T^{miss} required to be larger than 20 GeV.

5. Di-lepton mass cut: $m_{\ell\ell} > 12$ GeV in order to reject low mass resonances and QCD backgrounds.

6. Di-lepton p_T cut: $p_T^{\ell\ell} > 30$ GeV.

7. Transverse mass: $m_T > 60$ GeV to reject Drell-Yan to $\tau\tau$ events.

In addition to the WW-like preselection other cuts are applied in order to reduce the top quark background (both $t\bar{t}$ and tW), which is one of the main backgrounds in this final state. Two different selections are used depending on the number of jets with $p_T > 30$ GeV in the event. This is done to suppress the top quark background both in the low p_T^H region, where 0-jets events have the largest contribution, and for higher p_T^H values where also larger jet multiplicity events are important. The selection for 0-jets events relies on the soft-muon veto and on a soft jets (with $p_T < 30$ GeV) anti b-tagging requirement. The latter requirement exploits the TCHE algorithm to reject soft jets that are likely to come from b quarks hadronization.

For events with a jet multiplicity greater or equal than one, a different selection is applied. In this case we exploit the good b-tagging performances of the JP tagger to reject all the jets with $p_T > 30$ GeV that are likely to come from a b quark hadronization. The analysis selection requires to have no events containing b-tagged jets with $p_T > 30$ GeV.

A cut-flow plot is reported in Fig. 4.4, showing the effect of each selection using signal and background simulations. In the first bin, labelled as “No cut”, no selection is applied

and the bin content corresponds to the total expected number of events with a luminosity of 19.4 fb^{-1} . All the events in this bin have at least two leptons with a loose transverse momentum cut of 8 GeV. In the following bin the lepton cuts are applied, including the requirement to have two opposite-sign and opposite-flavour leptons and the extra lepton veto. Then all the other selections are progressively reported, showing the effect of each cut on the background and signal yields. For each selection the expected signal over background ratio is also shown, which, after the full selection requirements, reach a maximum value of about 3%.

4.3.2. Fiducial phase space

The Higgs boson transverse momentum is measured in a fiducial phase space, whose requirements are chosen in order to minimize the dependence of the measurements on the underlying model of the Higgs boson properties and its production mechanism.

The exact requirements are determined by considering the two following correlated quantities: the reconstruction efficiency for signal events originating from within the fiducial phase space (fiducial signal efficiency ϵ_{fid}), and the ratio of the number of reconstructed signal events that are from outside the fiducial phase space (“out-of-fiducial” signal events) to the number from within the fiducial phase space. The requirement of having a small fraction of out-of-fiducial signal events, while at the same time preserving a high value of the fiducial signal efficiency ϵ_{fid} , leads to a loosening of the requirements on the low-resolution variables, E_T^{miss} and m_T , with respect to the analysis selection.

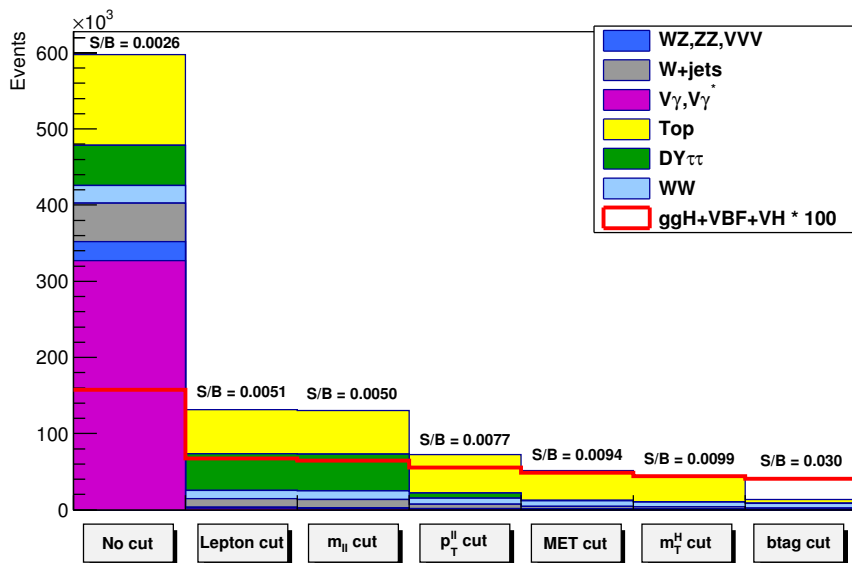


Figure 4.4.: Effect of single selections on MC samples. The signal (red line) is multiplied by 100 and superimposed on stacked backgrounds. In each bin, corresponding to a different selection, is reported the expected number of events in MC at a luminosity of 19.46 fb^{-1} .

The fiducial phase space used for the cross section measurements is defined at the particle level by the requirements given in Table 4.2. The leptons are defined as Born-level leptons, i.e. before the emission of final-state radiation (FSR), and are required not to originate from leptonic τ decays. The effect of including FSR is evaluated to be of the order of 5% in each p_T^H bin. For the VH signal process, the two leptons are required to originate from the $H \rightarrow WW \rightarrow 2\ell 2\nu$ decays in order to avoid including leptons coming from the associated W or Z boson.

Table 4.2.: Summary of requirements used in the definition of the fiducial phase space.

Physics quantity	Requirement
Leading lepton p_T	$p_T > 20 \text{ GeV}$
Subleading lepton p_T	$p_T > 10 \text{ GeV}$
Pseudorapidity of electrons and muons	$ \eta < 2.5$
Invariant mass of the two charged leptons	$m_{\ell\ell} > 12 \text{ GeV}$
Charged lepton pair p_T	$p_T^{\ell\ell} > 30 \text{ GeV}$
Invariant mass of the leptonic system in the transverse plane	$m_T^{\ell\ell\nu\nu} > 50 \text{ GeV}$
E_T^{miss}	$E_T^{\text{miss}} > 0$

A detailed description of the fiducial region definition and its optimization is given in appendix A.

4.3.3. Binning of the p_T^H distribution

Experimentally, the Higgs boson transverse momentum is reconstructed as the vector sum of the lepton momenta in the transverse plane and E_T^{miss} .

$$\vec{p}_T^H = \vec{p}_T^{\ell\ell} + \vec{p}_T^{\text{miss}} \quad (4.1)$$

Compared to other differential analysis of the Higgs cross section, such as those in the ZZ and $\gamma\gamma$ decay channels, this analysis has to cope with the limited resolution due to the E_T^{miss} entering the transverse momentum measurement. The effect of the limited E_T^{miss} resolution has two main implications on the analysis strategy. The first one is that the choice of the binning in the p_T^H spectrum needs to take into account the detector resolution. The second implication is that migrations of events across bins are significant and an unfolding procedure needs to be applied to correct for selection efficiencies and bin migration effects.

Given these aspects the criterion that was used to define the p_T^H bin size is devised to keep under control the bin migrations due to the finite resolution. For any given bin i we can define the purity P_i on a signal sample as the number events that are generated and also reconstructed in that bin, $N_i^{\text{GEN|RECO}}$, divided by the number of events reconstructed

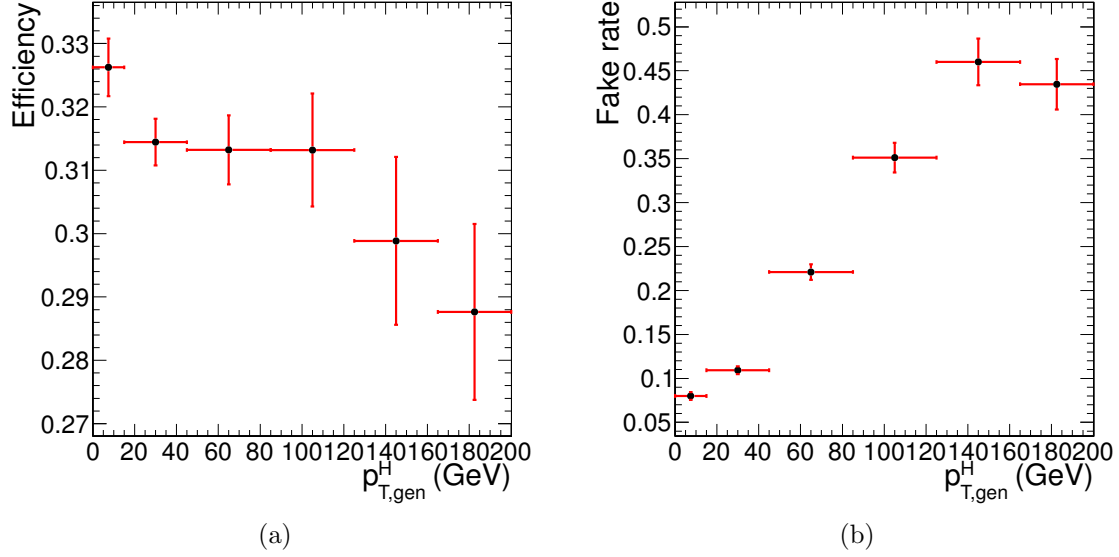


Figure 4.5.: Efficiency of the full selection (a) and fake rate (b) as a function of p_T^H .

1424 there, N_i^{RECO} :

$$P_i = \frac{N_i^{\text{GEN|RECO}}}{N_i^{\text{RECO}}} \quad . \quad (4.2)$$

1425 The bin width is chosen in such a way as to make the smallest bins able to ensure a purity
 1426 of about 60% on a ggH signal sample. Following this prescription we have divided the whole
 1427 p_T^H range in the following six bins: [0-15 GeV], [15-45 GeV], [45-85 GeV], [85-125 GeV],
 1428 [125-165 GeV], [165-∞ GeV].

1429 The efficiency of the analysis selection with respect to the fiducial phase space is reported
 1430 in Fig. 4.5 (a) for each p_T^H bin. The efficiency denominator is the number of events that
 1431 are inside the fiducial phase space, while the numerator is the number of events that pass
 1432 both the analysis and the fiducial phase space selections. The fake rate, defined by the
 1433 ratio of signal events that pass the analysis selection but are not within the fiducial phase
 1434 space, divided by the total number of events passing both the analysis and the fiducial
 1435 phase space selections is shown in Fig. 4.5 (b). For both the selection efficiency and the
 1436 fake rate, all the signal production mechanisms are included. The overall efficiency and
 1437 fake rate are $\epsilon = 0.362 \pm 0.005$ and $\text{fake rate} = 0.126 \pm 0.004$ respectively, where only
 1438 statistical uncertainties are taken into account.

1439 If a 4π acceptance is defined, requiring just that the Higgs decays to WW and then to
 1440 $2\ell 2\nu$, the efficiency becomes $\epsilon = 0.0396 \pm 0.0003$ and the fake rate is zero.

1441 4.4. Background estimation

1442 4.4.1. Top quark background

1443 In this analysis the top quark background is divided into two different categories depending
1444 on the number of jets in the event. In the two categories different selections are applied,
1445 especially concerning the b-tagging requirements.

1446 The general strategy for determining the residual top events in the signal region is to
1447 first measure the top tagging efficiencies from an orthogonal region of phase space in data.
1448 The orthogonal phase space is defined inverting the b-veto requirement of the signal region,
1449 in such a way to have a control region enriched in top quark events. Then, using this
1450 efficiency, the number of events with the associated uncertainty is propagated from the
1451 control region to the signal region. The number of surviving top events in the signal region
1452 would then be:

$$N_{bveto}^{\text{signal}} = N_{btag}^{\text{control}} \cdot \frac{1 - \epsilon_{\text{top}}}{\epsilon_{\text{top}}} \quad (4.3)$$

1453 where $N_{btag}^{\text{control}}$ is the number of events in the control region and ϵ_{top} is the efficiency as
1454 measured in data.

1455 The methods to estimate the top background contribution in the two jet categories are
1456 different and are explained below.

1457 0-jets category

1458 Most of the top background, composed of $t\bar{t}$ and tW processes, is rejected in the 0-jet bin
1459 by the jet veto. The top-tagging efficiency in the zero jet bin, $\epsilon_{\text{tag}}^{0-jet}$, is the probability for a
1460 top event to fail one of either the b-tagging veto or the soft muon veto, and is defined as:

$$\epsilon_{\text{tag}} = \frac{N_{\text{tag}}^{\text{control}}}{N^{\text{control}}} \quad , \quad (4.4)$$

1461 where N^{control} is the number of events in the top control phase space defined requiring
1462 one b-tagged jet with $p_T > 30$ GeV, and $N_{\text{tag}}^{\text{control}}$ is the subset of those events that pass
1463 either the soft muon tagging or the low- p_T b jet tagging. The purity of this control sample,
1464 as estimated from simulation, is about 97%. The remaining 3% background contribution is
1465 estimated from simulation and subtracted from the numerator and denominator of Eq. (4.5).
1466 The efficiency $\epsilon_{\text{top}}^{0-jet}$ can then be estimated using the following formula:

$$\epsilon_{\text{top}}^{0-jet} = f_{t\bar{t}} \cdot \epsilon_{2b} + f_{tW} \cdot (x \cdot \epsilon_{2b} + (1 - x) \cdot \epsilon_{\text{tag}}) \quad , \quad (4.5)$$

$$\epsilon_{2b} = 1 - (1 - \epsilon_{\text{tag}})^2 \quad , \quad (4.6)$$

where $f_{t\bar{t}}$ and f_{tW} are the $t\bar{t}$ and tW fractions respectively, x is the fraction of tW events containing 2 b jets, and ϵ_{2b} is the efficiency for a top event with 0 counted jets, i.e. two soft b jets, to pass the top veto. For the ratio of $t\bar{t}$ and tW cross-sections an uncertainty of 17% is assumed. The fraction $f_{t\bar{t}}$ is estimated using MC simulation of the $t\bar{t}$ and tW processes at NLO accuracy.

Using this procedure a data/simulation scale factor of 0.98 ± 0.17 is found, and is applied to correct the MC simulation in order to match the data.

Category with more than 0 jets

The strategy for the estimation of the top background in events with at least one jet with p_T greater than 30 GeV is the following. First of all the efficiency for tagging a b jet is measured both in data and simulation and the values are used to correct the simulation for different b-tagging efficiencies in data and simulation. This evaluation is performed in a control region, called CtrlTP, containing at least two jets, using a Tag&Probe technique. The procedure to extract these scale factors is presented in Sec. 4.4.1. Then a larger statistics control region, CtrlDD, is defined by requiring at least one b-tagged jet and we use the simulation, corrected for the previously computed b-tagging efficiency scale factor, to derive the factor that connects the number of events in CtrlDD to the number of events in the signal region. This second step is explained in detail in Sec. 4.4.1.

Tag&Probe

The Tag&Probe technique is a method to estimate the efficiency of a selection on data. It can be applied whenever one has two objects in one event, by using one of the two, the *tag*, to identify the process of interest, and using the second, the *probe*, to actually measure the efficiency of the selection being studied. In our case we want to measure the b-tagging efficiency, so what we need is a sample with two b-jets per event. The easiest way to construct such a sample is to select $t\bar{t}$ events.

The CtrlTP control region is defined selecting the events which pass the lepton preselection cuts listed in Sec. 4.3.1, and have at least two jets with p_T greater than 30 GeV. One of the two leading jets is required to have a *JetBProbability* score higher than 0.5. From events in this control region we built *tag-probe* pairs as follows. For each event the two leading jets are considered. If the leading jet passes the *JetBProbability* cut of 0.5, that is considered a *tag*, and the sub-leading jet is the *probe*. In order to avoid any bias that could arise from the probe being always the second jet, the pair is tested also in reverse order, meaning that the sub-leading jet is tested against the *tag* selection, and in case it passes, then the leading jet is used as *probe* in an independent *tag-probe* pair. This means that from each event passing the CtrlTP cuts one can build up to two *tag-probe* pairs.

If the *tag* selection were sufficient to suppress any non top events, one could estimate the efficiency by dividing the number of *tag-probe* pairs in which the *probe* passes the analysis cut $JetBProbability > 1.4$ (*tag-pass-probe*) by the total number of *tag-probe* pairs. However this is not the case. In order to estimate the efficiency in the presence of background a variable that discriminates between true b-jets and other jets in a $t\bar{t}$ sample is chosen. The variable is the p_T of the *probe* jet. For real b-jets this variable has a peak around 60 GeV, while it does not peak for other jets. The idea is to fit simultaneously the p_T spectrum for *probe* jets in *tag-pass-probe* and *tag-fail-probe* pairs, linking together the normalizations of the two samples as follows:

$$N_{TPP} = N_s \epsilon_s + N_b \epsilon_b \quad (4.7)$$

1511

$$N_{TFP} = N_s(1 - \epsilon_s) + N_b(1 - \epsilon_b) \quad (4.8)$$

where N_{TPP} is the number of *tag-pass-probe* pairs, N_{TFP} is the number of *tag-fail-probe* pairs, N_s is the number of *tag-probe* pairs in which the probe is a b-jet, N_b is the number of *tag-probe* pairs in which the probe is a not b-jet, ϵ_s is the b-tagging efficiency, ϵ_b is the probability of identifying as b-jet a non-b-jets, i.e. the mistag rate.

A χ^2 simultaneous fit of the *probe* p_T spectrum for *tag-pass-probe* and *tag-fail-probe* pairs is performed, deriving the shapes for true b-jets and non-b-jets from the simulation, and extracting N_s , N_b , ϵ_s and ϵ_b from the fit. The result of the fit on simulation is shown in Fig. 4.6. The relevant efficiencies are:

$$\epsilon_s^{MC} = 0.7663 \pm 0.0072 \quad (4.9)$$

1520

$$\epsilon_b^{MC} = 0.208 \pm 0.015 \quad (4.10)$$

We have checked that these values are consistent with the true value for the b-tagging efficiency. The true value is computed by selecting jets that are matched within a cone of $\Delta R < 0.5$ with a generator level b-quark, and counting the fraction of those that pass the $JetBProbability$ cut of 1.4. This means that the *tag-probe* method does not introduce biases within the simulation statistic accuracy.

In order to assess the robustness of the fit, 5000 toy MC samples have been generated with a statistics equivalent to the one expected in data and the same fit is performed. All the 5000 fit succeeded, and the pull distributions for ϵ_s and ϵ_b parameters are shown in Fig. 4.7. The plots show the pull of the efficiencies measured in the fit, where the pull variable for each toy i is defined as:

$$pull(\epsilon_{s(b)}) = \frac{\epsilon_{s(b)}^{\text{true}} - \epsilon_{s(b)}^i}{\sigma(\epsilon_{s(b)}^i)} \quad (4.11)$$

1531 The pulls are centered on 0 and have σ close to 1, as expected.

1532 An example fit for one of the toys is shown in Fig. 4.8

1533 Before running the fit on data, the shapes used in the fit have been validated. To do
 1534 so, a purer top enriched phase space has been defined by requiring exactly two jets with
 1535 *JetBProbability* score higher than 1.5 and no additional b-tagged jets, rejecting also jets
 1536 with p_T smaller than 30 GeV. On this purer sample we have compared data against the
 1537 shape used to fit the true b-jets in the *tag-pass-probe* distribution. The result is shown in
 1538 Fig. 4.9 and shows good agreement.

1539 Finally the fit has been performed on data, as shown in Fig. 4.10, providing the following
 1540 efficiencies:

$$\epsilon_s^{Data} = 0.769 \pm 0.022 \quad (4.12)$$

1541

$$\epsilon_b^{Data} = 0.121 \pm 0.054 \quad (4.13)$$

1542 Further studies have been performed to assess the effect of the relative uncertainty on
 1543 the $t\bar{t}$ and tW event fractions. The same procedure described above has been applied to
 1544 different simulation templates obtained varying the $t\bar{t}$ and tW fractions within theoretical
 1545 uncertainties, and the effect on the parameters extracted with the fit procedure is found to
 1546 be well below the fit uncertainties.

1547 Data driven estimation

1548 In addition to the b-tagging efficiency, the other ingredient to estimate the $t\bar{t}$ background is
 1549 the process cross section. The idea is to measure the cross section in a $t\bar{t}$ enriched control
 1550 region, that is called CtrlDD. CtrlDD is defined according to the lepton preselection cuts

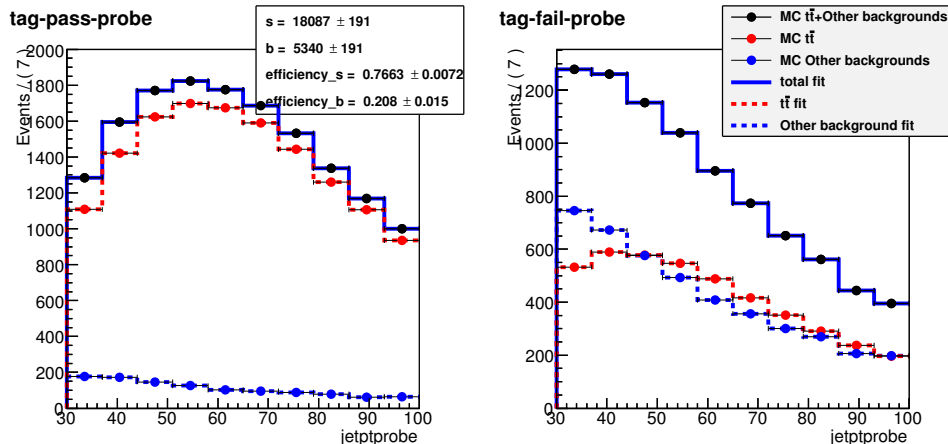


Figure 4.6.: Simultaneous fit of the *tag-pass-probe* and *tag-fail-probe* pairs in the MC.

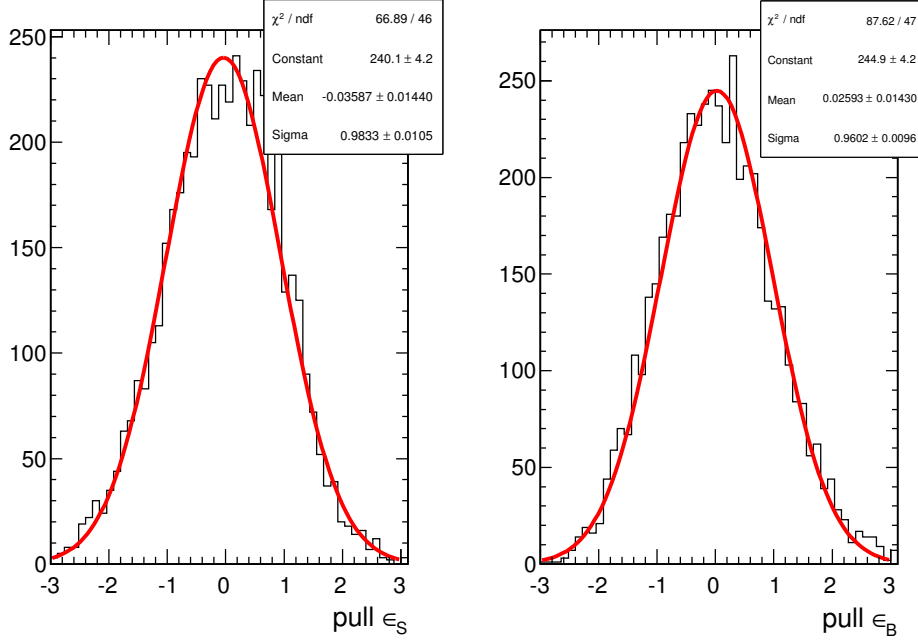


Figure 4.7.: Pulls of the ϵ_s and ϵ_b parameters in 5000 toy MC.

defined in Sec. 4.3.1, and requiring in addition at least one jet with *JetBProbability* score higher than 1.4.

From the simulation we derive the factor α that connects CrtlDD to the signal region, calculating the ratio of $t\bar{t}$ events in the two regions:

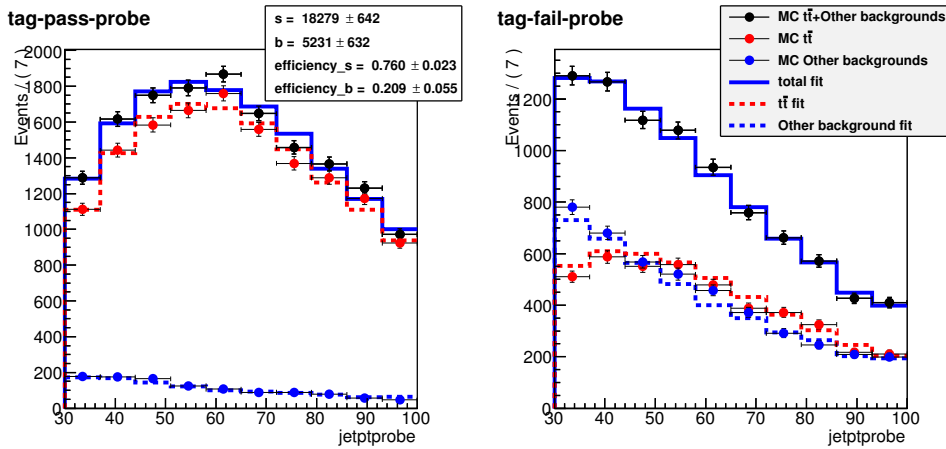


Figure 4.8.: Fit of a toy MC sample.

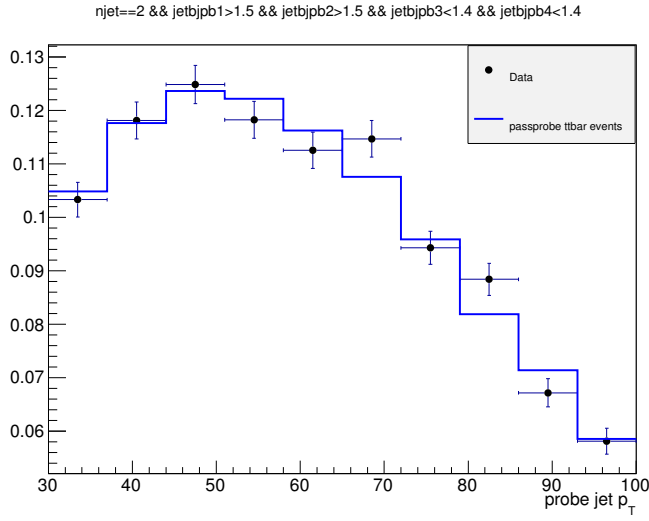


Figure 4.9.: Shape comparison for the *probe p_T* spectrum in data and in MC in a very pure $t\bar{t}$ sample.

$$\alpha = \frac{N_{tt \text{ MC}}^{SIG}}{N_{tt \text{ MC}}^{CtrlDD}} . \quad (4.14)$$

1555 The number of events in the CtrlDD region in data is counted, subtracting the expected
 1556 number of events from non- $t\bar{t}$ backgrounds, and obtaining $N_{tt \text{ Data}}^{CtrlDD}$. Finally the number of
 1557 expected $t\bar{t}$ events in the signal region ($N_{tt \text{ Data}}^{SIG}$) is obtained as:

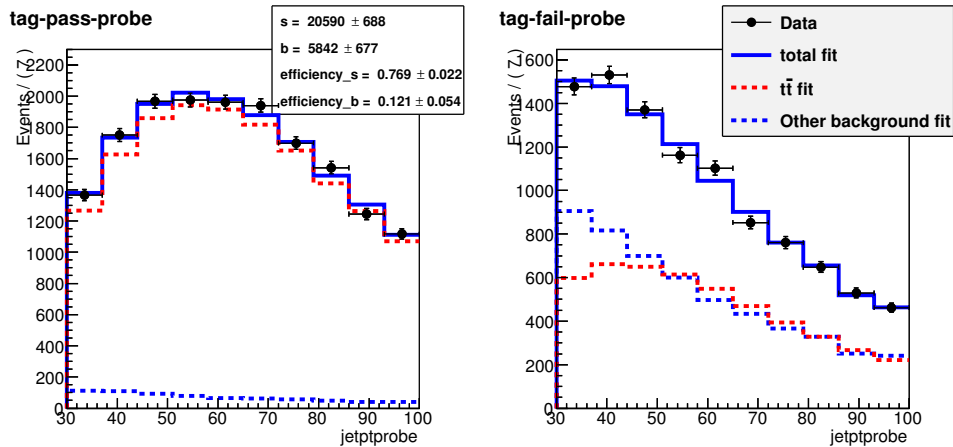


Figure 4.10.: Simultaneous fit of the *tag-pass-probe* and *tag-fail-probe* pairs in data.

$$N_{t\bar{t} Data}^{SIG} = \alpha N_{t\bar{t} Data}^{CtrlDD}. \quad (4.15)$$

1558 In evaluating α and its error the b-tagging efficiencies determined in Sec. 4.4.1 are
 1559 used. For each event an efficiency scale factor and a mistag rate scale factor are derived,
 1560 depending on whether the event falls in the signal or CtrlDD region.

$$SF_{SIG} = \left(\frac{1 - \epsilon_s^{Data}}{1 - \epsilon_s^{MC}} \right)^{\min(2, n_{b-jets})} \left(\frac{1 - \epsilon_b^{Data}}{1 - \epsilon_b^{MC}} \right)^{n_{non-b-jets}} \quad (4.16)$$

$$SF_{CtrlDD} = \left(\frac{\epsilon_s^{Data}}{\epsilon_s^{MC}} \right)^{(jet1 == b-jet)} \left(\frac{\epsilon_b^{Data}}{\epsilon_b^{MC}} \right)^{(jet1 == non-b-jets)} \quad (4.17)$$

1561 where n_{b-jets} is the number of true b-jets in the event and $n_{non-b-jets}$ is the number of
 1562 non-b-jets in the event. The writing $jet1 == b-jet$ ($jet1 == non-b-jets$) is a boolean
 1563 flag that is true when the leading jet, the one used for the CtrlDD selection, is (not) a true
 1564 b-jet.

1565 Since the efficiency and mistag rate that have been measured on data are close to the
 1566 one in the simulation, it was decided to assume a scale factor of 1 for both b-tagging
 1567 efficiency and mis-tag rate. This means that the central values of the scale factors defined
 1568 in Eq. 4.16 and Eq. 4.17 is 1, but these numbers have an error that is derived assuming an
 1569 uncertainty on ϵ_s^{Data} and ϵ_b^{Data} that covers both the statistical error from the fit of the two
 1570 quantities and the difference with respect to the simulation. This results in an up and a
 1571 down variation of the scale factors in the signal and CtrlDD regions, that is used to derive
 1572 an error on α .

1573 A data driven estimation of the top quark background with the method described above
 1574 is performed in each of the p_T^H bins independently. The reason to make this estimation
 1575 in p_T^H bins, rather than inclusively is explained in Fig. 4.11, where the p_T^H distribution is
 1576 shown in the CtrlDD region normalized to the cross section measured by a specific CMS
 1577 analysis [76]. As shown in the ratio plot, an overall normalization factor would not be able
 1578 to accommodate for the variations of the data/simulation ratio from bin to bin.

1579 The α factors for each bin and the number of events in signal, CtrlDD regions in MC as
 1580 well as in data are listed in Tab. 4.3.

1581 A comparison of the $m_{\ell\ell}$ distribution in the six p_T^H bins used in the analysis in CtrlDD
 1582 after the data driven correction is shown in Fig. 4.12

p_T^H [GeV]	N_{CTRL}^{DATA}	N_{CTRL}^{TOP}	N_{SIG}^{TOP}	α	$\Delta\alpha$
[0–15]	406.71	358.78	117.83	0.328	0.075
[15–45]	2930.14	2703.44	859.08	0.318	0.071
[45–85]	5481.02	5207.48	1506.05	0.289	0.065
[85–125]	4126.35	4032.56	861.22	0.214	0.052
[125–165]	1612.64	1654.27	304.69	0.184	0.055
[165– ∞]	647.50	760.37	201.70	0.265	0.147

Table 4.3.: Data driven scale factors related to the top quark background estimation.

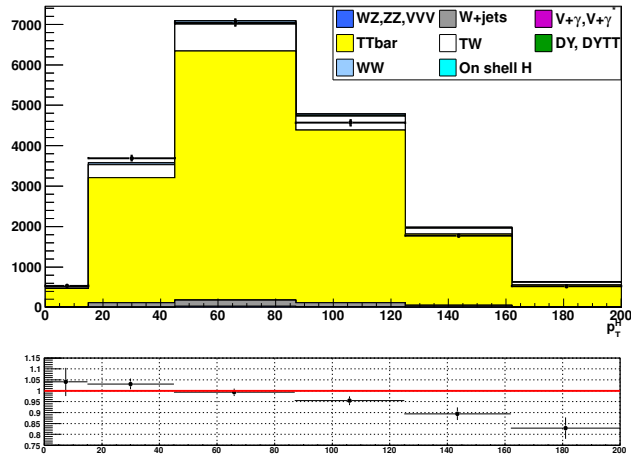


Figure 4.11.: p_T^H distribution in the CtrlDD control region.

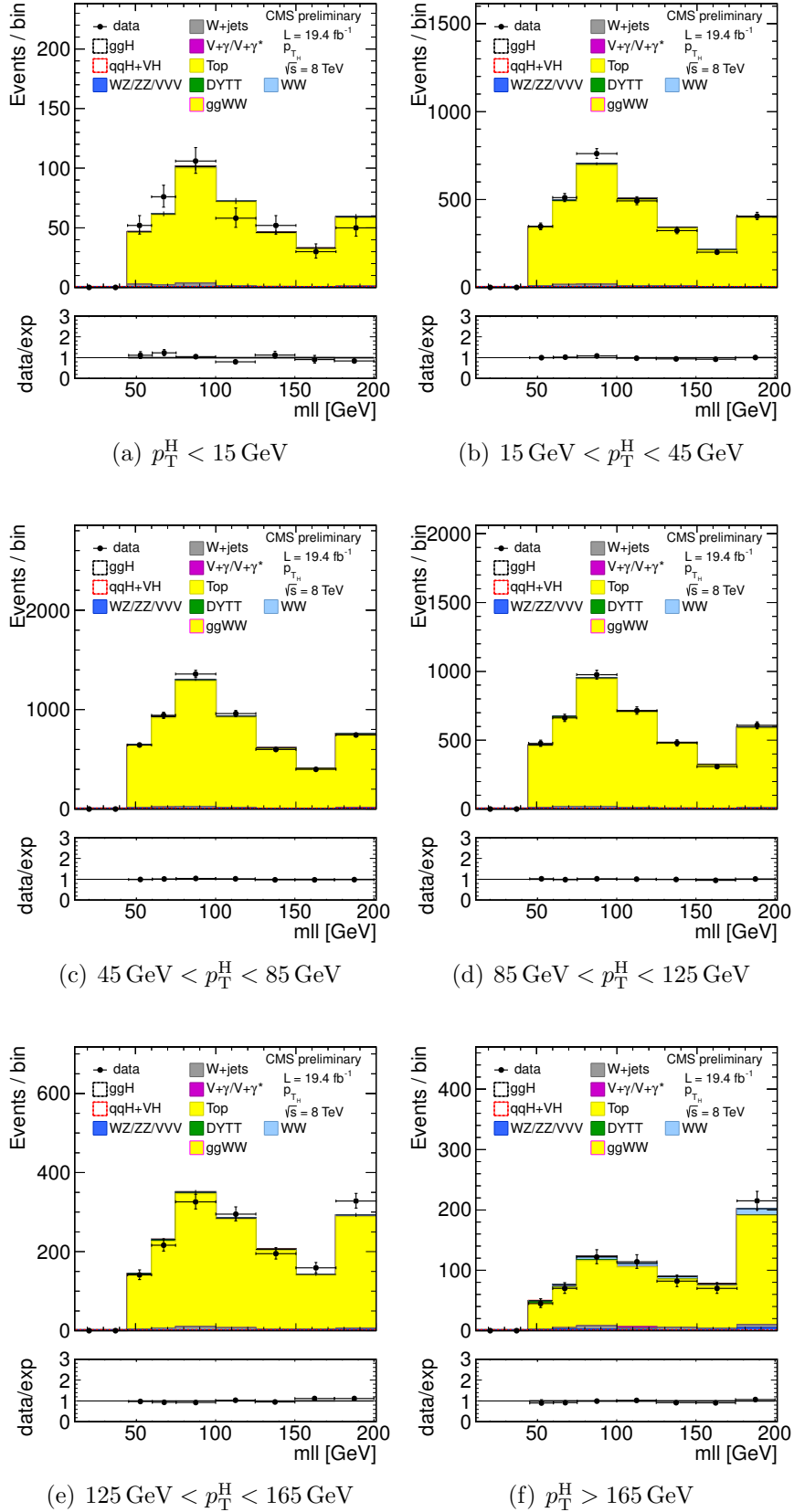


Figure 4.12.: $m_{\ell\ell}$ distributions in the CtrlDD region for the different p_T^H bins.

1583 **4.4.2. WW background**

1584 For what the $q\bar{q} \rightarrow W^+W^-$ background shape is concerned, the prediction from the simula-
 1585 tion is used. This background is divided into six different parts, corresponding to the six
 1586 p_T^H bins defined in the analysis. The normalization of the $q\bar{q} \rightarrow W^+W^-$ background is left
 1587 free to float in each bin, in such a way to adjust it in order to match the data during the fit
 1588 procedure. In this way the shape difference between the p_T^{WW} theory prediction and the
 1589 distribution provided by the simulation, which is obtained with the MADGRAPH generator,
 1590 is minimized.

1591 In figure 4.13 a comparison is shown between the p_T^{WW} spectra of two different $q\bar{q} \rightarrow W^+W^-$
 1592 samples: one obtained with the MADGRAPH generator and the other after applying to the
 1593 same distribution a reweighting in order to match the theoretical prediction at NLO+NNLL
 1594 precision.

1595 A shape discrepancy can be clearly observed and the effect becomes larger at high
 1596 values of p_T^H . In order to assess the effect of this discrepancy on the shapes of the variables
 1597 used for the signal extraction, $m_{\ell\ell}$ and m_T , the shapes have been checked in all p_T^H bins,
 1598 comparing different MC samples. The MADGRAPH sample used for the nominal shape is
 1599 compared to the MADGRAPH sample with NLO+NNLL reweighting, a POWHEG sample
 1600 with NLO accuracy and an AMC@NLO sample. The results of this comparison are shown
 1601 in figures 4.14 and 4.15. The shape discrepancy among the different models is included as
 1602 an additional systematic uncertainty.

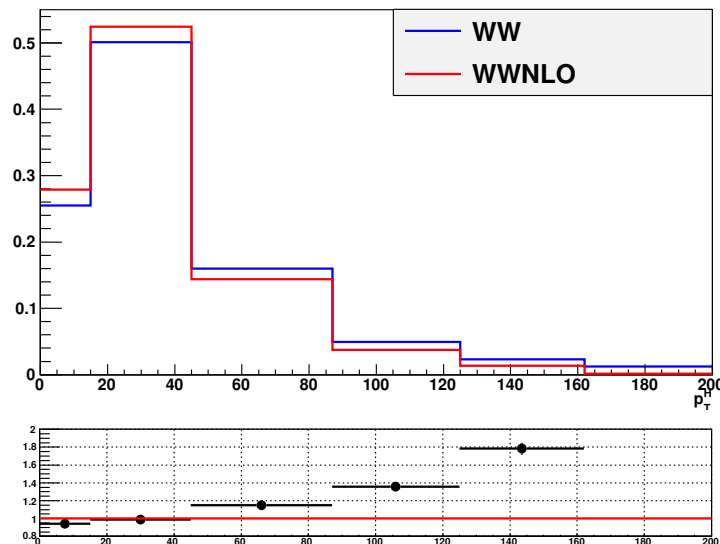


Figure 4.13.: Comparison between the p_T^{WW} distributions obtained with two different MC generators: the blue line corresponds to the MADGRAPH generator and the red line refers to the same sample in which a reweighting has been applied in order to match the theoretical prediction at NLO+NNLL precision.

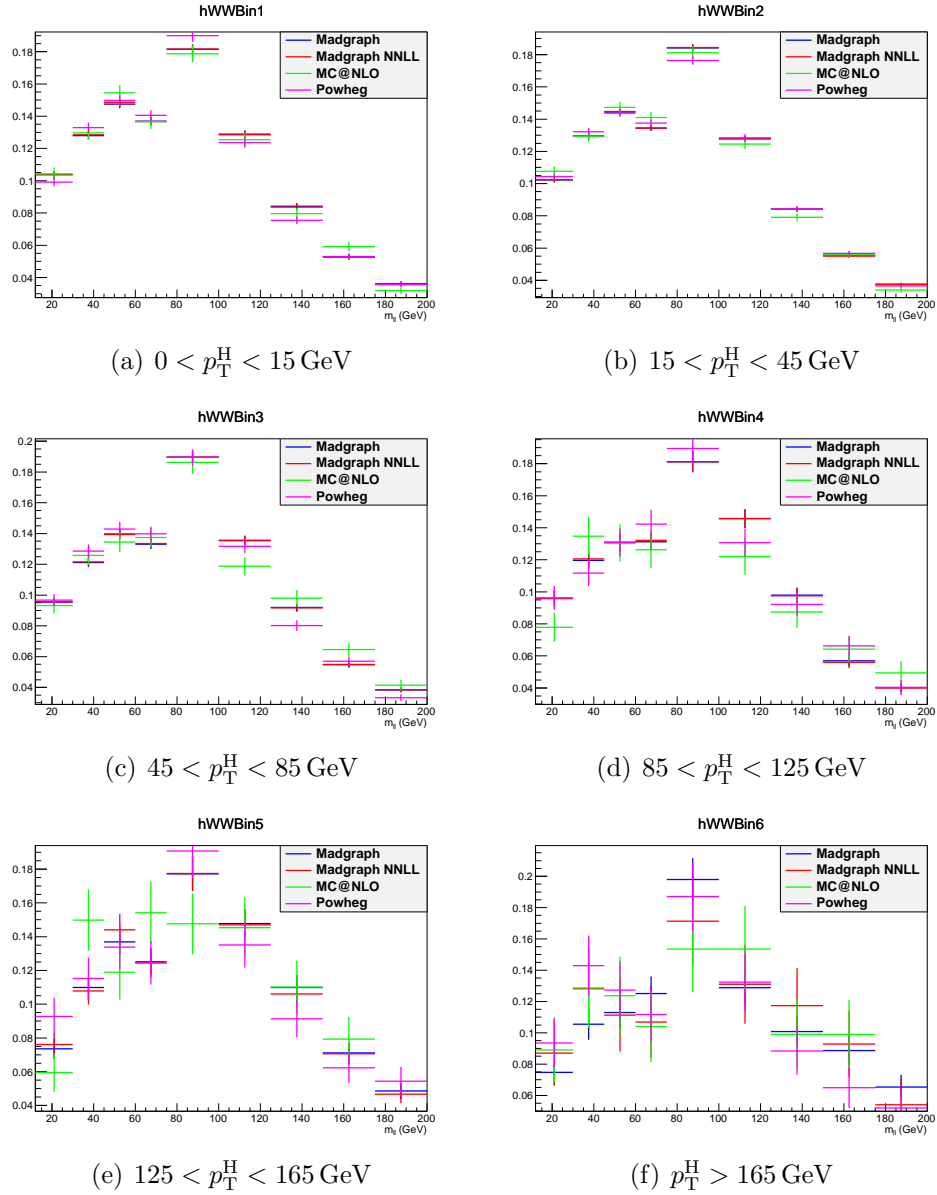


Figure 4.14.: Comparison between the default WW background sample and other theoretical models for the $m_{\ell\ell}$ distributions in every p_T^H bin.

The gluon-induced WW process, i.e. $gg \rightarrow W^+W^-$, has a sub-dominant contribution with respect to the quark-induced process, being the cross section ratio between the two of about 5%. The $m_{\ell\ell}$ and m_T shapes for this background are taken from simulation while the cross section is scaled to the approximate NLO calculation [60, 61].

The agreement of the $m_{\ell\ell}$ and m_T shapes between simulation and data for this background was checked in a signal-free control, defined selecting events with values of $m_{\ell\ell}$

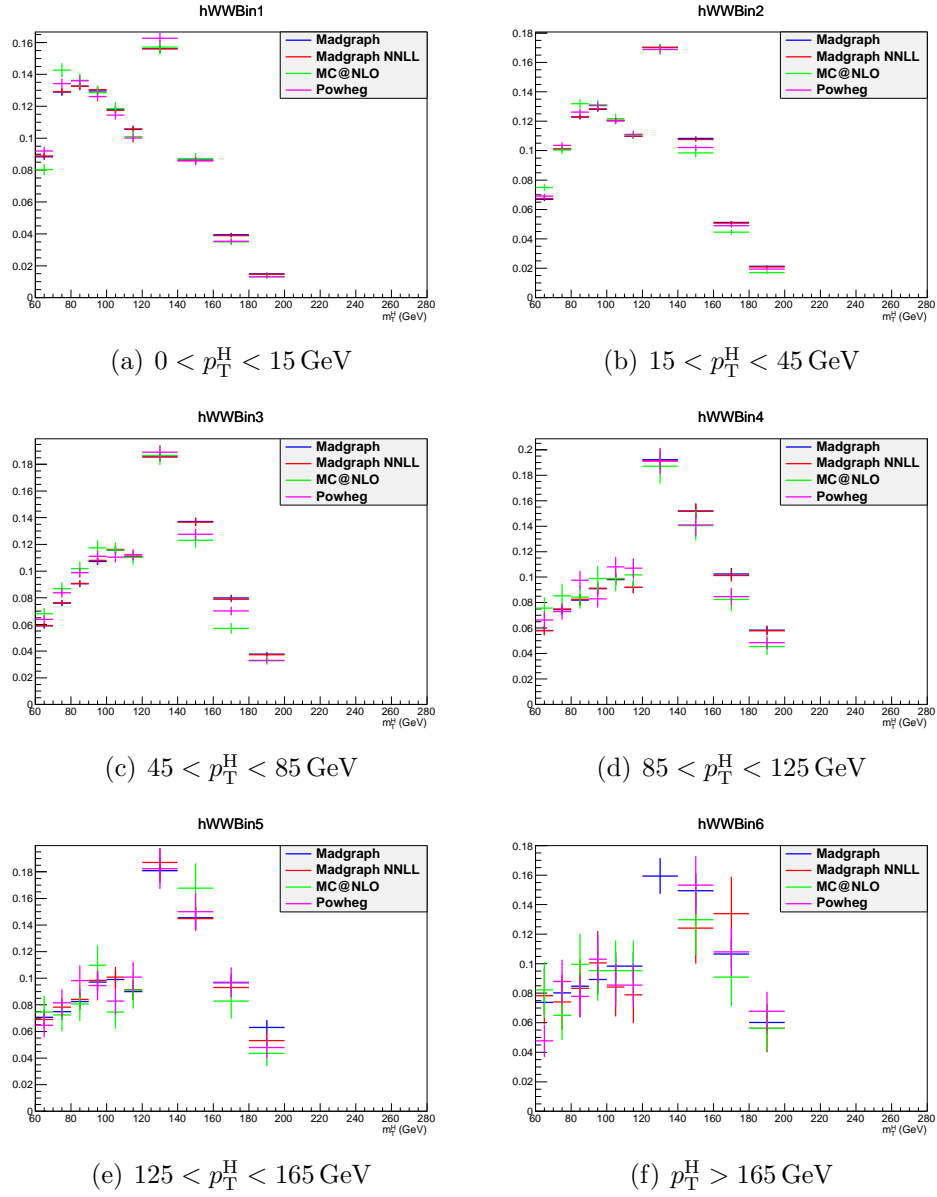


Figure 4.15.: Comparison between the default WW background sample and other theoretical models for the m_T distributions in every p_T^H bin.

1609 greater than 70 GeV. A comparison of the $m_{\ell\ell}$ and m_T shapes in data and simulation is
 1610 shown in Fig. 4.16 for events containing zero and one jets, inclusive in p_T^H .

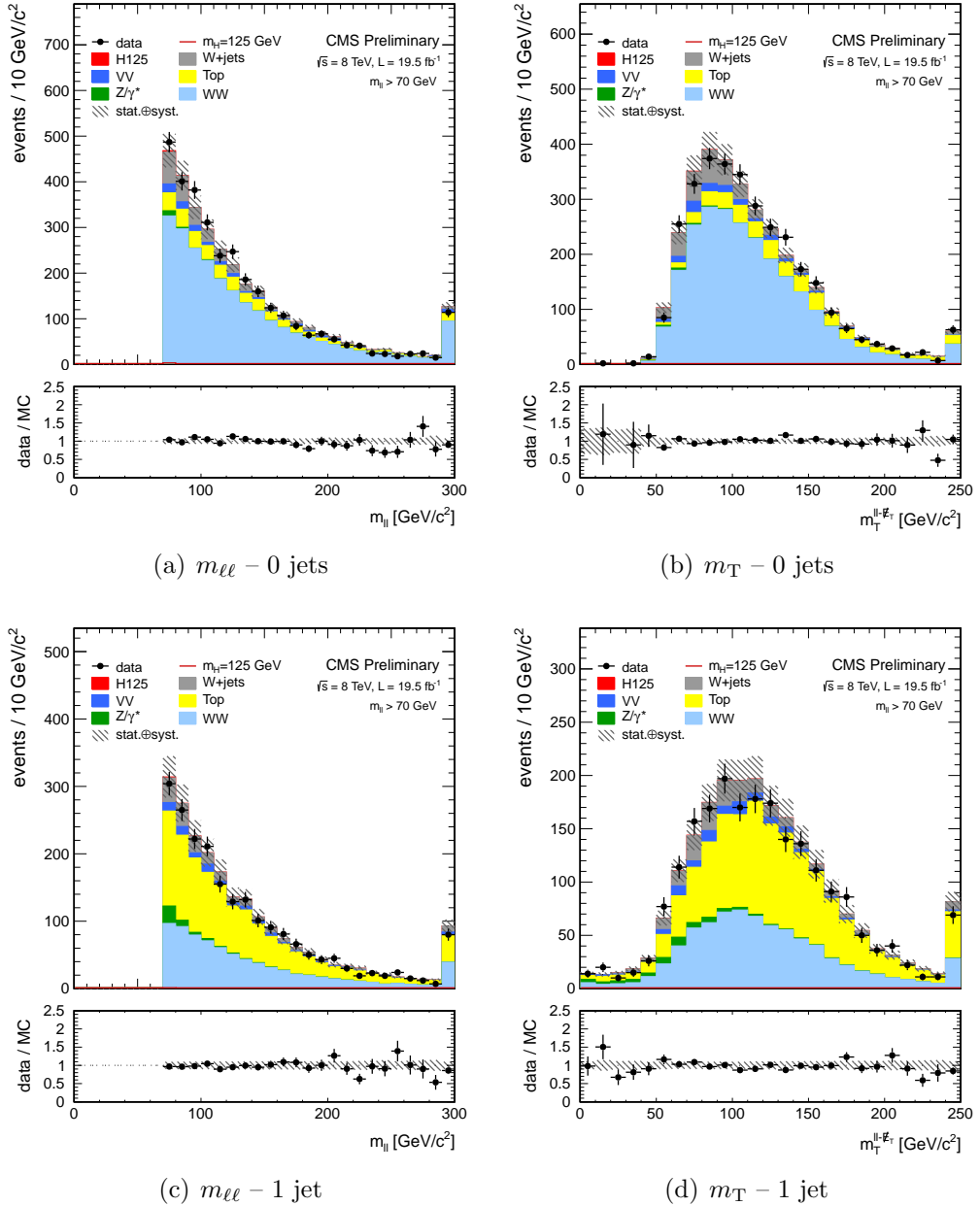


Figure 4.16.: Comparison of the $m_{\ell\ell}$ and m_T shapes in data and simulation for events with zero and 1 jets, inclusive in p_T^H . The events are required to pass the analysis requirements and, in order to define a signal-free control region, to have $m_{\ell\ell} > 70$ GeV.

1611 4.4.3. Other backgrounds

1612 W+jets background

1613 Events in which W bosons are produced in association with jets, as well as multi-jet events,
 1614 constitute a background for this analysis, because one or more jets can be misidentified as
 1615 leptons. The rate at which jets are misidentified as leptons may be not accurately described
 1616 in simulation, hence a data driven method is used to estimate this background.

1617 The idea is to estimate the background containing one or two fake leptons selecting
 1618 events with relaxed lepton quality criteria, i.e. looser with respect to the selections used at
 1619 the analysis level, and computing the efficiencies for real and fake leptons to pass the tight
 1620 lepton quality requirements of the analysis. A data-driven approach is pursued to estimate
 1621 this background. A set of loosely selected lepton-like objects, referred to as the “fakeable
 1622 object’ or “denominator” from here on, is defined in a data set of events dominated by
 1623 dijet production. To measure the fake rate we count how many fakeable objects pass the
 1624 full lepton selection of the analysis, parameterized as a function of the phase space of the
 1625 fakeable lepton, therefore it is extracted in bins of η and p_T . The ratio of the fully identified
 1626 lepton, referred as “numerator”, to the fakeable objects is taken as the probability for a
 1627 fakeable object to fake a lepton:

$$Fake\ Rate = \frac{\#of\ fully\ reconstructed\ leptons}{\#of\ fakeable\ objects} \quad (4.18)$$

1628 It is then used to extrapolate from the loose leptons sample to a sample of leptons
 1629 satisfying the full selection.

1630 The definition of the denominator is of large impact in the systematic uncertainties
 1631 related to this method. For the 2012 data taking period a summary of the selections used
 1632 for the numerator and the denominator of Eq. (4.18) is shown below for electrons and
 1633 muons respectively. For electrons the denominator is defined by the following requirements:

- 1634 • $\sigma_{inj\eta} < 0.01(0.03)$ for barrel (endcap);
- 1635 • $|\Delta\phi_{in}| < 0.15(0.10)$ for barrel (endcap);
- 1636 • $|\Delta\eta_{in}| < 0.007(0.009)$ for barrel (endcap);
- 1637 • $H/E < 0.12(0.10)$ for barrel (endcap);
- 1638 • electron conversion rejection;
- 1639 • $|d_0| < 0.02$ cm;
- 1640 • $\frac{\sum_{trk} E_T}{p_T^{ele}} < 0.2$;
- 1641 • $\frac{\sum_{ECAL} E_T}{p_T^{ele}} < 0.2$;
- 1642 • $\frac{\sum_{HCAL} E_T}{p_T^{ele}} < 0.2$.

1643 For muons the selection are loosened with respect to the tight analysis selection requiring
 1644 that:

- $|d_0| < 0.02$ cm;
- MVA isolation output > -0.6 .

The dijet enriched data set used for the fake rate measurement, which is selected using single lepton triggers with low p_T thresholds, it is not a pure sample containing just fake leptons, but may still contain prompt leptons coming from the W and Z boson decays. To reject muons from the W decay, the events are required to have $E_T^{\text{miss}} < 20$ GeV and a W transverse mass below 20 GeV as well. Muons from the Z decay are instead removed requiring $m_{\mu\mu} > 20$ GeV and $m_{\mu\mu} \notin [76, 106]$ GeV. For electrons the Z mass peak veto is enlarged to $m_{ee} \notin [60, 120]$ GeV. Finally both electrons and muons are required to be isolated from the leading jet in the event, i.e. $\Delta\phi(\ell, j) > 1$. The residual prompt lepton contamination from EW processes such as W/Z+jets production, which can bias the fake rate measurement, is estimated using simulation and subtracted from both the numerator and denominator. The contamination from EW processes is different for the numerator and denominator and is particularly important for relatively high lepton p_T values.

In addition to the fake rate, also a prompt lepton rate is evaluated, defined as the probability of a prompt lepton passing the loose requirements to also pass the tight analysis selections. The prompt rate is also measured in data, defining a control region enriched in $Z \rightarrow \ell\ell$ events, selecting dilepton events with an invariant mass of the two leptons in the Z peak mass region.

Both the fake and prompt rate are used to reweight the data samples used in the analysis in order to obtain directly from data the contribution of the fake lepton background. The method to apply those rates is explained below in the simple case of just one lepton in the data sample, i.e. data selected by single lepton triggers, but can be straightforwardly generalized to situations with more than one lepton. Suppose that the total number of leptons passing the loose requirements, N_ℓ , is made up of N_p prompt and N_f fake leptons. N_p and N_f cannot be directly measured but one can measure the number of events where no leptons, N_{t0} , or one lepton, N_{t1} , pass the tight analysis requirement. These numbers are related by the following equations:

$$\begin{aligned} N_\ell &= N_p + N_f = N_{t0} + N_{t1} \\ N_{t0} &= (1 - p)N_p + (1 - f)N_f \\ N_{t1} &= pN_p + fN_f \end{aligned} \tag{4.19}$$

where p and f are the prompt and fake rates respectively. Equation (4.19) can be inverted to obtain the number of prompt and fake leptons:

$$\begin{aligned} N_p &= \frac{1}{p - f} [(1 - f)N_{t1} - fN_{t0}] \\ N_f &= \frac{1}{p - f} [pN_{t0} - (1 - p)N_{t1}] \end{aligned} \tag{4.20}$$

The number of fake events passing the tight analysis requirement is $N_{\text{fake}} = fN_f$. The fake background contribution is estimated directly from data, applying the kinematics-dependent weights (f and p are estimated in bins of p_T and η) defined in Eq.(4.20).

The prompt and fake rate estimations after the removal of the EW contribution are shown in Tables 4.4 and 4.5 separately for electrons and muons.

Table 4.4.: Measured prompt rate for electrons and muons in bins of η , p_T . Only the statistical uncertainties are shown.

Electron prompt rate			
p_T range [GeV]	$0 < \eta \leq 1.4442$	$1.4442 < \eta \leq 1.566$	$1.566 < \eta$
$10 < p_T \leq 15$	0.5738 ± 0.0045	0.5366 ± 0.0204	0.2947 ± 0.0047
$15 < p_T \leq 20$	0.7091 ± 0.0020	0.5484 ± 0.0185	0.4477 ± 0.0034
$20 < p_T \leq 25$	0.7175 ± 0.0013	0.6297 ± 0.0067	0.6200 ± 0.0001
$25 < p_T \leq 50$	0.9219 ± 0.0002	0.8404 ± 0.0007	0.8509 ± 0.0001
$p_T > 50$	0.9693 ± 0.0002	0.9398 ± 0.0021	0.9385 ± 0.0005

Muon prompt rate		
p_T range [GeV]	$0 < \eta \leq 1.5$	$1.5 < \eta \leq 2.5$
$10 < p_T \leq 15$	0.7119 ± 0.0003	0.7582 ± 0.0006
$15 < p_T \leq 20$	0.8049 ± 0.0018	0.8495 ± 0.0001
$20 < p_T \leq 25$	0.9027 ± 0.0008	0.8948 ± 0.0012
$25 < p_T \leq 50$	0.9741 ± 0.0001	0.9627 ± 0.0002
$p_T > 50$	0.9900 ± 0.0001	0.9875 ± 0.0003

The region obtained by reversing the opposite sign lepton requirement in the analysis selection is enriched with W+jets events where one of the jets is misidentified as a lepton. The fake rate procedure can be applied to this same-sign control region to perform a closure test of the method. The results of the closure test on same-sign events gives good agreement with the expectations.

The systematic uncertainty on the prompt and fake rate estimation is evaluated by varying the jet thresholds in the dijet control sample, and an uncertainty on the background normalization is added according to the agreement with data in the same-sign control region. The systematic uncertainty amounts to about 36% of the fake background yield.

1689 Drell-Yan to $\tau\tau$ background

1690 The low E_T^{miss} threshold in the $e\mu$ final state requires the consideration of the contribution
1691 from $Z/\gamma^* \rightarrow \tau^+\tau^-$, that estimated from data. This is accomplished by selecting $Z/\gamma^* \rightarrow$

Table 4.5.: Measured electrons and muons fake rates in bins of η and p_T , after the EWK correction. Only statistical uncertainties are shown.

electron fake rate				
p_T range [GeV]	$0 < \eta \leq 1$	$1 < \eta \leq 1.479$	$1.479 < \eta \leq 2$	$2 < \eta \leq 2.5$
$10 < p_T \leq 15$	0.045 ± 0.005	0.033 ± 0.004	0.008 ± 0.002	0.021 ± 0.005
$15 < p_T \leq 20$	0.044 ± 0.003	0.049 ± 0.003	0.017 ± 0.001	0.017 ± 0.002
$20 < p_T \leq 25$	0.041 ± 0.002	0.064 ± 0.003	0.025 ± 0.002	0.025 ± 0.002
$25 < p_T \leq 30$	0.059 ± 0.003	0.101 ± 0.005	0.041 ± 0.003	0.043 ± 0.003
$30 < p_T \leq 35$	0.084 ± 0.006	0.111 ± 0.009	0.058 ± 0.006	0.066 ± 0.005

muon fake rate				
p_T range [GeV]	$0 < \eta \leq 1$	$1 < \eta \leq 1.479$	$1.479 < \eta \leq 2$	$2 < \eta \leq 2.5$
$10 < p_T \leq 15$	0.131 ± 0.002	0.154 ± 0.004	0.194 ± 0.005	0.241 ± 0.009
$15 < p_T \leq 20$	0.143 ± 0.007	0.191 ± 0.012	0.235 ± 0.016	0.308 ± 0.027
$20 < p_T \leq 25$	0.198 ± 0.005	0.239 ± 0.009	0.221 ± 0.011	0.271 ± 0.021
$25 < p_T \leq 30$	0.182 ± 0.011	0.228 ± 0.018	0.195 ± 0.022	0.287 ± 0.045
$30 < p_T \leq 35$	0.170 ± 0.021	0.244 ± 0.036	0.195 ± 0.041	0.289 ± 0.111

1692 $\mu^+\mu^-$ events in data and replacing both muons with a simulated $\tau \rightarrow \ell \nu_\tau \bar{\nu}_\ell$ decay [50], thus
1693 obtaining a “hybrid” event. The Z boson four-momentum is reconstructed in data from
1694 the four-momenta of the daughter muons. Then a simulation step allows the replacement
1695 of the muon objects with τ leptons, in such a way to preserve the Z boson momentum
1696 direction is preserved in its rest frame. The $Z/\gamma^* \rightarrow \tau^+\tau^-$ decay is simulated with the
1697 TAUOLA package [77] to correctly describe the τ -polarization effects.

1698 After replacing muons from $Z/\gamma^* \rightarrow \mu^+\mu^-$ decays with simulated τ decays, the set
1699 of pseudo-Z/ $\gamma^* \rightarrow \tau^+\tau^-$ events undergoes the reconstruction step. Good agreement in
1700 kinematic distributions for this sample and a MC based $Z/\gamma^* \rightarrow \tau^+\tau^-$ sample is found. The
1701 global normalization of pseudo-Z/ $\gamma^* \rightarrow \tau^+\tau^-$ events is checked in the low m_T spectrum
1702 where a rather pure $Z/\gamma^* \rightarrow \tau^+\tau^-$ sample is expected.

1703 This method allows to avoid the simulation of very large MC samples that would be
1704 needed for an accurate description of this process.

1705 ZZ, WZ and $W\gamma$ backgrounds

1706 The WZ and ZZ backgrounds are partially estimated from data when the two selected
1707 leptons come from the same Z boson. If the leptons come from different bosons the
1708 contribution is expected to be small. The WZ component is largely rejected by requiring
1709 only two high p_T isolated leptons in the event.

¹⁷¹⁰ The $W\gamma^{(*)}$ background, where the photon decays to an electron-positron pair, is expected
¹⁷¹¹ to be very small, thanks to the stringent photon conversion requirements. This background
¹⁷¹² also includes events where a real photon is produced in association with the W boson.
¹⁷¹³ These events constitute a background for this analysis because the photon can interact with
¹⁷¹⁴ the tracker material converting to an electron-positron pair.

¹⁷¹⁵ Since the WZ simulated sample has a generation level cut on the di-lepton invariant mass
¹⁷¹⁶ ($m_{\ell\ell} > 12$ GeV) and the cross-section raises quickly with the lowering of this threshold, a
¹⁷¹⁷ dedicated MADGRAPH sample has been produced with lower momentum cuts on two of
¹⁷¹⁸ the three leptons ($p_T > 5$ GeV) and no cut on the third one. The surviving contribution
¹⁷¹⁹ estimated with this sample is still very small, and since the uncertainty on the cross-section
¹⁷²⁰ for the covered phase space is large, a conservative 100% uncertainty has been given to it.
¹⁷²¹ A k -factor for $W\gamma^*$ of 1.5 ± 0.5 based on a dedicated measurement of tri-lepton decays,
¹⁷²² $W\gamma^* \rightarrow e\mu\mu$ and $W\gamma^* \rightarrow \mu\mu\mu$, is applied [50]. The contribution of $W\gamma^{(*)}$ is also constrained
¹⁷²³ by a closure test with same sign leptons on data, which reveals a good compatibility of the
¹⁷²⁴ data with the expected background.

¹⁷²⁵ 4.5. Systematic uncertainties

¹⁷²⁶ Systematic uncertainties play an important role in this analysis where no strong mass peak
¹⁷²⁷ is expected due to the presence of undetected neutrinos in the final state. One of the most
¹⁷²⁸ important sources of systematic uncertainty is the normalization of the backgrounds that
¹⁷²⁹ are estimated on data control samples whenever is possible.

¹⁷³⁰ A summary of the main sources of systematic uncertainty and the corresponding estimate
¹⁷³¹ is reported in Table 4.6. A detailed description of each source of systematic uncertainty is
¹⁷³² discussed in the following sections.

¹⁷³³ 4.5.1. Background normalization uncertainties

¹⁷³⁴ The signal extraction is performed subtracting the estimated backgrounds to the event
¹⁷³⁵ counts in data. This uncertainty depends on the background:

- ¹⁷³⁶ • **t \bar{t} and tW backgrounds:** The efficiency on jets b-tagging is estimated using the
¹⁷³⁷ Tag&Probe technique in data and simulation control regions, as explained in 4.4.1. A
¹⁷³⁸ per-jet scale factor, which takes into account the possibly different efficiency of the
¹⁷³⁹ anti b-tagging selection in data and simulation, is computed by means of the efficiency
¹⁷⁴⁰ measured with the Tag&Probe method. The Tag&Probe method has been used also
¹⁷⁴¹ to measure the mistag rates in data and simulation, which are the probability to b-tag
¹⁷⁴² a jet that is not produced by the hadronization of a b quark. These factors are used
¹⁷⁴³ to reweigh the Top MC samples as explained in 4.4.1. The uncertainties provided by
¹⁷⁴⁴ the Tag&Probe fit are then propagated to the factor α that is used in the top data
¹⁷⁴⁵ driven estimation 4.4.1. These uncertainties are embedded in a systematic error that
¹⁷⁴⁶ affects the shape of the Top background in each p_T^H bin.

Table 4.6.: Main sources of systematic uncertainties and their estimate. The first category reports the uncertainties in the normalization of background contributions. The experimental and theoretical uncertainties refer to the effect on signal yields. A range is specified if the uncertainty varies across the p_T^H bins.

Uncertainties in backgrounds contributions	
Source	Uncertainty
t <bar>t>, tW</bar>	20–50%
W+ jets	40%
WZ, ZZ	4%
W γ (*)	30%

Effect of the experimental uncertainties on the signal and background yields	
Source	Uncertainty
Integrated luminosity	2.6%
Trigger efficiency	1–2%
Lepton reconstruction and identification	3–4%
Lepton energy scale	2–4%
E_T^{miss} modelling	2%
Jet energy scale	10%
Pileup multiplicity	2%
b mistag modelling	3%

Effect of the theoretical uncertainties on signal yield	
Source	Uncertainty
b jet veto scale factor	1–2%
PDF	1%
WW background shape	1%

1747 Provided that the simulated samples include both tt> and tW processes, a systematic
 1748 uncertainty related to the tW/tt> fraction has been included. In fact, a relative variation
 1749 of the contribution of these two processes could modify the shape of the MC sample,
 1750 and is thus included as a shape uncertainty affecting the top quark background shape
 1751 in each p_T^H bin in a correlated way.

- 1752 • **W+jets background:** It is estimated with data control sample as described in
 1753 Sec.4.4.3. With 19.4 fb^{-1} at 8 TeV, the uncertainty receives similar contributions from
 1754 statistics and systematic error (mainly jet composition differences between the fake
 1755 rate estimation sample and the application sample), the total error being about 40%,
 1756 dominated by the closure test of the method on a same-sign control region.

- **WZ, ZZ, $W\gamma^{(*)}$ backgrounds:** those backgrounds, which are expected to give a small contribution, are estimated from simulation. Uncertainties on the cross sections reported in [78, 79] are 4% for WZ and 2.5% for ZZ. A 30% uncertainty is assigned to the $W\gamma$ [80] yield and another 30% on $W\gamma^{(*)}$ contribution according to the uncertainty on the normalization study (see Sec. 4.4.3).

4.5.2. Experimental uncertainties

The following experimental systematic sources have been taken into account:

- **Luminosity:** Using the online luminosity monitoring CMS reached an uncertainty on the luminosity of 2.6% at 8 TeV.
- **Trigger efficiency.** The uncertainties for both electrons and muons are at 1-2% level, which is added together to the lepton efficiency uncertainty.
- **Lepton reconstruction and identification efficiency:** The lepton reconstruction and identification efficiencies are measured with the Tag&Probe method in data. To correct for the difference in the lepton identification efficiencies between data and MC, a scale factor is applied to MC. The uncertainties resulting from this procedure on the lepton efficiencies are 4% for electrons and 3% for muons.
- **Muon momentum and electron energy scale:** The momentum scale of leptons have relatively large uncertainties due to different detector effects. For electrons a scale uncertainty of 2% for the barrel, and 4% for the endcaps respectively, is assigned. For muons, a momentum scale uncertainty of 1.5%, independent of its pseudorapidity, is assigned.
- **E_T^{miss} modeling:** The E_T^{miss} measurement is affected by the possible mis-measurement of individual particles addressed above, as well as the additional contributions from the pile-up interactions. The effect of the missing transverse momentum resolution on the event selection is studied by applying a Gaussian smearing of 10% on the x - and y -components of the missing transverse momentum. All correlated variables, like the transverse mass, are recalculated.
- **Jet energy scale (JES) uncertainties:** It affects both the jet multiplicity and the jet kinematic variables, such as m_{jj} . We estimate this uncertainty applying variations of the official jet uncertainties on the JES (which depend on η and p_T of the jet [81]) and compute the variation of the selection efficiency.
- **b jets mistag modeling:** A fraction of signal events is rejected because erroneously identified as b jets by the b-tagging algorithms. The mistag rate, as measured with the Tag&Probe technique described in Sec. 4.4.1, comes with an uncertainty due to different modeling of the b-tagging performance in data and simulation.
- **Pileup multiplicity:** Some of the variables used in the analysis are affected by the average number of pileup interactions. The simulated events have been reweighted according the instantaneous luminosity measured on data. The error in the average

number of pileup interactions measured in data and the simulation of the modeling and physics aspects of the pileup simulation gives an uncertainty of 5% on the distribution used in the reweighting procedure. This uncertainty is propagated through all the analysis, and the estimated uncertainty on the efficiency is 2%.

4.5.3. Theoretical uncertainties

- **QCD scale uncertainties:** The uncertainties on the total cross sections due to the choice of the renormalization and factorization scale are assigned to MC-driven backgrounds. For the signal processes these uncertainties are separated in two categories: those affecting the selection efficiency and those affecting the jet bin fractions. The effect of renormalization and factorization scale on the selection efficiency is of the order of 2% for all processes. Although this analysis is inclusive in number of jets, the effect of the QCD scale variation on the jet bin migrations has to be taken into account because of the b-tagging veto efficiency. The efficiency of this selection depends on jet multiplicity and the effect of the QCD scale variation has been evaluated using the Stewart-Tackman method, as explained in 4.5.3.
- **PDFs uncertainties:** The utilization of different PDF sets can affect both the normalization and the shapes of the signal contributions. The uncertainty related due to the variations in the choice of PDFs is considered following the PDF4LHC [82, 83] prescription, using CT10, NNPDF2.1 [84] and MSTW2008 [85] PDF sets.
- **WW:** Due to the fact that the WW shape is entirely taken from simulation, the analysis is strongly relying on theoretical models and can thus be strongly affected by their uncertainties. Especially higher order QCD radiative effects have an influence on the generated WW shape. To study this impact, the shapes of the distributions produced with the MADGRAPH generator (which is the generator for the MC simulation used in the analysis) are compared to the ones produced with MC@NLO. The comparison is performed separately in each bin of p_T^H and the uncertainty includes shape differences originating from the renormalization and factorization scale choice. A comparison of the $m_{\ell\ell}$ and m_T shapes for the WW background using different MC generators is reported in section 4.4.2.

Jet multiplicity uncertainty

The jet bin uncertainty on the ggH production mode has been evaluated using the Stewart-Tackman method, following the recipe proposed in Refs. [49, 86]. Three independent nuisance parameters have to be associated with the inclusive ggH production cross sections $\sigma_{\geq 0}$, $\sigma_{\geq 1}$ and $\sigma_{\geq 2}$, which corresponds to the cross sections with ≥ 0 jets, ≥ 1 jet and ≥ 2 jets respectively. According to the agreement on the treatment of uncertainties in the combination of ATLAS and CMS results [87], these nuisance parameters are labelled as $QCDscale_{ggH}$, $QCDscale_{ggH1in}$ and $QCDscale_{ggH2in}$. However, in case the analysis is split in exclusive jet multiplicity bins, the jet bin uncertainties can be evaluated taking into

account the correct correlations among the three nuisances following the Stewart-Tackman prescription. Even though this analysis is inclusive in number of jets, the jet binning uncertainties must be included due to the presence of the b-jet veto, that introduces a dependency of the selection efficiency on the number of jets in the event. The veto efficiency has been evaluated in all the p_T^H bins defined in the analysis and as a function of jets multiplicity. The results are shown in Figs. 4.17(a) and 4.17(b). The drop of the veto efficiency at high values of p_T^H is due to the correlation with jets multiplicity.

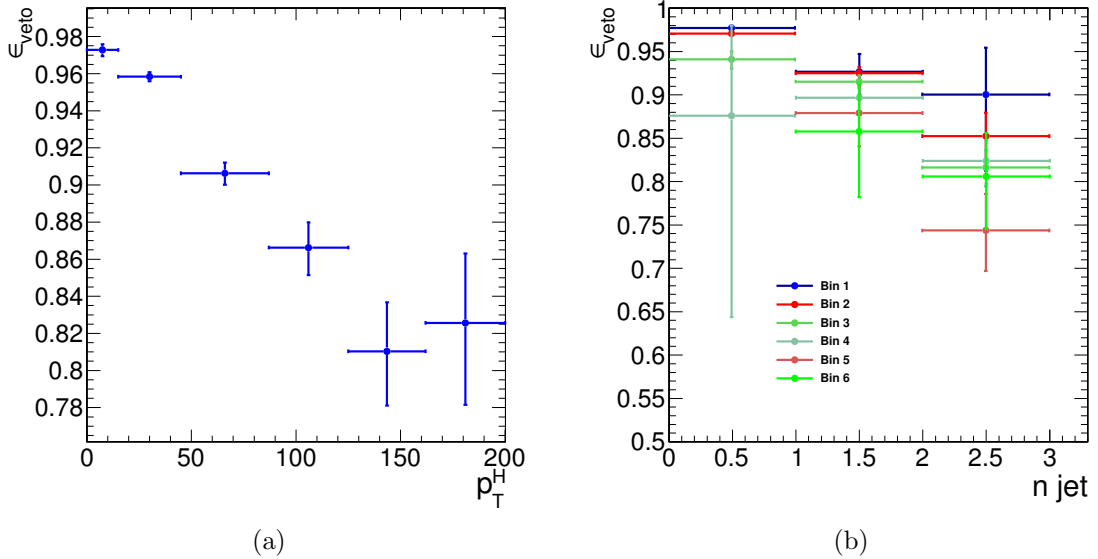


Figure 4.17.: (a) Efficiency of the b-tagging veto in different bins of p_T^H . (b) Efficiency of the b-tagging veto in different bins of p_T^H , as a function of number of jets.

The first step of this procedure is to take the inclusive ggH cross section, σ_{ggH} , and to convert the relative QCD up/down scale uncertainties, ϵ_+ and ϵ_- , to a log-normal uncertainty, i.e. $\kappa = \sqrt{\exp(\epsilon_+) \cdot \exp(\epsilon_-)}$. The exclusive cross sections, σ_0 , σ_1 and σ_2 , can be calculated starting from σ_{ggH} and using the selection efficiencies for the three jet bins. For every exclusive cross section the corresponding relative uncertainty is computed varying the renormalization (μ_R) and factorization (μ_F) scales independently of a factor 2 and 1/2, and taking the cross section value corresponding to half of the maximum variation. The inclusive cross sections are then obtained summing the exclusive cross sections and propagating the uncertainties, i.e. $\sigma_{\geq 0} = \sigma_0 + \sigma_1 + \sigma_2$, $\sigma_{\geq 1} = \sigma_1 + \sigma_2$, $\sigma_{\geq 2} = \sigma_2$.

The three nuisance parameters, including all the proper correlations among the jet bins, are defined according to Table 4.7, where the f_n constants represent the exclusive theoretical n jet bin fractions, i.e. $f_0 = \sigma_0/\sigma_{\geq 0}$, $f_1 = \sigma_1/\sigma_{\geq 0}$, $f_2 = \sigma_2/\sigma_{\geq 0}$.

Table 4.7.: Numerical calculation for the systematic uncertainties of jet binning.

Nuisance parameter	0-jet bin	1-jet bin	2-jet bin
QCDscale_ggH	$\Delta_{\geq 0}^0 = (\kappa_{\geq 0})^{\frac{1}{f_0}}$		
QCDscale_ggH1in	$\Delta_{\geq 1}^0 = (\kappa_{\geq 1})^{-\frac{f_1+f_2}{f_0}}$	$\Delta_{\geq 1}^1 = (\kappa_{\geq 1})^{\frac{f_1+f_2}{f_1}}$	
QCDscale_ggH2in		$\Delta_{\geq 2}^1 = (\kappa_{\geq 2})^{-\frac{f_2}{f_1}}$	$\Delta_{\geq 2}^2 = (\kappa_{\geq 2})$

The nuisance parameters reported in table 4.7 have then been calculated for each p_T^H bin embedding the b-jet veto efficiency and using the following formulas:

$$QCDscale_ggH = \frac{\Delta_{\geq 0}^0 \cdot f_0 \cdot \varepsilon_0 + \Delta_{\geq 1}^0 \cdot f_1 \cdot \varepsilon_1}{\Delta_{\geq 0}^0 \cdot f_0 \cdot \varepsilon_0 + \Delta_{\geq 1}^0 \cdot f_1 \cdot \varepsilon_0} \quad , \quad (4.21)$$

$$QCDscale_ggH1in = \frac{\Delta_{\geq 1}^1 \cdot f_1 \cdot \varepsilon_1 + \Delta_{\geq 2}^1 \cdot f_2 \cdot \varepsilon_2}{\Delta_{\geq 1}^1 \cdot f_1 \cdot \varepsilon_1 + \Delta_{\geq 2}^1 \cdot f_2 \cdot \varepsilon_1} \quad , \quad (4.22)$$

$$QCDscale_ggH2in = 1 \quad , \quad (4.23)$$

where ε_0 , ε_1 and ε_2 are the selection efficiencies for the three jet categories. These nuisance parameters are expected to be equal to one in case the efficiency is independent on the number of jets, i.e if $\varepsilon_0 = \varepsilon_1 = \varepsilon_2$.

The numerical values obtained following this procedure are reported in Table 4.8 for each p_T^H bin.

4.5.4. Statistics uncertainty of the simulated samples

Due to the large range of weights used to correct the simulated distributions in order to match those in data, the effective size of the MC samples are sometimes smaller than the actual number of events in the sample. The statistical uncertainties of the event yields estimated from MC samples are included as nuisance parameters in the fit and have a small impact on the final result.

Table 4.8.: Values of the jet binning nuisance parameters for different p_T^H bins.

Nuisance parameter	p_T^H bin [GeV]					
	[0-15]	[15-45]	[45-85]	[85-125]	[125-165]	[165-∞]
QCDscale_ggH	0.998	0.993	0.989	1.000	1.000	1.000
QCDscale_ggH1in	0.997	0.993	0.984	0.975	0.946	0.974

4.5.5. Treatment of systematic uncertainties in the shape analysis

One can distinguish between normalization uncertainties, where a systematic effect is changing the normalization of a given process assuming the shape is not affected, and shape uncertainties where the actual change in the shape of the distribution is taken into account. The normalization uncertainties enter the shape analysis as a constant normalization factor, whereas for shape uncertainties the nominal and the $+1\sigma$ and -1σ shapes enter the analysis in form of three histograms with the same normalization.

For the W+jets background, the shape differences for different jet p_T thresholds in the di-jet control sample are considered separately for electron and muon fakes, while the other sources of systematics are taken as normalization uncertainties as in the cut-based analysis.

Effects from experimental uncertainties are studied by applying a scaling and smearing of certain variables of the physics objects, followed by a subsequent recalculation of all the correlated variables. This is done for simulation, to account for possible systematic measurements of the data. All experimental sources from Section 4.5.2 but luminosity are treated both as normalization and shape uncertainties. For background with a data-driven normalization estimation, only the shape uncertainty is considered.

To account for statistical uncertainties, for each distribution going into the shape analysis, the $+1\sigma$ and -1σ shapes were obtained by adding/subtracting the statistical error in each bin and renormalizing it to the nominal distribution. In addition to this procedure a constant normalization uncertainty due to the finite statistics of the MC sample used to extract the shape is assigned.

4.6. Signal extraction

According to the “blinding” policy of the CMS Collaboration, the strategy of the analysis has been scrutinized and approved by a selected committee of internal reviewers before looking at the data in the signal region. This approach prevents the analysts from being biased by the data in the developing phase of the analysis. Below are shown the results after having looked at the data.

1895 4.6.1. Fitting procedure

1896 The signal, including ggH, VBF, and VH production mechanisms, is extracted in each bin
 1897 of p_T^H by performing a binned maximum likelihood fit simultaneously in all p_T^H bins to a
 1898 two-dimensional template for signals and backgrounds in the $m_{\ell\ell}$ - m_T plane. The variables
 1899 used for the two-dimensional template are chosen for their power to discriminate signal
 1900 and background contributions. This is shown in Fig. 4.18, where the two-dimensional MC
 1901 distributions are shown for the signal and background processes in the 0-jets category.

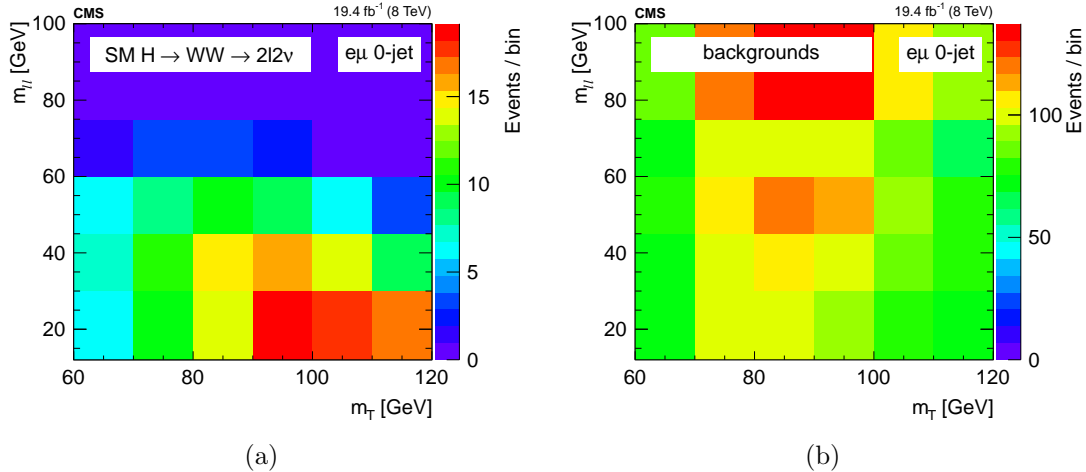


Figure 4.18.: Two-dimensional $m_{\ell\ell}$ - m_T distribution for signal (a) and background (b) processes in the 0-jets category.

1902 Six different signal strength parameters are extracted from the fit, one for each p_T^H bin.
 1903 The relative contributions of the different Higgs production mechanisms in the signal
 1904 template are taken to be the same as in the SM. The systematic uncertainty sources are
 1905 considered as nuisance parameters in the fit.

1906 The binning of the $m_{\ell\ell}$ and m_T templates is chosen to be:

- 1907 • $m_{\ell\ell}$: [12, 30, 45, 60, 75, 100, 125, 150, 175, 200]
- 1908 • m_T : [60, 70, 80, 90, 100, 110, 120, 140, 160, 180, 200, 220, 240, 280]

1909 To avoid a dependence of the results on the variables used for the template fit, $m_{\ell\ell}$ and
 1910 m_T need to be uncorrelated with respect to p_T^H . This has been verified and the correlation
 1911 between the discriminating variables and p_T^H is shown in Fig. 4.19 and Fig. 4.20 for ggH
 1912 and VBF production modes respectively.

1913 The relative contribution for different production mechanisms in the input signal template
 1914 is taken to be the same as the SM. The signal strength μ in each bin, i.e. the ratio between
 1915 the measured cross section and the SM one, $\mu = \sigma/\sigma_{SM}$, is allowed to float between -10 and
 1916 +10, thus allowing negative values. This is mainly intended to allow the error bars to float
 1917 below 0.

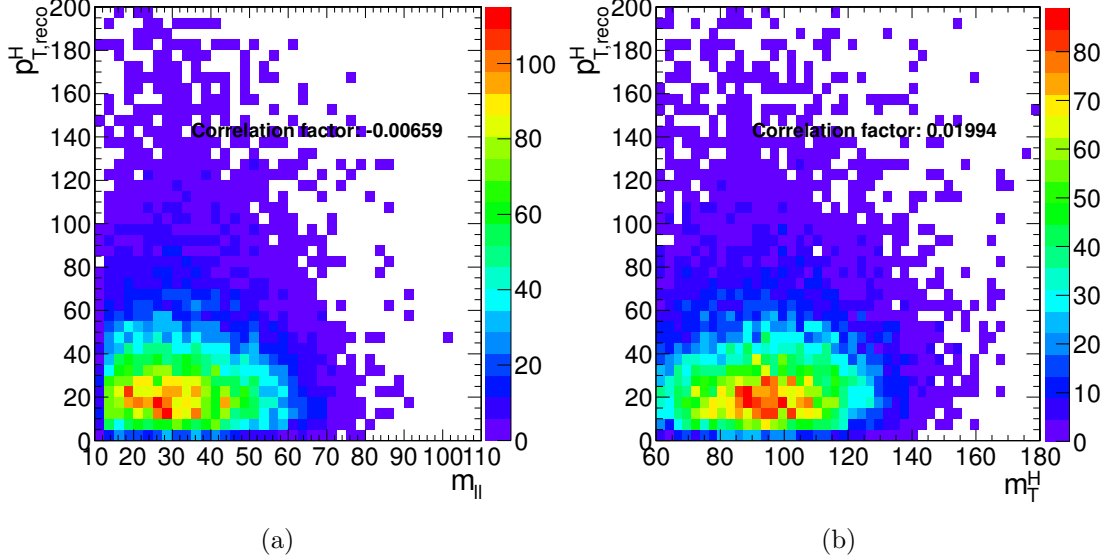


Figure 4.19.: Correlation between p_T^H and m_{ll} (a) and between p_T^H and m_T (b) after the full selection for the ggH production mode.

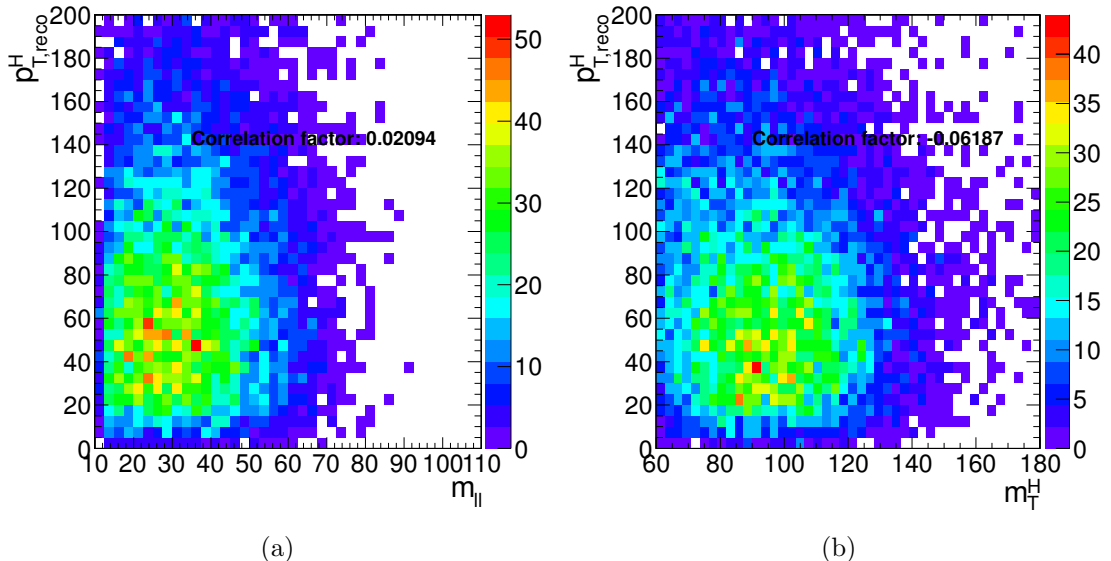


Figure 4.20.: Correlation between p_T^H and m_{ll} (a) and between p_T^H and m_T (b) after the full selection for the VBF production mode.

Because of detector resolution effects, some of the reconstructed $H \rightarrow WW$ signal events might originate from outside the fiducial phase space. These out-of-fiducial signal events cannot be precisely handled by the unfolding procedure and must be subtracted from the measured spectrum. The p_T^H distribution of the out-of-fiducial signal events is taken from

1922 simulation, and each bin is multiplied by the corresponding measured signal strength before
1923 performing the subtraction.

1924 At the end, the number of events in each bin i of the measured spectrum is:

$$N_i = \mu_i(s_i - f_i) , \quad (4.24)$$

1925 where s_i and f_i are respectively the number of signal and fake events expected from
1926 simulation and μ_i is the measured signal strength.

1927 The fit makes use of the binned maximum likelihood approach. The likelihood function,
1928 \mathcal{L} , restricted to the p_T^H bin j , can be written as: **CHECK!!**

$$\mathcal{L}(data|\mu_j, \theta) = \prod_{i=0}^{N_{\text{bins}}} \frac{(\mu_j s_i(\theta) + b_i(\theta))^{n_i}}{n_i!} e^{-\mu_j s_i(\theta) - b_i(\theta)} \cdot p(\tilde{\theta}|\theta) , \quad (4.25)$$

1929 where $data$ corresponds to the experimental observation and μ_j is the signal strength in
1930 the bin j , i.e. the parameter of interest of the fit, which multiplies the signal yield. The
1931 index i runs over the bins of the $m_{\ell\ell}-m_T$ two-dimensional histogram corresponding the p_T^H
1932 bin j , s_i and b_i are the expected number of signal and background events respectively in bin
1933 i , and n_i is the total number of observed events in bin i . The set of parameters θ represents
1934 the full suite of nuisance parameters used to incorporate the systematic uncertainties. Each
1935 nuisance parameter is constrained in the fit including the prior distributions functions $p(\tilde{\theta}|\theta)$
1936 in the likelihood, where $\tilde{\theta}$ is the set of default values for the θ parameters. For the major part
1937 of the nuisance parameters a log-normal prior distribution is used, with a standard deviation
1938 corresponding to the given systematic uncertainty. For some nuisance parameters, as the
1939 ones related to the statistical uncertainty coming from the background measurement in data
1940 control regions, a Gamma distribution is instead recommended. A log-uniform distribution
1941 is used for the uncertainty related to the normalization of background contributions that
1942 are left unconstrained in the fit, such as the WW background process. Finally, some of
1943 the experimental uncertainties, related to the shape of signal and background processes,
1944 are modelled by means of additional histograms as explained in Sec. 4.5.5. The nuisance
1945 parameters correlations across different p_T^H bins are taken into account. Moreover the
1946 nuisance parameters can also be correlated (or anti-correlated) between signal and different
1947 background processes. As an example, the uncertainty related to the integrated luminosity
1948 measurement is fully correlated for all the signal and background processes.

1949 Before running the fit on the data, the same procedure has been applied to the so called
1950 *Asimov data set*¹, which provides a simple method to estimate the signal sensitivity before
1951 looking at the data [88].

¹In a parallel reality imagined by the science fiction writer I. Asimov, politics was run in a peculiar way: instead of mobilizing millions of people to cast their vote to deliberate on something, an algorithm was used to select an individual “average” person, and then this person was asked to take the decision on that matter.

4.6.2. Signal and background yields

A comparison of data and background prediction is shown in Fig. 4.21, where the $m_{\ell\ell}$ distribution is shown for the six p_T^H bins. Distributions correspond to the m_T window of [60, 110] GeV, in order to emphasize the signal contribution [50]. The m_T distributions are shown in Fig. 4.22 and correspond to the $m_{\ell\ell}$ window of [12, 75] GeV.

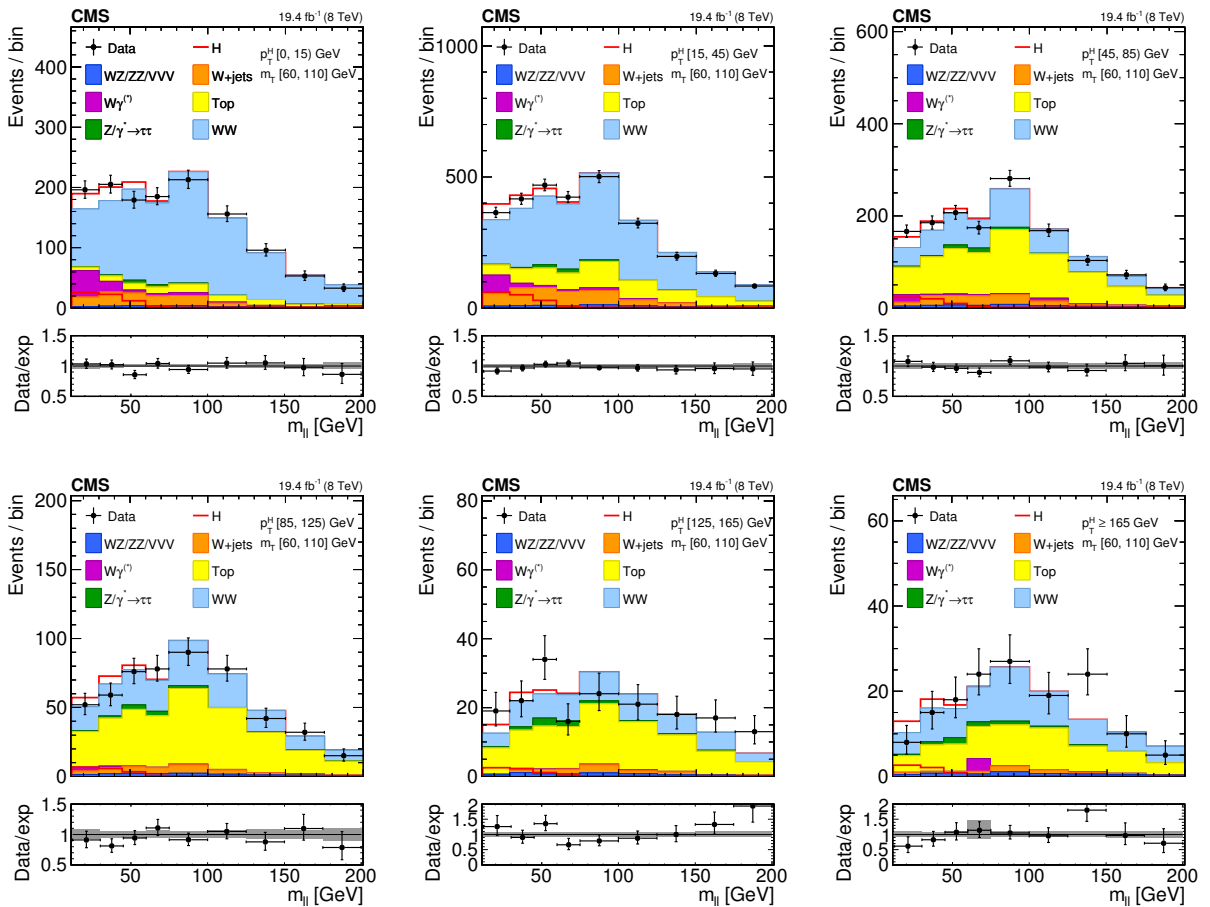


Figure 4.21.: Distributions of the $m_{\ell\ell}$ variable in each of the six p_T^H bins. Background normalizations correspond to the values obtained from the fit. Signal normalization is fixed to the SM expectation. The distributions are shown in an m_T window of [60,110] GeV in order to emphasize the Higgs boson (H) signal. The signal contribution is shown both stacked on top of the background and superimposed to it. Ratios of the expected and observed event yields in individual bins are shown in the panels below the plots. The uncertainty band shown in the ratio plot corresponds to the envelope of systematic uncertainties after performing the fit to the data.

The signal and background yields after the analysis selection are reported in Table 4.9.

The spectrum shown in Fig. 4.23 is obtained after having performed the fit and after the subtraction of the out-of-fiducial signal events, but before undergoing the unfolding pro-

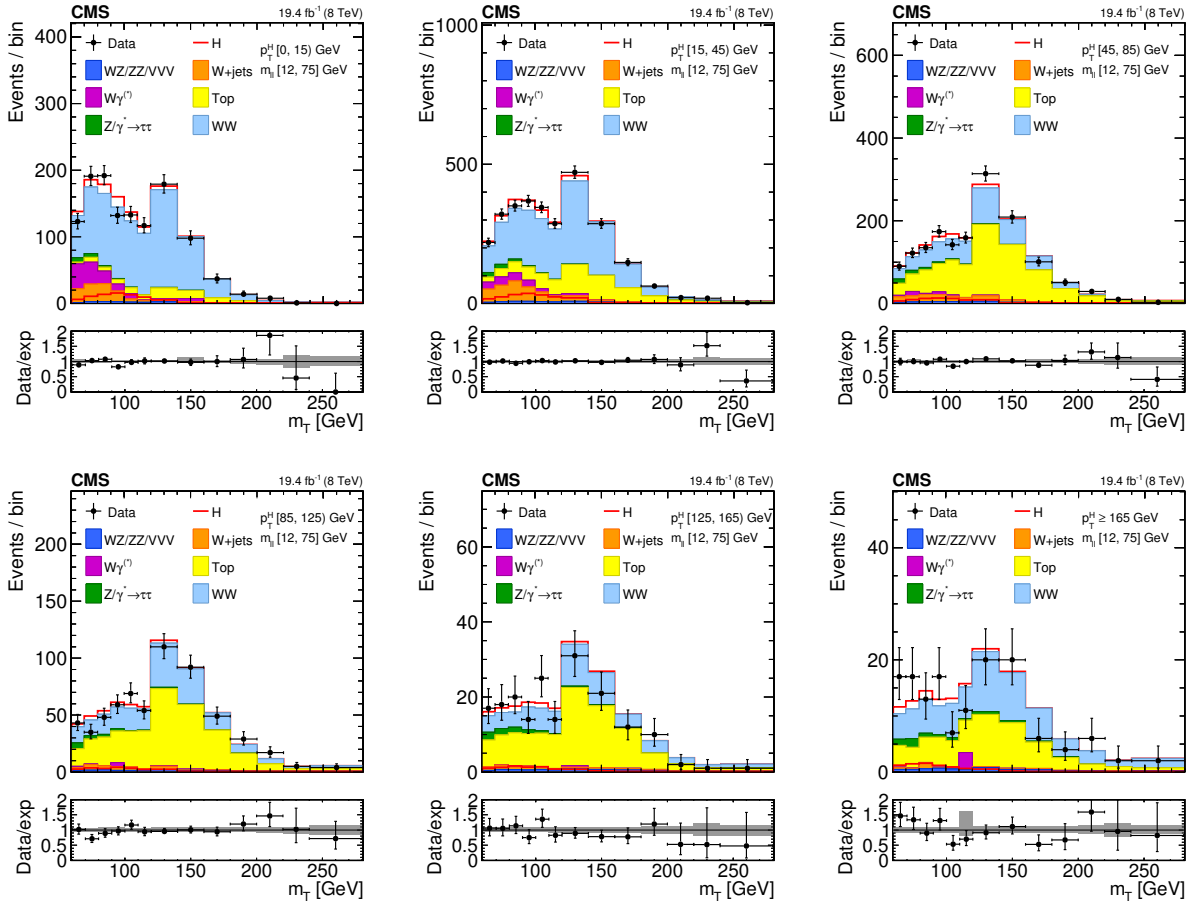


Figure 4.22.: Distributions of the m_T variable in each of the six p_T^H bins. Background normalizations correspond to the values obtained from the fit. Signal normalization is fixed to the SM expectation. The distributions are shown in an $m_{\ell\ell}$ window of [12,75] GeV in order to emphasize the Higgs boson (H) signal. The signal contribution is shown both stacked on top of the background and superimposed to it. Ratios of the expected and observed event yields in individual bins are shown in the panels below the plots. The uncertainty band shown in the ratio plot corresponds to the envelope of systematic uncertainties after performing the fit to the data.

Table 4.9.: Signal prediction, background estimates and observed number of events in data are shown in each p_T^H bin for the signal after applying the analysis selection requirements. The total uncertainty on the number of events is reported. For signal processes, the yield related to the ggH are shown, separated with respect to the contribution of the other production mechanisms (XH=VBF+VH). The WW process includes both quark and gluon induced contribution, while the Top process takes into account both $t\bar{t}$ and tW.

$p_T^H [\text{GeV}]$	0-15	15-45	45-85	85-125	125-165	165- ∞
ggH	73 ± 3	175 ± 5	59 ± 3	15 ± 2	5.1 ± 1.5	4.9 ± 1.4
XH=VBF+VH	4 ± 2	15 ± 4	16 ± 4	8 ± 2	3.8 ± 1.1	3.0 ± 0.8
Out-of-fiducial	9.2 ± 0.5	19.9 ± 0.7	11.4 ± 0.6	4.4 ± 0.3	1.6 ± 0.2	2.4 ± 0.2
Data	2182	5305	3042	1263	431	343
Total background	2124 ± 128	5170 ± 321	2947 ± 293	1266 ± 175	420 ± 80	336 ± 74
WW	1616 ± 107	3172 ± 249	865 ± 217	421 ± 120	125 ± 60	161 ± 54
Top	184 ± 38	1199 ± 165	1741 ± 192	735 ± 125	243 ± 51	139 ± 49
W+jets	134 ± 5	455 ± 10	174 ± 6	48 ± 4	14 ± 3	9 ± 3
WZ+ZZ+VVV	34 ± 4	107 ± 10	71 ± 7	29 ± 5	14 ± 3	13 ± 4
$Z/\gamma^* \rightarrow \tau^+\tau^-$	23 ± 3	67 ± 5	47 ± 4	22 ± 3	12 ± 2	10 ± 2
$W\gamma^{(*)}$	132 ± 49	170 ± 58	48 ± 30	12 ± 9	3 ± 3	5 ± 10

1960 cedure. The theoretical distribution after the detector simulation and event reconstruction
 1961 is also shown for comparison.

1962 In order to assess the robustness of the fit, several toy MC samples have been produced,
 1963 with a statistical accuracy corresponding to the one expected in data. The distribution
 1964 of the signal strengths extracted in each bin using the toy MC samples and the their pull
 1965 distributions are shown in Fig. 4.24.

1966 4.7. Unfolding

1967 To facilitate comparisons with theoretical predictions or other experimental results, the
 1968 signal extracted performing the fit has to be corrected for detector resolution and efficiency
 1969 effects and for the efficiency of the selection defined in the analysis. An unfolding procedure
 1970 is used relying on the ROOUNFOLD package [89], which provides the tools to run various
 1971 unfolding algorithms.

1972 The basic principle behind the unfolding procedure in this analysis is to use MC signal
 1973 samples to make the “true” distribution of the variable of interest, which is obtained using
 1974 simulated events before particle interaction with the detector, and the same distribution
 1975 obtained using events reconstructed after the full GEANT4 simulation of the CMS detector
 1976 and event reconstruction. These two distributions are used to calculate the detector response
 1977 matrix M :

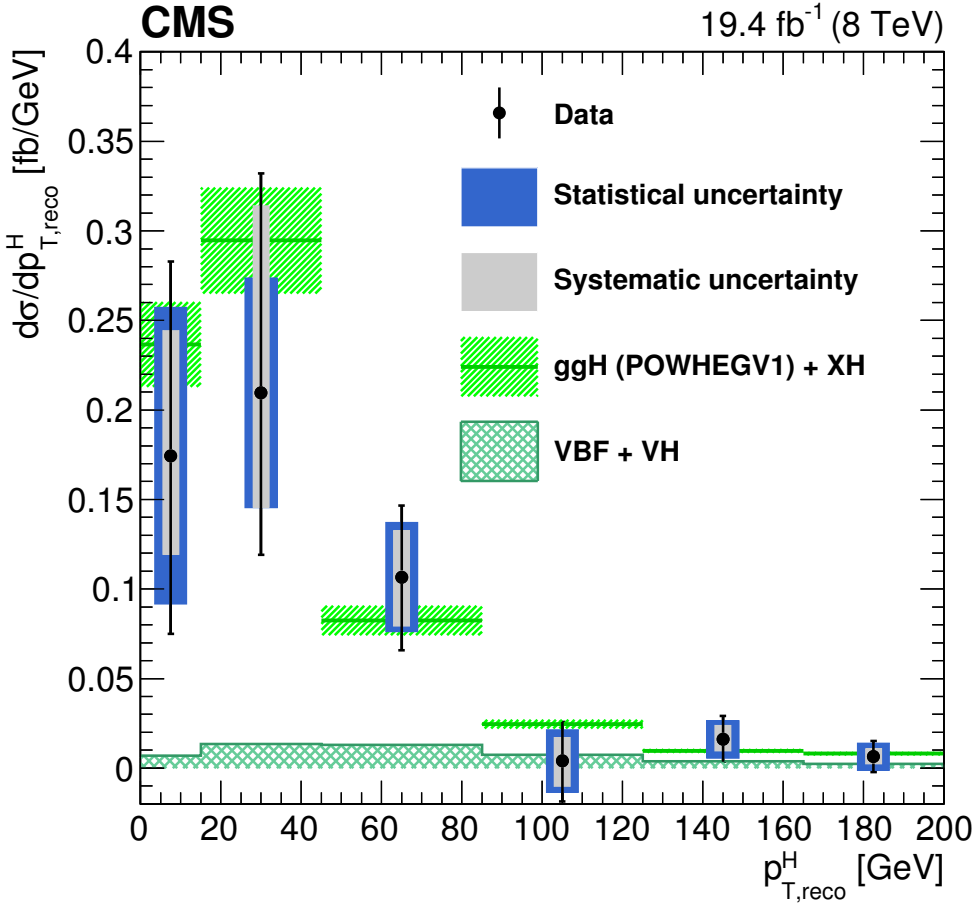


Figure 4.23.: Differential Higgs boson production cross section as a function of the reconstructed p_T^H , before applying the unfolding procedure. Data values after the background subtraction are shown together with the statistical and the systematic uncertainties, determined propagating the sources of uncertainty through the fit procedure. The line and dashed area represent the SM theoretical estimates in which the acceptance of the dominant ggH contribution is modelled by POWHEG V1. The sub-dominant component of the signal is denoted as XH=VBF+VH, and is shown with the cross filled area separately.

$$R_i^{\text{MC}} = \sum_{j=1}^n M_{ij} T_j^{\text{MC}} \quad , \quad (4.26)$$

where R^{MC} and T^{MC} are two n -dimensional vectors representing the distribution before and after event processing through CMS simulation and reconstruction. The dimension n of the two vectors corresponds to the number of bins in the distributions, equal to six in this analysis. The response matrix M includes all the effects related to the detector and

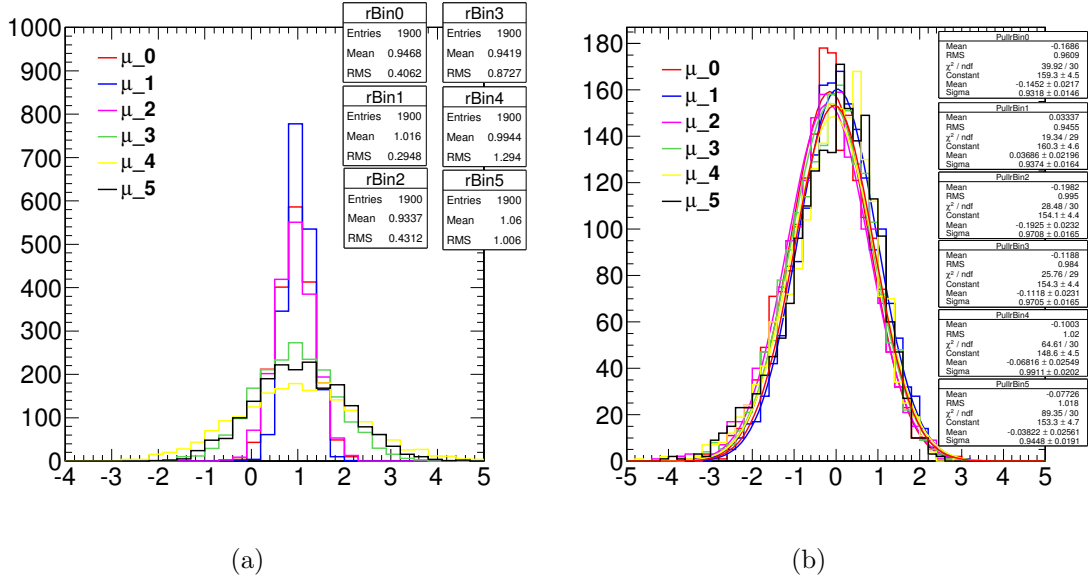


Figure 4.24.: Signal strength distribution as extracted from the fit of toy MC samples (a). Distribution of the pull of the signal strength parameters (b).

analysis selection that affect the R^{MC} distribution. The goal of the unfolding procedure is to obtain the T^{truth} distribution starting from the measured R^{observed} distribution by inverting the matrix M . To avoid the large variance and strong negative correlation between the neighbouring bins [51], the unfolding procedure in this analysis relies on the singular value decomposition [90] method based on the Tikhonov regularization function. Since the response matrix is in general limited by the statistical uncertainties of simulated samples and given the finite data statistical accuracy, a simple inversion could lead to large fluctuations between bins in the unfolded result. In particular, if the off-diagonal elements of the response matrix are sizeable, the unfolded distribution has large variance and strong negative correlations between the neighbouring bins [51]. Several unfolding methods with regularization are available in literature, such as a method based on the Bayes' theorem, which overcome the unfolding instability using an iterative procedure [91]. One possible solution is the utilization of regularization methods. Such methods introduce a regularization function that controls the smoothness of the distribution and depends generally on one regularization parameter, which can be controlled to achieve the desired degree of smoothness. The choice of the regularization parameter is particularly critical, and it should represent an optimal trade-off between taming the fluctuations in the unfolded result, and biasing the unfolded distribution towards the one used to build the response matrix. The main feature of this method is the use of the singular value decomposition of the response matrix, including an additional term to suppress the oscillatory component of the solution, i.e. the regularization term, which represents some *a priori* knowledge of the final solution. The regularization parameter is chosen to obtain results that are robust against numerical instabilities and statistical fluctuations, following the prescription

described in Ref. [90]. **Maybe I should add an appendix describing the SVD method in details**

The response matrix is built as a two-dimensional histogram, with the generator-level p_T^H on the y axis and the same variable after the reconstruction on the x axis, using the same binning for both distributions. The resulting detector response matrix, including all signal sources and normalized by row, is shown in Fig. 4.25(a). The value of the diagonal bins corresponds to the stability S . The same matrix, normalized by column, is shown in Fig. 4.25(b). In this case the diagonal bins correspond to the purity P . The S and P parameters, defined in Sec. 4.3, provide an estimate of the p_T^H resolution and migration effects. The main source of bin migrations effects in the response matrix is the limited resolution in the measurement of E_T^{miss} .

The resulting detector response matrix, which includes the effects of all signal sources and is represented by normalizing each row to unity is shown in Fig. 4.25(a). This representation shows the stability S in the diagonal bins, where S is defined as the ratio of the number of events generated and reconstructed in a given bin, and the number of events generated in that bin. In addition, a deconvolution matrix is constructed by normalizing each column to unity and is shown in Fig. 4.25(b). This latter representation shows the purity P in the diagonal bins, where P is defined as the ratio of the number of events generated and reconstructed in a given bin, and the number of events reconstructed in that bin. The S and P parameters provide an estimate of the p_T^H resolution and of migration effects. The response matrix built including all signal sources is shown in Fig. 4.25. In order to point out either the purity or the stability in diagonal bins, each column or row of the matrix was respectively normalized to unity. The matrix obtained in the first case is what is actually called detector response matrix, while in the other case the matrix is usually referred to as detector deconvolution matrix.

Several closure tests are performed in order to validate the unfolding procedure. To estimate the uncertainty in the unfolding procedure due to the particular model adopted for building the response matrix, two independent gluon fusion samples are used, corresponding to two different generators: POWHEG V1 and JHUGEN generators, both interfaced to PYTHIA 6.4. The JHUGEN generator sample is used to build the response matrix while the POWHEG V1 sample is used for the measured and the MC distributions at generator level. The result of this test shows good agreement between the unfolded and the distribution from MC simulation.

In order to further prove the choice of the regularization parameter, a large number of simulated pseudo-experiments has been generated to verify that the coverage of the unfolded uncertainties obtained with this procedure is as expected. From each pseudo-experiment the reconstructed p_T^H spectrum is obtained and then unfolded using the procedure described above, including only the statistical uncertainties. The coverage is calculated for each p_T^H bin, counting the number of pseudo-experiments for which the statistical uncertainty covers the true value. The confidence intervals are calculated using the Clopper-Pearson approach, and the results are shown in Table 4.10 for different values of the regularization parameter: starting from $k_{\text{reg}} = 2$ (stronger regularization) up to $k_{\text{reg}} = 5$ (weaker regularization). The criterion for choosing the best k_{reg} value is to increase the regularization as much as possible

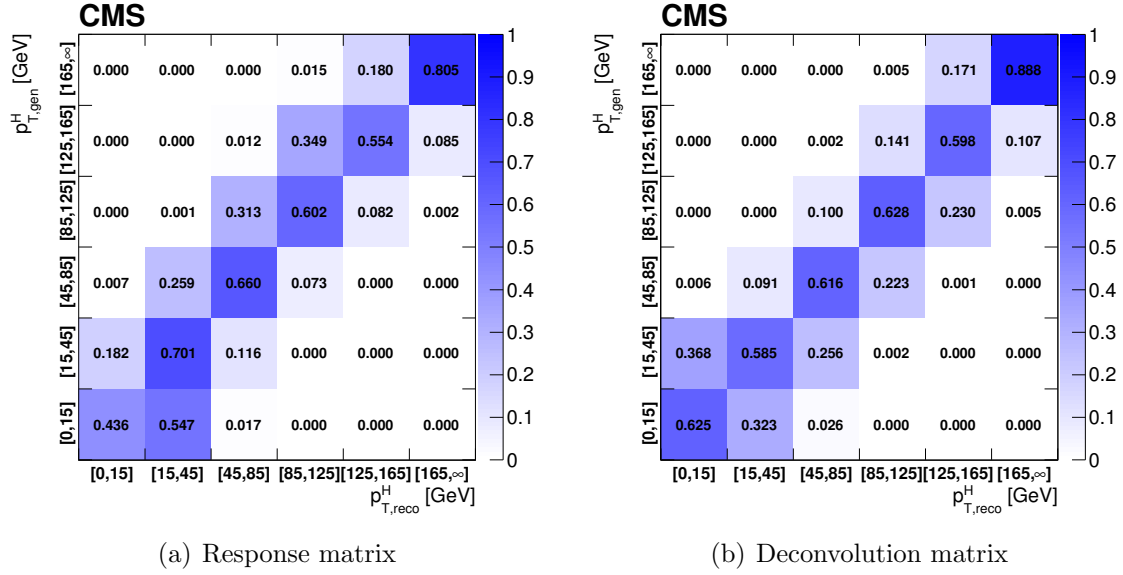


Figure 4.25.: Response matrix (a) and deconvolution matrix (b) including all signal processes. The matrices are normalized either by row (a) or by column (b) in order to show the purity or stability respectively in diagonal bins.

Table 4.10.: Coverage interval for each bin and for different values of the regularization parameter, obtained using pseudo-experiments.

p_T^H bin [GeV]	Coverage			
	$k_{\text{reg}} = 2$	$k_{\text{reg}} = 3$	$k_{\text{reg}} = 4$	$k_{\text{reg}} = 5$
0–15	$0.654^{+0.015}_{-0.016}$	$0.704^{+0.015}_{-0.015}$	$0.727^{+0.014}_{-0.015}$	$0.755^{+0.014}_{-0.014}$
15–45	$0.701^{+0.015}_{-0.015}$	$0.665^{+0.015}_{-0.016}$	$0.683^{+0.015}_{-0.015}$	$0.733^{+0.014}_{-0.015}$
45–85	$0.717^{+0.014}_{-0.015}$	$0.706^{+0.015}_{-0.015}$	$0.709^{+0.015}_{-0.015}$	$0.716^{+0.014}_{-0.015}$
85–125	$0.634^{+0.016}_{-0.016}$	$0.681^{+0.015}_{-0.015}$	$0.714^{+0.015}_{-0.015}$	$0.739^{+0.014}_{-0.015}$
125–165	$0.599^{+0.015}_{-0.016}$	$0.650^{+0.015}_{-0.016}$	$0.700^{+0.015}_{-0.015}$	$0.751^{+0.014}_{-0.014}$
165–∞	$0.632^{+0.016}_{-0.016}$	$0.674^{+0.015}_{-0.015}$	$0.701^{+0.015}_{-0.015}$	$0.722^{+0.014}_{-0.015}$

²⁰⁴⁸ without introducing a bias, i.e. until a 68% coverage is fulfilled. This criterion leads to the
²⁰⁴⁹ same result as the prescription described in Ref. [90], strengthening the choice of $k_{\text{reg}} = 3$.

²⁰⁵⁰ 4.7.1. Treatment of systematic uncertainties

²⁰⁵¹ An important aspect of this analysis is the treatment of the systematic uncertainties and
²⁰⁵² the error propagation through the unfolding procedure. The sources of uncertainty are

2053 divided into three categories, depending on whether the uncertainty affects only the signal
 2054 yield (type A), both the signal yield and the response matrix (type B), or only the response
 2055 matrix (type C). These three classes propagate differently through the unfolding procedure.

2056 Type A uncertainties are extracted directly from the fit in the form of a covariance
 2057 matrix, which is passed to the unfolding tool as the covariance matrix of the measured
 2058 distribution. The nuisance parameters belonging to this category are the background shape
 2059 and normalization uncertainties. To extract the effect of type A uncertainties a dedicated
 2060 fit is performed, fixing to constant all the nuisance parameters in the model, but type A
 2061 nuisance parameters. The correlation matrix among the six signal strengths corresponding
 2062 to the six p_T^H bins, including all type A uncertainties, is shown in Fig. 4.26. The correlation
 2063 $\text{cor}(i,j)$ of bins i and j is defined as:

$$\text{cor}(i,j) = \frac{\text{cov}(i,j)}{s_i s_j} , \quad (4.27)$$

2064 where $\text{cov}(i,j)$ is the covariance of bins i and j , and (s_i, s_j) are the standard deviations
 2065 of bins i and j , respectively.

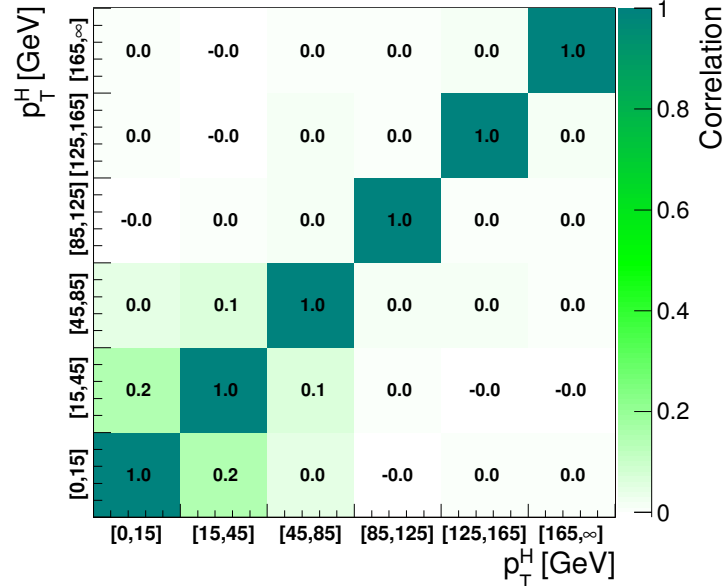


Figure 4.26.: Correlations among the signal strengths corresponding to the six p_T^H bins including all type A uncertainties.

2066 The nuisance parameters falling in the type B class are:

- 2067 • the b veto scale factor. It affects the signal and background templates by varying the
 2068 number of events with jets that enter the selection. It also affects the response matrix

2069 because the reconstructed spectrum is harder or softer depending on the number of
 2070 jets, which in turn depends on the veto.

- 2071 • the lepton efficiency scale factor. It affects the signal and background template
 2072 shape and normalization. It affects the response matrix by varying the reconstructed
 2073 spectrum;
- 2074 • the E_T^{miss} scale and resolution, which have an effect similar to the above;
- 2075 • lepton scale and resolution. The effect is similar to the above;
- 2076 • jet energy scale. It affects the signal and background template shape and normalization.
 2077 It also affects the response matrix because, by varying the fraction of events with jets,
 2078 the b veto can reject more or fewer events, thus making the reconstructed spectrum
 2079 harder or softer.

2080 The effect of each type B uncertainty is evaluated separately, since each one changes the
 2081 response matrix in a different way. In order to evaluate their effect on the signal strengths
 2082 parameters, two additional fits are performed, each time fixing the nuisance parameter
 2083 value to ± 1 standard deviation with respect to its nominal value. The results of the fits are
 2084 then compared to the results of the full fit obtained by floating all the nuisance parameters,
 2085 thus determining the relative uncertainty on the signal strengths due to each nuisance
 2086 parameter, as shown in Tab. 4.11. Using these uncertainties, the measured spectra for each
 2087 type B source are built. The effects are propagated through the unfolding by building the
 2088 corresponding variations of the response matrix and unfolding the measured spectra with
 2089 the appropriate matrix.

2090 Type C uncertainties are related to the underlying assumption on the Higgs boson
 2091 production mechanism used to extract the fiducial cross sections. These are evaluated
 2092 using alternative response matrices that are obtained by varying the relative fraction of
 2093 the VBF and ggH components within the experimental uncertainty, as given by the CMS
 2094 combined measurement [92]. Three different response matrices are built, corresponding to
 2095 the nominal, scaled up, and scaled down VBF/ggH ratio. The nominal matrix assumes
 2096 the SM VBF/ggH ratio, while up- and down-scaled matrices are constructed by varying
 2097 the SM signal strengths within the experimental constraints for VBF and ggH in such a
 2098 way as to obtain the maximal variation of the VBF/ggH ratio allowed by the experimental
 2099 constraints. These three matrices are used to unfold the reconstructed spectrum with the
 2100 nominal VBF/ggH fraction, and obtain an uncertainty on the unfolded spectrum.

2101 4.8. Results

2102 In order to unfold the spectrum, the procedure described in section 4.7 has been pursued.
 2103 The statistical plus type A systematic uncertainties are propagated by the unfolding
 2104 procedure into the final spectrum, taking into account the signal strengths covariance
 2105 matrix. The type B systematic uncertainty has been propagated using the following
 2106 procedure: for each p_T^H bin, we compute the upper bound of the systematic band computing

Table 4.11.: Effect of all the Type B uncertainties on the signal strengths of each bin. In the table are reported the signal strength variations corresponding to an up or down scaling of each nuisance.

Type B uncertainty	Effect on signal strength ($+1\sigma/-1\sigma$ [%])					
	[0–15]	[15–45]	[45–85]	[85–125]	[125–165]	[165– ∞]
b veto	-10.1/-8.8	7.3/12.2	-6.3/3.1	-14.4/-4.8	-5.4/14.5	-7.9/17.8
lepton efficiency	-14.7/-3.9	4.5/15.1	-5.7/2.5	-13.2/-5.3	-0.2/7.6	-0.1/6.8
E_T^{miss} resolution	-12.5/0.0	15.4/-0.0	-12.8/-0.0	8.7/0.0	-20.9/-0.0	10.5/0.0
E_T^{miss} scale	-14.4/-6.8	-0.0/17.7	-6.1/-7.1	9.6/-20.9	2.3/32.4	2.5/2.6
lepton resolution	-12.5/-0.0	11.2/0.0	-2.4/0.0	-13.4/-0.0	9.9/0.0	-4.6/-0.0
electron momentum scale	-2.7/-13.1	15.9/9.9	10.8/-16.8	16.2/-33.1	30.9/-14.4	12.6/-10.9
muon momentum scale	-7.0/-10.7	11.8/8.9	1.1/-8.7	-0.7/-14.4	14.5/-4.6	8.0/-1.6
jet energy scale	-10.9/-10.1	9.0/9.0	-3.0/-2.9	-10.3/-8.9	0.3/3.4	5.2/3.1

Table 4.12.: Differential cross section in each p_T^H bin, together with the total uncertainty and the separate components of the various sources of uncertainty.

p_T^H [GeV]	$d\sigma/dp_T^H$ [fb/GeV]	Total uncertainty [fb/GeV]	Statistical uncertainty [fb/GeV]	Type A uncertainty [fb/GeV]	Type B uncertainty [fb/GeV]	Type C uncertainty [fb/GeV]
0–15	0.615	+0.370/-0.307	± 0.246	± 0.179	+0.211/-0.038	+0.0782/-0.0608
15–45	0.561	+0.210/-0.157	± 0.120	± 0.093	+0.146/-0.041	+0.0395/-0.0327
45–85	0.215	+0.084/-0.078	± 0.059	± 0.037	+0.047/-0.034	+0.0089/-0.0084
85–125	0.071	+0.038/-0.038	± 0.029	± 0.017	+0.018/-0.017	+0.0018/-0.0022
125–165	0.027	+0.020/-0.019	± 0.016	± 0.009	+0.007/-0.007	+0.0003/-0.0006
165– ∞	0.028	+0.027/-0.027	± 0.023	± 0.012	+0.008/-0.007	+0.0002/-0.0006

the square sum of all the signal strength variations that deviate in the up direction with respect to the bin central value, whether or not this variation corresponds to the up or down shift of the systematic uncertainty. The same is done for the lower bound of the systematic band. If both the up and down shifts of a given nuisance parameter lead to a same direction variation of the signal strength, only the larger variation is considered.

The unfolded p_T^H spectrum is shown in Fig. 4.27. Statistical, systematic, and theoretical uncertainties are shown as separate error bands in the plot. The unfolded spectrum is compared with the SM-based theoretical predictions where the ggH contribution is modelled using the HRES and POWHEG V2 programs. The comparison shows good agreement between data and theoretical predictions within the uncertainties. The measured values for the differential cross section in each bin of p_T^H are reported together with the total uncertainty in Table 4.12.

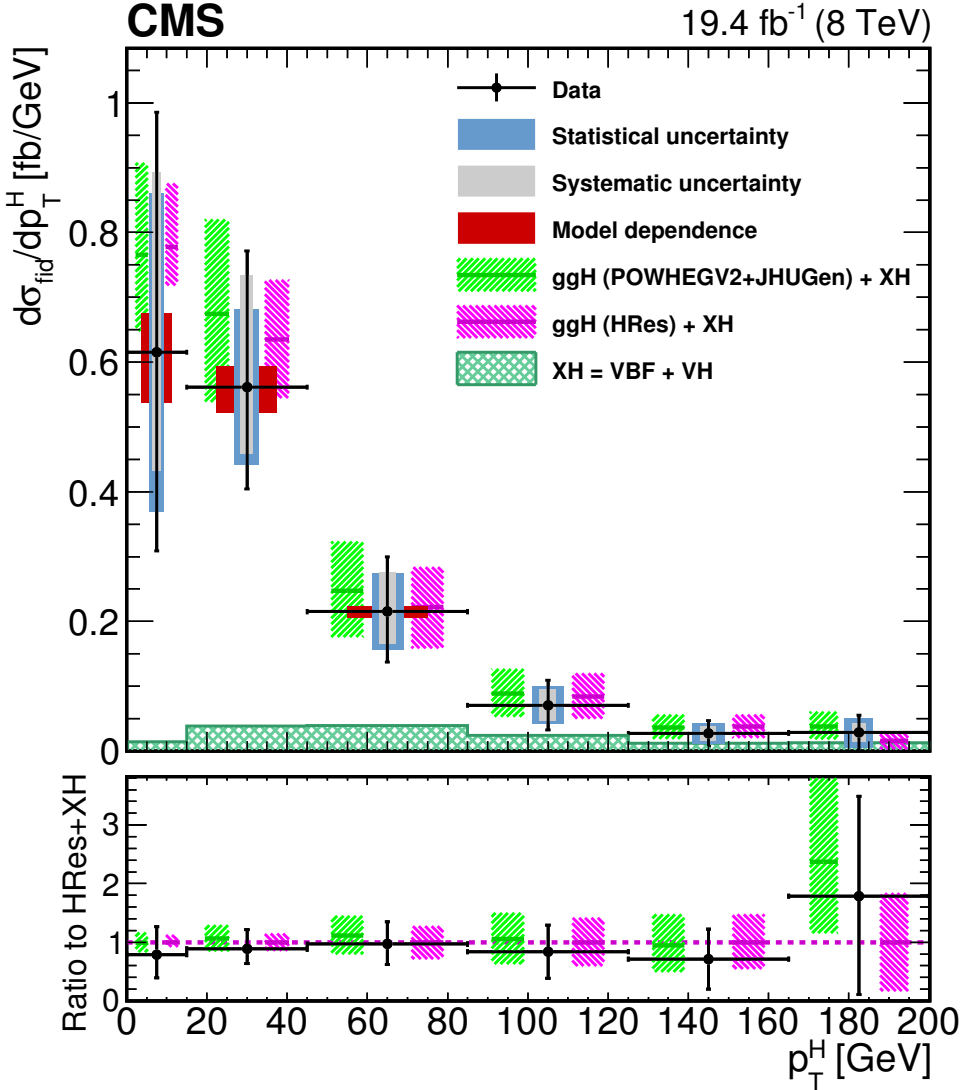


Figure 4.27.: Higgs boson production cross section as a function of p_T^H , after applying the unfolding procedure. Data points are shown, together with statistical and systematic uncertainties. The vertical bars on the data points correspond to the sum in quadrature of the statistical and systematic uncertainties. The model dependence uncertainty is also shown. The pink (and back-sashed filling) and green (and slashed filling) lines and areas represent the SM theoretical estimates in which the acceptance of the dominant ggH contribution is modelled by HRes and POWHEG V2, respectively. The subdominant component of the signal is denoted as $\text{XH}=\text{VBF}+\text{VH}$ and it is shown with the cross filled area separately. The bottom panel shows the ratio of data and POWHEG V2 theoretical estimate to the HRes theoretical prediction.

Figure 4.28 shows the correlation matrix for the six bins of the differential spectrum.
²¹¹⁹ The correlation of of bins is defined as in Eq. (4.27).

²¹²⁰

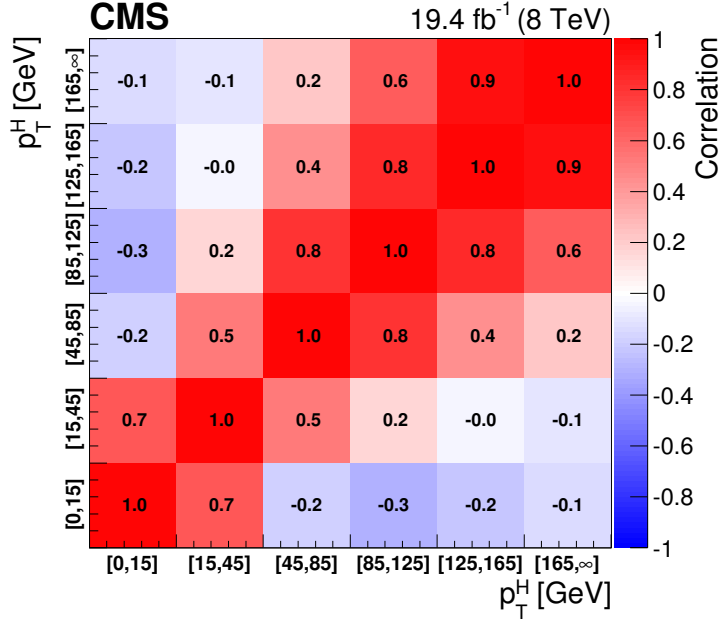


Figure 4.28.: Correlation matrix among the p_T^H bins of the differential spectrum.

To measure the inclusive cross section in the fiducial phase space, the differential measured spectrum is integrated over p_T^H . In order to compute the contributions of the bin uncertainties of the differential spectrum to the inclusive uncertainty, error propagation is performed taking into account the covariance matrix of the six signal strengths. For the extrapolation of this result to the fiducial phase space, the unfolding procedure is not needed, and the inclusive measurement has only to be corrected for the fiducial phase space selection efficiency ϵ_{fid} . Dividing the measured number of events by the integrated luminosity and correcting for the overall selection efficiency, which is estimated in simulation to be $\epsilon_{fid} = 36.2\%$, the inclusive fiducial $\sigma \times \mathcal{B}$, σ_{fid} , is computed to be:

$$\sigma_{fid} = 39 \pm 8 \text{ (stat)} \pm 9 \text{ (syst)} \text{ fb} \quad , \quad (4.28)$$

in agreement within the uncertainties with the theoretical estimate of 48 ± 8 fb, computed integrating the spectrum obtained with the POWHEG V2 program for the ggH process and including the XH contribution.

Chapter 5.

2133 **Search for the SM Higgs boson in the 2134 $H \rightarrow WW$ channel with the first 2135 13 TeV LHC data**

2136 **5.1. Introduction**

2137 In this chapter, the first search for the SM Higgs boson decaying to a W boson pair at
2138 13 TeV is presented, using a total integrated luminosity of 2.3 fb^{-1} , collected during the
2139 2015 proton proton data taking period of the LHC.

2140 Final states in which the two W bosons decay leptonically are studied. Therefore,
2141 events with a pair of oppositely-charged leptons, exactly one electron and one muon, a
2142 substantial amount of missing transverse energy, E_T^{miss} , due to the presence of neutrinos in
2143 the final state, and either zero or one jet are selected. This signature is common to other
2144 processes, which enter the analysis as backgrounds. The main background comes from
2145 WW production, irreducible background that shares the same final states and can only be
2146 separated by the use of certain kinematic properties. Another important background is
2147 $W+jets$, where a jet can mimick a leptonic signature. Background coming from top quark
2148 events, i.e. $t\bar{t}$ and single top production, is also important, followed by other processes such
2149 as Drell-Yan, WZ , and other EWK production. The analysis strategy follows the one used
2150 during Run 1 in the same channel, described in Chapter 4, with a few different aspects that
2151 are described in the next sections.

2152 With respect to 8 TeV, the ggH production cross section at 13 TeV is expected to
2153 increase of a factor of 2, thus raising the number of expected signal events. In addition, the
2154 cross section for the background processes is increasing as well. The WW production cross
2155 section increases of a factor of 1.8 and the $t\bar{t}$ cross section of a factor of 3.5, due to the
2156 enhancement of the gluon PDFs at higher center of mass energies.

2157 **5.2. Data and simulated samples**

2158 Data recorded in proton proton collisions at 13 TeV during 2015 was used in the analysis,
2159 with a total integrated luminosity of 2.3 fb^{-1} . Single and double lepton triggers are used

2160 similarly to the same analysis at 8 TeV. The HLT paths and descriptions of the triggers used
2161 in this analysis are described in Tables 5.1 and 5.2 for electrons and muons respectively.

Table 5.1.: HLT paths related to Electrons

HLT Path	Description
HLT_Ele23_WPLoose_Gsf_v*	Single Electron trigger. Best trigger to be used for 2015 data. In WW , we are using “Trigger safe” Id. Turn on is at around $\text{Ele } p_T = 30 \text{ GeV}$
HLT_Ele17_Ele12_CaloIdL_TrackIdL_IsoVL_DZ_v*	Double Electron Trigger. Best trigger to cover the turn on region from single electron trigger. “DZ” filter is also present. Its efficiency is also calculated separately.
HLT_Ele12_CaloIdL_TrackIdL_IsoVL_v*	This electron leg of HLT_Mu17_TrkIsoVVL_Ele12_CaloIdL_TrackIdL_IsoVL_v* same as Ele12 leg of double electron trigger.
HLT_Ele17_CaloIdL_TrackIdL_IsoVL_v*	This electron leg of HLT_Mu8_TrkIsoVVL_Ele17_CaloIdL_TrackIdL_IsoVL_v* same as Ele17 leg of double electron trigger.

2162 The trigger efficiencies are measured in data and applied on simulated events as described
2163 in Sec. 4.2.1.

2164 Concerning the simulated samples, several different Monte Carlo (MC) generators were
2165 used. In the simulation, ‘lepton’ includes also τ . Higgs signal samples have been simulated
2166 in all channels with POWHEG v2 [53, 66, 93], designed to describe the full NLO properties
2167 of these processes. In particular, for Higgs produced via gluon fusion [55], and vector-boson-
2168 fusion (VBF) [56], the decay of the Higgs boson into two W boson and subsequently into
2169 leptons was done using JHUGEN v5.2.5 [94]. For associated production with a vector boson
2170 (W^+H , W^-H , ZH) [95], including gluon fusion produced ZH ($ggZH$), the Higgs decay was
2171 done via PYTHIA 8.1 [75]. Alternative signal samples were produced with AMC@NLO [58],
2172 or with POWHEG v2 but decayed via PYTHIA 8.1 for gluon fusion and VBF assuming a
2173 Higgs boson mass of 125 GeV. In the following, the mass of the SM Higgs boson is assumed
2174 to be 125 GeV.

2175 The WW production, irreducible background for the analysis, was simulated in different
2176 ways. POWHEG v2 [96] was used for $q\bar{q}$ produced WW in different decays. The cross
2177 section used for normalizing WW processes produced via $q\bar{q}$ was computed at next-to-next-
2178 to-leading order (NNLO) [97]. In order to control the top quark background processes, the
2179 analysis is performed with events that have no more than one high- p_T jet. The veto on
2180 high- p_T jets enhances the importance of logarithms of the jet p_T , spoiling the convergence
2181 of fixed-order calculations of the $q\bar{q} \rightarrow WW$ process and requiring the use of dedicated
2182 resummation techniques for an accurate prediction of differential distributions [98, 99]. The
2183 p_T of the jets produced in association with the WW system is strongly correlated with its
2184 transverse momentum, p_T^{WW} , especially in the case where only one jet is produced. The

Table 5.2.: Muon trigger's elements description

HLT path	
HLT_IsoMu18_v*	single muon trigger
HLT_IsoTrMu20_v*	single muon trigger with tracker isolation
HLT_Mu17_TrkIsoVVL	leg for the HLT_Mu17_TrkIsoVVL_Mu8_TrkIsoVVL_DZ_v*, HLT_Mu17_TrkIsoVVL_TkMu8_TrkIsoVVL_DZ_v* and HLT_Mu17_TrkIsoVVL_Ele12_CaloIdL_TrackIdL_IsoVL_v* double lepton triggers
HLT_Mu8_TrkIsoVVL	leg for the HLT_Mu17_TrkIsoVVL_Mu8_TrkIsoVVL_DZ_v* and HLT_Mu8_TrkIsoVVL_Ele17_CaloIdL_TrackIdL_IsoVL_v* double lepton triggers
HLT_TkMu8_TrkIsoVVL	leg for the HLT_Mu17_TrkIsoVVL_TkMu8_TrkIsoVVL_DZ_v* double muon trigger
$DZ_{\mu\mu}$	efficiency of DZ cut in the HLT_Mu17_TrkIsoVVL_Mu8_TrkIsoVVL_DZ_v* and HLT_Mu17_TrkIsoVVL_TkMu8_TrkIsoVVL_DZ_v* double muon triggers, it is around 95%

2185 simulated $q\bar{q} \rightarrow WW$ events are reweighted to reproduce the p_T^{WW} distribution from the
 2186 p_T -resummed calculation.

2187 Gluon fusion produced WW was generated, with and without Higgs diagrams, using
 2188 MCFM v7.0 [100]. A $t\bar{t}$ sample dilepton sample was also generated using POWHEG v2. The
 2189 WW and $t\bar{t}$ samples produced specifically for this analysis are presented in Table 5.3. Other
 2190 background samples are used, a list of the most relevant ones is presented in Table 5.4.

Table 5.3.: Simulated samples for $t\bar{t}$ and WW production. The $gg \rightarrow WW \rightarrow 2\ell 2\nu$ (H diagr.) sample includes both ggH production, the $ggWW$ component and the interference.

Process	$\sigma \times \mathcal{B}$ [pb]
$t\bar{t} \rightarrow WW b\bar{b} \rightarrow 2\ell 2\nu b\bar{b}$	87.31
$q\bar{q} \rightarrow WW \rightarrow 2\ell 2\nu$	12.178
$gg \rightarrow WW \rightarrow 2\ell 2\nu$	0.5905
$gg \rightarrow WW \rightarrow 2\ell 2\nu$ (H diagr.)	0.9544

2191 All processes are generated using the NNPDF2.3 [101, 102] parton distribution functions
 2192 (PDF) for NLO generators, while the LO version of the same PDF is used for LO generators.
 2193 All the event generators are interfaced to PYTHIA 8.1 [75] for the showering of partons

Table 5.4.: Simulated samples for other backgrounds used in the analysis.

Process	$\sigma \times \mathcal{B}$ [pb]
Single top	71.7
Drell-Yan ($10 \text{ GeV} < m_{\ell\ell} < 50 \text{ GeV}$)	20471.0
Drell-Yan ($m_{\ell\ell} > 50 \text{ GeV}$)	6025.26
$WZ \rightarrow 2\ell 2q$	5.5950
$ZZ \rightarrow 2\ell 2q$	3.2210
WWZ	0.1651
WZZ	0.05565
ZZZ	0.01398

and hadronization, as well as including a simulation of the underlying event (UE) and multiple interaction (MPI) based on the CUET8PM1 tune [103]. To estimate the systematic uncertainties related to the choice of UE and MPI tune, the signal processes and the WW events are also generated with two alternative tunes which are representative of the errors on the tuning parameters. The showering and hadronization systematic uncertainty is estimated by interfacing the same MC samples with the HERWIG ++ 2.7 parton shower [104, 105]. For all processes, the detector response is simulated using a detailed description of the CMS detector, based on the GEANT4 package [67].

The simulated samples are generated with distributions for the number of pileup interactions that are meant to roughly cover, though not exactly match, the conditions expected for the different data-taking periods. In order to factorize these effects, the number of true pileup interactions from the simulation truth is reweighted to match the data. The re-weighting is propagated automatically to both the in-time pile up and the out-of-time one. In Fig. 5.1, the effect of this reweighting on a sample enriched in Drell-Yan events is shown. Before the reweighting the simulation is presented in the open red histogram; after the reweighting, it is represented by the solid green histogram that matched well the data. In order to select this sample, events with two leptons with $p_T > 20 \text{ GeV}$, opposite sign, and same flavour, are selected only if $|m_{\ell\ell} - m_Z| < 15 \text{ GeV}$.

The average number of pileup is approximately 11.5.

Different sources and calculations are used to obtain the cross sections for the different processes at 13 TeV. For Higgs signal, the cross sections used are the ones reported by the LHC Higgs Cross Section Working Group [106], computed at NNLO and NNLL QCD and NLO EW for gluon fusion, and at NNLO QCD and NLO EW for the rest of the production modes. The branching fractions are the ones reported in Ref. [49].

The cross section used for normalizing $q\bar{q}$ produced WW processes was computed at next-to-next-to-leading order (NNLO) [97]. The leading-order (LO) cross section for $ggWW$ is obtained directly from MCFM. For gluon fusion, the difference between LO and NNLO cross sections is significantly big. A scale factor of 1.4 is theoretically calculated [107].

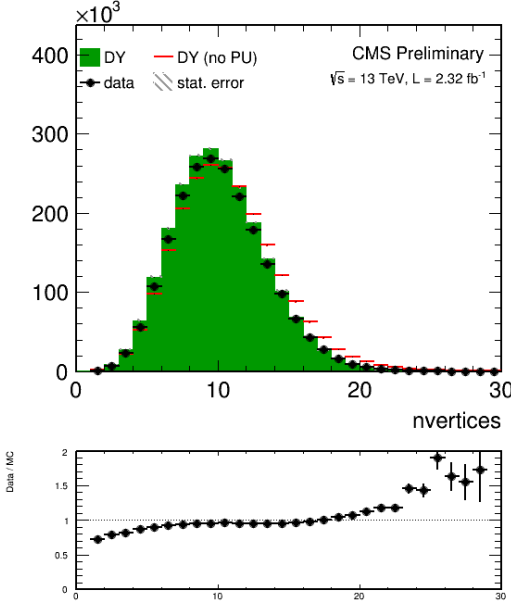


Figure 5.1.: Distributions of the number of vertices in a Drell-Yan enriched sample in data, together with the simulation before (red) and after (solid green) the pileup reweighting.

For the LO simulation of the interference between $gg \rightarrow WW$ and gluon fusion produced $H \rightarrow WW$ a k-factor of 1.87 is applied. This k-factor is obtained as the average between LO to NNLO ggH scale factor and LO to NLO ggWW scale factor.

The cross sections of the different single top processes are estimated by the LHC Top Working group [108] at NLO. The $t\bar{t}$ cross section is also provided by the LHC Top Working group [109], and it is computed at NNLO, with NNLL soft gluon resummation.

Drell-Yan (DY) production of Z/γ^* is generated using AMC@NLO [58]. Other multi-boson processes, such as WZ, ZZ , and VVV ($V=W/Z$), are generated with AMC@NLO and normalized to the cross section obtained at NLO in generation.

All processes are generated using the NNPDF2.3 [101, 102] parton distribution functions (PDF) for NLO generators, while the LO version of the same PDF is used for LO generators. All the event generators are interfaced to PYTHIA 8.1 for the showering of partons and hadronization, as well as including a simulation of the underlying event (UE) and multiple interaction (MPI) based on the CUET8PM1 tune [103].

2236 5.3. Analysis strategy

2237 5.3.1. Event reconstruction

2238 Regarding the electrons, muons, jets and E_T^{miss} definition and reconstruction, the standard
 2239 CMS recommendations described in Chapter 2 are used. The specific selections used in
 2240 this analysis are briefly summarised below.

2241 Muons are identified according to the CMS recommendations for the medium working
 2242 point, with the addition of some extra cuts, as defined by the following selections:

- 2243 • identified by the standard medium muon selection described in Sec. ??; Not yet defined
 2244 :)
- 2245 • $p_T > 10 \text{ GeV}$;
- 2246 • $|\eta| < 2.4$;
- 2247 • $|d_{xy}| < 0.01 \text{ cm}$ for $p_T < 20 \text{ GeV}$ and $|d_{xy}| < 0.02 \text{ cm}$ for $p_T > 20 \text{ GeV}$, d_{xy} being the
 2248 transverse impact parameter with respect to the primary vertex;
- 2249 • $|d_z| < 0.1 \text{ cm}$, where d_z is the longitudinal distance of the muon track in the tracker
 2250 extrapolated along the beam direction.

2251 For the muon isolation, the CMS recommended particle flow isolation based on the
 2252 tight working point is used, corresponding to a requirement on the isolation variable of
 2253 $ISO_{\text{tight}} < 0.15$. In addition a tracker relative isolation is also applied.

2254 For the electron identification, the tight working point is used. In addition some
 2255 additional cuts to make the selection “trigger-safe” are included. This is done because the
 2256 electron triggers already include some identification and isolation requirements that are
 2257 based on the raw detector information, while the offline selections make use of particle flow
 2258 requirements. The “trigger-safe” selections are defined to make the the offline identification
 2259 and isolation requirements tighter with respect to the online triggers.

2260 The simulated events are corrected for the lepton trigger, identification and isolation
 2261 efficiencies measured in data using the same techniques described in Sec. 4.3.1.

2262 Jets are defined clustering the particle flow objects using the anti- k_t algorithm with a
 2263 distance parameter of 0.4. The CHS pileup mitigation technique is used. The L1, L2, L3
 2264 and L2L3 jet energy correction described in Sec. ?? are applied. The reject jets coming from
 2265 calorimeter or readout electronics noise, the loose working point for PF jet identification is
 2266 used.

2267 The b-tagging algorithm for this analysis is chosen comparing the performances of
 2268 different algorithms using simulations for signal and background contributions in the phase
 2269 space defined by the analysis kinematic requirements. More precisely, two MC samples are
 2270 used, one corresponding the the $H \rightarrow WW \rightarrow 2\ell 2\nu$ signal produced via the ggH production
 2271 mode and another corresponding to the $t\bar{t}$ process. In fact, the first sample is enriched
 2272 in light jets, i.e. originating by the hadronization of light quarks like u,d,c and s quarks,
 2273 while the second sample is enriched in b jets, coming from the top quark decay. The b-veto
 2274 efficiency, ϵ_{bveto} , is computed separately for the two samples and for the various b tagging

algorithms. To compare the b tagging performance $\epsilon_{b\text{veto}}$ is computed for different working points, i.e. different selections on the specific b tagging discriminator, and the results are reported in the form of a ROC curve. The ROC curves corresponding to events with 0, 1 and ≥ 2 jets are shown in Fig. 5.2. Events considered for this study are the ones passing the WW baseline selection.

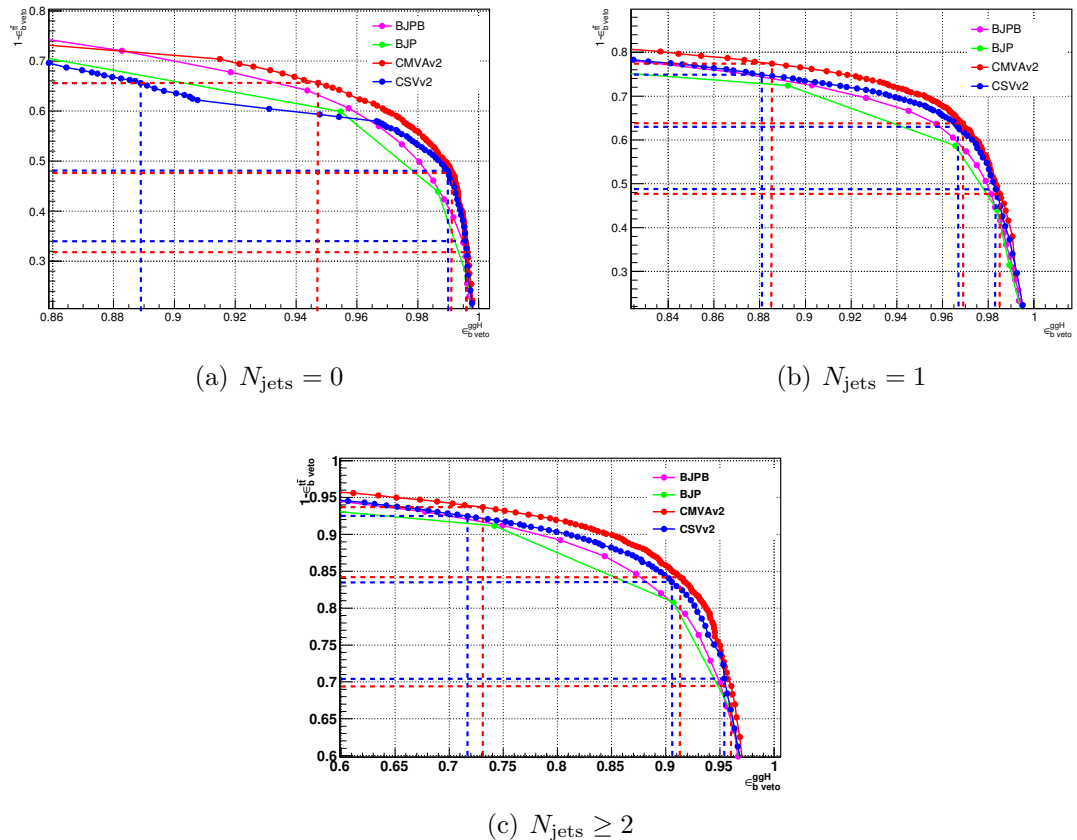


Figure 5.2.: ROC curve for the b veto efficiency on signal and background events. The blue and red lines point out the signal efficiency and the background rejection corresponding to the three working points considered for the CSVv2 and the cMVAv2 algorithms respectively.

The ROC curves show that the cMVAv2 algorithm has the best performance for the analysis phase space among the algorithms taken into account. For both the CSVv2 and cMVAv2 algorithms, three working points are defined corresponding to the mistag rates¹ of 10% for the loose, 1% for the medium and 0.1% for the tight working point. The distribution of the cMVAv2 discriminator associated to the leading jet both for the ggH and the t̄t MC sample is shown in figure 5.3.

¹The mistag rate is defined as the probability for a light jet to be identified as a b-jet by the b tagging algorithms.

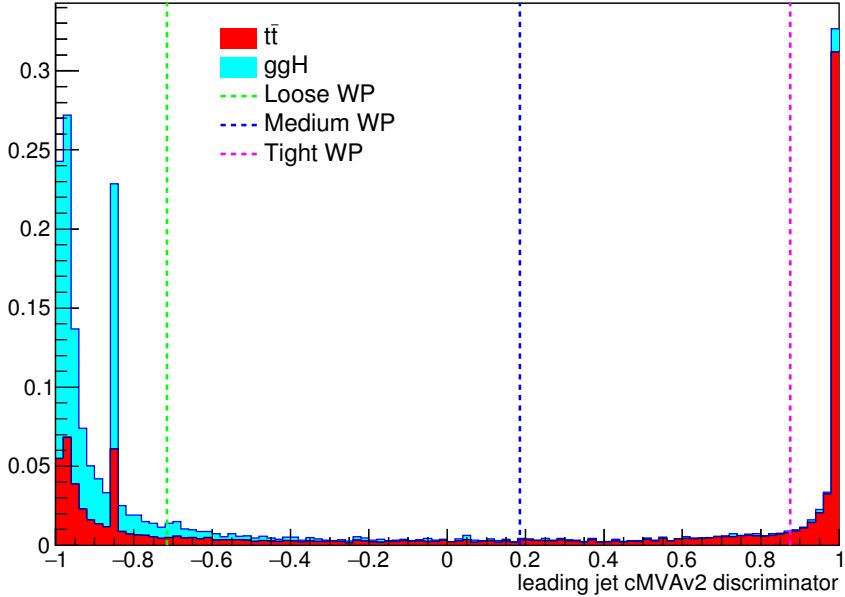


Figure 5.3.: cMVAv2 discriminator associated to the leading jet (with $p_T > 30$ GeV) both for the ggH and the $t\bar{t}$ processes. The two processes are normalized to unity and stacked. The vertical dashed lines show the discriminator value corresponding to the three working points.

2286 In order to determine the best working point for this analysis a preliminary significance
 2287 assessment is performed, using a complete analysis procedure in which only statistical
 2288 effects are taken into account (no systematics are included). The significance assessment
 2289 was performed using a two dimensional discriminating variable consisting of the dilepton
 2290 invariant mass versus the transverse mass. The assessment was performed with the following
 2291 leptonic selection:

- 2292 • two leptons, an electron and a muon with opposite charge, with leading lepton p_T
 2293 greater than 20 GeV and sub-leading lepton p_T greater than 13 GeV;
- 2294 • no other lepton (electron or muon) with p_T greater than 10 GeV;
- 2295 • $m_{\ell\ell}$ greater than 12 GeV;
- 2296 • PF type 1 corrected MET greater than 20 GeV;
- 2297 • $p_T^{\ell\ell}$ greater than 30 GeV.

2298 In addition to this global selection, two categories were identified:

- 2299 • 0 jets: no jets above 30 GeV, jets between 20 GeV and 30 GeV are b-vetoed with the
 2300 cMVAv2 WP under study;
- 2301 • 1 jet: exactly 1 jet above 30 GeV, no b-tagged jets above 30 GeV according to the
 2302 cMVAv2 WP under study.

Table 5.5.: Significance corresponding to the three working points and for different jet categories using a shape analysis.

Jet category	Loose WP (-0.715)	Medium WP (0.185)	Tight WP (0.875)
0 jets	2.022	2.043	2.036
1 jet	1.439	1.404	1.305
0 + 1 jets	2.481	2.479	2.420

2303 The two categories were eventually combined together and the significance assessment was
 2304 repeated for the three working points. With these selection we find the significance values
 2305 listed in Table 5.5 for the three working points.

2306 The working point providing the best significance in the combined 0 + 1 jets category is
 2307 found to be the loose one.

2308 To correct for a possible different b tagging efficiency in data and simulation, the
 2309 simulated events are reweighted using scale factors computed in bins of the jet η and p_T .
 2310 These scale factors and the corresponding uncertainties are centrally calculated for each
 2311 working point, in such a way to be employable by all the CMS analyses. The prescription
 2312 to reweight the simulated events is the following. First of all one has to compute the b
 2313 tagging efficiency using the MC samples, $\varepsilon_{\text{MC}}(p_T, \eta, f)$, for the chosen working point in bins
 2314 of jet p_T and η . The efficiency has to be computed for different flavours f of the jets, b,
 2315 c and light (u,d,s), using the jet matching information² which is available in all the MC
 2316 samples. An MC-based event weight is then calculated computing the probability P_{MC} of a
 2317 given b tagging configuration to occur, e.g.:

$$P_{\text{MC}} = \prod_{i \in \text{b-tagged-jets}} \varepsilon_{\text{MC}_i} \prod_{j \in \text{non-b-tagged-jets}} (1 - \varepsilon_{\text{MC}_j}) \quad (5.1)$$

2318 Afterwards, a similar probability is computed using data:

$$P_{\text{DATA}} = \prod_{i \in \text{b-tagged-jets}} SF_i \varepsilon_{\text{MC}_i} \prod_{j \in \text{non-b-tagged-jets}} (1 - SF_j \varepsilon_{\text{MC}_j}) , \quad (5.2)$$

2319 where SF_i is the provided scale factor value for the relevant jet flavour, p_T and η . Products
 2320 in Eqs. 5.1 and 5.2 run over all jets. The event weight is finally given by the ration
 2321 $P_{\text{DATA}}/P_{\text{MC}}$.

2322 The b tagging efficiencies to be fed into Eq. 5.1 and Eq. 5.2 are derived using $t\bar{t}$ simulated
 2323 events and applying basic leptonic selections. These efficiencies are shown in Fig. 5.4 for

²There are a couple of techniques developed by the CMS Collaboration to assess the flavour of a reconstructed jet in simulation. The technique used here makes use of the flavour of the hadrons clustered into a jet.

light (a), c-jets (b) and b-jets (c), in bins of η and p_T . The uncertainties associated to the efficiencies are representative of the statistics of the simulated $t\bar{t}$ sample, and are computed according to a binomial distribution.

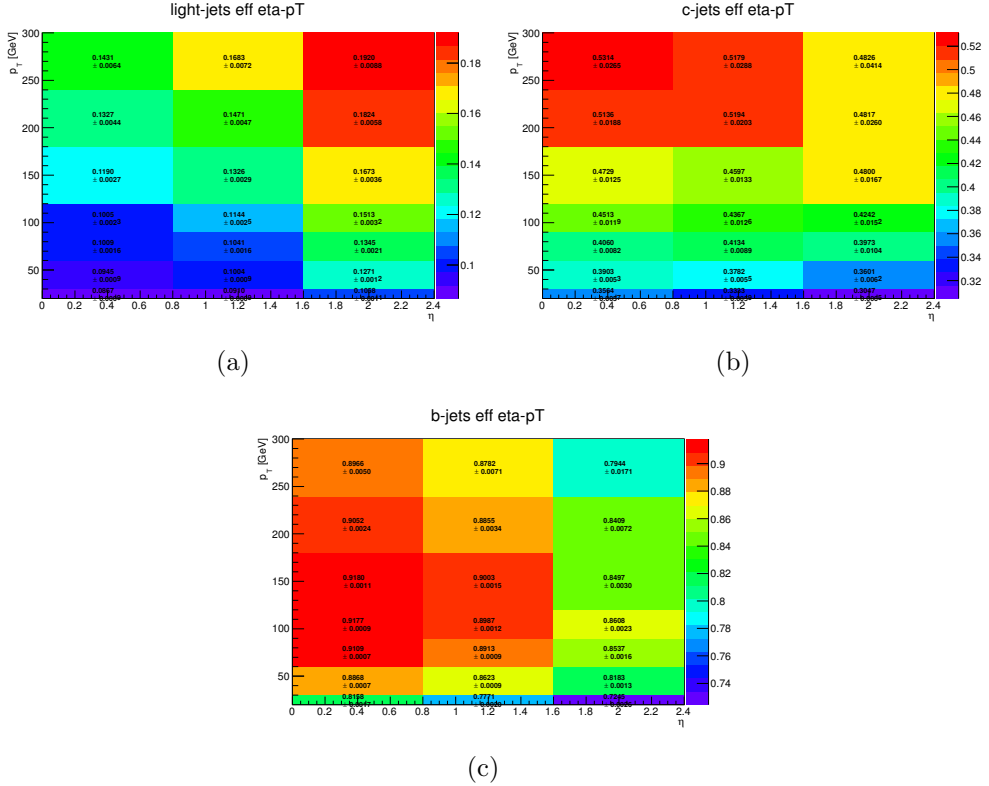


Figure 5.4.: B tagging efficiencies for light jets (a), c-jets (b) and b jets (c), as a function of η and p_T .

The effect of the event reweighting is to correct the shape of the b tagging discriminator in simulation, moving events from the b tag region (discriminator greater than > -0.715) to the b veto region (discriminator < -0.715) and viceversa. A data/simulation comparison of the b tagging discriminator for the leading and subleading jets is performed to check the agreement after the application of the event weights. In order to evaluate the data/simulation agreement for b-jets, the data and simulation are compared in a top enriched control region, defined by the following requirements:

- two leptons, an electron and a muon with opposite charge, with leading lepton p_T greater than 20 GeV and sub-leading lepton p_T greater than 15 GeV;
- no other lepton (electron or muon) with p_T greater than 10 GeV;
- lepton invariant mass greater than 50 GeV;
- at least two jets with p_T greater than 30 GeV;

- 2339 • at least one of the two leading jets with cMVAv2 btagging score greater than -0.715
 2340 (i.e. the loose working point).

2341 In order to evaluate the agreement for light jets, a second control region is defined, populated
 2342 by Z+light jet events, defined as follows:

- 2343 • two leptons, two electrons or two muons with opposite charge, with leading lepton p_T
 2344 greater than 20 GeV and sub-leading lepton p_T greater than 15 GeV.
 2345 • no other lepton (electron or muon) with p_T greater than 10 GeV.
 2346 • lepton invariant mass greater between 80 GeV and 110 GeV.
 2347 • at least two jets with p_T greater than 30 GeV.
 2348 • at least one jet above 30 GeV.
 2349 • no jets above 20 GeV with a TCHE score above 2.1.

2350 Although a Z+jets sample is dominated by light flavor jets, a b-veto on an alternative
 2351 algorithm (TCHE) is applied to reduce the contamination from b-jets, especially above the
 2352 cMVAv2 cut. This helps mitigating possible data/simulation discrepancies in the modeling
 2353 of the heavy/light flavour ratio. The comparison between data and simulation after the
 2354 event reweighting is shown in Figs. 5.5 and 5.6 for the b-jets and light jets enriched control
 2355 regions, respectively.

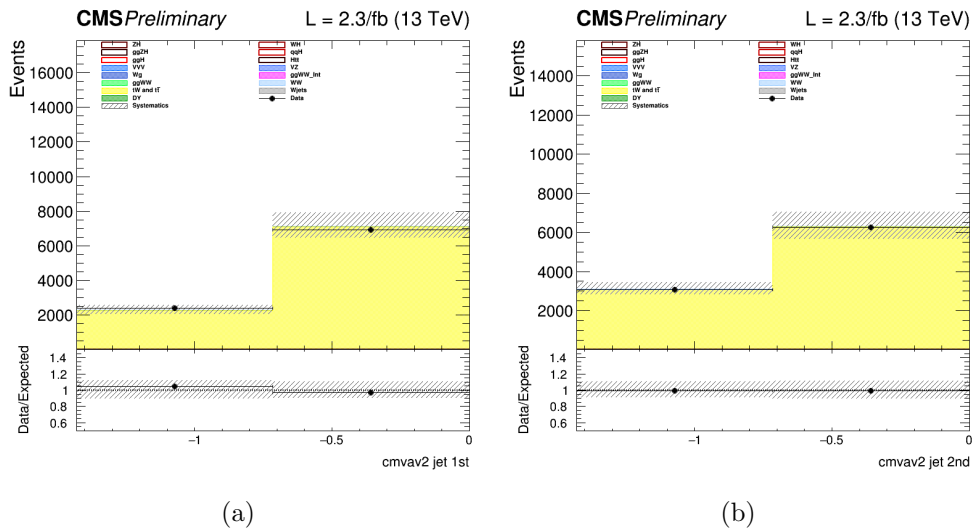


Figure 5.5.: B tagging cMVAv2 discriminator for the leading (a) and the subleading (b) jet in the b-jets enriched control region.

2356 5.3.2. Event selection and background rejection

2357 Since the ggH production mechanism, which is the main production mode for a Higgs
 2358 mass of around 125 GeV, is characterized by the emission of few jets arising from initial

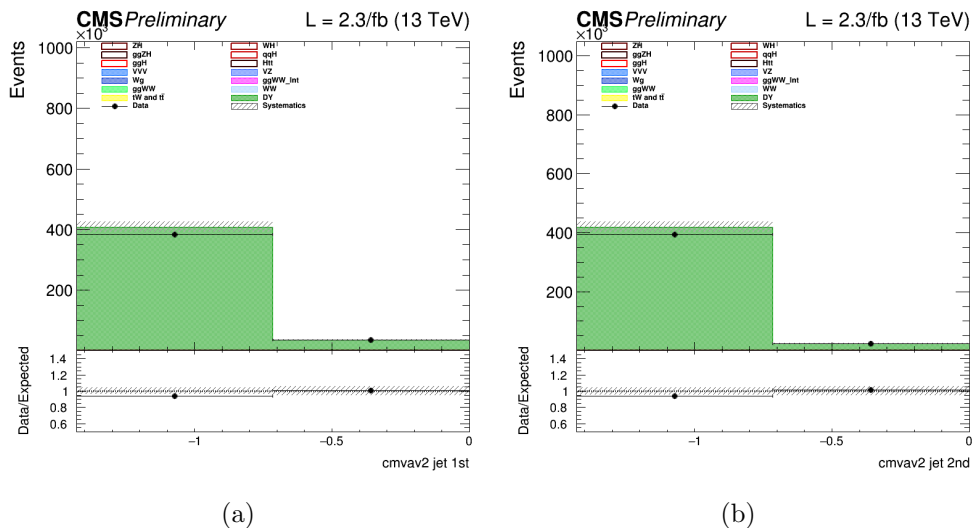


Figure 5.6.: B tagging cMVAv2 discriminator for the leading (a) and the subleading (b) jet in the light jets enriched control region.

2359 or final state radiation, this analysis is limited to events with no jets or one jet. Due to
 2360 the large DY background in di-electrons and di-muons events, only the $e\mu$ final state is
 2361 studied in this early Run 2 data analysis, including the indirect contribution from τ leptons
 2362 decaying to electron or muons. Exactly one electron and one muon are required to be
 2363 reconstructed in the event with opposite charges and a minimum p_T of 10 (13) GeV for
 2364 the muon (electron). One of the two leptons should also have a p_T greater than 20 GeV
 2365 and both leptons are required to be well identified and isolated to reject fake leptons and
 2366 leptons coming from QCD sources. To suppress background processes with three or more
 2367 leptons in the final state, such as ZZ, WZ, Z γ , W γ , or tri-boson production, no additional
 2368 identified and isolated lepton with $p_T > 10$ GeV should be reconstructed. The low $m_{\ell\ell}$
 2369 region dominated by QCD production of leptons is not considered in the analysis and
 2370 $m_{\ell\ell}$ is requested to be higher than 12 GeV. To suppress the background arising from DY
 2371 events decaying to a τ lepton pair which subsequently decays to an $e\mu$ final state and
 2372 suppress processes without genuine E_T^{miss} , a minimal E_T^{miss} of 20 GeV is required. The DY
 2373 background is further reduced by requesting $p_T^{\ell\ell} > 30$ GeV. Finally the contribution from
 2374 leptonic decays of single top and t \bar{t} production is reduced by requesting that no jets with
 2375 $p_T > 20$ GeV are identified by the b tagging algorithm as originating from a b quark in the
 2376 event.

The requirements described above define the WW baseline selection. After those requirements the data sample is dominated by events arising from the non-resonant WW production and $t\bar{t}$ production. To further reduce the effect of these backgrounds on the signal sensitivity, the events are categorized depending on the jet multiplicity, counting jets with $p_T > 30 \text{ GeV}$. Events with zero associated jets mainly arise from the WW production, while WW and $t\bar{t}$ productions have a similar contribution in the category with one jet.

2383 Higher jet multiplicity categories, which are sensitive to other Higgs production mechanisms,
2384 such as VBF, are not included in this analysis, given the very low expected yield for other
2385 production modes with the analysed integrated luminosity.

2386 Distributions of some variables of interest for the 0 and 1 jet categories separately,
2387 but merging the $e\mu$ and μe final states together, are shown in Figs. 5.7, 5.8 and 5.9 after
2388 applying the WW baseline selections, with the addition of a cut on $m_{\ell\ell}$ to remove the Higgs
2389 signal contribution ($m_{\ell\ell} > 80$ GeV), and a cut on m_T to be orthogonal to the $Z\gamma^* \rightarrow \tau\tau$
2390 background control region ($m_T > 60$ GeV).

2391 The $W+jets$ background, where one jet can be misidentified as a lepton, is a sub-
2392 dominant background in the phase space defined by the analysis kinematic requirements.
2393 The 0 ad 1 jets categories are further split according to the lepton flavour to $e\mu$ and μe ,
2394 where the first lepton refers to the leading one. In this way an improvement of about 10% in
2395 terms of the signal significance can be achieved, exploiting the different $W+jets$ background
2396 contribution in the two categories. Indeed the probability for a jet to be misidentified as an
2397 electron or a muon is not the same.

2398 5.3.3. Signal extraction

2399 To extract the Higgs boson signal contribution in the four previously mentioned categories,
2400 a similar approach to the one used in the Run 1 analysis [50] is pursued. The analysis is
2401 based on two-dimensional templates of $m_{\ell\ell}$ versus m_T to discriminate signal and background
2402 contributions. The $m_{\ell\ell}$ template is defined using 5 bins from $m_{\ell\ell} = 10$ GeV up to $m_{\ell\ell} =$
2403 110 GeV, while for the m_T template 7 bins are defined in the range 60 GeV $< m_T < 200$ GeV.
2404 The phase space with $m_T < 60$ GeV is used as an orthogonal control region to extract the
2405 normalization of the DY background. A binned maximum likelihood fit to the signal and
2406 background two-dimensional templates is performed to extract the signal strength in the
2407 four categories.

2408 Distributions of the $m_{\ell\ell}$ and m_T variables after the WW level selection are shown in
2409 Fig. 5.10 for the 0 and 1 jet categories separately, but merging the $e\mu$ and μe final states
2410 together.

2411 The statistical methodology used to interpret the data and to combine the results from
2412 the independent 0-jet and 1-jet categories in the $e\mu$ and μe final states has been developed
2413 by the ATLAS and CMS collaborations in the context of the LHC Higgs Combination
2414 Group [92, 110]. The number of events in each category and in each bin of two-dimensional
2415 template is modelled as a Poisson random variable, with a mean value given by the sum
2416 of the contributions from all the processes under consideration. Systematic uncertainties
2417 are represented by individual nuisance parameters with log-normal distributions. The
2418 uncertainties affect the overall normalization of the signal and backgrounds as well as the
2419 shape of the predictions across the distribution of the observables. Correlation between
2420 systematic uncertainties in different categories are taken into account.

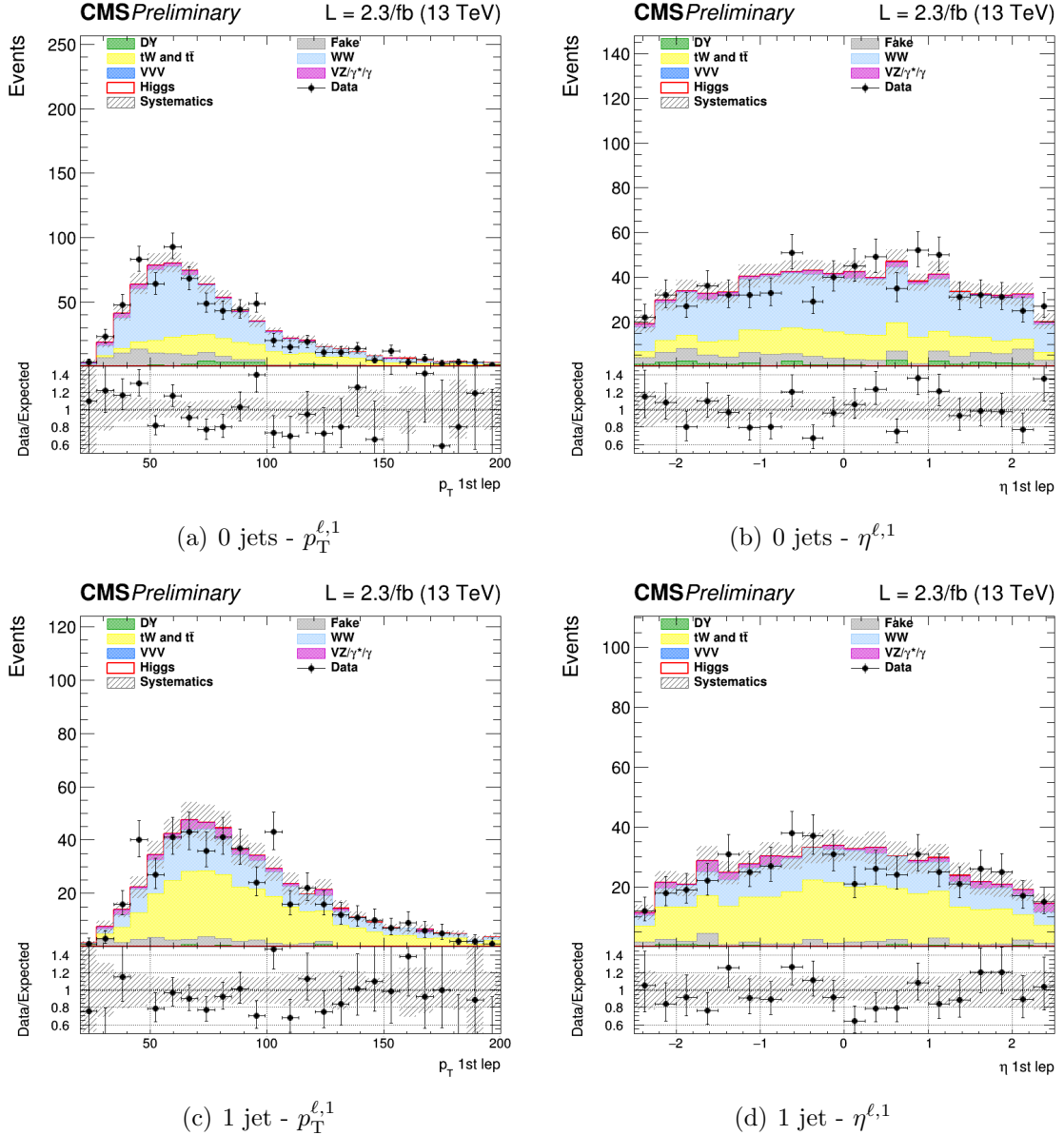


Figure 5.7.: Distributions of p_T (left) and η (right) of the leading lepton for events with 0 jet (upper row) and 1 jet (lower row), for the main backgrounds (stacked histograms), and for a SM Higgs boson signal with $m_H = 125$ GeV (superimposed and stacked red histogram) at the WW selection level. The last bin of the histograms includes overflows. The simulation of the WW background is normalized to data.

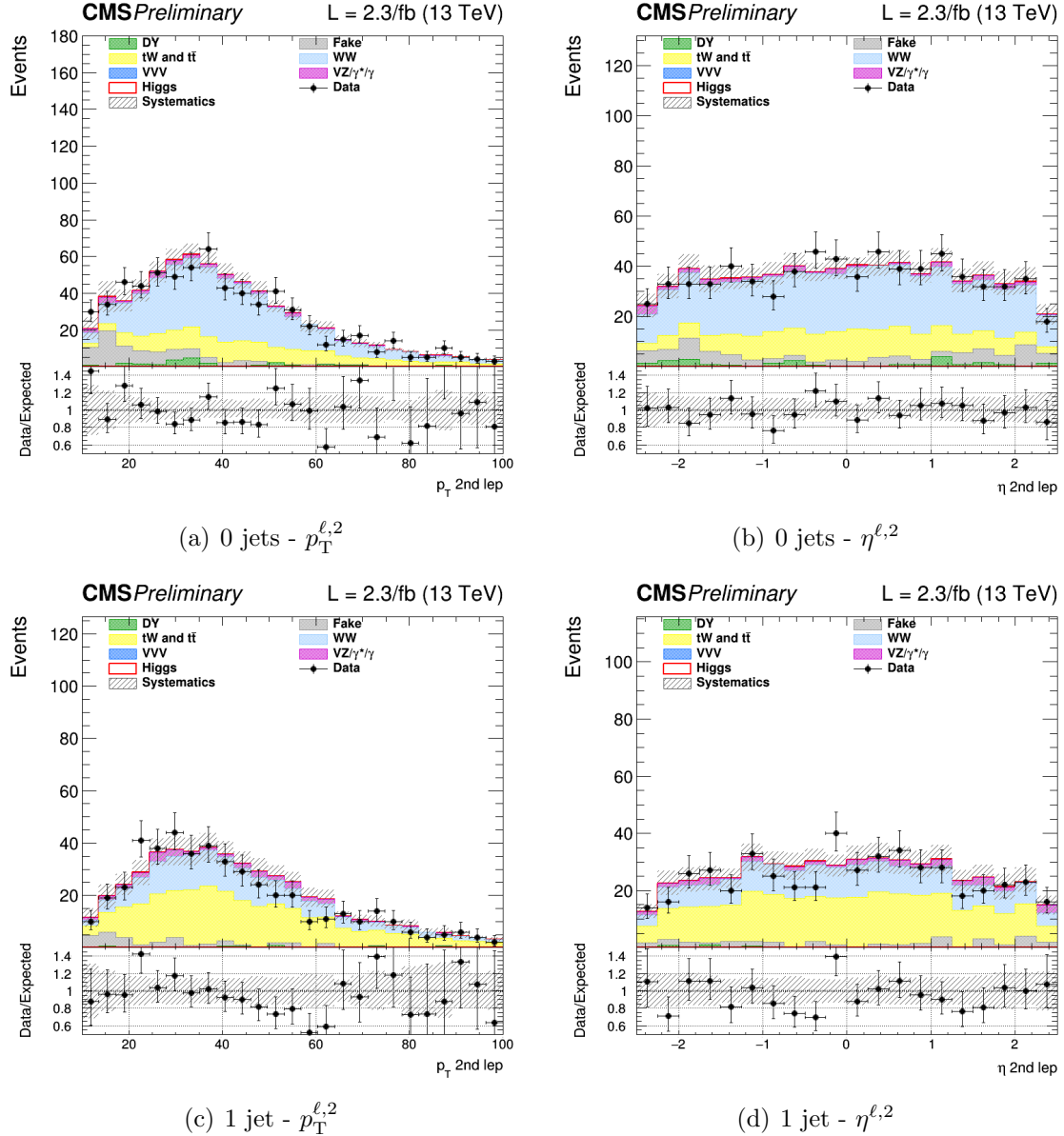


Figure 5.8.: Distributions of p_T (left) and η (right) of the subleading lepton for events with 0 jets (upper row) and 1 jet (lower row), for the main backgrounds (stacked histograms), and for a SM Higgs boson signal with $m_H = 125$ GeV (superimposed and stacked red histogram) at the WW selection level. The last bin of the histograms includes overflows. The simulation of the WW background is normalized to data.

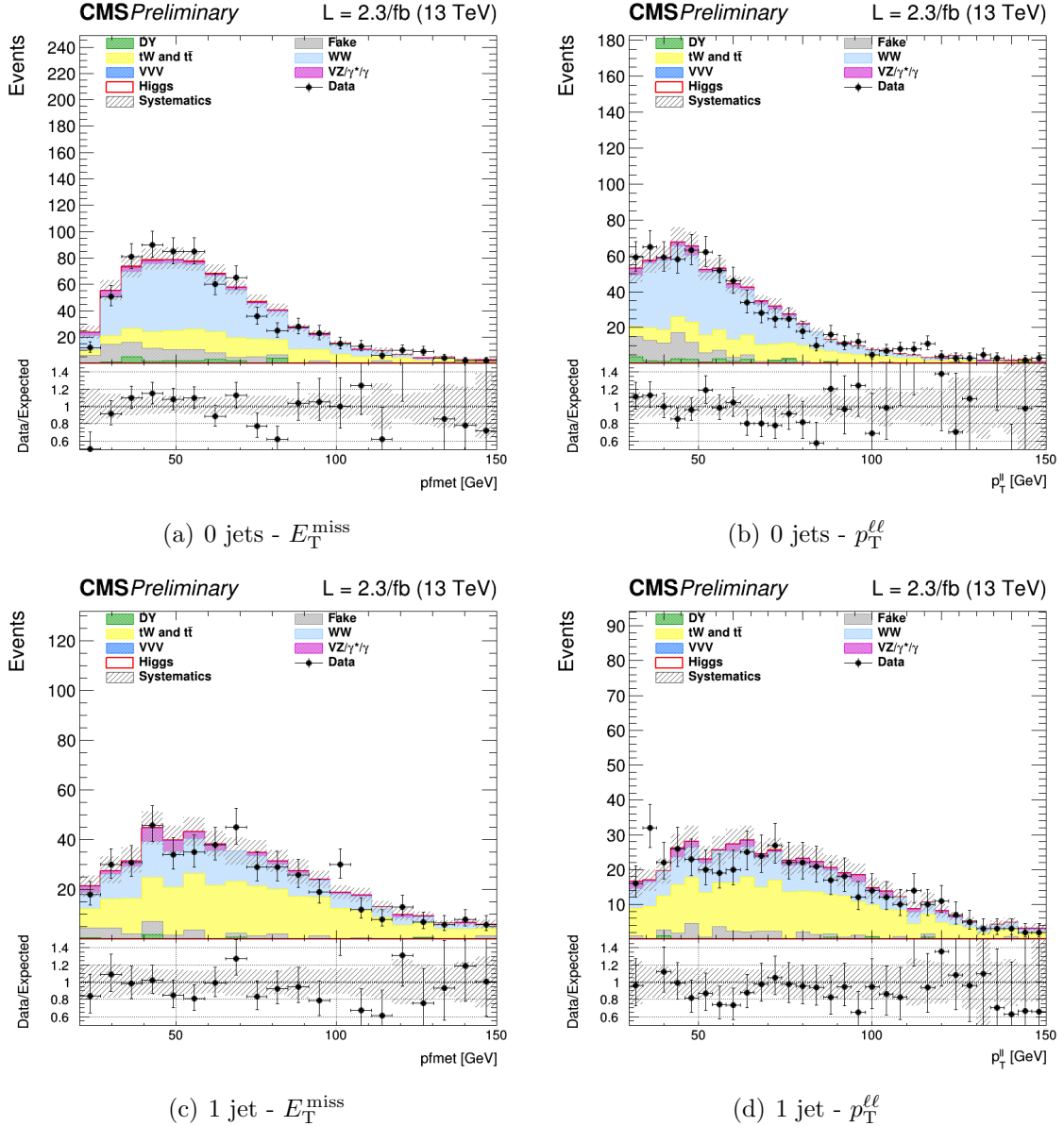


Figure 5.9.: Distributions of E_T^{miss} (left) and $p_T^{\ell\ell}$ (right) for events with 0 jets (upper row) and 1 jet (lower row), for the main backgrounds (stacked histograms), and for a SM Higgs boson signal with $m_H = 125 \text{ GeV}$ (superimposed and stacked red histogram) at the WW selection level. The last bin of the histograms includes overflows. The simulation of the WW background is normalized to data.

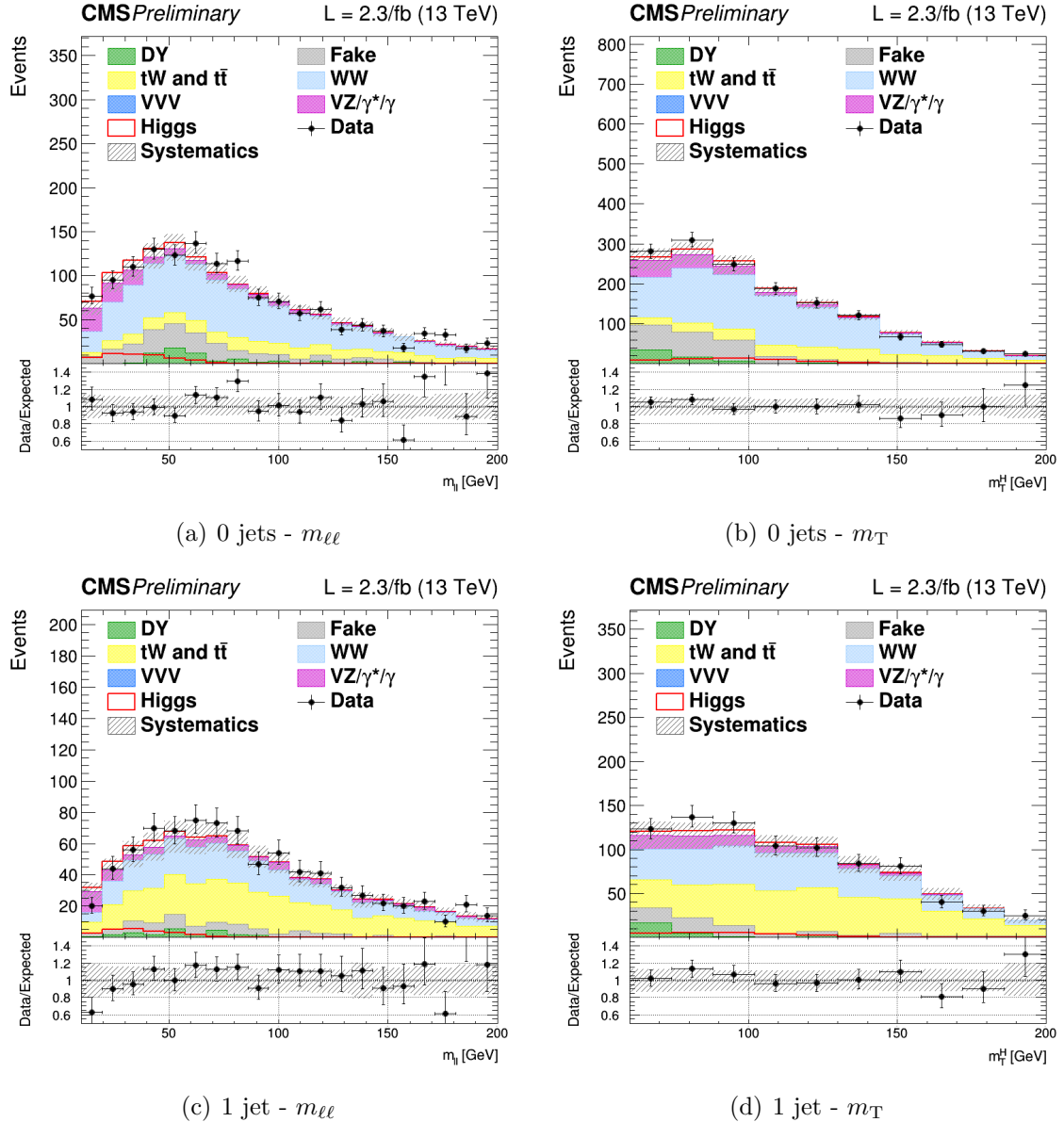


Figure 5.10.: Distributions of $m_{\ell\ell}$ (left) and m_T (right) for events with 0 jets (upper row) and 1 jet (lower row), for the main backgrounds (stacked histograms), and for a SM Higgs boson signal with $m_H = 125$ GeV (superimposed and stacked red histogram) at the WW selection level. The last bin of the histograms includes overflows. The simulation of the WW background is normalized to data.

2421 5.4. Background estimation

2422 The main background processes affecting the analysis signature, non-resonant WW pro-
 2423 duction and top quark processes, are estimated using data. Backgrounds arising from an
 2424 experimental misidentification of the objects, such as W+jets (also called “Fake”), are
 2425 estimated using data as well. The other minor backgrounds are generally estimated directly
 2426 from simulation as described in the following subsections.

2427 5.4.1. WW background

2428 The quark-induced WW background is simulated with NLO accuracy in perturbative
 2429 QCD, and the transverse momentum of the diboson system is reweighted to match the
 2430 NNLO+NNLL accuracy from theoretical calculations [98, 99]. However, given the large
 2431 uncertainties on the jet multiplicity distribution associated to this process, the normalization
 2432 of this background is measured from data separately for the 0 and 1 jet categories. The
 2433 normalization k-factors are extracted directly from the fit together with the signal strengths,
 2434 leaving the WW normalization free to float separately in the two jet multiplicity categories.
 2435 An orthogonal control region for the WW background normalization estimation is not
 2436 needed in this case, owing to the different $m_{\ell\ell}$ - m_T shape for signal and background.

2437 The gluon-induced WW production is sub-dominant with respect to the quark-induced
 2438 production, and its shape and normalization is fully taken from simulation, scaling the
 2439 cross section to the theoretical prediction with NLO accuracy [107].

2440 5.4.2. Top quark background

2441 As explained in Sec. 5.3, the production of top quark pairs represents one of the dominant
 2442 backgrounds in this analysis given its large cross section and a similar final state compared
 2443 to the signal. A b-jet veto, based on the *cMVAv2* b tagging algorithm, is used to suppress
 2444 this background and a reweighting procedure is applied on top of the simulated events to
 2445 correct for different b tagging efficiency in data and simulation.

2446 The top quark background normalization is measured using data, defining a b-jets
 2447 enriched control region by inverting the b-jet veto. More precisely, the b-jets enriched
 2448 control region for the 0-jet category is defined with the same WW baseline selection but
 2449 requiring at least one jet with $20 < p_T < 30$ GeV to be identified as a b jet and no other
 2450 jets with $p_T > 30$ GeV. For the 1-jet category, the b-jets enriched region is defined requiring
 2451 exactly one jet with $p_T > 30$ GeV identified as a b-jet. To reduce other backgrounds in
 2452 these two regions, the dilepton mass has to be greater than 50 GeV. Distributions of the
 2453 $m_{\ell\ell}$ and m_T variables in the b-jets enriched control regions after applying the data driven
 2454 estimation are shown in Figure 6.5, for the 0 and 1 jet categories separately.

2455 The top quark background normalization is constrained during the fit procedure sepa-
 2456 rately in the two jet categories, by means of the control regions defined above, which are
 2457 treated in the fit as two additional categories.

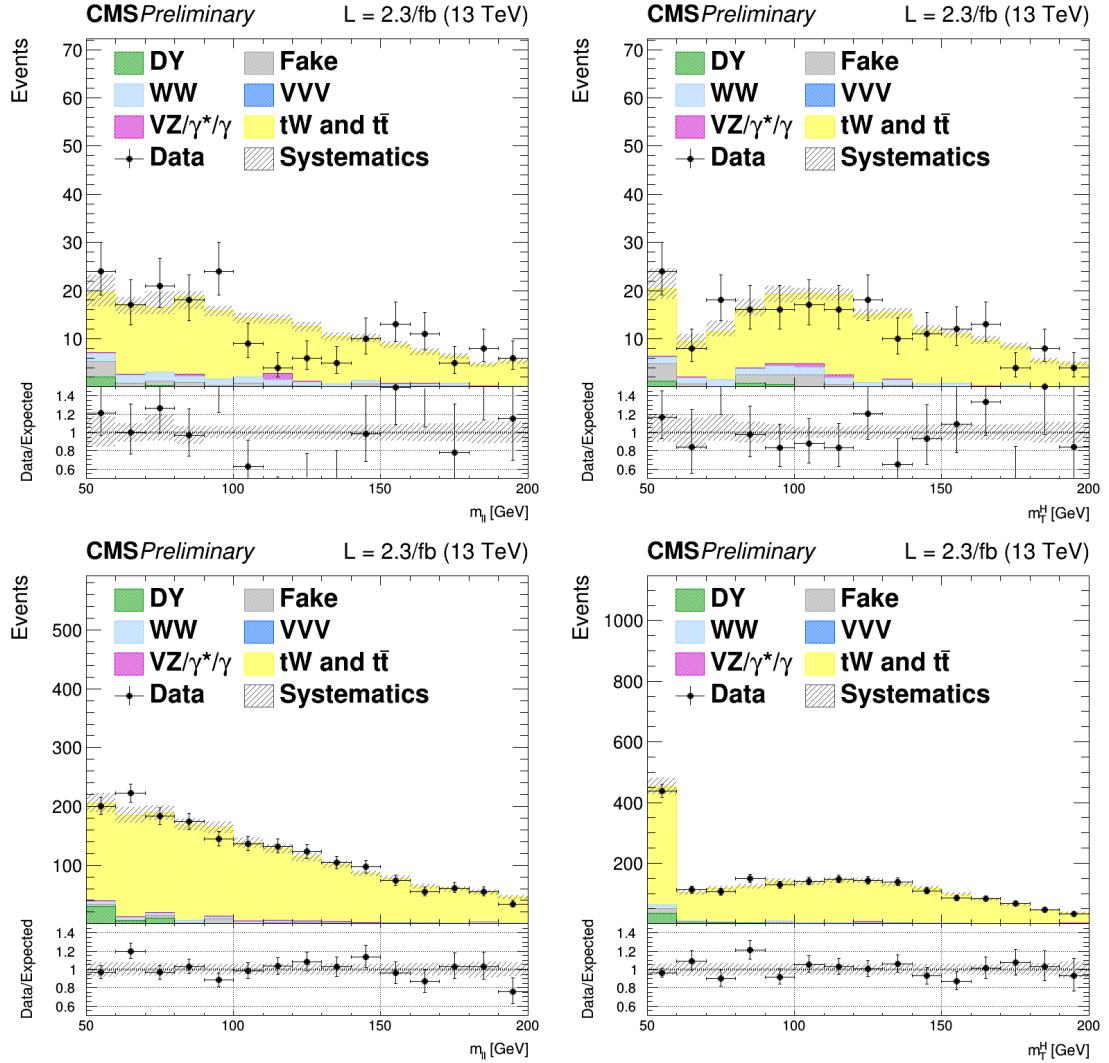


Figure 5.11.: Distributions of $m_{\ell\ell}$ (left) and m_T (right) for events with 0 jet (top) and 1 jet (bottom) in top enriched phase space. Scale factors estimated from data are applied. The first (last) bin includes underflows (overflows).

2458 5.4.3. Jet-induced (or Fake) background

2459 One of the primary source belonging to this category arises from the misidentification of
 2460 leptons in $W+jets$ processes in the 0 jet category. Also, semileptonic $t\bar{t}$ decays contribute
 2461 especially for higher jet multiplicities. Multijet production and hadronic $t\bar{t}$ decays are also
 2462 taken into account, but have a much smaller contribution.

2463 This background is fully estimated using data, with the technique described in Sec. 4.4.3.
 2464 To check the agreement of the background estimated in this way with data, a control sample
 2465 enriched in jet-induced events is defined. The events in the control sample are selected
 2466 applying the WW baseline requirements but requesting an $e\mu$ pair with same charge, which
 2467 significantly suppresses the WW and $t\bar{t}$ processes. The $m_{\ell\ell}$ distributions in this control
 2468 region for the 0 and 1 jet categories are shown in Fig. 5.12. From the crosscheck in this
 2469 control region, a global normalization factor of 0.8 is derived and applied to the jet-induced
 2470 background.

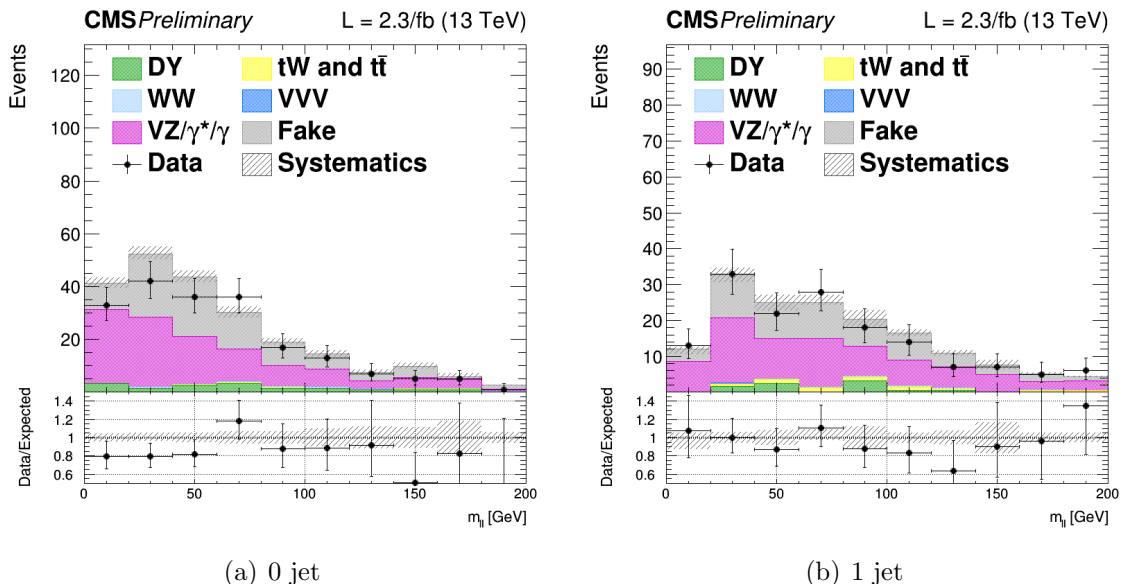


Figure 5.12.: Control plots for $m_{\ell\ell}$ in a fakes enriched phase space for events with 0 and 1 jet with $p_T > 30$ GeV, in $e\mu$ final state. Fake contribution has been scaled by 0.8 to match data.

2471 5.4.4. DY background

2472 This background contributes to the analysis phase space because of the Z/γ^* decays to a
 2473 pair of τ leptons, which consequently decays to an $e\mu$ pair. This background process is
 2474 predominant in the low m_T region, which is used as an orthogonal control region to determine
 2475 the background normalization in the 0 and 1 jet categories separately. In particular this
 2476 control region is defined by selecting events with $m_T < 60$ GeV and 30 GeV $< m_{\ell\ell} < 80$ GeV.

2477 The $m_{\ell\ell}$ distributions in these control regions for the 0 and 1 jet categories are shown in
 2478 Fig. 5.13.

2479 As for the top quark background, the normalization of this background in the 0 and 1
 2480 jet categories, is constrained directly in the fit by means of the control regions, which are
 2481 treated as two additional categories.

2482 The kinematics of this background is taken from simulation, after reweighting the Z
 2483 boson p_T spectrum to match the observed distribution measured in data. In fact, this
 2484 variable is not well reproduced by the MC generator used for simulating this process,
 2485 especially in the bulk of the distribution, the discrepancy being ascribed to the missing
 2486 contribution from resummed calculations.

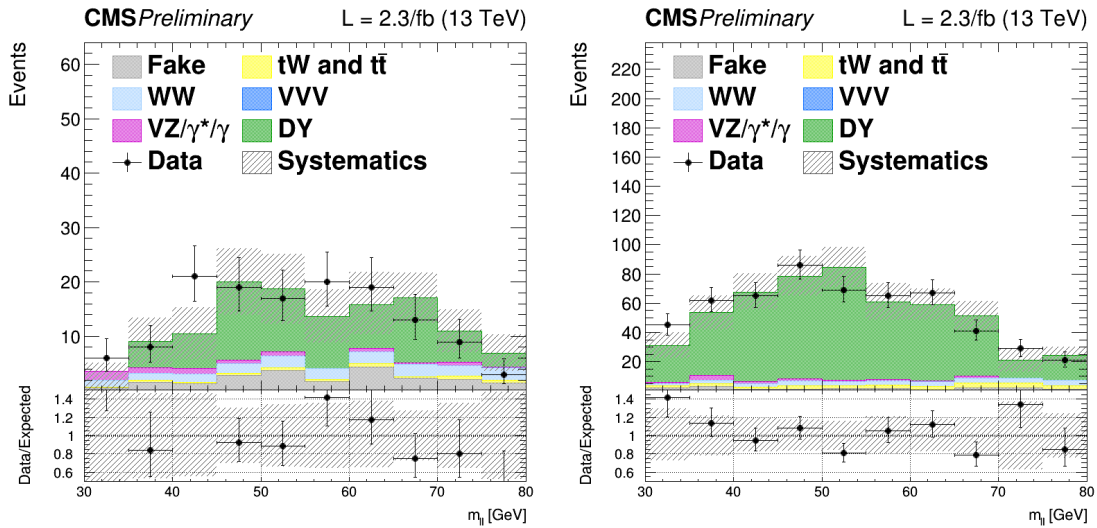


Figure 5.13.: Distributions of $m_{\ell\ell}$ for events with 0 jet (left) and 1 jet (right) in the $DY \rightarrow \tau\tau$ enriched control region. Scale factors estimated from data are applied.

2487 5.4.5. Other backgrounds

2488 The $W\gamma^*$ and the WZ electroweak processes can be gathered in the same physical process,
 2489 although the final state kinematics is rather different. In particular, the invariant mass of
 2490 the leptons arising from the γ^* decays is generally below 4 GeV, while the leptons from the
 2491 Z boson decay are characterized by a larger invariant mass. Another background which can
 2492 be experimentally identical to those is the $W\gamma$ production, where a real photon is produced
 2493 in association with a W boson and consequently undergoes a photon conversion to leptons
 2494 due to the interaction with the material constituting the first layers of the silicon tracker.

2495 All these backgrounds may contribute to the signal phase space whenever one of the three
 2496 leptons escape from the detector acceptance or is not identified. The shape and cross section
 2497 of these backgrounds are taken from simulation. The only exception is the normalization of
 2498 the $W\gamma^*$ background, being this process dominant in the low $m_{\ell\ell}$ region, which is scaled

2499 to data defining a proper control region. The control region is defined selecting events
 2500 with three isolated muons, with $p_T > 10,5$ and 3 GeV for the first three leading muons
 2501 respectively. The selection is further defined by $E_T^{\text{miss}} < 25\text{ GeV}$ and E_T^{miss} projected to the
 2502 leading muon $< 45\text{ GeV}$. The pair of muons with the smallest invariant mass is taken as
 2503 coming from the γ^* decay. The k-factor measured in data for this background to be applied
 2504 in the simulation is 1.98 ± 0.54 .

2505 All remaining backgrounds from di-boson and tri-boson production, which are of mi-
 2506 nor importance in the analysis phase space, are normalized according to their expected
 2507 theoretical cross sections.

2508 5.5. Systematic uncertainties

2509 The systematic uncertainties affecting this measurement can be divided into three categories:
 2510 the uncertainties on the background estimation, experimental uncertainties and theoretical
 2511 uncertainties.

2512 The first category includes the uncertainties related to the background normalization
 2513 and shape. For the non-resonant WW production the shape is taken from simulation.
 2514 The input normalization to the fit is set to the expected value from simulation, and an
 2515 unconstrained nuisance parameter with a flat distribution is associated to this number.
 2516 This is done separately for the two jet categories.

2517 The top quark background shape is taken from simulation after correcting for the b
 2518 tagging scale factors. An uncertainty due to these scale factors is included and affects
 2519 both the normalization and the shape of the top quark background. The uncertainties on
 2520 the normalization are treated similarly to the WW background case, but constraining the
 2521 corresponding nuisances by means of the two control regions orthogonal to the signal phase
 2522 space. A similar procedure is used for the DY background.

2523 Effects due to experimental uncertainties are studied by applying a scaling and smearing
 2524 of certain variables related to the physics objects, e.g. the p_T of the leptons, followed by
 2525 a subsequent recalculation of all the correlated variables. This is done for simulation, to
 2526 account for possible systematic mismodeling.

2527 All experimental sources, except luminosity, are treated both as normalization and shape
 2528 uncertainties, and are correlated among the signal and background processes and all the
 2529 categories. The following experimental uncertainties are considered:

- 2530 • the uncertainty determined by the CMS online luminosity monitoring, 2.7% for the
 2531 first data collected at $\sqrt{s} = 13\text{ TeV}$;
- 2532 • the acceptance uncertainty associated with the combination of single and double lepton
 2533 triggers, which is 2%;
- 2534 • the lepton reconstruction and identification efficiencies uncertainties, that are in the
 2535 range 0.5-5% for electrons and 1-7% for muons depending on p_T and η ;
- 2536 • the muon momentum and electron energy scale and resolution uncertainties, that
 2537 amount to 0.01-0.5% for electrons and 0.5-1.5% for muons depending on p_T and η ;

- 2538 • the jet energy scale uncertainties, that vary between 1-11% depending on the p_T and
2539 η of the jet;
- 2540 • the E_T^{miss} resolution uncertainty, that is taken into account by propagating the corre-
2541 sponding uncertainties on the leptons and jets;
- 2542 • the scale factors correcting the b tagging efficiency and mistagging rate, that are varied
2543 within their uncertainties. This systematic uncertainty is anticorrelated between the
2544 top control regions and the other ones.

2545 The uncertainties in the signal and background production rates due to theoretical
2546 uncertainties include several components, which are assumed to be independent: the PDFs
2547 and α_s , the underlying event and parton shower model, and the effect of missing higher-order
2548 corrections via variations of the renormalization and factorization scales.

2549 The effects of the variation of PDFs, α_s and renormalization/factorization QCD scales,
2550 mainly affect the signal processes, being the most important backgrounds estimated using
2551 data driven techniques. However, the uncertainties on minor backgrounds that are estimated
2552 from simulation are taken into account. These uncertainties are split in the uncertainties
2553 on the cross section, which are computed by the LHC cross section working group [111],
2554 and on the selection efficiency [112]. The PDFs and α_s signal cross section normalization
2555 uncertainties are $^{+7.4\%}_{-7.9\%}$ and $^{+7.1\%}_{-6.0\%}$ for ggH and $\pm 0.7\%$ and $\pm 3.2\%$ for VBF Higgs production
2556 mechanism. The PDFs and α_s acceptance uncertainties are less than 1% for gluon- and
2557 quark-induced processes. The effect of the QCD scales variation on the selection efficiency is
2558 around 1-3% depending on the specific process. To estimate these uncertainties, the events
2559 are reweighted according to different QCD scales or different PDF sets and the selection
2560 efficiency is recomputed each time. For the QCD scale uncertainty the maximum variation
2561 with respect to the nominal value is taken as the uncertainty. For the case of PDF and α_s
2562 uncertainties, the distribution of the selection efficiency is built taking into account all the
2563 replicas in the NNPDF3.0 set and the uncertainty is estimated as the standard deviation of
2564 that distribution.

2565 In addition, the categorization of events based on jet multiplicity introduces additional un-
2566 certainties on the ggH production mode related to missing higher order corrections. These un-
2567 certainties are evaluated following the prescription described in Sec. [subsec:stewart-tackman]
2568] and correspond to 5.6% for the 0-jet and 13% for the 1-jet bin categories.

2569 The underlying event uncertainty is estimated by comparing two different PYTHIA
2570 8 tunes, while parton shower modelling uncertainty is estimated by comparing samples
2571 interfaced with the PYTHIA 8 and HERWIG++ parton shower programs. The effect on the
2572 ggH (VBF) signal expected yield is about 5% (5%) for the PYTHIA 8 tune variation and
2573 about 7% (10%) for the parton shower description.

2574 Other specific theoretical uncertainties are associated to some backgrounds. An uncer-
2575 tainty on the ratio of the $t\bar{t}$ and tW cross sections is included. Indeed, these two processes
2576 are characterized by a different number of b-jets in the final state (2 b-jets for $t\bar{t}$ and 1
2577 for tW) and the b-veto acts differently for the two. A variation of the relative ratio of the
2578 cross sections can thus cause a migration of events from the 0 to the 1 jet categories and

viceversa. The corresponding uncertainty is of 8%, according to the theoretical cross section calculations [108, 109].

The $gg \rightarrow WW$ background LO cross section predicted by the MCFM generator is scaled to the NLO calculation, applying a k-factor of 1.4 with an uncertainty of 15% [107]. The interference term between the $gg \rightarrow WW$ and the ggH signal is also included and simulated with LO accuracy using MCFM. The k-factor to scale the interference term is 1.87, given by the geometrical average of the LO to NNLO $gg \rightarrow H \rightarrow WW$ scale factor (2.5) and the LO to NLO $gg \rightarrow WW$ scale factor (1.4). The uncertainty on this value is estimated as the maximum variation with respect to the two scale factors mentioned above, and is found to be of 25%. Anyway, with the current amount of integrated luminosity, the interference contribution is found to be negligible.

For what the $qq \rightarrow WW$ background shape is concerned, an uncertainty related to the diboson p_T reweighting is evaluated varying the renormalization, factorization and resummation QCD scales.

Finally, the uncertainties due to the limited statistical accuracy of the MC simulations are also taken into account, including an independent uncertainty for each bin of the two-dimensional distribution, and for each category. The uncertainty for a certain bin and process is given by the standard deviation of the Poisson distribution with mean corresponding to the number of MC events in that bin.

5.6. Results

The expected and observed signal significance are shown in Table 5.6 for all the categories separately. Also, the observed signal strengths and the corresponding uncertainties are shown. The best fit signal strength obtained combining all the categories together is found to be $0.3^{+0.5}_{-0.5}$, corresponding to an observed significance of 0.7σ , to be compared with the expected significance of 2.0σ for a Higgs boson mass of 125 GeV.

Maybe I should add the nuisances impact plots...

Table 5.6.: Observed and expected significance and signal strength the SM Higgs boson with a mass of 125 GeV for the 0-jet and 1-jet, μe and $e\mu$, categories.

Category	Expected significance	Observed significance	σ/σ_{SM}
0-jet μe	1.1	1.3	$1.13^{+0.9}_{-0.9}$
0-jet $e\mu$	1.3	0.4	$0.33^{+0.7}_{-0.7}$
1-jet μe	0.8	0	$-0.11^{+0.5}_{-1.7}$
1-jet $e\mu$	0.9	0	$-0.54^{+1.4}_{-1.4}$
0-jet	1.6	1.3	$0.71^{+0.6}_{-0.5}$
1-jet	1.2	0	$-0.56^{+1.0}_{-1.0}$
Combination	2.0	0.7	$0.33^{+0.5}_{-0.5}$

Chapter 6.

2605 **Search for high mass resonances 2606 decaying to a W boson pair with first 2607 13 TeV LHC data**

2608 **6.1. Introduction**

2609 In this chapter, a search for a high mass spin-0 particle (from now on denoted as X)
2610 in the $X \rightarrow WW \rightarrow \ell\nu\ell'\nu'$ decay channel is presented, where ℓ and ℓ' refer to an different
2611 flavour lepton pair, i.e. $e\mu$. The search is based upon proton-proton collision data samples
2612 corresponding to an integrated luminosity of up to 2.3 fb^{-1} at $\sqrt{s} = 13 \text{ TeV}$, recorded by
2613 the CMS experiment at the LHC during 2015. This analysis represents a general extension
2614 of the SM Higgs boson search presented in 5 and is performed in a range of heavy scalar
2615 masses from $M_X = 200 \text{ GeV}$ up to 1 TeV , extending the range studied in a similar analysis
2616 performed using Run 1 LHC data [113], which provided upper limits on the production
2617 cross section of new scalar resonances up to 600 GeV .

2618 Despite the discovery of a particle consistent with the SM Higgs boson in 2012, there is a
2619 possibility that this particle is only a part of a larger Higgs sector, and hence only partially
2620 responsible of the EW symmetry breaking. This can be achieved in different theoretical
2621 models that extends the SM, such as the two-Higgs-doublet models [114–116], or models in
2622 which the SM Higgs boson mixes with a heavy EW singlet, which predict the existence
2623 of an additional resonance at high mass, with couplings similar to those of the SM Higgs
2624 boson, as most recently described in [117, 118].

2625 This analysis reports a generic search for a scalar particle with different resonance decay
2626 widths hypothesis, produced via the ggH and VBF production mechanisms. The results
2627 can then be interpreted in terms of different theoretical models. This analysis is heavily
2628 based on the SM Higgs search described in 5, in terms of physics objects, selections and
2629 background estimation. The differences and similarities are discussed in this chapter.

2630 **6.2. Data and simulated samples**

2631 The data sets, triggers, pile up reweighting, lepton identification and isolation used in this
2632 analysis are the same as the SM Higgs search and are described in Sec. 5.2.

Also, the same MC simulations are used for the background processes, the only exception being the DY background, for which the MG5_AMC@NLO generator is used with LO QCD accuracy, matching together events with up to four jets in addition to the vector boson with the MLM [119] matching scheme. Given that this analysis aims to probe regions of phase space where the DY contribution is very small, like in the high transverse mass region, the usage of a simulation of the inclusive DY process may lead to large uncertainties due to the limited simulation statistics in the sample. To partially overcome this issue, different DY samples are generated in restricted portions of the phase space defined by the H_T variable, i.e. the scalar sum of all the partons p_T in the event. For $H_T < 100$ GeV the inclusive simulation is used, while different samples are used for higher values of H_T . The samples are merged using the parton level information, and it has been verified that a smooth transition between different H_T regions is achieved, as shown in Fig. 6.1. The DY LO cross section obtained from the simulation is scaled using the LO to NNLO k-factor of 1.23.

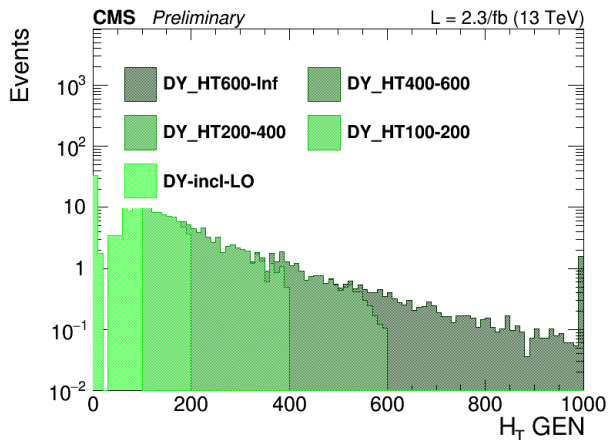


Figure 6.1.: Generator level H_T distribution for the merged DY sample.

In order to perform the resonance search in a large part of the mass spectrum, several signal samples for the gluon-gluon fusion and the vector boson fusion mechanisms have been generated corresponding to different Higgs boson masses in the range between 200 GeV and 1 TeV. The signal width for each mass point corresponds to the one expected for a SM Higgs boson at that mass. The samples are produced with a mass step of 50 GeV from 250 to 800 GeV and of 100 GeV from 800 to 1000 GeV. A finer stepping is used between 200 and 250 GeV. All the signal samples are generated with the POWHEG V2 generator, interfaced with the JHUGEN v6.2.8 generator, which handles the decay of the Higgs boson to $W^+W^- \rightarrow 2\ell 2\nu$.

The interference effects among $gg \rightarrow X \rightarrow WW$, $gg \rightarrow WW$ and $gg \rightarrow H \rightarrow WW$ are evaluated using the MCFM and JHUGEN generators, as implemented in the MELA (Matrix Element Likelihood Approach) framework [94]. Details about the interference effects are given in Sec. 6.3.

2660 6.3. Analysis strategy

2661 The analysis strategy for the first results on the high mass search in the $W^+W^- \rightarrow 2\ell 2\nu$
 2662 decay channel closely follows the strategy presented in the 13 TeV SM Higgs search in the
 2663 $H \rightarrow W^+W^- \rightarrow 2\ell 2\nu$ channel regarding the 0 and 1 jet categories. In addition a dedicated
 2664 category to the VBF production mechanism is added, given that this production mode is
 2665 particularly important in the high mass region. Indeed, assuming a SM Higgs boson, the
 2666 ratio of cross sections $\sigma_{\text{VBF}}/\sigma_{\text{ggH}}^1$ increases with the Higgs boson mass, making the VBF
 2667 production mechanism more and more important as the mass of the resonance approaches
 2668 to high values.

2669 This analysis is affected essentially by the same background processes as the SM Higgs
 2670 boson search, with the difference that in this case the SM Higgs boson processes, including
 2671 all production modes, are treated as backgrounds.

2672 In addition to requiring the events to pass the single or double lepton triggers, exactly
 2673 one electron and one muon are required to be reconstructed in the event with opposite
 2674 charges and a minimum p_T of 20 GeV for both the muon and electron. Both leptons are
 2675 required to be well identified and isolated to reject fake leptons and leptons coming from
 2676 decays in flight. To suppress background processes with three or more leptons in the final
 2677 state, such as diboson or triboson production, events with any additional identified and
 2678 isolated lepton with $p_T > 10$ GeV are rejected. To suppress the contribution of the SM
 2679 production of the Higgs boson at 125 GeV, $m_{\ell\ell}$ is requested to be higher than 50 GeV. The
 2680 other event requirements are identical to the 125 GeV Higgs boson search and are described
 2681 in Sec. 5.3.2.

2682 In addition to the 0 and 1 jet categories, a specific category sensitive to the VBF
 2683 production mode is defined exploiting the characteristic signature of this process, where
 2684 two energetic jets are emitted in the forward region of the detector and with large $\Delta\eta$
 2685 gap. Events belonging to the VBF-enriched category are selected by requiring at least
 2686 two jets with $p_T > 30$ GeV, an invariant mass $m_{jj} > 500$ GeV and a gap in pseudorapidity
 2687 $\Delta\eta_{jj} > 3.5$.

2688 In addition to the transverse mass variable m_T , which is used in the analysis selection
 2689 to define the DY background control region, an additional variable is defined, that from
 2690 now on will be labelled as “improved transverse mass” m_T^i . This variable is defined as
 2691 the invariant mass of the four momentum resulting from the sum of the two leptons four
 2692 momenta ($p_{\ell\ell}, \vec{p}_{\ell\ell}$) and four momentum $\mathbf{E}_T^{\text{miss}} = (E_T^{\text{miss}}, \vec{p}_T^{\text{miss}})$, i.e.:

$$m_T^i = \sqrt{(p_{\ell\ell} + E_T^{\text{miss}})^2 - (\vec{p}_{\ell\ell} + \vec{p}_T^{\text{miss}})^2} \quad . \quad (6.1)$$

2693 This variable allows having a better sensitivity to different resonance mass hypothesis
 2694 as shown in Fig. 6.2, where the shape of the m_T^i variable is shown for different SM Higgs
 2695 mass hypothesis and it is compared to the standard m_T variable. The usage of this variable

¹The ggH notation is used for the gluon-gluon fusion production mode, even in the cases where a non-SM Higgs boson is created in the process.

also provide a good discriminating power between signal and background, which depends on the particular signal mass hypothesis.

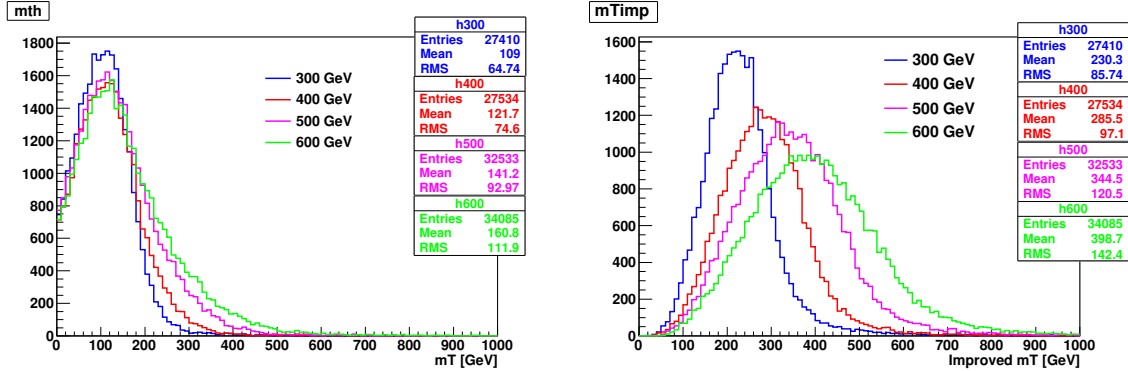


Figure 6.2.: Distribution of the m_T and m_T^i variables at generator level for different resonance mass hypothesis.

The signal extraction is based on a binned maximum likelihood fit using the m_T^i distribution for signal and background contributions as templates. The m_T^i template is defined using the following bin boundaries:

- **0/1 jet:** $[100, 150, 200, 250, 300, 350, 400, 450, 500, 600, 700, 1000]$,
- **VBF:** $[100, 150, 200, 250, 300, 350, 400, 500, 700, 1000]$,

where the first number represents the lower edge of the first bin while the other numbers represent the upper edges. The last bin is an overflow bin.

In order to test different resonance decay widths hypotheses, the signal samples, which are generated with a decay width corresponding to the expected value for a SM Higgs boson at that mass (Γ_{SM}), are reweighted to obtain the desired width value (Γ'). In particular the following values are used: $\Gamma' = \Gamma_{\text{SM}}$, $\Gamma' = 0.49 \times \Gamma_{\text{SM}}$, $\Gamma' = 0.25 \times \Gamma_{\text{SM}}$ and $\Gamma' = 0.09 \times \Gamma_{\text{SM}}$. The reweighting is performed at generator level by computing the ratio of two relativistic Breit Wigner distributions with different decay widths, $f(E, \Gamma', M_X)/f(E, \Gamma_{\text{SM}}, M_X)$, where:

$$f(E) \propto \frac{1}{(E^2 - M^2)^2 + M^2 \Gamma^2} \quad . \quad (6.2)$$

Here, $f(E, \Gamma_{\text{SM}}, M_X)$ represents the distribution used for the simulation of the signal at a mass M_X , and $f(E, \Gamma', M_X)$ the distribution with the new decay width. Each event is multiplied by this ratio (which depends on the energy E of the event) to obtain the reweighted distribution.

When a resonance with a non negligible width is considered, it is important to take into account the interference effects both with the $gg \rightarrow WW$ background and the SM Higgs boson off-shell tail. A study of the interference effects for a resonance X produced through the gluon fusion mechanism is performed within the MCFM+JHUGEN framework, and

including NNLO corrections for cross section using HNNLO program [120] based on MCFM. The matrix element package MELA supports all of these processes and allows fast MC re-weighting and optimal discriminant calculation. The basic idea of this approach is to compute the matrix elements of the processes under study with the MCFM and JHUGEN generators, including the interference terms, and using these matrix elements to compute an event weight used to reweight the simulated samples. Using this approach the simulated events can be reweighted according to different scenarios, for instance including some or all the interference terms, allowing a detailed study of the interference contribution. The effect of the various interference terms for the M_X variable at generator level is shown in Fig. 6.3, after having applied the WW baseline selections. As can be observed the contribution of the interference of the scalar resonance with the $gg \rightarrow WW$ background and with SM Higgs boson have opposite sign and partially cancel out. This cancellation effect is different for different resonance masses and depends on the event selection. In particular the interference term with the SM Higgs off-shell tail is positive for values below M_X while it turns negative above M_X . The contribution of the interference with the $gg \rightarrow WW$ background is instead characterized by an opposite sign lineshape, thus leading to a partial cancellation when considering the total interference.

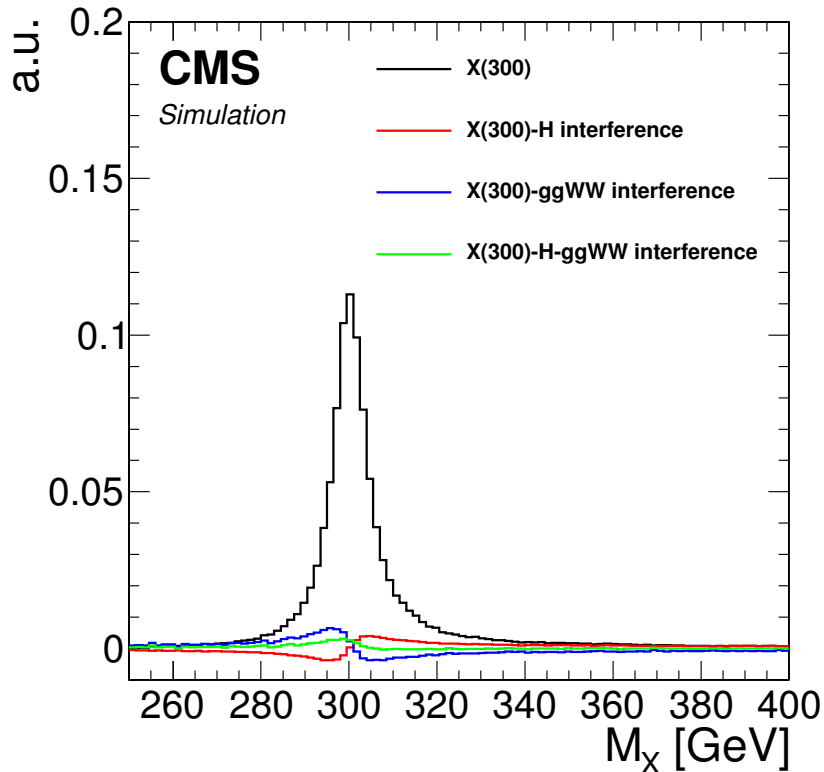


Figure 6.3.: Distribution of the M_X variable for a resonance mass of 300 GeV, showing the various interference terms after the WW baseline selections.

2736 The effect of the resulting interference contribution including all the different terms is
 2737 shown in Fig. 6.4 for the m_T^i signal templates, in the three categories separately and for
 2738 different M_X hypotheses.

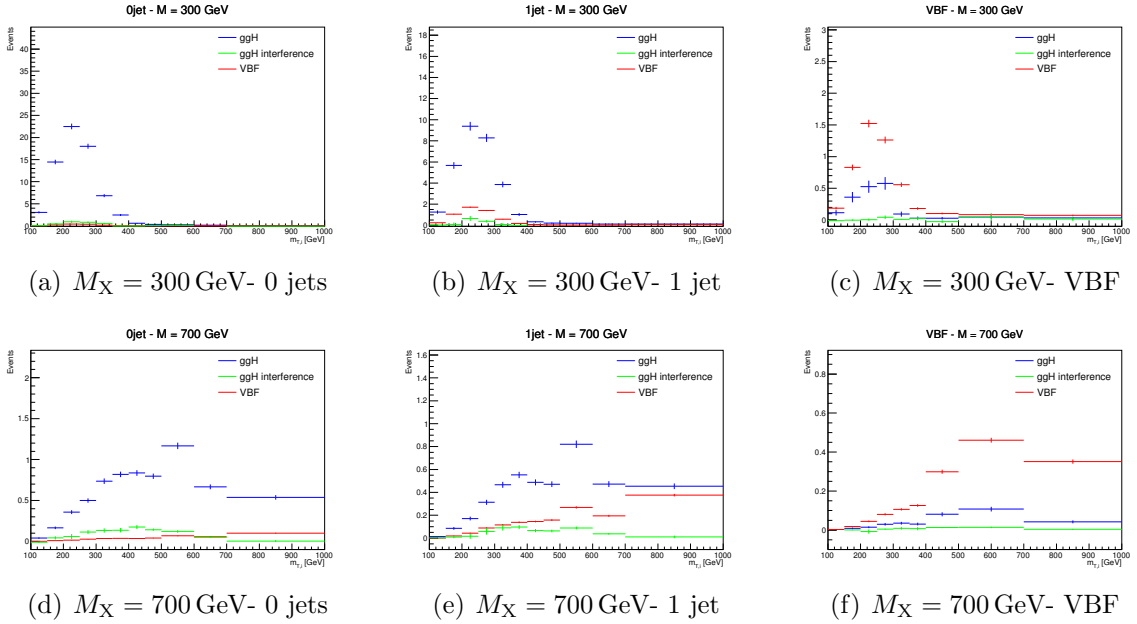


Figure 6.4.: Distributions of the m_T^i variable for $M_X = 300$ and 700 GeV , showing the signal (both the ggH and VBF processes) and the interference contributions in the three jet categories.

2739 The interference contribution is thus not negligible, especially for large values of M_X ,
 2740 and is included in the analysis as part of the signal contribution. More specifically, during
 2741 the fit procedure the signal yield is scaled by the signal strength parameter μ (which is the
 2742 parameter of interest of the fit), while the interference yield is scaled by $\sqrt{\mu}$.

2743 6.4. Background estimation

2744 The background processes affecting the analysis phase space are the same as the ones
 2745 contributing to the SM Higgs search described in Sec. 5.4. The techniques used for the
 2746 background estimation are the same as well.

2747 The most relevant difference is the addition of the 2 jets category. The WW, top
 2748 quark and DY background normalizations are estimated in this category using data driven
 2749 techniques, similarly to the other jet bins.

2750 Given the slightly different WW baseline selection with respect to the SM Higgs search,
 2751 also the control regions for the top quark and DY backgrounds estimation change, while the
 2752 WW background normalization is estimated from data in the three signal regions separately,
 2753 owing to the different m_T^i shapes for signal and background.

For the estimation of the top quark background, three control regions enriched in b-jets are defined by selecting events that pass the WW baseline selections and applying a b tagging requirement which depends on the jet category as follows:

- 0 jets category: at least one b-tagged jet with $20 < p_T < 30$ GeV is required;
- 1 jet category: exactly one b-tagged jet with p_T above 30 GeV is required;
- 2 jets category: at least one b-tagged jet with p_T above 30 GeV is required.

Distributions of the $m_{T,j}^i$ variable in the 0 jets, 1 jet and 2 jets top quark enriched control regions after applying the data driven estimation are shown in Fig. 6.5.

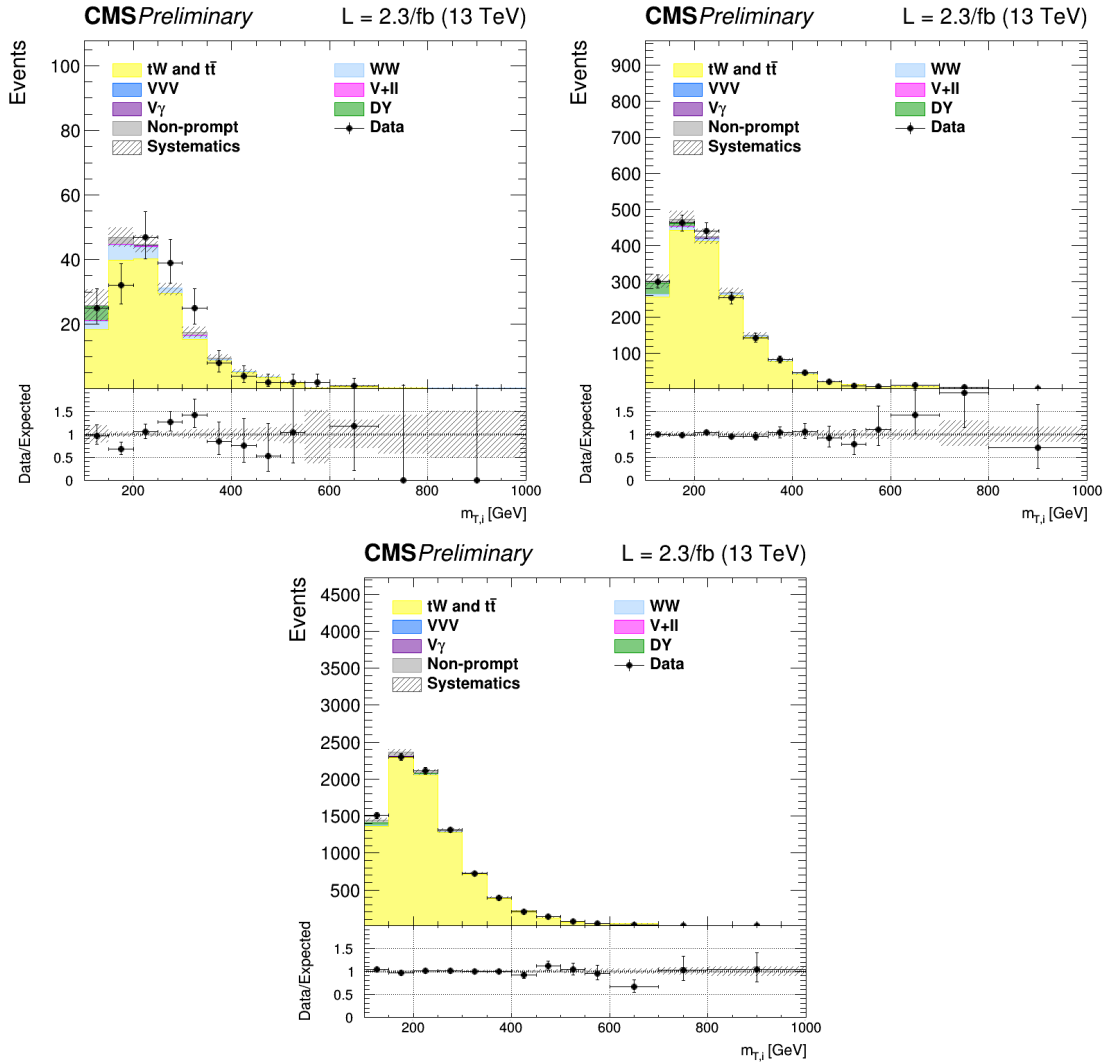


Figure 6.5.: Distributions of $m_{T,j}^i$ for events with 0 jet (top left), 1 jet (top right) and 2 jets (bottom) in top enriched control region. Scale factors estimated from data are not applied in the plots.

2762 The jet induced background, also labelled as “non-prompt” background, so as to highlight
 2763 that these events do not contain prompt leptons, is estimated using the same fake rate
 2764 method described in 4.4.3. A crosscheck is performed selecting events passing the WW
 2765 baseline selection but with an $e\mu$ pair with same charge. The m_T^i distributions for this
 2766 phase space are shown in Fig. 6.6 for the three jet categories separately, showing agreement
 2767 between data and simulation within the uncertainties.

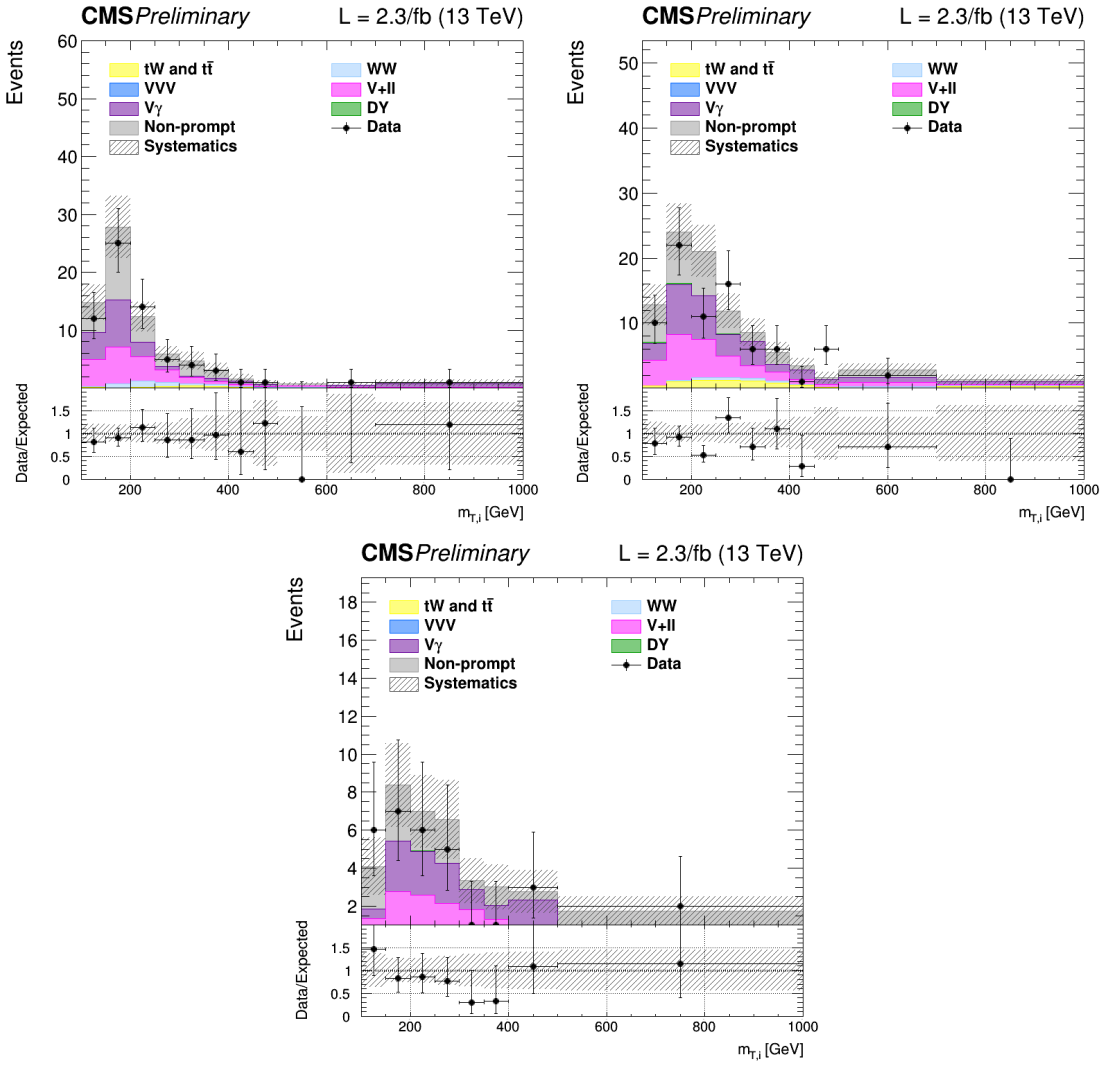


Figure 6.6.: Distributions of m_T^i for events with 0 jet (top left), 1 jet (top right) and 2 jets (bottom) in the same-charge dilepton control region. The last bin of the histograms includes overflows.

2768 Due to the cuts on the leptons p_T and on $m_{\ell\ell}$ in the WW baseline requirements, the
 2769 contribution of the DY background decaying to a pair of τ leptons is very small in the
 2770 signal regions, especially in the VBF phase space. The normalization of this background is
 2771 estimated from a control region in data, defined in the same way as explained in 5.4.4, for

²⁷⁷² the 0 and 1 jet categories. In the VBF category, given the very small number of expected
²⁷⁷³ events, the normalization of this background is taken from simulation.

²⁷⁷⁴ Other minor background processes are estimated as described in 5.4.5.

²⁷⁷⁵ 6.5. Systematic uncertainties

²⁷⁷⁶ The systematic uncertainties affecting this analysis are the same discussed in Sec. 5.5. The
²⁷⁷⁷ differences with respect to the SM Higgs boson search are described below.

²⁷⁷⁸ The PDF and α_s uncertainties on the signal cross sections are taken from the computa-
²⁷⁷⁹ tions performed by the LHC cross section working group [111], and are included for all
²⁷⁸⁰ the mass points. The value of these uncertainties depends on the resonance mass and vary
²⁷⁸¹ from 3 and 5% for ggH and from 2 and 3% for VBF production modes. The PDFs and α_s
²⁷⁸² uncertainties on the signal selection are evaluated for every resonance mass and are found
²⁷⁸³ to be less than 1% for both ggH and VBF.

²⁷⁸⁴ The theoretical uncertainties in the signal yields due to the jet categorization are
²⁷⁸⁵ evaluated for all the ggH signals following the prescription described in Sec. 4.5.3.

²⁷⁸⁶ An additional uncertainty on the modelling of the top pair background is derived from
²⁷⁸⁷ the observed discrepancy between data and POWHEG V2 plus PYTHIA 8.1 simulation
²⁷⁸⁸ on the top quark p_T spectrum [121], which is particularly important in the tail of the m_T^i
²⁷⁸⁹ distribution. Another uncertainty affecting the m_T^i tail for the top quark background is the
²⁷⁹⁰ parton shower uncertainty. This is evaluated comparing the generator level m_T^i distributions
²⁷⁹¹ corresponding to two different simulations of the $t\bar{t}$ process: one obtained using PYTHIA
²⁷⁹² 8.1 for the showering and hadronization of the simulated events, and the other using
²⁷⁹³ HERWIG++. The difference between the two is used to extract a shape uncertainty, which
²⁷⁹⁴ is less than 1% for low m_T^i values and reaches about 6% in the m_T^i tail.

²⁷⁹⁵ 6.6. Signal extraction and limit setting

²⁷⁹⁶ The signal yield, including both the ggH and VBF production modes, is extracted performing
²⁷⁹⁷ a combined fit of the three categories to the m_T^i simulation templates for backgrounds and
²⁷⁹⁸ signal, and is repeated for each resonance mass hypothesis. Moreover, fixed the mass of
²⁷⁹⁹ the resonance, the fit is performed again for the various hypotheses of the resonance decay
²⁸⁰⁰ width. A single signal strength μ is extracted from the fit, which multiplies both the ggH
²⁸⁰¹ and VBF contributions. In other words it is assumed that the ratio of the two production
²⁸⁰² mechanism stays the same as the one predicted by the SM².

²⁸⁰³ The background yields expected from simulation corresponding to the three jet categories
²⁸⁰⁴ and after the analysis event selection are shown in Table 6.1. The signal yields corresponding
²⁸⁰⁵ to a selection of mass points and assuming $\Gamma' = \Gamma_{SM}$ are shown in Table 6.2.

²This is an approximation which limits the amount of models that can be tested with the provided results.

A future development of this analysis will also include the cases for which different ggH and VBF relative contributions are expected.

Table 6.1.: Expected yields estimated from simulation (except for the non-prompt contribution which is estimated using data) for each background process in the three analysis categories, after the analysis event selection. The uncertainties are shown for the processes estimated from simulation.

Background process	0 jets	1 jet	VBF
qq \rightarrow WW	501.93 ± 0.00 (0%)	198.72 ± 0.00 (0%)	4.54 ± 0.00 (0%)
gg \rightarrow WW	37.28 ± 5.77 (15%)	19.63 ± 3.04 (15%)	1.05 ± 0.16 (15%)
Top quark	188.75 ± 0.00 (0%)	330.05 ± 0.00 (0%)	25.06 ± 0.00 (0%)
DY	33.24 ± 0.00 (0%)	12.99 ± 0.00 (0%)	0.28 ± 0.00 (0%)
Non-prompt	64.21 ± 19.26 (30%)	31.69 ± 9.51 (30%)	2.10 ± 0.63 (30%)
V γ	26.62 ± 0.72 (3%)	14.18 ± 0.38 (3%)	0.64 ± 0.02 (3%)
V γ^*	4.44 ± 1.12 (25%)	3.39 ± 0.85 (25%)	0.14 ± 0.04 (25%)
VZ	13.51 ± 0.76 (6%)	11.67 ± 0.66 (6%)	0.28 ± 0.02 (6%)
VVV	0.01 ± 0.00 (3%)	0.02 ± 0.00 (3%)	0.00 ± 0.00 (3%)
SM H \rightarrow WW	6.04 ± 0.40 (7%)	3.10 ± 0.11 (5%)	0.34 ± 0.02 (7%)
SM H \rightarrow $\tau\tau$	0.50 ± 0.05 (9%)	0.43 ± 0.04 (9%)	0.04 ± 0.00 (9%)
Total background	876.5	625.9	34.5

The strategy for computing the exclusion limits is based on the modified frequentist approach, also referred to as CL_s , as described in [110]. The first step is to construct the likelihood function $\mathcal{L}(data|\mu, \theta)$:

$$\mathcal{L}(data|\mu, \theta) = Poisson(data|\mu \cdot s(\theta) + b(\theta)) \cdot p(\tilde{\theta}|\theta) , \quad (6.3)$$

where $data$ represents the experimental observation, s and b are the expected signal and background yields respectively and θ is the full set of nuisance parameters constrained by the prior distribution functions $p(\tilde{\theta}|\theta)$. The default values for the nuisance parameters are labelled as $\tilde{\theta}$.

For a binned shape analysis, $Poisson(data|\mu \cdot s + b)$ is the product of the Poisson probabilities to observe n_i events in bin i :

$$\prod_i \frac{(\mu \cdot s_i + b_i)^{n_i}}{n_i!} e^{-\mu \cdot s_i - b_i} . \quad (6.4)$$

In order to test the compatibility of the data with the signal plus background (or the background only) hypothesis, the test statistic \tilde{q}_μ is constructed based on the profile

Table 6.2.: Expected signal yields for the ggH and VBF production modes estimated from simulation after the analysis event selection for different mass hypothesis assuming $\Gamma' = \Gamma_{\text{SM}}$ in the three analysis categories. The errors correspond to the theoretical uncertainties in the signal estimation.

Mass (GeV)	0 jets	1 jet	VBF
ggH signal yields			
200	90.21 ± 6.67 (7%)	37.47 ± 1.81 (5%)	1.25 ± 0.26 (21%)
400	66.35 ± 4.90 (7%)	32.65 ± 1.57 (5%)	2.04 ± 0.42 (21%)
600	13.86 ± 1.05 (8%)	8.56 ± 0.44 (5%)	0.68 ± 0.14 (21%)
800	3.20 ± 0.25 (8%)	2.32 ± 0.13 (6%)	0.22 ± 0.05 (21%)
1000	0.88 ± 0.07 (8%)	0.70 ± 0.04 (6%)	0.07 ± 0.02 (21%)
VBF signal yields			
200	1.54 ± 0.06 (4%)	6.18 ± 0.25 (4%)	5.05 ± 0.20 (4%)
400	0.91 ± 0.04 (4%)	3.42 ± 0.14 (4%)	3.19 ± 0.13 (4%)
600	0.50 ± 0.02 (4%)	1.95 ± 0.08 (4%)	1.88 ± 0.08 (4%)
800	0.33 ± 0.01 (4%)	1.21 ± 0.05 (4%)	1.16 ± 0.05 (4%)
1000	0.22 ± 0.01 (4%)	0.79 ± 0.03 (4%)	0.69 ± 0.03 (4%)

2817 likelihood ratio:

$$\tilde{q}_\mu = -2 \ln \frac{\mathcal{L}(\text{data}|\mu, \hat{\theta}_\mu)}{\mathcal{L}(\text{data}|\hat{\mu}, \hat{\theta})} \quad \text{with } 0 \leq \hat{\mu} \leq \mu \quad , \quad (6.5)$$

2818 where $\hat{\theta}_\mu$ refers to the conditional maximum likelihood estimators of θ , given the signal
2819 strength μ . The parameter estimators $\hat{\mu}$ and $\hat{\theta}$ correspond to the global maximum of the
2820 likelihood. The $0 \leq \hat{\mu}$ constraint is imposed to have a positive signal yield, e.g. background
2821 underfluctuations are forbidden, while $\hat{\mu} \leq \mu$ is imposed to have a one-sided confidence
2822 interval. The observed test statistic for the signal strength μ under test is referred to as
2823 $\tilde{q}_\mu^{\text{obs}}$. The values of the nuisance parameters obtained maximising the likelihood function are
2824 labelled as $\hat{\theta}_0^{\text{obs}}$ and $\hat{\theta}_\mu^{\text{obs}}$ for the background only and signal plus background hypotheses,
2825 respectively. The pdf of the test statistic is constructed by generating toy MC pseudo-data
2826 for both the background only and signal plus background hypotheses, i.e. $f(\tilde{q}_\mu|\mu, \hat{\theta}_\mu^{\text{obs}})$ and
2827 $f(\tilde{q}_\mu|0, \hat{\theta}_0^{\text{obs}})$. These distributions can be used to define two p-values corresponding to the

2828 two hypotheses, p_μ and p_b :

$$p_\mu = P(\tilde{q}_\mu \geq \tilde{q}_\mu^{\text{obs}} | \text{signal + background}) = \int_{\tilde{q}_\mu^{\text{obs}}}^{\infty} f(\tilde{q}_\mu | \mu, \hat{\theta}_\mu^{\text{obs}}) d\tilde{q}_\mu \quad , \quad (6.6)$$

2829

$$1 - p_b = (\tilde{q}_\mu \geq \tilde{q}_\mu^{\text{obs}} | \text{background only}) = \int_{\tilde{q}_0^{\text{obs}}}^{\infty} f(\tilde{q}_\mu | 0, \hat{\theta}_0^{\text{obs}}) d\tilde{q}_\mu \quad . \quad (6.7)$$

2830 According to these definitions, p_μ and p_b can be identified with CL_{s+b} and $1 - \text{CL}_b$, 2831 respectively. The $\text{CL}_s(\mu)$ is calculated using the following ratio:

$$\text{CL}_s(\mu) = \frac{\text{CL}_{s+b}}{\text{CL}_b} = \frac{p_\mu}{1 - p_b} \quad . \quad (6.8)$$

2832 If, for a given signal strength μ , $\text{CL}_s \leq \alpha$, then the hypothesis is excluded with a $(1 - \alpha)$ 2833 confidence level (CL). For instance, if one wants to quote the upper limit on μ with a 95% 2834 CL, the signal strength has to be adjusted until $\text{CL}_s = 0.05$.

2835 The expected median upper limit, as well as the $\pm 1\sigma$ (68% CL) and $\pm 2\sigma$ (95% CL) 2836 bands, are determined generating a large amount of pseudo-data in the background only 2837 hypothesis and calculating CL_s and the 95% CL upper limit for each of them, as if they 2838 were real data. Then the cumulative distribution of the 95% CL upper limits is built and 2839 the median expected value is identified as the value at which the cumulative distribution 2840 crosses the 50% quantile. The $\pm 1\sigma$ ($\pm 2\sigma$) band is defined by the values at which the 2841 cumulative distribution crosses the 16% (2.5%) and 84% (97.5%) quantiles.

2842 In order to assess the sensitivity of the analysis, the expected upper exclusion limits at 2843 95% CL on the signal strength are shown in Fig. 6.7 for the three jet categories separately. 2844 For a given mass of the resonance, the limits are derived assuming a signal decay width 2845 $\Gamma' = \Gamma_{\text{SM}}$ and a cross section equal to the one expected from a SM Higgs boson at that 2846 mass. The other decay width hypothesis have also been tested, showing a very similar 2847 expected exclusion limit, suggesting that this analysis is not strongly sensitive to variations 2848 of the resonance decay width.

2849 The 0 jets category is the most sensitive especially in the low mass region, while for 2850 very large masses of the resonance the 1 jet and VBF categories start being important. 2851 This is explained mainly by the fact that the VBF contribution increases, with respect to 2852 ggH, as the mass increases. The expected exclusion limit on the signal strength after the 2853 combination of the three categories is shown in Fig. 6.8. Comparing the limits in the single 2854 categories with the combination of the three it is evident how the higher jet multiplicity 2855 categories help in improving the results for large values of M_X .

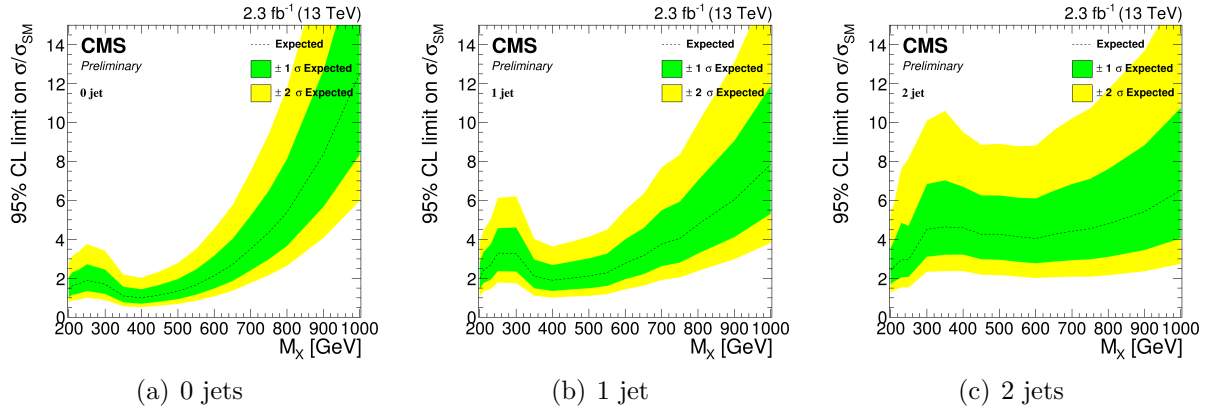


Figure 6.7.: Expected exclusion upper limits at 95% CL on the signal strength in the three categories, as a function of the resonance mass. The dashed line corresponds to median upper limit, while the green and yellow regions represent the $\pm 1\sigma$ and $\pm 2\sigma$ uncertainty bands, respectively. Limits are derived assuming a SM Higgs boson cross section and decay width for each mass point.

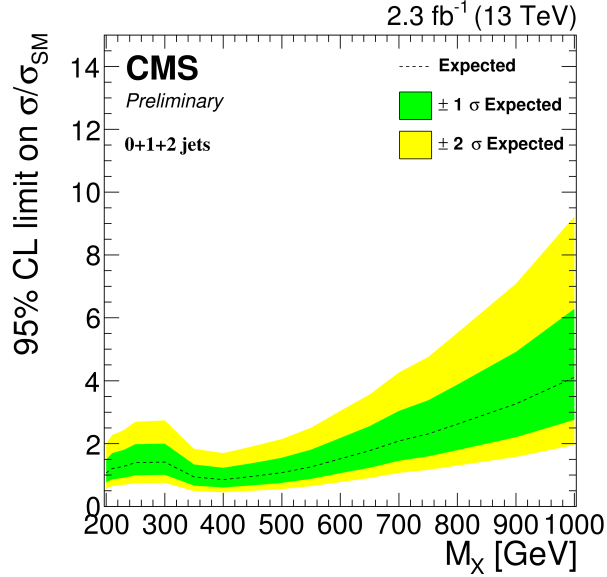


Figure 6.8.: Expected exclusion upper limit at 95% CL on the signal strength for the combination of the three categories, as a function of the resonance mass. The dashed line corresponds to median upper limit, while the green and yellow regions represent the $\pm 1\sigma$ and $\pm 2\sigma$ uncertainty bands. The limit is derived assuming a SM Higgs boson cross section and decay width for each mass point.

2856 6.7. Results

2857 The m_T^i distributions for the signal region after the full analysis selection are shown
 2858 in Fig. 6.9 for the three jet categories. Two different signal hypotheses corresponding

²⁸⁵⁹ to $M_X = 400\text{ GeV}$ and $M_X = 800\text{ GeV}$ are shown superimposed on the background for
²⁸⁶⁰ comparison.

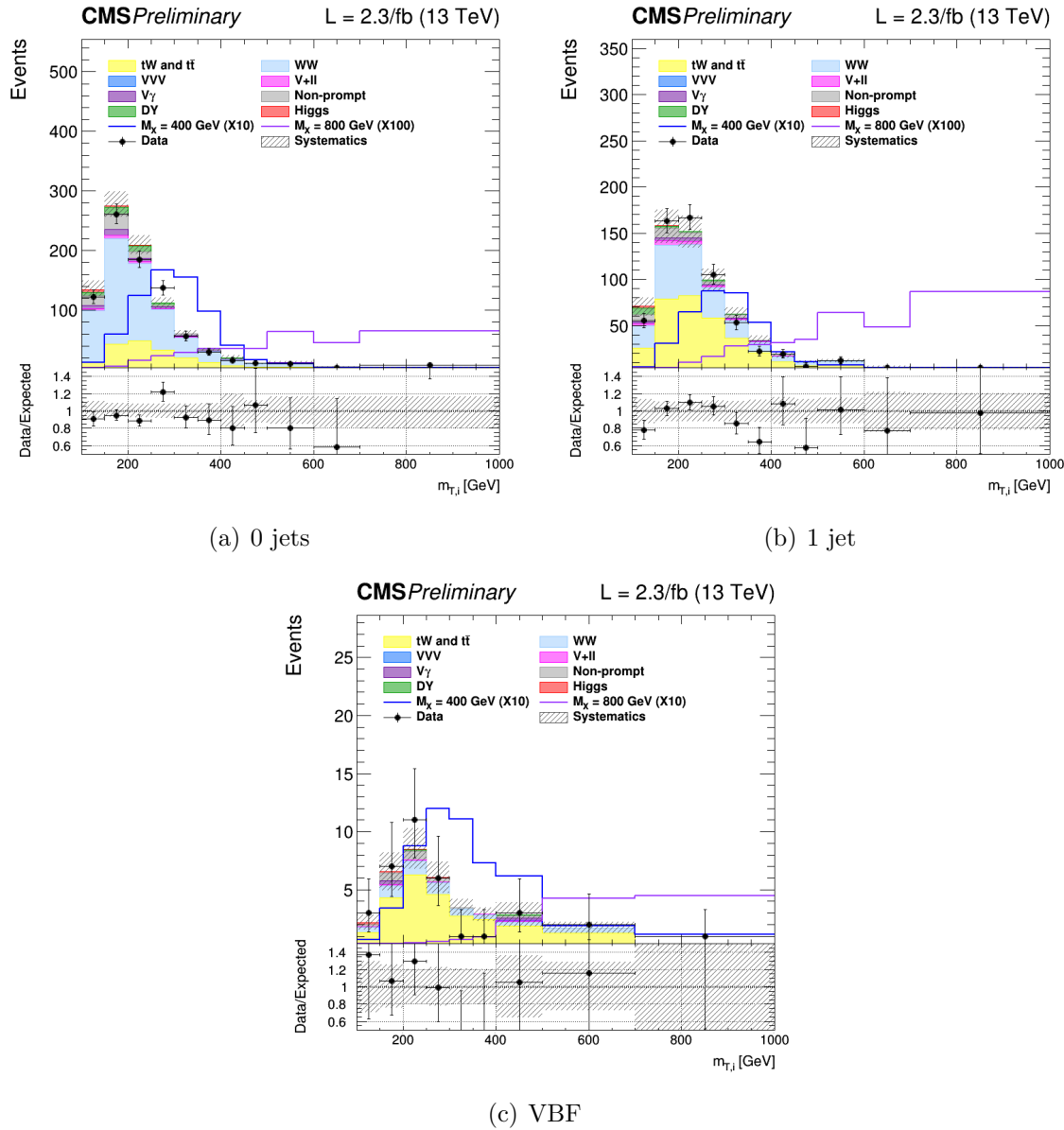


Figure 6.9.: Distributions of m_T^j in the signal region for the 0 jets, 1 jet and VBF categories. Background normalisations correspond to the pre-fit value. Signal contributions for two mass hypotheses, $M_X = 400 \text{ GeV}$ and $M_X = 800 \text{ GeV}$, are shown superimposed on the background and scaled to facilitate the comparison.

For every mass point from 200 GeV up to 1 TeV the observed p-value and the 95% CL upper exclusion limit are calculated for five hypothesis of the signal width. The observed

2863 p-value as a function of the resonance mass for the combination of the three jet categories
2864 is shown in Table 6.3.

Table 6.3.: Observed p-value and corresponding significance (set to 0 in case of underfluctuations of the observed number of events) for the combination of the three jet categories for different resonance masses. Different values of the signal width are shown.

Mass [GeV]	$\Gamma = 0.09 \times \Gamma_{SM}$ p-value (signif.)	$\Gamma = 0.25 \times \Gamma_{SM}$ p-value (signif.)	$\Gamma = 0.49 \times \Gamma_{SM}$ p-value (signif.)	$\Gamma = \Gamma_{SM}$ p-value (signif.)
200	0.50 (0)	0.50 (0)	0.50 (0)	0.56 (0)
210	0.58 (0)	0.45 (0.1)	0.35 (0.4)	0.24 (0.7)
230	0.21 (0.8)	0.22 (0.8)	0.23 (0.7)	0.26 (0.6)
250	0.29 (0.5)	0.20 (0.8)	0.15 (1.0)	0.12 (1.2)
300	0.014 (2.2)	0.015 (2.2)	0.016 (2.1)	0.018 (2.1)
350	0.16 (1.0)	0.17 (1.0)	0.18 (0.9)	0.23 (0.7)
400	0.50 (0)	0.49 (0)	0.49 (0)	0.57 (0)
450	0.51 (0)	0.50 (0)	0.50 (0)	0.52 (0)
500	0.50 (0)	0.51 (0)	0.50 (0)	0.52 (0)
550	0.50 (0)	0.51 (0)	0.51 (0)	0.51 (0)
600	0.50 (0)	0.50 (0)	0.51 (0)	0.51 (0)
650	0.50 (0)	0.50 (0)	0.54 (0)	0.50 (0)
700	0.50 (0)	0.50 (0)	0.50 (0)	0.50 (0)
750	0.50 (0)	0.54 (0)	0.50 (0)	0.40 (0.3)
800	0.50 (0)	0.55 (0)	0.39 (0.3)	0.29 (0.6)
900	0.29 (0.6)	0.27 (0.6)	0.24 (0.7)	0.22 (0.8)
1000	0.18 (0.9)	0.18 (0.9)	0.18 (0.9)	0.18 (0.9)

2865 In order to be independent on the particular model assumed for the signal cross section,
2866 the results are interpreted as exclusion limits on $\sigma \times \mathcal{B}$, where σ stands for the sum of
2867 the ggH and VBF cross sections, and \mathcal{B} represents the $X \rightarrow WW \rightarrow 2\ell 2\nu$ branching ratio
2868 including all lepton flavours. The expected and observed upper exclusion limits on $\sigma \times \mathcal{B}$
2869 for $\Gamma' = \Gamma_{SM}$ are shown in Fig. 6.10.

2870 A mild excess is observed in the 0 jets category and, more evident, in the 1 jet category
2871 around 250-300 GeV. A deficit is instead in the VBF category around 250 GeV, which is
2872 mainly due to an underfluctuation of the background. This effect can be understood looking
2873 at the VBF shape in Fig. 6.9, where two adjacent data points, corresponding to the fifth

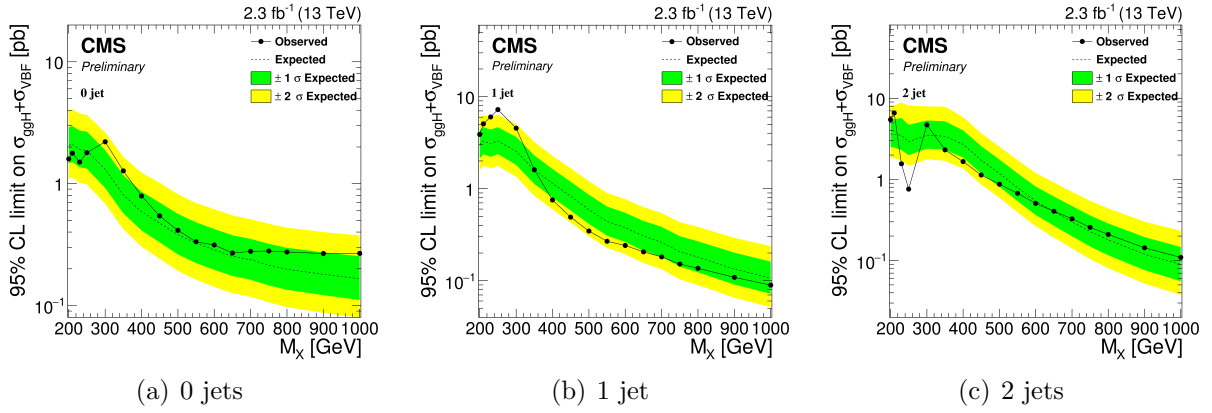


Figure 6.10.: Expected and observed exclusion upper limits at 95% CL on $\sigma \times \mathcal{B}$ in the three categories, as a function of the resonance mass. The dashed line corresponds to median upper limit, while the green and yellow regions represent the $\pm 1\sigma$ and $\pm 2\sigma$ uncertainty bands, respectively. The dotted line represents the observed limit. Limits are derived assuming $\Gamma' = \Gamma_{\text{SM}}$ for each mass point.

and sixth bins, clearly underfluctuate with respect to the background prediction, causing the dip in the observed limit.

The exclusion limit resulting from the combination of the three categories is shown in Fig. 6.11, for the five Γ' hypotheses discussed before. From the combined exclusion limits no significant evidence of a deviation from the SM prediction is observed. The presence of a scalar resonance with $\sigma \times \mathcal{B}$ higher than the values reported in Fig. 6.11 is thus excluded with a 95% CL for masses ranging from 200 GeV up to 1 TeV.

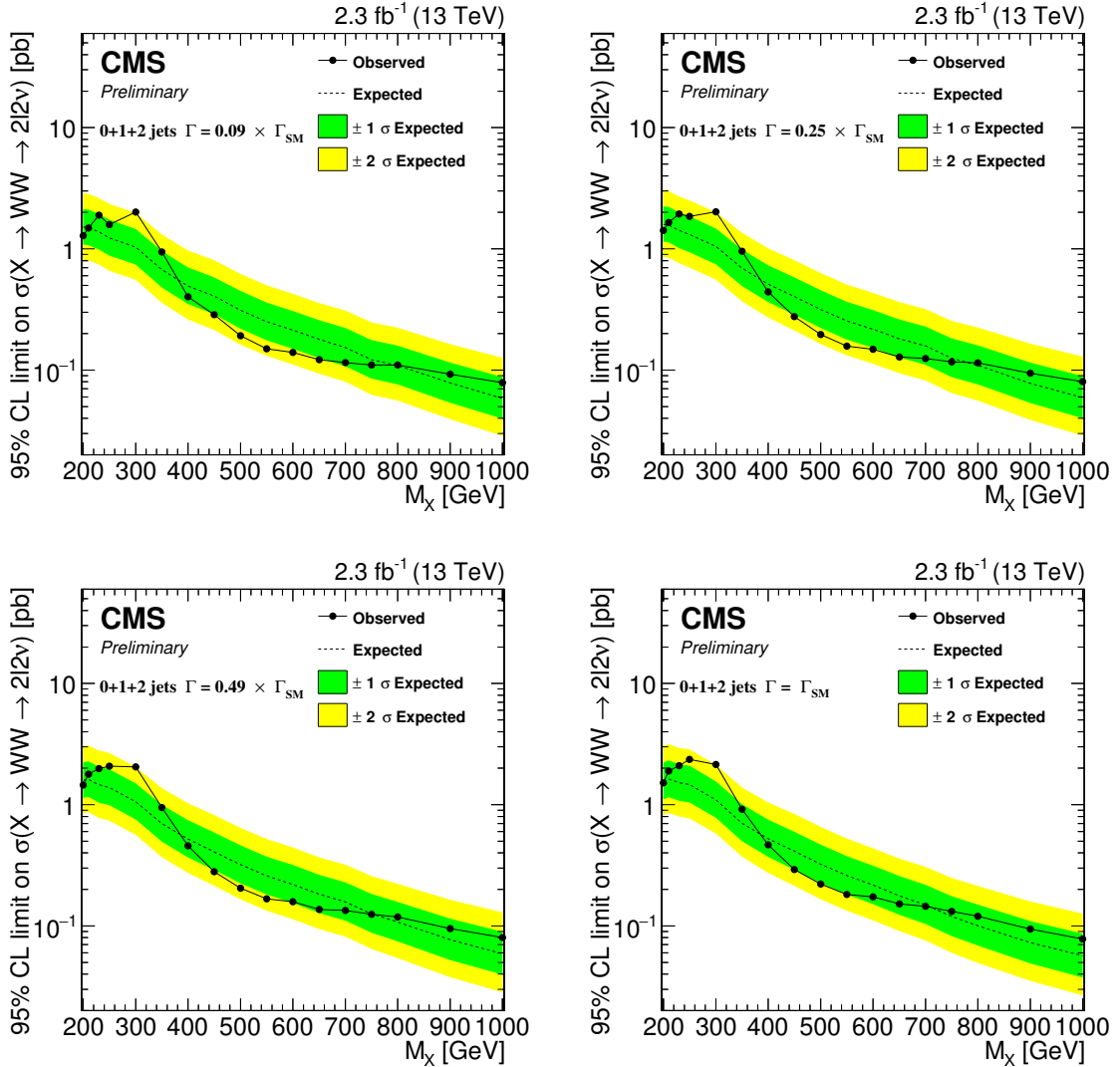


Figure 6.11.: Expected and observed exclusion limits at 95% CL on $\sigma \times \mathcal{B}$ for the combination of the three jet categories as a function of the resonance mass. The black dotted line corresponds to the observed value while the yellow and green bands represent the $\pm 1\sigma$ and $\pm 2\sigma$ uncertainties respectively. Limits are shown for four hypotheses of the resonance decay width.

Chapter 7.

Conclusions

2881

Appendix A.

²⁸⁸² Fiducial region definition and ²⁸⁸³ optimization

²⁸⁸⁴ The fiducial region must be chosen in such a way to be as close as possible to the selections
²⁸⁸⁵ applied in the analysis, in order to reduce the model dependence in the extrapolation step.
²⁸⁸⁶ That means that for optimizing the fiducial volume definition, the efficiency has to be
²⁸⁸⁷ maximized. Another parameter entering the game is the number of fake events, in other
²⁸⁸⁸ words the number of reconstructed events which do not belong to the fiducial phase space.
²⁸⁸⁹ This parameter should instead be as small as possible. Even if we have to observe the trend
²⁸⁹⁰ of these two quantities as a function of p_T^H , we can maximize the ratio between the overall
²⁸⁹¹ efficiency and the overall fake rate as a proxy for establishing the “goodness” of the fiducial
²⁸⁹² region.

²⁸⁹³ Several different fiducial region definitions were tested and the results show that:

- ²⁸⁹⁴ • **of cut:** The fiducial region definition must include only the opposite flavor combination
²⁸⁹⁵ including one electron and one muon. If we include also the combinations involving
²⁸⁹⁶ τ 's the efficiency falls down.
- ²⁸⁹⁷ • **Lepton cut:** Since the resolution on lepton transverse momentum is good, there is no
²⁸⁹⁸ need to loosen the cuts related these variables, i.e. we can use the same cuts defined
²⁸⁹⁹ in the analysis selection ($p_T^{\ell,1} > 20 \text{ GeV}$, $p_T^{\ell,2} > 10 \text{ GeV}$).
- ²⁹⁰⁰ • **Di-lepton p_T cut:** As stated in the previous point, there is no need to loosen this
²⁹⁰¹ cut, so we kept the same value as the analysis selection, i.e. $p_T^{\ell\ell} > 30 \text{ GeV}$.
- ²⁹⁰² • **Di-lepton mass cut:** $m_{\ell\ell} > 12 \text{ GeV}$ as discussed before.
- ²⁹⁰³ • **neutrino pair p_T cut:** Since the resolution on the measurement of the missing
²⁹⁰⁴ transverse energy is poor, the neutrino pair cut should not be included in the definition
²⁹⁰⁵ of the fiducial region, because it would increase the fake rate without increasing the
²⁹⁰⁶ efficiency, thus resulting in a lower ratio between overall efficiency and fake rate.
- ²⁹⁰⁷ • **m_T cut:** Also the m_T cut that we have in the analysis selection, i.e. $m_T > 60 \text{ GeV}$,
²⁹⁰⁸ should be loosened or removed because it involves neutrinos and then increase the
²⁹⁰⁹ fake rate. We decided eventually to keep this cut, loosening it to 50 GeV, because in
²⁹¹⁰ addition to increase the number of fake events, it increases the efficiency as well.

²⁹¹¹ The fake rate and the efficiency as a function of p_T^H after the optimization discussed
²⁹¹² before are shown in figure A.1. To obtain these plots the fiducial region was modified

2913 adding in sequence the various cuts and computing the efficiency and the fake rate each
 2914 time. In that way we can asses the composition of those distributions.

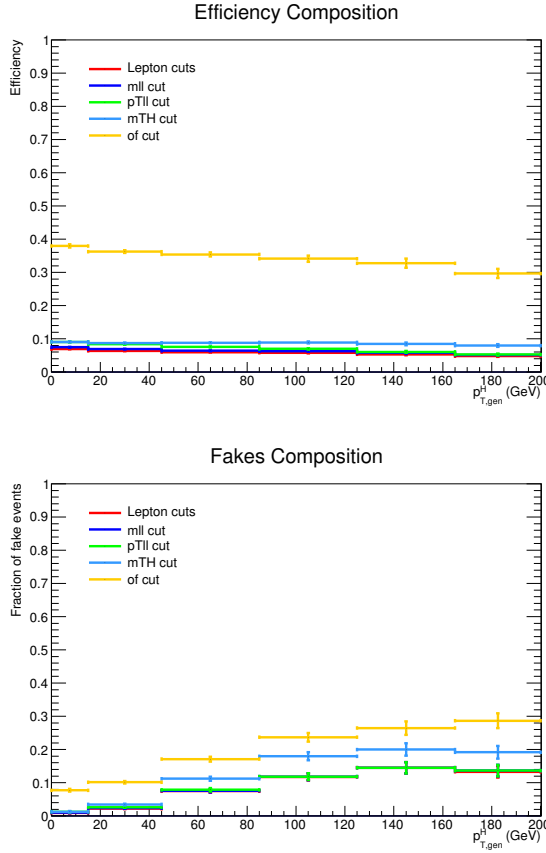


Figure A.1.: Efficiency and fake rate as a function on Higgs transverse momentum. The plots correspond to the optimized fiducial region definition and show the effect of adding each of the mentioned cuts in sequence.

2915 The efficiency and fraction of fake events have been measured also as a function of the
 2916 E_T^{miss} and m_T cuts in the fiducial region. Since these two variables are correlated, the
 2917 results are reported as two-dimensional histograms. In Fig. A.2 are reported the efficiency
 2918 and fraction of fake events for these two variables.

2919 The criterion adopted to define the fiducial region is a tradeoff between having a large
 2920 efficiency and a small fraction of fake events. Especially when looking at the low resolution
 2921 variables, such as E_T^{miss} and m_T , a suitable figure of merit has to be chosen for the estimation
 2922 of the best cuts. Several different figures of merit have been checked, such as ϵ/f , $\epsilon - f$
 2923 and $(1 - f)/\epsilon$. The results for these three different figures of merit are shown in Fig. A.3 as
 2924 a function of the E_T^{miss} and m_T cuts in the fiducial region.

2925 Following the same criterion, similar plots as above have been obtained for an alternative
 2926 model, given by varying up the ggH/VBF ratio within the experimental uncertainties. The

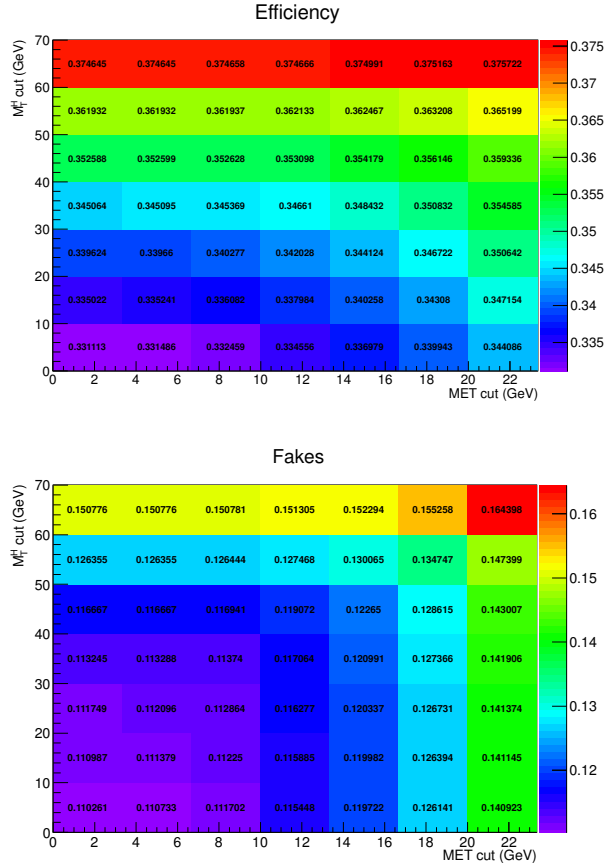


Figure A.2.: Efficiency and fake rate as a function of E_T^{miss} and m_T cuts in the fiducial region.

results, shown in Fig. A.4 and Fig. A.5, show a similar trend with respect to the model with nominal ggH/VBF ratio.

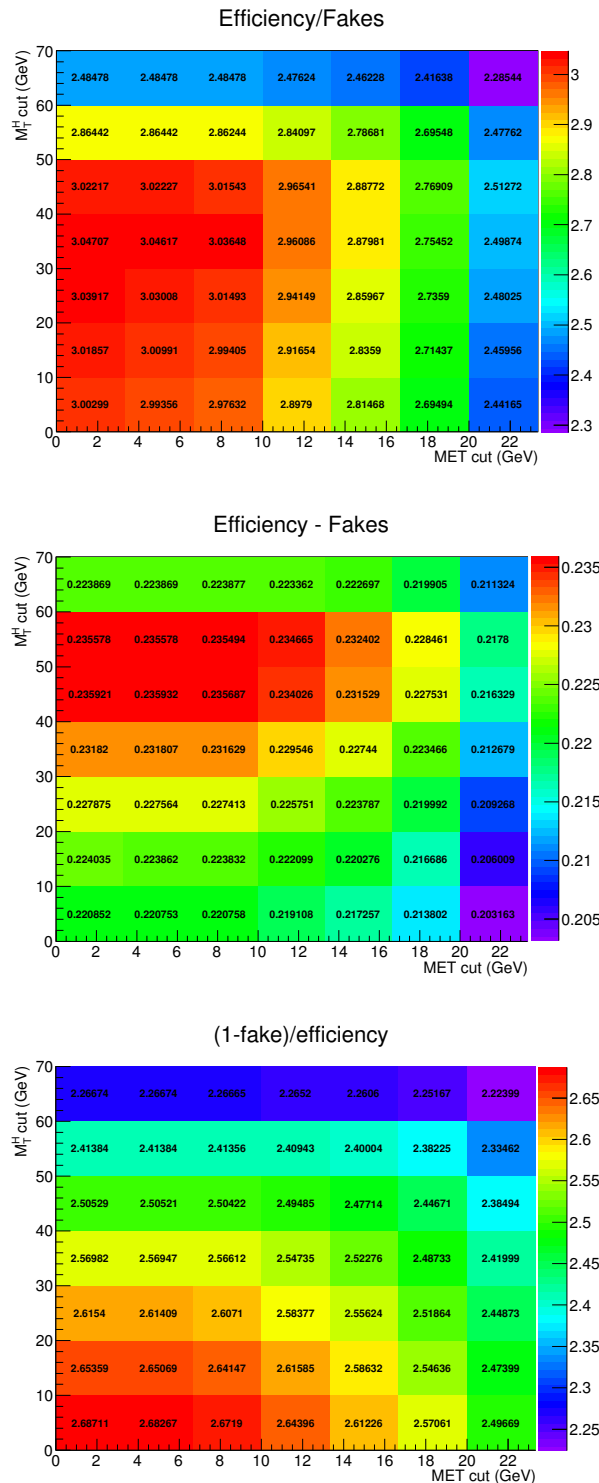


Figure A.3.: Different figures of merit as a function of E_T^{miss} and m_T cuts in the fiducial region.

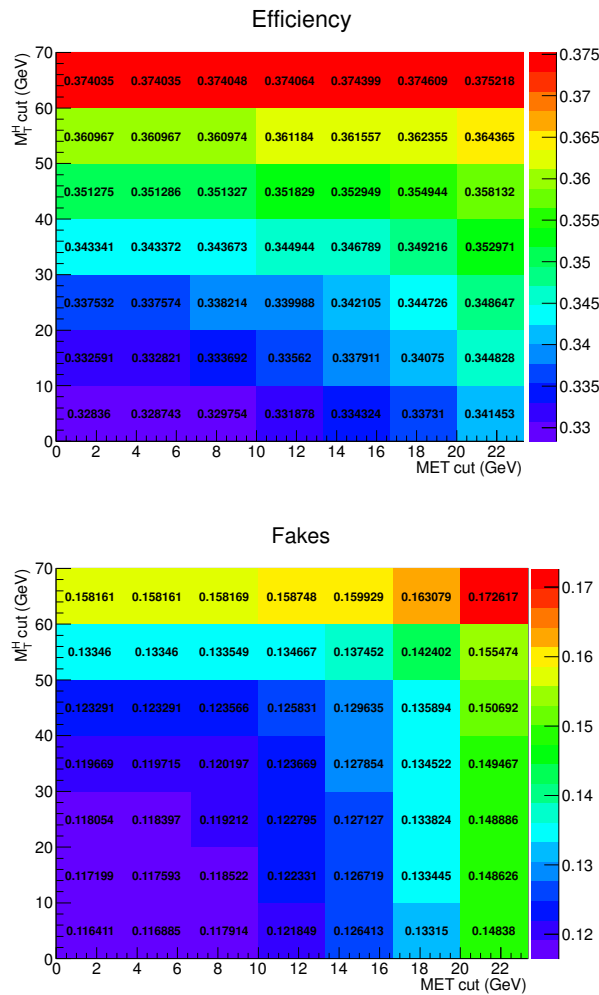


Figure A.4.: Efficiency and fake rate as a function of E_T^{miss} and m_T cuts in the fiducial region, for the alternative model with an up variation of the ggH/VBF ratio.

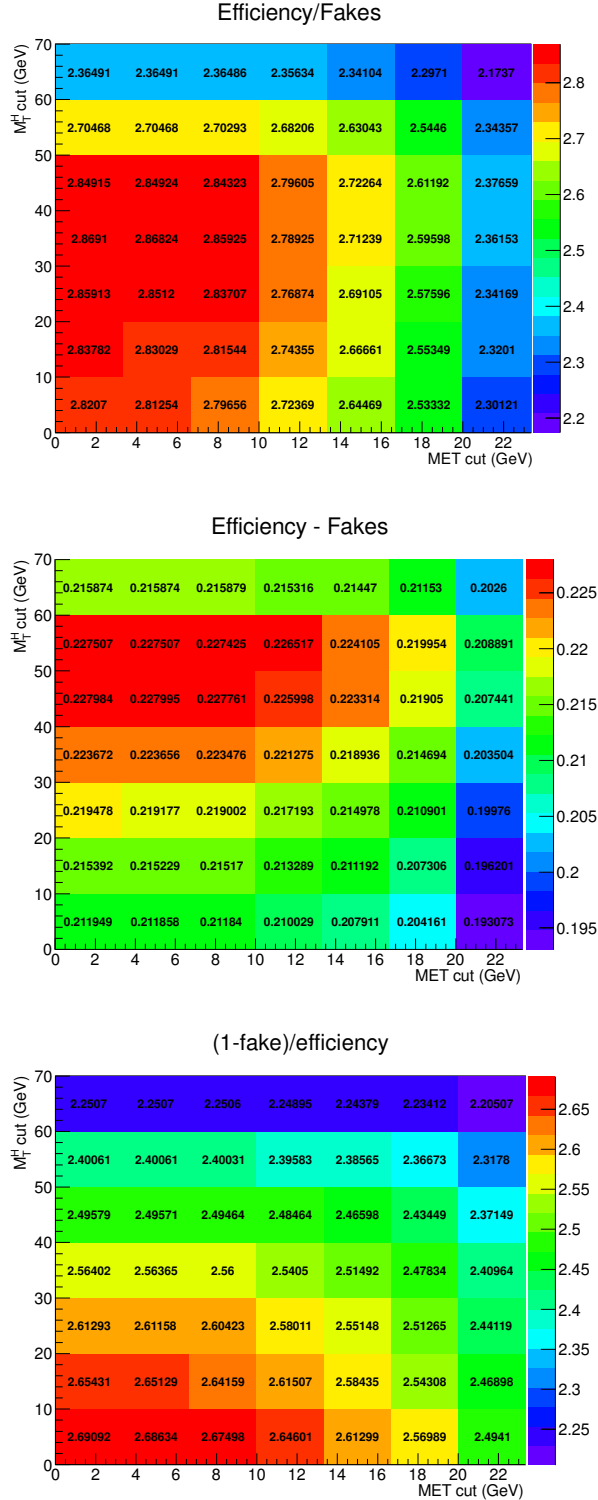


Figure A.5.: Different figures of merit as a function of E_T^{miss} and m_T cuts in the fiducial region, for the alternative model with an up variation of the ggH/VBF ratio.

2930 Bibliography

- 2931 [1] Thomas Sven Pettersson and P Lefèvre. *The Large Hadron Collider: conceptual*
2932 *design*. Tech. rep. CERN-AC-95-05-LHC. Oct. 1995. URL: <http://cds.cern.ch/record/291782>.
- 2934 [2] Oliver Sim Brüning et al. *LHC Design Report*. Geneva: CERN, 2004. URL: <http://cds.cern.ch/record/782076>.
- 2936 [3] Oliver Sim Brüning et al. *LHC Design Report*. Geneva: CERN, 2004. URL: <http://cds.cern.ch/record/815187>.
- 2938 [4] Michael Benedikt et al. *LHC Design Report*. Geneva: CERN, 2004. URL: <http://cds.cern.ch/record/823808>.
- 2940 [5] *LEP design report*. By the LEP Injector Study Group. Geneva: CERN, 1983. URL:
2941 <http://cds.cern.ch/record/98881>.
- 2942 [6] *LEP design report*. Copies shelved as reports in LEP, PS and SPS libraries. Geneva:
2943 CERN, 1984. URL: <http://cds.cern.ch/record/102083>.
- 2944 [7] Carlo Wyss. *LEP design report, v.3: LEP2*. Vol. 1-2 publ. in 1983-84. Geneva: CERN,
2945 1996. URL: <http://cds.cern.ch/record/314187>.
- 2946 [8] S. Chatrchyan et al. “The CMS experiment at the CERN LHC”. In: *JINST* 3 (2008),
2947 S08004. DOI: [10.1088/1748-0221/3/08/S08004](https://doi.org/10.1088/1748-0221/3/08/S08004).
- 2948 [9] G. Aad et al. “The ATLAS Experiment at the CERN Large Hadron Collider”. In:
2949 *JINST* 3 (2008), S08003. DOI: [10.1088/1748-0221/3/08/S08003](https://doi.org/10.1088/1748-0221/3/08/S08003).
- 2950 [10] A. Augusto Alves Jr. et al. “The LHCb Detector at the LHC”. In: *JINST* 3 (2008),
2951 S08005. DOI: [10.1088/1748-0221/3/08/S08005](https://doi.org/10.1088/1748-0221/3/08/S08005).
- 2952 [11] K. Aamodt et al. “The ALICE experiment at the CERN LHC”. In: *JINST* 3 (2008),
2953 S08002. DOI: [10.1088/1748-0221/3/08/S08002](https://doi.org/10.1088/1748-0221/3/08/S08002).
- 2954 [12] G. Anelli et al. “The TOTEM experiment at the CERN Large Hadron Collider”. In:
2955 *JINST* 3 (2008), S08007. DOI: [10.1088/1748-0221/3/08/S08007](https://doi.org/10.1088/1748-0221/3/08/S08007).
- 2956 [13] O. Adriani et al. “The LHCf detector at the CERN Large Hadron Collider”. In:
2957 *JINST* 3 (2008), S08006. DOI: [10.1088/1748-0221/3/08/S08006](https://doi.org/10.1088/1748-0221/3/08/S08006).
- 2958 [14] *The CMS magnet project: Technical Design Report*. Technical Design Report CMS.
2959 Geneva: CERN, 1997. URL: <http://cds.cern.ch/record/331056>.
- 2960 [15] *The CMS electromagnetic calorimeter project: Technical Design Report*. Technical
2961 Design Report CMS. Geneva: CERN, 1997. URL: <http://cds.cern.ch/record/349375>.

- [16] Philippe Bloch et al. *Changes to CMS ECAL electronics: addendum to the Technical Design Report*. Technical Design Report CMS. Geneva: CERN, 2002. URL: <http://cds.cern.ch/record/581342>.
- [17] *The CMS hadron calorimeter project: Technical Design Report*. Technical Design Report CMS. Geneva: CERN, 1997. URL: <http://cds.cern.ch/record/357153>.
- [18] *The CMS muon project: Technical Design Report*. Technical Design Report CMS. Geneva: CERN, 1997. URL: <http://cds.cern.ch/record/343814>.
- [19] S. Dasu et al. “CMS. The TriDAS project. Technical design report, vol. 1: The trigger systems”. In: (2000).
- [20] Sergio Cittolin, Attila Rácz, and Paris Sphicas. *CMS The TriDAS Project: Technical Design Report, Volume 2: Data Acquisition and High-Level Trigger. CMS trigger and data-acquisition project*. Technical Design Report CMS. Geneva: CERN, 2002. URL: <http://cds.cern.ch/record/578006>.
- [21] CMS Collaboration. *Particle-Flow Event Reconstruction in CMS and Performance for Jets, Taus, and E_T^{miss}* . CMS Physics Analysis Summary CMS-PAS-PFT-09-001. 2009. URL: <http://cdsweb.cern.ch/record/1194487>.
- [22] Serguei Chatrchyan et al. “Description and performance of track and primary-vertex reconstruction with the CMS tracker”. In: *JINST* 9.10 (2014), P10009. DOI: [10.1088/1748-0221/9/10/P10009](https://doi.org/10.1088/1748-0221/9/10/P10009). arXiv: [1405.6569 \[physics.ins-det\]](https://arxiv.org/abs/1405.6569).
- [23] Pierre Billoir and S. Qian. “Simultaneous pattern recognition and track fitting by the Kalman filtering method”. In: *Nucl. Instrum. Meth. A* 294 (1990), p. 219. DOI: [10.1016/0168-9002\(90\)91835-Y](https://doi.org/10.1016/0168-9002(90)91835-Y).
- [24] Wolfgang Adam et al. *Reconstruction of Electrons with the Gaussian-Sum Filter in the CMS Tracker at the LHC*. Tech. rep. CMS-NOTE-2005-001. Geneva: CERN, Jan. 2005. URL: <https://cds.cern.ch/record/815410>.
- [25] Serguei Chatrchyan et al. “Performance of CMS muon reconstruction in pp collision events at $\sqrt{s} = 7$ TeV”. In: *JINST* 7 (2012), P10002. DOI: [10.1088/1748-0221/7/10/P10002](https://doi.org/10.1088/1748-0221/7/10/P10002). arXiv: [1206.4071 \[physics.ins-det\]](https://arxiv.org/abs/1206.4071).
- [26] *Electron reconstruction and identification at $\sqrt{s} = 7$ TeV*. Tech. rep. CMS-PAS-EGM-10-004. Geneva: CERN, 2010. URL: <http://cds.cern.ch/record/1299116>.
- [27] Vardan Khachatryan et al. “Performance of Electron Reconstruction and Selection with the CMS Detector in Proton-Proton Collisions at $\sqrt{s} = 8$ TeV”. In: *JINST* 10.06 (2015), P06005. DOI: [10.1088/1748-0221/10/06/P06005](https://doi.org/10.1088/1748-0221/10/06/P06005). arXiv: [1502.02701 \[physics.ins-det\]](https://arxiv.org/abs/1502.02701).
- [28] Gavin P. Salam. “Towards Jetography”. In: *Eur. Phys. J.* C67 (2010), pp. 637–686. DOI: [10.1140/epjc/s10052-010-1314-6](https://doi.org/10.1140/epjc/s10052-010-1314-6). arXiv: [0906.1833 \[hep-ph\]](https://arxiv.org/abs/0906.1833).

- 2999 [29] Gerald C. Blazey et al. “Run II jet physics”. In: *QCD and weak boson physics in*
3000 *Run II. Proceedings, Batavia, USA, March 4-6, June 3-4, November 4-6, 1999.* 2000,
3001 pp. 47–77. arXiv: hep-ex/0005012 [hep-ex]. URL: http://lss.fnal.gov/cgi-bin/find_paper.pl?conf=00-092.
- 3003 [30] Serguei Chatrchyan et al. “Determination of jet energy calibration and transverse
3004 momentum resolution in CMS”. In: *JINST* 6 (2011), P11002. DOI: 10.1088/1748-
3005 0221/6/11/P11002. arXiv: 1107.4277 [physics.ins-det].
- 3006 [31] B. Abbott et al. “Determination of the absolute jet energy scale in the D0 calorimeters”. In: *Nucl. Instrum. Meth.* A424 (1999), pp. 352–394. DOI: 10.1016/S0168-
3007 9002(98)01368-0. arXiv: hep-ex/9805009 [hep-ex].
- 3009 [32] Wolfgang Waltenberger. *Adaptive Vertex Reconstruction*. Tech. rep. CMS-NOTE-
3010 2008-033. Geneva: CERN, July 2008. URL: <https://cds.cern.ch/record/1166320>.
- 3011 [33] M. Spira et al. “Higgs boson production at the LHC”. In: *Nucl. Phys.* B 453
3012 (1995), pp. 17–82. DOI: 10.1016/0550-3213(95)00379-7. arXiv: hep-ph/9504378
3013 [hep-ph].
- 3014 [34] Robert Harlander and Philipp Kant. “Higgs production and decay: Analytic results
3015 at next-to-leading order QCD”. In: *JHEP* 12 (2005), p. 015. DOI: 10.1088/1126-
3016 6708/2005/12/015. arXiv: hep-ph/0509189 [hep-ph].
- 3017 [35] V. Ravindran, J. Smith, and W. L. van Neerven. “NNLO corrections to the total
3018 cross-section for Higgs boson production in hadron hadron collisions”. In: *Nucl.*
3019 *Phys.* B 665 (2003), pp. 325–366. DOI: 10.1016/S0550-3213(03)00457-7. arXiv:
3020 hep-ph/0302135 [hep-ph].
- 3021 [36] Stefano Catani and Massimiliano Grazzini. “An NNLO subtraction formalism in
3022 hadron collisions and its application to Higgs boson production at the LHC”. In:
3023 *Phys. Rev. Lett.* 98 (2007), p. 222002. DOI: 10.1103/PhysRevLett.98.222002.
3024 arXiv: hep-ph/0703012 [hep-ph].
- 3025 [37] Charalampos Anastasiou et al. “Higgs Boson Gluon-Fusion Production in QCD at
3026 Three Loops”. In: *Phys. Rev. Lett.* 114 (2015), p. 212001. DOI: 10.1103/PhysRevLett.
3027 114.212001. arXiv: 1503.06056 [hep-ph].
- 3028 [38] X. Chen et al. “NNLO QCD corrections to Higgs boson production at large transverse
3029 momentum”. In: (2016). arXiv: 1607.08817 [hep-ph].
- 3030 [39] Massimiliano Grazzini and Hayk Sargsyan. “Heavy-quark mass effects in Higgs boson
3031 production at the LHC”. In: *JHEP* 09 (2013), p. 129. DOI: 10.1007/JHEP09(2013)
3032 129. arXiv: 1306.4581 [hep-ph].
- 3033 [40] Aleksandr Azatov and Ayan Paul. “Probing Higgs couplings with high p_T Higgs
3034 production”. In: *JHEP* 01 (2014), p. 014. DOI: 10.1007/JHEP01(2014)014. arXiv:
3035 1309.5273 [hep-ph].

- 3036 [41] Robert V. Harlander and Tobias Neumann. “Probing the nature of the Higgs-gluon
3037 coupling”. In: *Phys. Rev. D* 88 (2013), p. 074015. DOI: 10.1103/PhysRevD.88.
3038 074015. arXiv: 1308.2225 [hep-ph].
- 3039 [42] David Marzocca, Marco Serone, and Jing Shu. “General Composite Higgs Models”.
3040 In: *JHEP* 08 (2012), p. 013. DOI: 10.1007/JHEP08(2012)013. arXiv: 1205.0770
3041 [hep-ph].
- 3042 [43] Andrea Banfi, Adam Martin, and Veronica Sanz. “Probing top-partners in Higgs+jets”.
3043 In: *JHEP* 08 (2014), p. 053. DOI: 10.1007/JHEP08(2014)053. arXiv: 1308.4771
3044 [hep-ph].
- 3045 [44] Georges Aad et al. “Fiducial and differential cross sections of Higgs boson production
3046 measured in the four-lepton decay channel in pp collisions at $\sqrt{s} = 8$ TeV with the
3047 ATLAS detector”. In: *Phys. Lett. B* 738 (2014), p. 234. DOI: 10.1016/j.physletb.
3048 2014.09.054. arXiv: 1408.3226 [hep-ex].
- 3049 [45] Georges Aad et al. “Measurements of fiducial and differential cross sections for Higgs
3050 boson production in the diphoton decay channel at $\sqrt{s} = 8$ TeV with ATLAS”.
3051 In: *JHEP* 09 (2014), p. 112. DOI: 10.1007/JHEP09(2014)112. arXiv: 1407.4222
3052 [hep-ex].
- 3053 [46] Georges Aad et al. “Measurements of the Total and Differential Higgs Boson Production
3054 Cross Sections Combining the $H \rightarrow \gamma\gamma$ and $H \rightarrow ZZ^* \rightarrow 4\ell$ Decay Channels at
3055 $\sqrt{s} = 8$ TeV with the ATLAS Detector”. In: *Phys. Rev. Lett.* 115 (2015), p. 091801.
3056 DOI: 10.1103/PhysRevLett.115.091801. arXiv: 1504.05833 [hep-ex].
- 3057 [47] Vardan Khachatryan et al. “Measurement of differential cross sections for Higgs
3058 boson production in the diphoton decay channel in pp collisions at $\sqrt{s} = 8$ TeV”. In:
3059 *Eur. Phys. J. C* 76 (2016), p. 13. DOI: 10.1140/epjc/s10052-015-3853-3. arXiv:
3060 1508.07819 [hep-ex].
- 3061 [48] Vardan Khachatryan et al. “Measurement of differential and integrated fiducial cross
3062 sections for Higgs boson production in the four-lepton decay channel in pp collisions
3063 at $\sqrt{s} = 7$ and 8 TeV”. In: *JHEP* 04 (2016), p. 005. DOI: 10.1007/JHEP04(2016)005.
3064 arXiv: 1512.08377 [hep-ex].
- 3065 [49] LHC Higgs Cross Section Working Group. *Handbook of LHC Higgs cross sections: 3.
3066 Higgs properties*. CERN Report CERN-2013-004. 2013. DOI: 10.5170/CERN-2013-
3067 004. arXiv: 1307.1347 [hep-ph].
- 3068 [50] Serguei Chatrchyan et al. “Measurement of Higgs boson production and properties
3069 in the WW decay channel with leptonic final states”. In: *JHEP* 01 (2014), p. 096.
3070 DOI: 10.1007/JHEP01(2014)096. arXiv: 1312.1129 [hep-ex].
- 3071 [51] G. Cowan. “A survey of unfolding methods for particle physics”. In: *Conf. Proc.*
3072 C0203181 (2002), p. 248.

- 3073 [52] Michael Krämer, Stephen Mrenna, and Davison E. Soper. “Next-to-leading order
3074 QCD jet production with parton showers and hadronization”. In: *Phys. Rev. D* 73
3075 (2006), p. 014022. DOI: 10.1103/PhysRevD.73.014022. arXiv: hep-ph/0509127
3076 [hep-ph].
- 3077 [53] Stefano Frixione, Paolo Nason, and Carlo Oleari. “Matching NLO QCD computations
3078 with Parton Shower simulations: the POWHEG method”. In: *JHEP* 11 (2007), p. 070.
3079 DOI: 10.1088/1126-6708/2007/11/070. arXiv: 0709.2092 [hep-ph].
- 3080 [54] Nils Lavesson and Leif Lonnblad. “Extending CKKW-merging to one-loop matrix
3081 elements”. In: *JHEP* 12 (2008), p. 070. DOI: 10.1088/1126-6708/2008/12/070.
3082 arXiv: 0811.2912 [hep-ph].
- 3083 [55] Simone Alioli et al. “NLO Higgs boson production via gluon fusion matched with
3084 shower in POWHEG”. In: *JHEP* 04 (2009), p. 002. DOI: 10.1088/1126-6708/2009/
3085 04/002. arXiv: 0812.0578 [hep-ph].
- 3086 [56] Paolo Nason and Carlo Oleari. “NLO Higgs boson production via vector-boson
3087 fusion matched with shower in POWHEG”. In: *JHEP* 02 (2010), p. 037. DOI:
3088 10.1007/JHEP02(2010)037. arXiv: 0911.5299 [hep-ph].
- 3089 [57] Simone Alioli, Sven-Olaf Moch, and Peter Uwer. “Hadronic top-quark pair-production
3090 with one jet and parton showering”. In: *JHEP* 01 (2012), p. 137. DOI: 10.1007/
3091 JHEP01(2012)137. arXiv: 1110.5251 [hep-ph].
- 3092 [58] J. Alwall et al. “The automated computation of tree-level and next-to-leading order
3093 differential cross sections, and their matching to parton shower simulations”. In: *JHEP*
3094 07 (2014), p. 079. DOI: 10.1007/JHEP07(2014)079. arXiv: 1405.0301
3095 [hep-ph].
- 3096 [59] T. Binoth et al. “Gluon-induced W -boson pair production at the LHC”. In: *JHEP*
3097 12 (2006), p. 046. DOI: 10.1088/1126-6708/2006/12/046. arXiv: hep-ph/0611170
3098 [hep-ph].
- 3099 [60] Marco Bonvini et al. “Signal-background interference effects for $gg \rightarrow H \rightarrow W^+W^-$
3100 beyond leading order”. In: *Phys. Rev. D* 88 (2013), p. 034032. DOI: 10.1103/
3101 PhysRevD.88.034032. arXiv: 1304.3053 [hep-ph].
- 3102 [61] Giampiero Passarino. “Higgs CAT”. In: *Eur. Phys. J. C* 74 (2014), p. 2866. DOI:
3103 10.1140/epjc/s10052-014-2866-7. arXiv: 1312.2397 [hep-ph].
- 3104 [62] Torbjörn Sjöstrand, Stephen Mrenna, and Peter Skands. “PYTHIA 6.4 physics and
3105 manual”. In: *JHEP* 05 (2006), p. 026. DOI: 10.1088/1126-6708/2006/05/026.
3106 arXiv: hep-ph/0603175 [hep-ph].
- 3107 [63] Hung-Liang Lai et al. “Uncertainty induced by QCD coupling in the CTEQ global
3108 analysis of parton distributions”. In: *Phys. Rev. D* 82 (2010), p. 054021. DOI:
3109 10.1103/PhysRevD.82.054021. arXiv: 1004.4624 [hep-ph].

- [64] Hung-Liang Lai et al. “New parton distributions for collider physics”. In: *Phys. Rev. D* 82 (2010), p. 074024. DOI: 10.1103/PhysRevD.82.074024. arXiv: 1007.2241 [hep-ph].
- [65] LHC Higgs Cross Section Working Group. “Handbook of LHC Higgs Cross Sections”. In: *arXiv:1101.0593* (2011).
- [66] Simone Alioli et al. “A general framework for implementing NLO calculations in shower Monte Carlo programs: the POWHEG BOX”. In: *JHEP* 06 (2010), p. 043. DOI: 10.1007/JHEP06(2010)043. arXiv: 1002.2581 [hep-ph].
- [67] S. Agostinelli et al. “GEANT4: A simulation toolkit”. In: *Nucl. Instrum. Meth. A* 506 (2003), p. 250. DOI: 10.1016/S0168-9002(03)01368-8.
- [68] D. de Florian et al. “Higgs boson production at the LHC: transverse momentum resummation effects in the $H \rightarrow 2\gamma$, $H \rightarrow WW \rightarrow l\nu l\nu$ and $H \rightarrow ZZ \rightarrow 4l$ decay modes”. In: *JHEP* 06 (2012), p. 132. DOI: 10.1007/JHEP06(2012)132. arXiv: 1203.6321 [hep-ph].
- [69] E. Bagnaschi et al. “Higgs production via gluon fusion in the POWHEG approach in the SM and in the MSSM”. In: *JHEP* 02 (2012), p. 088. DOI: 10.1007/JHEP02(2012)088. arXiv: 1111.2854 [hep-ph].
- [70] Stefano Actis et al. “NLO Electroweak Corrections to Higgs Boson Production at Hadron Colliders”. In: *Phys. Lett. B* 670 (2008), p. 12. DOI: 10.1016/j.physletb.2008.10.018. arXiv: 0809.1301 [hep-ph].
- [71] Stefano Catani et al. “Soft gluon resummation for Higgs boson production at hadron colliders”. In: *JHEP* 07 (2003), p. 028. DOI: 10.1088/1126-6708/2003/07/028. arXiv: hep-ph/0306211 [hep-ph].
- [72] Yanyan Gao et al. “Spin determination of single-produced resonances at hadron colliders”. In: *Phys. Rev. D* 81 (2010), p. 075022. DOI: 10.1103/PhysRevD.81.075022. arXiv: 1001.3396 [hep-ph].
- [73] Sara Bolognesi et al. “Spin and parity of a single-produced resonance at the LHC”. In: *Phys. Rev. D* 86 (2012), p. 095031. DOI: 10.1103/PhysRevD.86.095031. arXiv: 1208.4018 [hep-ph].
- [74] Ian Anderson et al. “Constraining anomalous HVV interactions at proton and lepton colliders”. In: *Phys. Rev. D* 89 (2014), p. 035007. DOI: 10.1103/PhysRevD.89.035007. arXiv: 1309.4819 [hep-ph].
- [75] Torbjorn Sjöstrand, Stephen Mrenna, and Peter Z. Skands. “A Brief Introduction to PYTHIA 8.1”. In: *Comput. Phys. Commun.* 178 (2008), p. 852. DOI: 10.1016/j.cpc.2008.01.036. arXiv: 0710.3820 [hep-ph].
- [76] Vardan Khachatryan et al. “Measurement of the $t\bar{t}$ production cross section in the $e\mu$ channel in proton-proton collisions at $\sqrt{s} = 7$ and 8 TeV”. In: (2016). arXiv: 1603.02303 [hep-ex].

- 3148 [77] Stanislaw Jadach, Johann H. Kuhn, and Zbigniew Was. “TAUOLA: A Library of
3149 Monte Carlo programs to simulate decays of polarized tau leptons”. In: *Comput.
3150 Phys. Commun.* 64 (1990), p. 275. DOI: 10.1016/0010-4655(91)90038-M.
- 3151 [78] CMS Collaboration. “Standard Model Cross Sections for CMS at 7 TeV”. In: *CMS
3152 Generator Group Twiki* (2010).
- 3153 [79] John M. Campbell, R. Keith Ellis, and Ciaran Williams. “Vector boson pair pro-
3154 duction at the LHC”. In: *JHEP* 07 (2011), p. 018. DOI: 10.1007/JHEP07(2011)018.
3155 arXiv: 1105.0020 [hep-ph].
- 3156 [80] J. Ohnemus. “Order alpha-s calculations of hadronic W+- gamma and Z gamma
3157 production”. In: *Phys. Rev.* D47 (1993), pp. 940–955. DOI: 10.1103/PhysRevD.47.
3158 940.
- 3159 [81] JetMET group. “Jet energy uncertainties, [https://twiki.cern.ch/twiki/bin/
3160 view/CMS/JECUncertaintySources#2012_JEC](https://twiki.cern.ch/twiki/bin/view/CMS/JECUncertaintySources#2012_JEC)”. In: (). URL: [https://twiki.cern.
ch/twiki/bin/view/CMS/JECUncertaintySources%5C#2012_JEC](https://twiki.cern.
3161 ch/twiki/bin/view/CMS/JECUncertaintySources%5C#2012_JEC).
- 3162 [82] Sergey Alekhin et al. “The PDF4LHC Working Group Interim Report”. 2011.
- 3163 [83] Michiel Botje et al. “The PDF4LHC Working Group Interim Recommendations”.
3164 2011.
- 3165 [84] Richard D. Ball et al. “Impact of Heavy Quark Masses on Parton Distributions
3166 and LHC Phenomenology”. In: *Nucl. Phys. B* 849 (2011), p. 296. DOI: 10.1016/j.
3167 nuclphysb.2011.03.021. arXiv: 1101.1300 [hep-ph].
- 3168 [85] A. D. Martin et al. “Parton distributions for the LHC”. In: *Eur. Phys. J. C* 63 (2009),
3169 p. 189. DOI: 10.1140/epjc/s10052-009-1072-5. arXiv: 0901.0002 [hep-ph].
- 3170 [86] Iain W. Stewart and Frank J. Tackmann. “Theory uncertainties for Higgs and other
3171 searches using jet bins”. In: *Phys. Rev. D* 85 (2012), p. 034011. DOI: 10.1103/
3172 PhysRevD.85.034011. arXiv: 1107.2117 [hep-ph].
- 3173 [87] “Procedure for the LHC Higgs boson search combination in summer 2011”. In:
3174 (2011).
- 3175 [88] Glen Cowan et al. “Asymptotic formulae for likelihood-based tests of new physics”.
3176 In: *Eur. Phys. J. C* 71 (2011). [Erratum: *Eur. Phys. J.* C73,2501(2013)], p. 1554. DOI:
3177 10.1140/epjc/s10052-011-1554-0, 10.1140/epjc/s10052-013-2501-z. arXiv:
3178 1007.1727 [physics.data-an].
- 3179 [89] Tim Adye. “Unfolding algorithms and tests using RooUnfold”. 2011.
- 3180 [90] Andreas Hocker and Vakhtang Kartvelishvili. “SVD approach to data unfolding”. In:
3181 *Nucl. Instrum. Meth. A* 372 (1996), p. 469. DOI: 10.1016/0168-9002(95)01478-0.
3182 arXiv: hep-ph/9509307 [hep-ph].
- 3183 [91] G. D’Agostini. “A Multidimensional unfolding method based on Bayes’ theorem”.
3184 In: *Nucl. Instrum. Meth. A* 362 (1995), pp. 487–498. DOI: 10.1016/0168-9002(95)
3185 00274-X.

- 3186 [92] Vardan Khachatryan et al. “Precise determination of the mass of the Higgs boson
 3187 and tests of compatibility of its couplings with the standard model predictions using
 3188 proton collisions at 7 and 8 TeV”. In: *Eur. Phys. J. C* 75 (2015), p. 212. DOI:
 3189 10.1140/epjc/s10052-015-3351-7. arXiv: 1412.8662 [hep-ex].
- 3190 [93] Paolo Nason. “A New method for combining NLO QCD with shower Monte Carlo
 3191 algorithms”. In: *JHEP* 11 (2004), p. 040. DOI: 10.1088/1126-6708/2004/11/040.
 3192 arXiv: hep-ph/0409146 [hep-ph].
- 3193 [94] S. Bolognesi, Y. Gao and A.V. Gritsan *et al.* “JHUGen”. In: URL <http://www.pha.jhu.edu/spin/>
 3194 (2011).
- 3195 [95] Gionata Luisoni et al. “ $HW^\pm/HZ + 0$ and 1 jet at NLO with the POWHEG BOX
 3196 interfaced to GoSam and their merging within MiNLO”. In: *JHEP* 10 (2013), p. 083.
 3197 DOI: 10.1007/JHEP10(2013)083. arXiv: 1306.2542 [hep-ph].
- 3198 [96] Tom Melia et al. “W+W-, WZ and ZZ production in the POWHEG BOX”. In: *JHEP*
 3199 11 (2011), p. 078. DOI: 10.1007/JHEP11(2011)078. arXiv: 1107.5051 [hep-ph].
- 3200 [97] T. Gehrmann et al. “ W^+W^- Production at Hadron Colliders in Next to Next to
 3201 Leading Order QCD”. In: *Phys. Rev. Lett.* 113.21 (2014), p. 212001. DOI: 10.1103/
 3202 PhysRevLett.113.212001. arXiv: 1408.5243 [hep-ph].
- 3203 [98] Patrick Meade, Harikrishnan Ramani, and Mao Zeng. “Transverse momentum resum-
 3204 mation effects in W^+W^- measurements”. In: *Phys. Rev.* D90.11 (2014), p. 114006.
 3205 DOI: 10.1103/PhysRevD.90.114006. arXiv: 1407.4481 [hep-ph].
- 3206 [99] Prerit Jaiswal and Takemichi Okui. “Explanation of the WW excess at the LHC
 3207 by jet-veto resummation”. In: *Phys. Rev.* D90.7 (2014), p. 073009. DOI: 10.1103/
 3208 PhysRevD.90.073009. arXiv: 1407.4537 [hep-ph].
- 3209 [100] John M. Campbell, R. Keith Ellis, and Ciaran Williams. “Bounding the Higgs width
 3210 at the LHC: Complementary results from $H \rightarrow WW$ ”. In: *Phys. Rev.* D89.5 (2014),
 3211 p. 053011. DOI: 10.1103/PhysRevD.89.053011. arXiv: 1312.1628 [hep-ph].
- 3212 [101] Richard D. Ball et al. “Parton distributions with QED corrections”. In: *Nucl. Phys.*
 3213 B877 (2013), pp. 290–320. DOI: 10.1016/j.nuclphysb.2013.10.010. arXiv:
 3214 1308.0598 [hep-ph].
- 3215 [102] Richard D. Ball et al. “Unbiased global determination of parton distributions and
 3216 their uncertainties at NNLO and at LO”. In: *Nucl. Phys.* B855 (2012), pp. 153–221.
 3217 DOI: 10.1016/j.nuclphysb.2011.09.024. arXiv: 1107.2652 [hep-ph].
- 3218 [103] Vardan Khachatryan et al. “Event generator tunes obtained from underlying event
 3219 and multiparton scattering measurements”. In: (2015). arXiv: 1512.00815 [hep-ex].
- 3220 [104] Peter Richardson and Alexandra Wilcock. “Monte Carlo Simulation of Hard Radia-
 3221 tion in Decays in Beyond the Standard Model Physics in Herwig++”. In: *Eur. Phys.*
 3222 *J.* C74 (2014), p. 2713. DOI: 10.1140/epjc/s10052-014-2713-x. arXiv: 1303.4563
 3223 [hep-ph].

- 3224 [105] J. Bellm et al. “Herwig++ 2.7 Release Note”. In: (2013). arXiv: 1310.6877 [hep-ph].
- 3225 [106] *SM Higgs production cross sections at $\sqrt{s} = 13\text{--}14 \text{ TeV}$* . <https://twiki.cern.ch/twiki/bin/view/LHCPhysics/CERNYellowReportPageAt1314TeV>.
- 3226
- 3227 [107] Fabrizio Caola et al. “QCD corrections to W^+W^- production through gluon fusion”. In: *Phys. Lett.* B754 (2016), pp. 275–280. DOI: 10.1016/j.physletb.2016.01.046. arXiv: 1511.08617 [hep-ph].
- 3228
- 3229
- 3230 [108] *NLO single-top channel cross sections*. <https://twiki.cern.ch/twiki/bin/view/LHCPhysics/SingleTopRefXsec>.
- 3231
- 3232 [109] *NNLO+NNLL top-quark-pair cross sections*. <https://twiki.cern.ch/twiki/bin/view/LHCPhysics/TtbarNNLO>.
- 3233
- 3234 [110] *Procedure for the LHC Higgs boson search combination in Summer 2011*. Tech. rep. CMS-NOTE-2011-005. ATL-PHYS-PUB-2011-11. Geneva: CERN, Aug. 2011.
- 3235
- 3236 [111] *LHC Higgs Cross Section Working Group*. <https://twiki.cern.ch/twiki/bin/view/LHCPhysics/LHCHXSWG>.
- 3237
- 3238 [112] Jon Butterworth et al. “PDF4LHC recommendations for LHC Run II”. In: *J. Phys.* G43 (2016), p. 023001. DOI: 10.1088/0954-3899/43/2/023001. arXiv: 1510.03865 [hep-ph].
- 3239
- 3240
- 3241 [113] Vardan Khachatryan et al. “Search for a Higgs Boson in the Mass Range from 145 to 1000 GeV Decaying to a Pair of W or Z Bosons”. In: *JHEP* 10 (2015), p. 144. DOI: 10.1007/JHEP10(2015)144. arXiv: 1504.00936 [hep-ex].
- 3242
- 3243
- 3244 [114] G. C. Branco et al. “Theory and phenomenology of two-Higgs-doublet models”. In: *Phys. Rept.* 516 (2012), p. 1. DOI: 10.1016/j.physrep.2012.02.002. arXiv: 1106.0034 [hep-ph].
- 3245
- 3246
- 3247 [115] N. Craig and T. Scott. “Exclusive signals of an extended Higgs sector”. In: *JHEP* 11 (2012), p. 083. DOI: 10.1007/JHEP11(2012)083. arXiv: 1207.4835 [hep-ph].
- 3248
- 3249 [116] H. Haber and O. Stal. “New LHC benchmarks for the CP-conserving two-Higgs-doublet model”. In: *Eur. Phys. J. C* 75 (2015), p. 491. DOI: 10.1140/epjc/s10052-015-3697-x. arXiv: 1507.04281 [hep-ph].
- 3250
- 3251
- 3252 [117] Suyong Choi, Sunghoon Jung, and P. Ko. “Implications of LHC data on 125 GeV Higgs-like boson for the Standard Model and its various extensions”. In: *JHEP* 1310 (2013), p. 225. DOI: 10.1007/JHEP10(2013)225. arXiv: 1307.3948.
- 3253
- 3254
- 3255 [118] Tania Robens and Tim Stefaniak. “Status of the Higgs singlet extension of the standard model after LHC run 1”. In: *Eur. Phys. J. C* 75 (2015), p. 105. DOI: 10.1140/epjc/s10052-015-3323-y. arXiv: 1501.02234 [hep-ph].
- 3256
- 3257
- 3258 [119] Johan Alwall et al. “Comparative study of various algorithms for the merging of parton showers and matrix elements in hadronic collisions”. In: *Eur. Phys. J. C* 53 (2008), pp. 473–500. DOI: 10.1140/epjc/s10052-007-0490-5. arXiv: 0706.2569 [hep-ph].
- 3259
- 3260
- 3261

- 3262 [120] Massimiliano Grazzini. “NNLO predictions for the Higgs boson signal in the $H \rightarrow WW \rightarrow$
3263 $\ell\nu\ell\nu$ and $H \rightarrow ZZ \rightarrow 4\ell$ decay channels”. In: *JHEP* 02 (2008), p. 043. DOI: 10.1088/
3264 1126-6708/2008/02/043. arXiv: 0801.3232 [[hep-ph](#)].
- 3265 [121] Vardan Khachatryan et al. “Measurement of the differential cross section for top
3266 quark pair production in pp collisions at $\sqrt{s} = 8$ TeV”. In: *Eur. Phys. J. C* 75.11
3267 (2015), p. 542. DOI: 10.1140/epjc/s10052-015-3709-x. arXiv: 1505.04480
3268 [[hep-ex](#)].